GEORG-AUGUST-UNIVERSITÄT GÖTTINGEN

GÖTTINGEN GRADUATE SCHOOL OF NEUROSCIENCES, BIOPHYSICS,
AND MOLECULAR BIOSCIENCES (GGNB)
OF THE
GEORG-AUGUST UNIVERSITY SCHOOL OF SCIENCES (GAUSS)
WITHIN THE DOCTORAL PROGRAMME
PHYSICS OF BIOLOGICAL AND COMPLEX SYSTEMS

Impact of mechanically-regulated auxin transport dynamics on plant morphogenesis

---

Dissertation

for the award of the degree "Doctor rerum naturalium"

submitted by
João Rafael Diniz RAMOS

Göttingen, 2021

Thesis Advisory committee

Prof. Dr. Karen Alim
Biological Physics and Morphogenesis
Max Planck Institute for Dynamics and Self-Organization Göttingen
& Technische Universität München

Prof. Dr. Stefan Klumpp
Theoretical Biophysics
Institute for the Dynamics of Complex Systems at the Georg-August-University Göttingen

Prof. Dr. Alexis Maizel
Cell and Developmental Biology
Centre for Organismal Studies Heidelberg

Examination Board

Prof. Dr. Karen Alim (Referee)
Biological Physics and Morphogenesis
Max Planck Institute for Dynamics and Self-Organization Göttingen
& Technische Universität München

Prof. Dr. Stefan Klumpp (Referee)
Theoretical Biophysics
Institute for the Dynamics of Complex Systems at the Georg-August-University Göttingen

Prof. Dr. Alexis Maizel
Cell and Developmental Biology
Centre for Organismal Studies Heidelberg

Prof. Dr. Sebastian Kruss
Physical Chemistry II: Functional materials and bio-systems
Bochum University
& Institute for Physical Chemistry at the Georg-August-University Göttingen

Prof. Dr. Timo Betz
Betz-Lab
3rd Institute of Physics at the Georg-August-University Göttingen

Dr. David Zwicker
Theory of Biological Fluids
Max Planck Institute for Dynamics and Self-Organization Göttingen

Date of oral examination: July 22nd 2021

Abstract

Auxin is a major plant growth regulator whose interaction with cell wall properties is central to its role. Efflux carriers of this phytohormone of the PIN-FORMED family (PIN) respond to the mechanical state of the tissue. As patterns of auxin and of its transport are at the onset of plant morphogenesis, the work herein focuses on how mechanical cues contribute to the auxin flows underlying developmental patterning. We approach this task by developing a vertex model mathematical description of an epithelial tissue and build biophysical models of plant tissue upon it. The mechanical state is perturbed by mechanical property changes induced by auxin, which in turn feeds back onto auxin through the binding of its carriers induced by mechanical stresses within the tissue.

In an abstract setting the model predicts sharper auxin spot patterns and higher PIN polarity, a phenomenon mediated by stress patterns arising from auxin-dependent stiffness gradients. Moreover, we find a more robust distinction of auxin-dependent cell-fate. We show, under this hypothesis, that auxin maxima can exist in cell turgor minima, revealing developmental history to be just as important for predicting auxin maxima. Form these findings we highlight how plant mechanical responses have the potential to strengthen already existing signals.

We then move to lateral root formation as a model system for studying the interactions of auxin flows and mechanics under this hypothesis. We show how cell wall remodelling of endodermal cells alone can potentiate founder cell swelling by implementing a cell wall growth model. By predicting mechanical perturbation effects on auxin of founder cells prior to swelling we found longitudinal stress of walls parallel to the root surface to be crucial for auxin accumulation, highlighting the role of endodermal auxin reflux. By coupling growth and auxin transport, we argue what mechanical state founder cells have to exhibit in order for growth to induce a PIN polarity shift towards the endodermis.

With this work, not only have we highlighted how mechanical auxin transport regulation can positively impact different developmental patterning processes, but we also have made predictions on the lateral root formation system that inspire new approaches, both theoretical and empirical, to test this hypothesis.

Contents

List of Figures

Author's contributions

This thesis contains a published scientific article (in Chapter 4) and its supplementary material (in Appendix E), both without modification.

The published article in Chapter 4 is authored by João Rafael Diniz Ramos, Alexis Maizel, and Karen Alim. JRDR, AM and KA designed research. JRDR performed the research. JRDR, AM and KA wrote the article.

Acknowledgements

As bashful as I am, I will keep it short and sweet.

First, I would like to express my gratitude to Prof. Dr. Karen Alim who gave me this wonderful opportunity, and whose guidance and support were crucial for attaining this achievement. Furthermore, I am thnakful for the freedom afforeded to me in this scientific pursuit. I would also like to show my appreciation to Prof. Dr. Alexis Maizel and Prof. Dr. Stefan Klumpp for tempering the path taken with criticism and encouragement. In particular, I would like to thank Prof. Dr. Alexis Maizel as his expertise played a large role in keeping the project grounded in the biological reality of the systems studied.

My sincere thanks to all members of the Biological Physics and Morphogenesis group, current and former, for their comradery in both research, and outside of it. I would also want to show my appreciation to other students in the Plant Morphodynamics (FOR2581) research unit. On a particular note, I want to thank Komal Bhattacharyya and Mirna Kramar for having put up with me in the same office.

I would like to express my thanks for the warm welcome I received from the Max Planck Institute for Dynamics and Self-Organization, as everything possible was done to acommodate my stay.

My sincerest thanks Barbara Kutz for the unending patience and support provided when faced with forms I seldom have patience for. On a similar vein, I would also like to thank Antje Erdmann and Frauke Bergmann for how smoothly the interaction with the graduate school has been.

Queria agradecer a todas as pessoas que partilharam a sua amizade comigo e me acompanharam até ter partido para esta aventura. Por fim, queria expressar a minha sincera e vasta gratidão à minha família sem a qual não estaria onde estou hoje. Uma gratidão tal, que palavras me falham para a articular.

Chapter 1

Introduction

Morphogenesis is the process by which living beings are shaped. The emergence of tissue shape from a small set of initial cells is a result of cell-cell communication and external cues. Coupling the resulting tissue shape with a pattern of cell differentiation is what enables the complex behaviour responsible for the observed function of living tissues. This joint process, along with a proper growth control so as to maintain an organism's proportions, gives rise to organs, a process often called organogenesis. As a crucial component of developmental biology, a thorough study of morphogenesis is required to reach an understanding of the process known as life, as well as the potential for application of such knowledge. In terms of application, understanding the mechanisms behind morphogenesis can provide insight into several challenges in modern medicine and into a plethora of other emergent phenomena.

Naturally, the regulation of morphogenesis can range from being fine tuned to an extreme degree, with a predictable output due to its criticality, to having the output constrained within a wider, yet acceptable, range for survival. Regulatory defects of morphogenesis during development, therefore, can impact an organism from a minor nuisance up to the failiure to live. Aside from its developmental impact, morphogenesis can also occur to repair damaged tissues, a process often denoted as wound healing [1]. In spite of being necessary for organisms to acquire and maintain their form, morphogenesis can also manifest as a pathology, for instance, as the abnormal growth and shape observed in cancer [2]. Understanding the capacity of specific chemical and physical mechanisms to affect tissue shape is the key to learning how to wield morphogenesis to our benefit. This is, in fact, already the case in the rapidly evolving fields of tissue engineering and regenerative medicine [3–6]. Moreover, succeeding in replicating tissue development *in vitro* would help biophysical research by offering a controllable testing environment closer to the target [7].

The variety of tissue shapes is, by necessity, a product of the spatiotemporal dependence with which cells divide and grow. Patterns of oriented cell divisions give rise to predictable shape [8], for instance, if a cell layer at the surface of a tissue divides perpendicular to it then all cell daughters will belong to the same layer. Regions with different growth rates have the potential to bend the tissue, whether it is a faster patch of growing cells at the tissue surface without anywhere to grow but outwards, or two layers of a tissue having a different growth rate causing the tissue to bend towards the slower growing region. Growth can also be anisotropic, giving rise to tissues of elongated cells. Moreover, external constraints may also play a factor in which shapes a tissue can have. Tissue shape diversity is expanded even further when accounting for modulation due to variations of mechanical properties. Understanding morphogenesis, therefore, includes figuring out how cells can read relative or absolute positional information, be it form external cues or from one another. The origin of differences in behaviour between cells include genetic regulation and, hence, the spatiotemporal dependence often arises via pre-patterning of molecules involved in regulating gene activation or inhibition.

Reaction-diffusion models for different chemical species are famous for their capability of forming spatial patterns of concentration of said molecules. Effectively, the resulting chemical patterns have been proposed as a basis for morphogenesis in the famous article by Alan Turing [9]. A cell capable of distinguishing different states based on the concentration of such interacting chemicals are, therefore, able to distinguish themselves from cells with a different position. Transport models with pattern formation capabilities are not limited to the reaction-diffusion kind. Accounting for active transport of molecules, for instance due to membrane-bound carriers, severely impacts the diversity of ways in which pattern formation can occur. Active matter, in general, offers a plethora of ways phenomena in this category can emerge. For example, motility-induced phase separation can be observed in self-propelled particles by simply assuming a decrease in mobility caused by crowding [10]. To study morphogenesis, therefore, not only includes revealing the cues which tissue cells read, but also how is their transport regulated or, equivalently, how they are communicated.

The current understanding of morphogenesis includes tissue mechanics as another possible environmental cue [11–14]. If cells are able to read and respond to strain or stress, because these two fields depend on tissue shape, then tissue shape is itself information used in its own development. Albeit relatively simple in its conception, its execution is a promising source of shape complexity. This is because, in addition to the already established geometrical dependence, cell division and growth (isotropic or otherwise) would also contribute to mechanical patterning of the tissue. Adopting mechanical cues such as strain or stress, therefore, invites necessarily intertwined feedback mechanisms of largely unknown potential. The study of tissue self-organisation via mechanical cues is an exciting avenue along which to push the field of morphogenesis forward.

Plant tissue is an example of such mechanical coupling, since growth itself is turgor-pressure-driven. Auxin is a phytohormone that plays a major role in coordinating plant responses [15–18], namely cell growth. This molecule is implicated in other processes such as phototropism, gravitropism, and cell differentiation. Plant organ primoridia correlate with increased auxin response factors [19–21]. Auxin patterns, therefore, are currently understood to be the onset of phyllotactic patterning, the ordered arrangement of plant organs [22–24]. High degrees of auxin signalling have also been found to establish the lateral root primordium [25]. In plants, although passive transport of auxin is present, polar auxin flows are mediated by membrane-bound carrier proteins [24, 26, 27]. Patterns of auxin concentration are, therefore, a result of patterns of polar auxin flow, by which we mean patterns of polarity of auxin carriers [22–24]. Uncovering how auxin polar flows are established is critical to understand how to affect auxin patterns and, by extension, plant shape.

To be able to control plant growth and shape is an attractive prospect in regards to the efficiency of agriculture. Mastery of developmental patterning in plants has the potential for controlling yield, by manipulating flower primordia density or size, or quality, by optimisation of foliage structure for sunlight absorption or root structure for nutrient intake. Another approach would be to include the mechanical aspects of plant morphogenesis in already existing auxin treatments [28] so as to improve their efficacy. Furthermore, understanding the factors implicated in plant morphogenesis will enable us to predict changes of plant morphology under different environmental conditions. This is of special importance today in order to better predict the impact of global warming on different ecosystems and on agriculture alike [29]. Lastly, similarly to how chemical patterning inspired mechanisms for auxin pattern generation, study of the mechanisms underlying plant tissue morphogenesis can help inspire and motivate similar mechanisms in other systems.

Several factors contribute to the plant system being an extraordinarily interesting system from a mechanical point of view. Plant cells are capable of generating and withstanding high turgor pressure, regulated by the transport of ions and water between cells [30, 31]. Auxin promotes growth by modulation of cell wall mechanical properties [32]. By interacting with cell wall constituents, it facilitates cell wall's fibres to flow along its length, as to extend it upon constant remodelling, in response to turgor generated wall stress. As it stands, the degree of complexity of mechanical feedback is extraordinary [20, 21, 33]. Due to the heavy impact of mechanics in plant systems, plant development is still puzzling and requires an interdisciplinary approach. Moreover, the hypothesis of mechanically-regulated auxin flows [34, 35], subject to study herein, ties morphogenesis to itself once more resulting in an unknown potential for dynamical behaviour.

1.1 Biophysical role of plant cell constituents

Being eukaryotic, plant cells share organelles with cells from the animal kingdom, including a nucleus, rough and smooth endoplasmatic reticulum, Golgi apparatus, mitochondria, cytoskeletal filaments, and plasma membrane. In addition, plant cells have structures unique to them, namely vacuoles, plastids, and a cell wall composed of cellulose fibres. Chloroplasts are plastids responsible for the photosynthetic capabilities which plants are famous for. The cell wall and the vacuole, however, play a more prominent role in the context of causing, and be subject to, physical cues.

At the expense of mobility, the existence of a cell wall offers structural stability and protection [36, 37], in addition to it being an interface for cell-cell communication. Transport through the cell wall can occur via the apoplastic pathway, freely diffusing around adjacent walls outside the plasma membrane, or via the symplastic way, from cytoplasm to cytoplasm through openings in the cell wall called plasmodesmata. The plasma membrane plays a major role by bridging communication between the cell wall and the intracellular space. The structural integrity of the cell wall derives from how its constituents interact. Cross-linked cellulose microfibrils confer the cell wall with the capacity to endure large turgor and hydrostatic pressures. Hemicellulose and pectin are key players in the cross-linking of cellulose microfibrils. In fact, pectin is a well-known gelling agent responsible for the consistency of jams and marmalade.

The cross-linking present in the cell wall is critical to defining its mechanical properties and, therefore, is involved closely with plant cell elongation [38, 39]. Cell wall growth implies a balance between the rupture of old cross-linking bonds, cellulose synthesis, and the formation of new cross-links. Factors, both chemical and mechanical, that affect cross-linking molecule binding and unbinding rates contribute to cell wall remodelling and, hence, affect cell wall growth [38]. An interesting feature of plants is that cell turgor pressure positively contributes to cell wall growth by straining the cross-link bonds. Models for turgor-driven cell wall growth have been proposed for quite some time [40–42]. Also, necessarily, chemical agents that act to break cellulose cross-links change the mechanical properties of the tissue to some extent [38]. A specific example of such is auxin [43, 44], whose mechanical consequences are explored throughout this work.

To complicate the matter further, cellulose fibres have been shown to have some degree of polarity in regards to their orientation [38, 39, 45]. Therefore, the stiffness of the cell wall is, in general, anisotropic. In plants, cortical microtubules are located at the intracellular side of the plasma membrane and define the orientation of cellulose deposition on the wall [38, 39, 45]. Because strain is implicated in cell wall growth, stiffness anisotropy results in growth anisotropy. Ablation experiments indicate the capacity for microtubules to respond to mechanical stress [46] making cell growth, and by extension plant tissue morphogenesis, even more convoluted. The sheer potential for regulation of plant tissue growth with mechanical factors alone is astounding.

Turgor pressure refers to the hydrostatic pressure generated by water flows caused by osmotic potentials. The existence of open plasmodesmata between cells allow water to flow through the symplastic pathway. Maintaining the plant cell in a turgid state is what allows the plasmatic membrane to remain in contact with, and push against, the cell wall [30]. In this context, the cell wall is also vital to prevent lysis due to the pressure generated. High turgor is required for cell growth, for communicating with neighbouring cells, and for maintaining plants upright, and, therefore, it is the typical and healthy state of plant cells. Maintaining homeostasis, therefore, requires regulation of turgor pressure. Plant cell membranes are equipped with aquaporins, membrane-bound proteins with the function to actively regulate water flows directly [47]. Active ion channels, bound to the plasma membrane play a complementary role in osmoregulation. This is, however, not the end of how plant cells achieve turgor regulation.

The vacuole, aside from its storage and waste disposal functions, plays a key role in regulating turgor pressure. Although deceptively simple, the importance of this mostly water-filled large vesicle hinges on the functionality of its membrane. Namely, aquaporins and ion channels also exist on the membrane of the vacuole [47, 48]. By regulating ion intake, it pressurises the cell through osmotic potential and regulates water uptake by the cell [49]. This organelle is also responsible for maintaining the pH inside the cell at homeostatic levels, affecting the transport of protons through the plasma membrane [48]. One such example is the plant hormone, auxin [50].

Growth, water transport, and mechanics are capable of feedback leading to different topological features of the tissue [31, 51, 52]. The richness of biophysical processes feeding off each other contribute to plant morphogenesis being poorly understood, demanding the careful study of how the processes discussed in this section interact.

1.2 Auxins are plant growth regulators

Auxins are a specific class of plant hormones primarily responsible for promoting cell growth. The most common auxin is indole-3-acetic acid (IAA) [18]. In fact, exogenous application of auxin has been observed to induce flower primordia at the shoot apical meristem [53]. This set of messenger molecules are ubiquitous in all processes related to plant development, for instance many genes involved in the cell cycle are induced by auxin [16]. So much so that auxin is often said to do everything, conveyed with varying degrees of negative emotion. Many plant hormones exist, yet auxin seems unique in that it not only behaves as an hormone, but also as a target of hormonal response [16]. It is also seemingly capable of having tissue-specific action and trigger different types of cell identity [25]. Perhaps, an insightful way to summarise the significance of auxin is that it acts as currency at the cellular level, an analogy entertained by [15, 16]. The full range of auxin action is massive, yet what ultimately happens depends on the entities involved in the transaction and under what circumstances it takes place.

Growth and developmental processes also play a role in coordinating plant responses, for instance plants exhibit tropism as a way to adapt to their environment [54]. Phototropism is the process by which plants reorient their growth in order to optimise sunlight absorption. In fact, auxin was first discovered in this context as the main contributor to the growth heterogeneity causing the plant meristem to bend in response to light [55]. Auxin has also been shown to play a role in gravitropism [56], the bending of roots in response to gravity. Plant development, in contrast to animals, is as much a means for a plant to shape itself and establish the function of its tissues as it is a means of exhibiting behaviour in the course of its life.

The main way auxin can affect cell behaviour is through changes in gene transcription [15, 16, 18]. The main auxin signal transduction pathway is deceptively short. The family of repressors Aux/IAA inhibit the action of transcription factors from the auxin response factor (ARF) family [57]. Together with proteins from the family TIR1/AFB, auxin marks Aux/IAA proteins for degradation [58]. The diversity of auxin response arises because different ARFs activate or repress different genes [59]. Part of the cell type specificity of auxin action is a consequence of ARFs present and in which proportion [15, 16]. Furthermore, because several types of Aux/IAA and AFB proteins exist with different auxin sensitivity and binding affinities [58], different cell types have the potential of perceiving auxin differently. Besides being extremely tuneable, the pathway being short allows for auxin transcriptional response to be detected within a few minutes [60, 61]. Another proposed auxin signalling pathway is via the membrane-bound-auxin-binding protein-1 (ABP1) [62]. The ABP1 pathway has been shown to affect cell growth and is auxin-dependent [63], yet evidence for its physiological significance is controversial [15].

Interestingly enough, responses to auxin of the order of seconds were measured [64], implying auxin signaling is not limited to its transcriptional pathways. There is also evidence for nontranscriptional auxin-induced influx of Ca^{2+} ions by membrane-bound gates affecting growth [15]. A categorically different reason for the assumption of non-transcriptional auxin response is the polarity of its transporters during phyllotaxis. Even if pattern formation is possible by passive transport alone, exclusive transcription regulation of auxin transport lacks symmetry breaking features required for the polarity of auxin flows seen as the cause for patterning [15].

Auxin transcriptional and non-transcriptional action modulates cell wall mechanical properties. As mentioned previously, cell wall composition and remodelling plays a central role in cell growth and elongation. Expression of expansin via ARF7 has been shown to play an important role in promoting cell elongation via its wall loosening capabilities [32].

The acidic pH of auxin contributes to the activation of these specific proteins, as well as pectin demethylesterification which has been shown to alter the mechanical properties of the cell wall drastically [43, 44]. This process of cell elongation via lowering pH is often termed acid growth. Auxin, via TIR1/AFB machinery, promotes the activation of membrane-bound proton channels to further induce acidification of the cell wall. The expression of genes encoding the proteins of proton and potassium channels are also affected by auxin. Balancing the wall loosening effect of auxin with the biosynthesis of wall components is the key to elongating the cell wall without rupture [32, 38, 39]. Lastly, auxin has been shown to regulate aquaporin activity during lateral root emergence [65].

Auxin maxima are, therefore, regions of fast cell growth that define the placement of organ primordia in plants and inform cell fate. Our current understanding of how these auxin patterns occur is by self-organisation of auxin transport [22, 26, 27]. Understanding how auxin transport is regulated is paramount to uncovering the organ placement and, hence, plant morphogenesis (Fig. 1.1).

1.3 Auxin transport mechanisms

Passive diffusion of auxin into the cytoplasm is a passive process. Auxin is a small molecule and, as such, diffuses rapidly inside the cell. Auxin inside the cell is usually in its anionic form due to the pH of the medium and, as such, is unable to passively bypass the plasma membrane [50]. Outside the plasma membrane, because the medium is acid, the anion form and protonated form coexist. The protonated form can bypass the plasma membrane due to being small and apolar. In order for an auxin flow to be established, cells require membrane-bound auxin carriers. For instant, proteins of the AUX1 family are a major membrane-bound importer of anionic auxin [66]. Another set of influx carriers relevant in the root system are members of the LAX family, particularly important during development of lateral roots [67].

These importers, however, are usually apolar and and do not contribute to polar auxin flows. In contrast, the PIN-FORMED (PIN) family are efflux auxin carriers [68] and have been shown to have a polar distribution around plant cells [69]. Patterns of PIN polarity at the shoot apical meristem have been shown to converge on primordia, where DR5 response spikes, an indirect measure of auxin levels [70]. Another layer of complexity is added when we take into account that the gene expression of all transporters mentioned so far is auxin-dependent [23, 59]. The connection between PIN transporters, auxin flows and auxin concentration patterns can be observed throughout most developmental processes of plants [27].

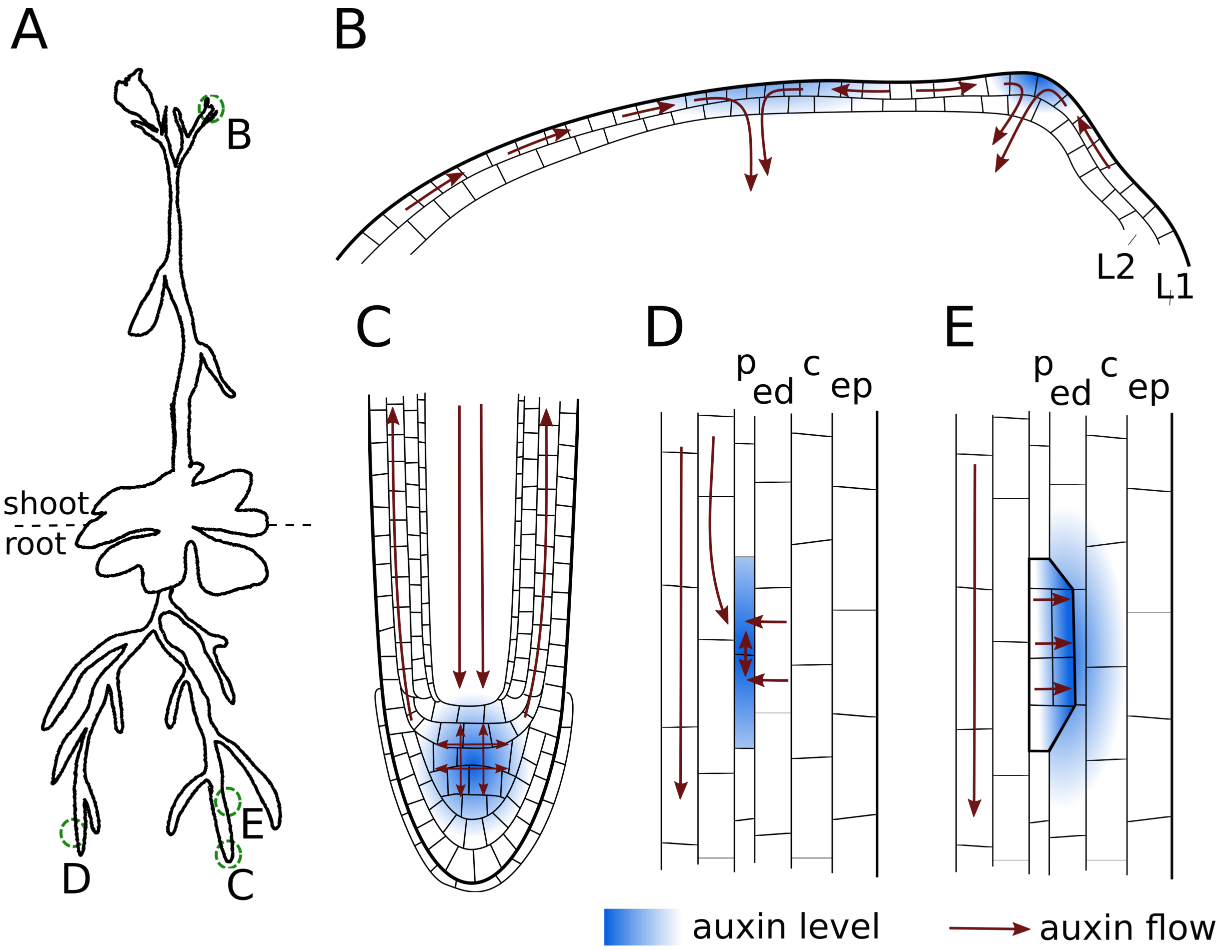

Figure 1.1: Schematic representation of the shoot and root systems of *Arabidopsis thaliana*, as well as auxin patterning examples found therein. (A) The plant can be roughly subdivided into its aerial part, the shoot, and its root system. Developmental phenomena happen in both systems throughout the life of the organism. (B) The shoot apical meristem (only the first two layers, L1 and L2, are depicted) is characterised by high auxin response in the central zone, and auxin spots in the peripheral zone which give rise to leaf and flower primordia. (C) Auxin accumulates in the root meristem allowing for growth, despite the fountain-like auxin flow patterns. (D) Lateral root founder cell identity is triggered by high auxin concentration in the pericycle (p). (E) As the founder cells divide and grow a new auxin gradient is established inside the lateral root primordium. The overlaying layers, endodermis (ed), cortex (c), and epidermis (ep), show auxin response at different stages enabling the mechanical remodelling necessary for the lateral root to emerge.

1.3.1 Polar auxin transport

The shoot apical meristem (SAM) of the *Arabidopsis thaliana pin1-1* mutant, a mutant showing a sharp decrease in polar auxin transport, as well as an auxin-transport-inhibitor-treated vegetative tomato shoot apical meristem, have a meristematic tissue void of primordia [53]. Moreover, exogenous application of auxin in both cases was able to rescue a primordium at the application site. Another interesting result in the same study is, after prolonged exposure to a medium with auxin transport inhibitor, after transferring to a inhibitor-free medium these meristems manifested different phyllotactic patterns. These data show how critical polar auxin transport is to auxin pattern emergence preceding organogenesis and suggest that the process by which PIN polarity is established is self-organised [53, 71].

For self-organisation of auxin transport to occur, we require some sort of auxin flow self-reinforcement. Recently, ARF5, also called *monopteros*, has been shown to be required for the convergence of PIN patterns in the SAM and, hence, localised organogenesis [72]. Furthermore, in the same study, *monopteros* was shown that it acts as a polarising cue for PIN of neighbouring cells. Unfortunately, besides being a result of the TIR1 signalling pathway and its involvement with development, how this response translates into the actual cell-cell communication mechanism is still far from understood. Notwithstanding, auxin-concentration-mediated PIN polarity regulation is an organising principle with the capacity for auxin pattern emergence [73, 74].

Intracellular auxin gradients have been found to determine the position of emerging root hairs in epidermal cells [15]. This alludes to a mechanism of intracellular auxin gradient perception by the plant. In the root epidermis, PIN2 binds to the anticlinal walls of these elongated root cells and, depending on the exact parameters for influx and efflux, an auxin gradient can be established within the cell, with auxin being depleted towards to the efflux carrier high density region. This observation opens up the possibility of PIN molecules being regulated by the internal auxin gradients generated by their own efflux activity. An hypothesis for auxin transport in line with this observation, proposed in the context of formation of vascular tissue upon wound healing [75], is the canalisation model for auxin pattern formation [74], relying on the assumption of auxin flow feeding back on itself. Alternative explanations for this mode of auxin transport include a self-reinforced accumulation of PIN molecules at the plasma membrane modulated by extracellular auxin and ABP1 [76], or through inhibiting endocytosis of PIN molecules [77]. Nevertheless, these hypothetical organising principles underlying PIN regulation have yet to be proven, and evidence for them relies in the observed emerging PIN polarity pattern properties that they share.

Two large classes of auxin transport models emerged while studying this system in detail. Auxin concentration feedback models, with the characteristic behaviour of up-the-gradient auxin flows, and auxin flow feedback models whose patterns exhibit a PIN polarisation with-the-flux [74]. While auxin concentration models capture the auxin spot arrangement typical of developmental patterning in the SAM [71, 73, 78–80], canalisation models have a better track record at describing auxin transport behaviour tied to vascular tissues [81–85]. In this context, understanding morphogenesis requires an in-depth study of how PIN is regulated in order to unify both models, or explain why they cannot be unified. Some attempts have been made to unify these models from a theoretical point of view [84, 86–89]. Although successful to some extent, they requires a lot of layer and tissue specific tuning. Fountain-like patterns during primordia emergence are especially difficult to generate since both up-the-gradient and down-the-gradient auxin flows exist simultaneously. The search for an organisational principle capable of manifesting the whole range of PIN polarity patterns is currently at full throttle.

1.3.2 Mechanical regulation of PIN transporters

The hypothesis here explored is the mechanical regulation of auxin transport. This choice is oozing with potential given the already established link of auxin, mechanics, and growth. Different patterns of strain and stress could explain different PIN flow polarity in different tissues by virtue only of their geometry and architecture. Besides tissue morphology, the capacity for cell wall loosening of auxin offers another way for growth to feedback on itself. The mechanism by which plant cells are capable of perceiving mechanical strain or stress is still being uncovered.

An insightful study in this regard shows evidence for microtubule orientation being regulated by mechanical stress in the SAM. It correlates the observed microtubule orientation with stress patterns predicted solely by geometry [46]. In the same study, ablation experiments show that microtubules orient according to simulated stress patterns of the same experiment, suggesting a causal relationship. There is evidence to suggest that plant cells do indeed read mechanical cues [90]. Curiously, microtubules have been proposed to mediate plant cell mechano-transduction [91]. The microtubule orientation dependence on stress is fascinating in its own right since microtubule orientation defines the orientation of cellulose deposition. This results in a mechanical feedback of stress and anisotropic growth capable of shaping cells around faster growing regions around primordia in the SAM and promoting organ outgrowth [92, 93].

A subsequent study observed PIN polarity patterns and how they correlate with microtubule orientation on a similar setup [34]. PIN molecules were observed to bind to the plasma membrane parallel to microtubule orientation. The same study showed PIN polarity was affected very little when microtubules were disrupted by means of an oryzalin treatment. Furthermore, the kinase PINOID, a known regulator of PIN polarity [94], has been shown to be required for this alignment. By modifying mechanical loads on the shoot apical meristem, mechanical strain and/or stress has been shown to regulate PIN polarity [35]. Not only did this study changed turgor pressure and applied mechanical forces, but also the resulting effects were rescued by each other and via modulation of the mechanical properties of the plasma membrane. This reinforces the idea that the plasma membrane acts as a mediator for the cell. By itself, this new concept for PIN regulation already offers the capacity of growth feedback by cell expansion contributing to auxin transport.

The capacity of auxin modulating cell wall mechanical properties suggests another layer of complexity to this feedback. By softening the cell wall, auxin shifts mechanical stress to the adjacent cell wall of its neighbour. This enables a plant cell a mechanism by which to sense the auxin concentration of its neighbours via stress. The impact of auxin on mechanics and, consequently, PIN polarity has been shown to be sufficient for auxin patterns to emerge [34, 95]. This new model for auxin transport is still in its infancy and, because of its intimate tie to tissue mechanics and shape, has great potential to describe different type of patterns. It might very well be a necessary piece of the auxin transport unification puzzle.

Evidence of this type of PIN regulation is difficult to come by due to its apparent redundancy with other up-the-gradient models, at least in the SAM. Using this model, it is possible to make predictions about auxin pattern formation behaviour in different tissues and subject to different conditions. This allows us to motivate new experiments in order to understand which components of the auxin transport mechanism are indeed mechanically governed. Unfortunately, the techniques necessary to measure mechanics on different tissues, and in tandem with PIN polarity measurements, are still under development.

1.4 Objective and scope

We propose to study the degree to which resulting PIN polarity is affected when considering mechanical regulation, as opposed to other regulatory hypotheses. In line with the aforementioned opportunity, we aim to predict the consequences of the mechanical regulatory hypothesis for PIN polarity. Because of the strong link between auxin transport and growth, to ascertain the morphogenic potential of this model we will consider both. Caution must be taken in this regard, since establishing cause is as difficult as the complexity of the model used. As such, we will first try to draw as much information from the mechanically-regulated auxin transport model alone, and add new pieces as necessary.

The current understanding PIN polarity implies a great degree of interacting components [33], described throughout this chapter (Fig 1.2), whose mechanisms elude us. Even if mechanical regulation is a part of the explanation, or even if it is a considerable one, it is certainly not all of it. One could model all known components of the PIN polarity in hopes of a good description of auxin transport and morphogenesis. Our purpose, however, is arguably the exact opposite, for it is to be able to tell them apart. With this in mind, we opt to limit our scope to mechanically-regulated PIN polarity alone.

Our first task is to build a flexible enough mathematical framework to allow us to describe and model different types of plant tissue. By flexible enough here refers to being able to model different tissues, as well as to be extended to describe biological

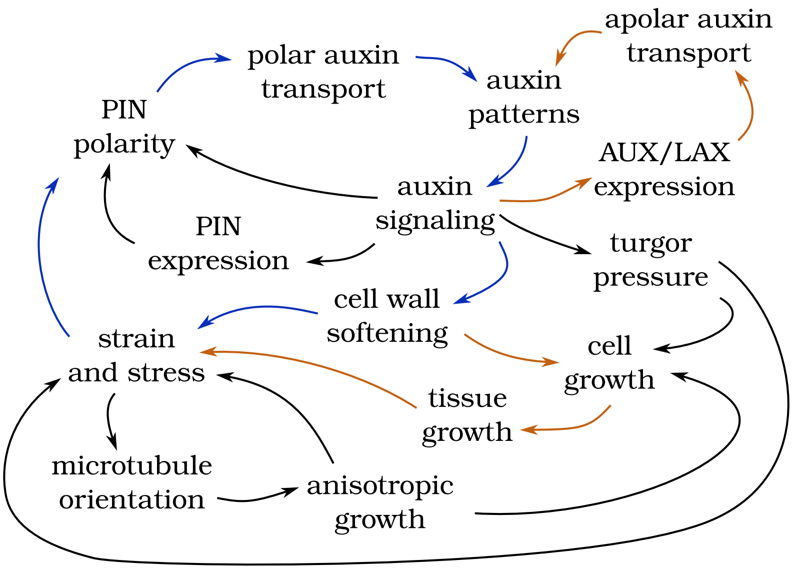

Figure 1.2: Schematic summary of the interactions of tissue mechanics, cell growth, and auxin signalling. Notably, the plant cell water transport module and the PIN canalisation hypothesis are omitted. Among these interactions the most speculative ones are, arguably, auxin signalling affecting turgor through aquaporin regulation, auxin signalling affecting PIN polarity in a different mode, for example via *monopteros*, and the mechanical regulation of PIN polarity. The feedback represented by the blue closed path has been shown to result in auxin spot patterns and will be explored in depth in Chapter 4. As we move to the root (in Chapter 5) we include the interactions in orange, by modelling growth and, for convenience, auxin apolar importers.

processes that follow logically from this work such as cell division. It should also not be constrained to two dimensions since, because of the heavy influence of mechanics in plant morphogenesis, the dimensionality of the problem might be a deciding factor. This will require a careful mathematical descriptions of the tissue as a geometrical, mechanical and biological entity. The description used that combines most of the features we deem worthy of tracking is a vertex model description [96]. On top of the mechanical vertex model, we will adapt the mechanically-regulated auxin transport model from previously established ones [34, 73]. We dedicate Chapter 2 to describe and develop the geometrical basis of the model we intend to use. The chapter after that one, Chapter 3, describes how we introduce mechanical models and auxin transport models in some detail.

In our first deep dive into the model, we cannot help but wonder about the extent to which plant cells benefit from auxin transport mechanical feedback. The explanation for two adjacent cells sharing a single wall is straightforward and has been proposed by [34]. It is less obvious, however, predicting what happens when the whole tissue is considered. Just how much more efficient, or robust, is auxin pattern formation when accounting for mechanics? We will attempt to pose this question more concretely and to come up with an answer to it in Chapter 4. The setting used for this will be more abstract so as to improve the range of applicability of our prediction.

Lateral root formation (LRF) of *Arabidopsis thaliana* is a system whose mechanical signalling has been shown to drive its development from initiation until emergence [97–99]. The richness of mechanical involvement in this system makes it a prime target for a mechanically-regulated auxin transport hypothesis. With our current understanding of the mechanical implications during this process, can we predict auxin flows in this system? Or, conversely, what is mechanically required to happen for auxin flows to be what we observe? These predictions will help us rule out, or corroborate, mechanical PIN regulation in this specific tissue once a protocol for measuring the used observables, or good enough proxies, is established.

Even before the first cell division round of the lateral root primordium (LRP), LRF is filled to the brim with mechanical remodelling and dynamical PIN polarisation. Auxin accumulation in the lateral root founder cells (FCs) has been observed to involve auxin flows from the underlying vasculature as well as reflux from the overlaying cell layers [100]. Being in-line with the up-the-gradient setup, auxin reflux from the endodermis to the FCs might not seem too confusing. The presence of auxin in the endodermis, the layer overlaying the FCs, being required for the signalling cascade that kickstarts lateral root emergence [101], however, is. It might be due to a higher expression of auxin, expression of auxin importers, or simply diffusion. Nevertheless, perhaps we do not need any new assumptions and, therefore, we will tackle this system in Chapter 5. Is mechanically-regulated PIN regulation enough to explain endodermal auxin? What happens to PIN polarity patterns when we include growth? What needs to happen mechanically to the endodermis for FCs to pursue swelling, initiating lateral root emergence? Or, conversely, why do FCs not grow until SHY2 response happens? More details regarding LRF will be outlined when we shift our focus exclusively to that system, in Chapter 5.

Chapter 2

Mathematical description of the tissue

Any mechanical description or integration method relies upon a mathematical description of the tissue. In this section we go through assumptions about tissue topology, the process of describing the tissue, and how to infer geometrical data from the tissue state.

Mathematical tissue modelling has been done in a myriad of ways [102]. One main class of models are those that rely on a lattice underlying the tissue. Depending on the scale, we can have each unit cell of the lattice be a single cell of the tissue, or we could use the lattice for integrating vector and scalar fields be it at a mesoscale or a sub-cellular scale. We could take into account the shape of each cell by tracking the set of lattice elements belonging to each cell and how they evolve. Examples of these types of models include, but not limited to, compartment models [73, 86, 89], cellular automata models [103, 104], phase-field models [105–107], cellular Potts models [108–111].

In contrast, off-lattice models do not require an underlying grid to evolve the system or infer the spatial dependence of quantities ascribed to cells in the tissue. It usually entails integrating forces acting on points representing cells, or parts thereof, in order to evolve the trajectory over time. For instance, cell-center-based models [112, 113] regard cells as points and consider cell-cell interaction potentials, the sub-cellular element method [114, 115] regards a cell as a collection of points interacting with intracellular and extracellular interaction potentials, and vertex models [12, 13, 96, 116–118] that represent the tissue by cell junctions and the connection between between them, representing cell-cell interfaces, and write the mechanical energy of the system as a function of junction coordinates.

In general, tissue modelling need not be spatial, for an interaction network could suffice depending on the target phenomenon. Since we are interested in the evolution of tissue shape, however, we need to concern ourselves with a spatial description. The approach in this work is that of a vertex model and, therefore, we use a polygonal mesh to describe the tissue (Fig. 2.1 top left). This mesh consists of a set of vertices, faces, and edges which correspond to cell junctions, cells, and cell walls, respectively. The tissue state is uniquely defined by vertex positions and any type of mathematical object from which we can infer which vertices are connected by an edge.

2.1 Topology

As novel as it might be to model biological systems in the surface of a Klein bottle, it would be a far more insightful exercise in the field of Mathematics than in the field of Biology and, as such, we restrict our tissues to be an orientable closed two-dimensional manifold embedded in three-dimensional Euclidian space with genus 0. In short, we assume the topology of a spherical surface.

By using a Quad-Edge data structure we ensure that all operations for lattice tessellation preserve the topology of the tissue. The Quad-Edge data structure was described by Guibas and Stolfi [119], where for each edge we save both directed edges and the two directed edges representing the dual edges (Fig. 2.1 top right) Furthermore, for each directed edge we save the origin vertex and the next counter-clockwise edge with the same origin. By composing these movement operations we can traverse the whole surface. Interestingly, iterating around the edges of a single vertex or around the edges of a polygon are trivial to implement. Moreover, Euler operators on vertices and faces are trivial ($O(1)$) operations and correspond to topological transitions of the tissue, for instance cell division, and vertex merging or splitting.

For objects part of the tissue we reserve lower indexing for labelling faces and vertices, and upper indices for components (Fig. 2.1 top left). Furthermore, lower latin indices refer to junctions of the tissue whereas lower greek indices refer to cells of the tissue. At some point in time we will have N vertices and M faces, meaning the indices i and α can take the values $i = 1, \ldots, N$ and $\alpha = 1, \ldots, M$.

In the course of describing the tissue, we will make heavy use of summations around cells and junctions (Fig. 2.1 bottom left). We will denote $\sum_{\gamma \in \mathcal{N}_\alpha}$ as a sum over the edges around cell α where γ is the label of the neighbouring cell. Note that if a cell shares more than one wall with a neighbor, two different terms will appear in the summation, yet refer to the same cell. In this context, we will refer to γ as a neighbouring region of α. The summation is always ordered counter-clockwise (CCW) and has an arbitrary starting edge. Also, $\gamma + 1$ refers to the next CCW edge and $\gamma - 1$ refer to the previous CCW edge. Another recurring summation setup is to focus on the vertices around a polygon. We will adopt a very similar convention as above but for vertices, $\sum_{i \in \mathcal{V}_\alpha}$. In the same way, this sum has an arbitrary starting point and $i + 1$ refers to the next CCW vertex and $i - 1$ refer to the previous CCW vertex. Since we are intimately linked with the tissue's dual, we can just as easily define sums around vertices. Let $\sum_{\gamma \in \mathcal{N}_i}$ represent a sum around all polyhedron faces around junction i in the same CCW fashion. Analogously, we could define $\mathcal{V}_i$ as the CCW ordered set of vertices connected to vertex i, yet we found no need to in the description herein. All presented sums go over each vertex/edge exactly once.

Even though it is somewhat useful to iterate over vertices connected to a specific one we will only need such a sum in the context of a triangulated surface. For this reason we would also like to introduce one last sum, $\sum_{j \in \mathcal{T}_i}$. This will represent a sum over the vertices of a triangulated surface connected to a vertex i of the same triangulated surface. By triangulated surface we mean any surface composed of only triangles fitted to the geometry of the tissue. In our case, we generate the triangulation by taking the centroid of each face, promoting it to a vertex, and connect it to all vertices surrounding each face (Fig. 2.1 bottom right). We use both latin indices in the lower argument of the sum to distinguish from the previous sums, and can assume immediately that i and j are vertices of the triangulated surface.

2.2 Geometry

The variables that define the state of the tissue are the junction positions which we denote by $\boldsymbol{x}_i$. All geometrical quantities will be defined from these position vectors. Most of the time we will end up writing the mechanical energy of the system with only the geometrical quantities involved. This also means that if one were to compute forces by which junctions move, we need to differentiate the geometric quantities defined herein.

2.2.1 Geometrical quantities

Cell perimeter

We define l_{ij} to be the length of a segment that connects junction j to junction i. It is simply the Euclidean distance between two points. In a similar way, we could define edge length as $l_{\alpha\beta}$, $\beta \in \mathcal{N}_\alpha$, as the length of the edge that separates face α from neighbouring region β. The perimeter is, therefore,

$$L_\alpha = \sum_{\beta \in \mathcal{N}_\alpha} l_{\alpha\beta} = \sum_{i \in \mathcal{V}_\alpha} l_{i+1 i}, \qquad\qquad l_{ij} = \left\| \boldsymbol{x}_i - \boldsymbol{x}_j \right\|, \tag{2.1}$$

where $\|\cdot\|$ represents the Euclidean norm of a vector.

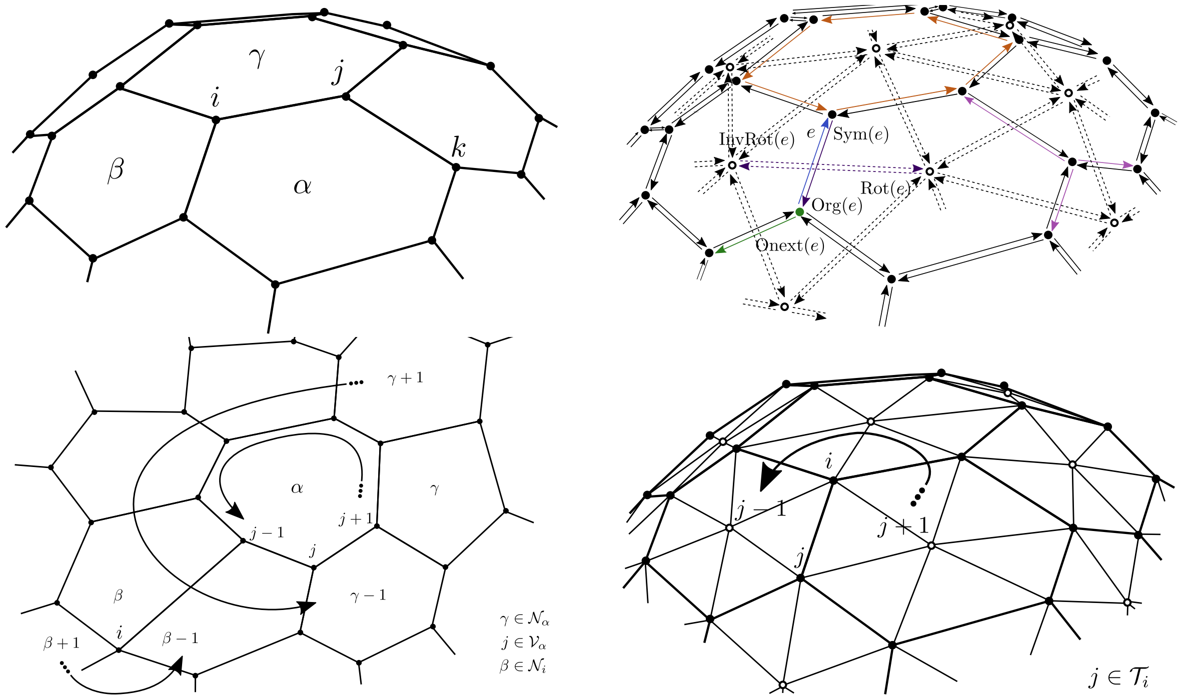

Figure 2.1: Schematic representation of the mathematical structure upon which we build the vertex model. (top left) Tissue representation as a connected graph with the topology of a spherical surface. Vertices (labeled with Latin indices) and the connections between them, which define the faces of the polyhedron (labeled with Greek indices), fully define the tissue geometry. (top right) Quad-edge representation of the tissue used as the basis for all tissue operations of tessellation and transversal. A directed edge (blue) belongs to a structure called quad-edge (purple) containing the directed edges pertaining to the primal graph and its dual. Each directed edge contains information about its origin vertex (or face in the dual version) and the next edge CCW around its origin (green). We can now easily define iterators that traverse the outgoing edges around a vertex (pink) and CCW around a face (orange). (bottom left) A planar tissue can be represented in the same way. To be easier to express geometrical quantities, we will introduce the sets of vertices and faces around a specific face ($\mathcal{V}_\alpha$ and $\mathcal{N}_\alpha$ respectively), as well as faces around a specific vertex ($\mathcal{N}_i$). All these set definitions follow immediately from the defined quad-edge iterators. (bottom right) It will be very useful, for more delicate quantities, to introduce a triangulated mesh generated from the initial tissue. Promoting the centroid of each face to a vertex of its own, we can treat the tissue composed of individual triangles. We also find it useful to introduce the set of triangulated vertices, cell centers or tissue vertices, around a specific triangulated vertex ordered CCW ($\mathcal{T}_i$). In this instance, we will use Latin indices exclusively.

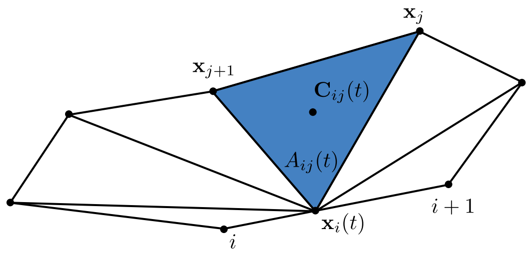

Figure 2.2: Schematic pertaining to the computation of the centroid herein defined. For each point along the path (at t), a fan triangulation is performed. The centroid of the generated triangles, each of which with area $A_{ij}(t)$ (in blue) and centroid $\boldsymbol{C}_{ij}(t)$, is computed. We then average the obtained centroid along the path.

Cell centroid

If the polygon were planar, we could in principle use the formula for the centroid presented in Appendix A. In general, the polygon that makes up a cell is not planar. Therefore, the question of assigning it a centroid is not well posed in general. We will ground our answer in four different properties we make sure to enforce:

1. The point in space that represents the centroid should not be dependent on the choice of basis used to describe positions of junctions.
2. Resulting position should not depend on arbitrary choices which a computation procedure might allow, for instance an initial state of an iterative procedure or a choice of triangulation.
3. The expression has to yield the known result if the polygon is planar.
4. Junctions that do not affect the polygon shape should not affect the position of the centroid. This means any junction, i, that can be written as $\boldsymbol{x}_i = (1-t)\,\boldsymbol{x}_{i-1} + t\boldsymbol{x}_{i+1}$, $t \in \,]0,1[$, ought not change the resulting centroid.

Our pick for computing the centroid is the average of all centroids obtained by fan triangulations from any point along the path of the polygon (Fig. 2.2). A fan triangulation is a procedure to separate a polygon into triangles by taking a vertex and creating an edge from it to all other vertices. We extend this definition to work starting on any point along the path of the polygon. This definition results in the expression

$$\boldsymbol{X}_\alpha = \frac{\sum_{i\in\mathcal{V}_\alpha} l_{i+1i}\int_{-1}^{1}\boldsymbol{C}_i\left(t\right)\mathrm{d}t}{2L_\alpha}, \qquad \boldsymbol{C}_i\left(t\right) = \frac{\sum_{j\in\mathcal{V}_\alpha} A_{ij}\left(t\right)\boldsymbol{C}_{ij}\left(t\right)}{\sum_{j\in\mathcal{V}_\alpha} A_{ij}\left(t\right)}, \tag{2.2}$$

$$A_{ij}\left(t\right) = \frac{1}{2}\left\|\boldsymbol{u}_{ji}\left(t\right)\times\boldsymbol{u}_{j+1i}\left(t\right)\right\|, \qquad \boldsymbol{C}_{ij}\left(t\right) = \frac{\boldsymbol{x}_i\left(t\right)+\boldsymbol{x}_j+\boldsymbol{x}_{j+1}}{3}, \tag{2.3}$$

$$\boldsymbol{u}_{ji}\left(t\right) = \boldsymbol{x}_j - \boldsymbol{x}_i\left(t\right), \qquad \boldsymbol{x}_i\left(t\right) = \frac{\boldsymbol{x}_{i+1}+\boldsymbol{x}_i}{2} + t\frac{\boldsymbol{x}_{i+1}-\boldsymbol{x}_i}{2}, \tag{2.4}$$

where $t \in \,]-1,1[$, and $i,j\in\mathcal{V}_\alpha$.

Note that writing the same expressions for the transformed coordinates, $\boldsymbol{x}'_i = \boldsymbol{x}_i - \boldsymbol{R}$ where $\boldsymbol{R}$ is a constant displacement vector, $\boldsymbol{x}'_i\left(t\right) = \boldsymbol{x}_i\left(t\right) - \boldsymbol{R}$, $\boldsymbol{u}'_{ji}\left(t\right) = \boldsymbol{u}_{ji}\left(t\right)$, $\boldsymbol{C}'_{ij}\left(t\right) =$

$\boldsymbol{C}_{ij}(t) - \boldsymbol{R}$, $A'_{ij}(t) = A_{ij}(t)$, $\boldsymbol{C}'_i(t) = \boldsymbol{C}_{ij}(t) - \boldsymbol{R}$, $l'_{i+1i} = l_{i+1i}$, $L'_\alpha = L_\alpha$, and – finally – $\boldsymbol{X}'_\alpha = \boldsymbol{X}_\alpha - \boldsymbol{R}$. The centroid formula as presented follows the same displacement as the junctions and, hence, fulfils property 1. Even if the choice of parametrisation can be arbitrary, the value of the integral itself is the same, and so property 2 is verified. If the polygon is planar, $\boldsymbol{C}_i(t)$ is the same for all choices of t and $i \in \mathcal{N}_\alpha$, and is the actual centroid for a two-dimensional polygon, giving the correct result, $\boldsymbol{X}_\alpha = \boldsymbol{C}_i(t)\,, \forall i \in \mathcal{V}_\alpha$, $t \in \,]-1, 1[$, ensuring property 3. The formulation of the path integral ensures we go over each point in the path only once. Property 4 follows by construction of this quantity as a path integral. Another way to verify it is when partitioning a segment to artificially create more junctions all generated triangles lie on the same plane and do not overlap which, by the definition of centroid, is equivalent to using the centroid and area of the triangle before breaking it apart. We will perform the integration using a six point Gaussian quadrature. The high precision here is needed since this error will inevitably propagate to other quantities.

Cell area

Equipped with a uniquely defined centroid, we can define a unique area for each polygon by triangulating from the centroid yielding

$$A_\alpha = \sum_{i \in \mathcal{N}_\alpha} a_i, \qquad a_i = \frac{1}{2} \left\| (\boldsymbol{x}_i - \boldsymbol{X}_\alpha) \times (\boldsymbol{x}_{i+1} - \boldsymbol{X}_\alpha) \right\|. \tag{2.5}$$

Had we not made the assumption that our tissue was embedded in three-dimensional space, we would be able to simplify the expressions for cell area and centroid significantly. In the aforementioned case we would use the shoelace formula presented in Appendix A. An illustration of the resulting geometrical quantifications can be found in Fig. 2.3, namely for face polygon area and segment length.

Cell normal unit vector

Since the surface is orientable, we can define a normal unit vector perpendicular to the cell, ω_α. The definition used in this description is,

$$\boldsymbol{w}_\alpha = \frac{\boldsymbol{N}_\alpha}{\|\boldsymbol{N}_\alpha\|}, \quad \boldsymbol{N}_\alpha = \sum_{i \in \mathcal{V}_\alpha} \boldsymbol{n}_i = \sum_{i \in \mathcal{V}_\alpha} (\boldsymbol{x}_i - \boldsymbol{X}_\alpha) \times (\boldsymbol{x}_{i+1} - \boldsymbol{X}_\alpha) = \sum_{i \in \mathcal{V}_\alpha} (\boldsymbol{x}_i \times \boldsymbol{x}_{i+1})\,, \tag{2.6}$$

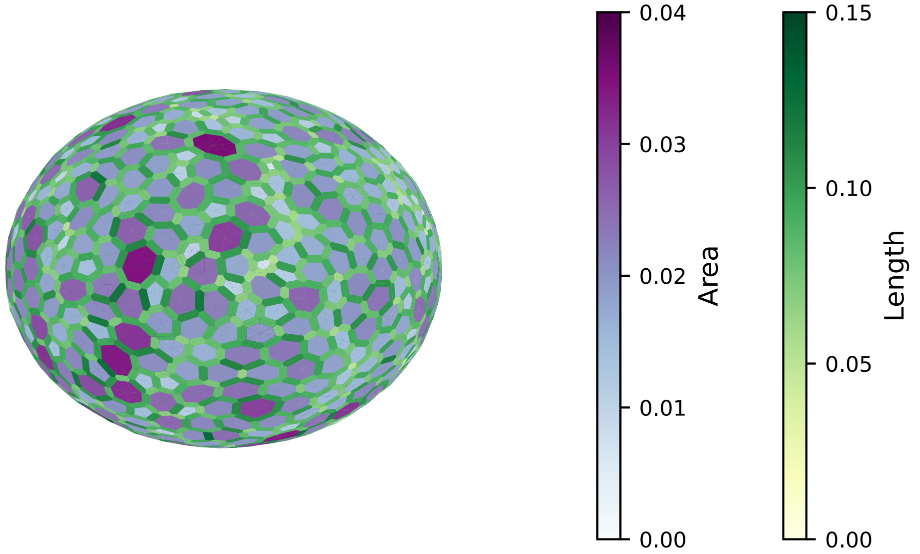

Figure 2.3: Geometrical quantities of a sample tissue resulting from a Voronoi tesselation of a spherical surface of radius equal to one unit. Here we display edges colored by their length, and faces of the polyhedron coloured according to their area. Credit to Mathias Höfler for the Voronoi tessellation.

where we defined the quantities $\boldsymbol{n}_i$, useful later on, even if it is not necessary for the computation of $\boldsymbol{w}_\alpha$[1]. Suppose we are triangulating the polygon from the centroid, then expression Eq 2.6 is the equivalent to a weighted average of the normal of the triangles that compose the polygon, since $\|\boldsymbol{n}_i\| = 2a_i$.

Tissue volume

Using the centroid to triangulate the surface, computing the volume enclosed by the surface is rather straightforward. We simply add all triangular pyramids whose base is a triangle of the surface and the opposing vertex is some reference point. By using a signed volume, the reference point can be anywhere, including the origin. This can be expressed as,

$$V = \sum_{\alpha=1}^{M} v_\alpha, \qquad v_\alpha = \sum_{i\in\mathcal{V}_\alpha} \frac{1}{6}\boldsymbol{X}_\alpha \cdot \boldsymbol{n}_i = \frac{1}{6}\boldsymbol{X}_\alpha \cdot \boldsymbol{N}_\alpha. \tag{2.7}$$

---

[1] The proof relies on the fact that the polygons are closed. Distributing the cross product in Eq. 2.6 implies,

$$\boldsymbol{N}_\alpha = \sum_{i\in\mathcal{V}_\alpha} \left(\boldsymbol{x}_i \times \boldsymbol{x}_{i+1} - \boldsymbol{X}_\alpha \times (\boldsymbol{x}_{i+1} - \boldsymbol{x}_i)\right) = \sum_{i\in\mathcal{V}_\alpha} \left(\boldsymbol{x}_i \times \boldsymbol{x}_{i+1}\right) - \boldsymbol{X}_\alpha \times \sum_{i\in\mathcal{V}_\alpha} \left(\boldsymbol{x}_{i+1} - \boldsymbol{x}_i\right),$$

where the last term vanishes since we can manipulate the index of the sum because the starting position is arbitrary. Equivalently, the last term sums vectors corresponding to the edges of the polygon and, therefore, always ends where it starts.

This expression is analogous to the shoelace formula for computing the area of a two-dimensional polygon in three dimensions. The independence of the pyramid vertex position is a result for the tissue surface being closed[2].

Mixed Voronoi regions

It is useful to be able to assign a region or an area to a vertex. This is essential when modelling curvature, but is useful for other applications, for instance, assigning inertia to a junction in hopes of modelling dynamics. In short, it is useful for surface integration of any kind of quantity defined at junctions and at polygon centroids.

We base our approach on the Voronoi region of each triangle surrounding each vertex, and each centroid made vertex, during triangulation. The notation will now treat faces as vertices with a lower latin index, as well as the set $\mathcal{T}_i$ will refer to the vertices surrounding vertex at $\boldsymbol{x}_i$ in the triangulated surface, whether they are junctions of centroids of cells. The Voronoi regions are the output of the process called Voronoi tessellation: given a set of points, return the regions in space closest to each of the input points. Note that this definition admits several possible topologies and metrics. Because integration over the surface requires each surface element to be represented equally, we require that any subdivision we choose needs to tile the same surface we had initially. This poses a problem for the Voronoi region of polygons which have obtuse angles, in which the typical formula for the Voronoi area admits portions outside the triangle itself. The concept itself remains well-defined inside the manifold that is the surface, yet becomes difficult to compute.

In order to overcome this difficulty, we will split the area formula into the Voronoi formula for acute triangles and we will assume that the point where the three regions meet will be at most at half-way through the hypotenuse. This results in what is called the mixed Voronoi region [120, 121], which we exemplify in Fig. 2.4 left. For a triangle with vertices at $\boldsymbol{x}_i$, $\boldsymbol{x}_j$, and $\boldsymbol{x}_k$ the area of the mixed region we assign to vertex at $\boldsymbol{x}_i$

---

[2] Consider Eq. 2.7 expanded to include a reference point, with position $\boldsymbol{R}$, to be

$$v_\alpha = \sum_{i \in \mathcal{V}_\alpha} \frac{1}{6} (\boldsymbol{X}_\alpha - \boldsymbol{R}) \cdot \boldsymbol{n}_i, \qquad V = \frac{1}{6} \sum_{\alpha=1}^{M} \boldsymbol{X}_\alpha \cdot \boldsymbol{N}_\alpha - \frac{1}{6} \boldsymbol{R} \cdot \sum_{\alpha=1}^{M} \boldsymbol{N}_\alpha .$$

It is not diffcult to see that the second term is zero for a closed surface if we focus on a single edge. Suppose $\boldsymbol{x}_i$ and $\boldsymbol{x}_j$ are connected by an edge, then we have two adjacent polygons corresponding to two terms in the sum, i.e.,

$$\sum_{\alpha=1}^{M} \boldsymbol{N}_\alpha = \dots + \underbrace{[\dots + \boldsymbol{x}_i \times \boldsymbol{x}_j + \dots]}_{\text{polygon left of edge } i \to j} + \dots + \underbrace{[\dots + \boldsymbol{x}_j \times \boldsymbol{x}_i + \dots]}_{\text{polygon right of edge } i \to j} + \dots = \boldsymbol{0},$$

since they will always show up reversed due to the counter clockwise cyclic sums. Because the surface is closed, all edges have two surrouding polygons and all terms cancel.

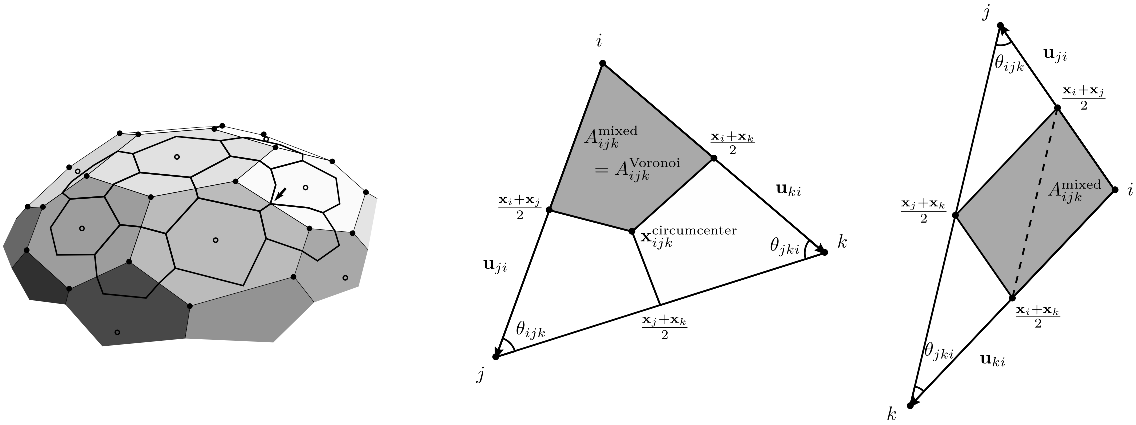

Figure 2.4: (left) Schematic representation of the mixed regions assigned to each triangulated vertex. Ideally, each of these region are the set of points closest to the corresponding triangulated vertex. The arrow shows an example where the mixed region area for an obtuse triangle was employed to facilitate computation of the region in question. (center and right) Triangle obtained via triangulation of the tissue split into the mixed regions for each of its vertices. (center) In the case of an acute triangle, the Voronoi region is used and the circumcenter lies within the triangle itself. (right) An obtuse triangle will be split as if the circumcenter now lies at the half-way point of the segment opposite to the obtuse angle. Note that all triangles shown in the decomposition of the obtuse triangle have the same area.

is

$$A_{ijk}^{\text{mixed}} = \begin{cases} \dfrac{\left\|\boldsymbol{u}_{ji} \times \boldsymbol{u}_{ki}\right\|}{4}, & (\boldsymbol{u}_{ji} \cdot \boldsymbol{u}_{ki}) \leq 0, \\ \dfrac{\left\|\boldsymbol{u}_{ji} \times \boldsymbol{u}_{ki}\right\|}{8}, & (\boldsymbol{u}_{kj} \cdot \boldsymbol{u}_{ij})\,(\boldsymbol{u}_{ik} \cdot \boldsymbol{u}_{jk}) \leq 0, \\ \dfrac{\left\|\boldsymbol{u}_{ki}\right\|^2 \cot(\theta_{ijk}) + \left\|\boldsymbol{u}_{ji}\right\|^2 \cot(\theta_{jki})}{8}, & \text{otherwise}, \end{cases} \qquad \boldsymbol{u}_{ji} = \boldsymbol{x}_j - \boldsymbol{x}_i, \tag{2.8}$$

where $\theta_{ijk} = \angle ijk$, i.e., the internal angle at j of the triangle formed by vertices i, j, k. The first two expressions correspond to the case where the triangle is obtuse, where the expression of the area is given through triangle resemblance arguments (Fig. 2.4 left). The first expression is used when the triangle has the obtuse angle at vertex i, and the second otherwise. Note that we do not need to compute the angle directly, since $\cot(\theta_{ijk}) = \boldsymbol{u}_{kj} \cdot \boldsymbol{u}_{ij} / \left\|\boldsymbol{u}_{kj} \times \boldsymbol{u}_{ij}\right\|$. The third expression is the Voronoi area [120] which is used for an acute triangle (Fig.2.4 center). The total area around a vertex of the triangulated surface is, therefore,

$$A_i^{\text{mixed}} = \sum_{j \in \mathcal{T}_i} A_{ijj+1}^{\text{mixed}}. \tag{2.9}$$

We also intend to compute the path around the mixed region of each triangulated vertex. For this we need to find out the position of all mixed region intersections. Not only this will enable us to plot these regions, but also to assign a normal vector to it in much the same way we do for each cell. We know the mixed Voronoi region of i, of the triangle i, j, k, has to cross each side of the triangle at the half-way point, $(\boldsymbol{x}_i + \boldsymbol{x}_j)/2$ and $(\boldsymbol{x}_i + \boldsymbol{x}_k)/2$, by the definition of Voronoi region (Fig. 2.4 center and right). If the triangle is obtuse we assign the intersection of the three regions to always be half-way through the hypotenuse, i.e., at $(\boldsymbol{x}_j + \boldsymbol{x}_k)/2$. If the triangle is acute the regions will meet at the circumcenter[3] of the triangle,

$$\boldsymbol{x}_{ijk}^{\text{circumcenter}} = \boldsymbol{x}_i + \left(\frac{\boldsymbol{u}_{ji} \times \boldsymbol{u}_{ki}}{\|\boldsymbol{u}_{ji} \times \boldsymbol{u}_{ki}\|}\right) \times \frac{\|\boldsymbol{u}_{ki}\|^2 \boldsymbol{u}_{ji} - \|\boldsymbol{u}_{ji}\|^2 \boldsymbol{u}_{ki}}{2\|\boldsymbol{u}_{ji} \times \boldsymbol{u}_{ki}\|}, \tag{2.10}$$

since it is the point equidistant to all the triangle vertices belonging to the same plane (Fig. 2.4 center).

Triangulated surface normal unit vectors

We previously defined the normal to a polygon. If the surface is triangulated, we can define for each vertex a normal vector, regardless of it representing a junction or a cell. We can used the same formula as Eq. 2.6 considering the mixed Voronoi region boundaries instead of edges around a polygon. Note that the normal of the mixed Voronoi region of the triangulated vertex of a cell ought to be similar to the cell normal computed with Eq. 2.6, due to how the centroid is computed. We will admit this approximation for triangulated vertices assigned to cells, $\boldsymbol{w}_i \approx \boldsymbol{w}_\alpha$, and we will use same scheme as in Eq. 2.6 adapted for the mixed Voronoi regions of triangulated vertices assigned to junctions, $\boldsymbol{w}_i$.

---

[3] It corresponds to the intersection of the perpendicular bisectors of two of the sides of the triangle. Let $\boldsymbol{m} = (\boldsymbol{u}_{ji} \times \boldsymbol{u}_{ki}) / \|\boldsymbol{u}_{ji} \times \boldsymbol{u}_{ki}\|$. Then the intersection can be written as

$$\begin{aligned}\boldsymbol{x}_{ijk}^{\text{circumcenter}} &= \boldsymbol{x}_i + \frac{\boldsymbol{u}_{ji}}{2} + \alpha \boldsymbol{m} \times \boldsymbol{u}_{ji} = \boldsymbol{x}_i + \frac{\boldsymbol{u}_{ki}}{2} - \beta \boldsymbol{m} \times \boldsymbol{u}_{ki} \\ &= \boldsymbol{x}_i + \boldsymbol{m} \times \left(\alpha \boldsymbol{u}_{ji} - \frac{\boldsymbol{m} \times \boldsymbol{u}_{ji}}{2}\right) = \boldsymbol{x}_i + \boldsymbol{m} \times \left(-\beta \boldsymbol{u}_{ki} - \frac{\boldsymbol{m} \times \boldsymbol{u}_{ki}}{2}\right),\end{aligned}$$

where we used $\boldsymbol{u}_{ji} = -\boldsymbol{m} \times (\boldsymbol{m} \times \boldsymbol{u}_{ji})$ and $\boldsymbol{u}_{ki} = -\boldsymbol{m} \times (\boldsymbol{m} \times \boldsymbol{u}_{ki})$. The equality holds if and only if

$$\alpha \boldsymbol{u}_{ji} - \frac{\boldsymbol{m} \times \boldsymbol{u}_{ji}}{2} = -\beta \boldsymbol{u}_{ki} - \frac{\boldsymbol{m} \times \boldsymbol{u}_{ki}}{2} \overset{\boldsymbol{u}_{ji}\times}{\Rightarrow} \beta = \frac{\|\boldsymbol{u}_{ji}\|^2 - \boldsymbol{u}_{ji} \cdot \boldsymbol{u}_{ki}}{2\|\boldsymbol{u}_{ji} \times \boldsymbol{u}_{ki}\|}.$$

Also, note that

$$\boldsymbol{m} \times \boldsymbol{u}_{ki} = \frac{(\boldsymbol{u}_{ji} \cdot \boldsymbol{u}_{ki}) \boldsymbol{u}_{ki} - \|\boldsymbol{u}_{ki}\|^2 \boldsymbol{u}_{ji}}{\|\boldsymbol{u}_{ji} \times \boldsymbol{u}_{ki}\|}.$$

Plugging the value of β and $\boldsymbol{m} \times \boldsymbol{u}_{ki}$ back in $\boldsymbol{x}_{ijk}^{\text{circumcenter}}$ yields the result in Eq. 2.10

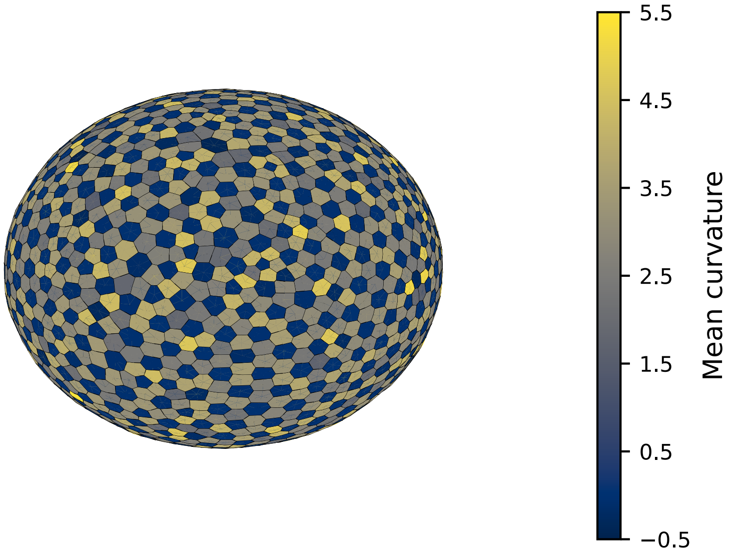

Figure 2.5: Mean curvature for each mixed region in the previously shown sample tissue. The sample tissue was obtained via voronoi tessellation of a spherical surface with radius equal to one unit. Note that the triangulated vertices belonging to the faces of the polyhedron have very low mean curvature, indicating that our centroid at least succeeds in keeping the expected shape of the tissue. Credit to Mathias Höfler for the initial tissue geometry.

Tissue curvature

Consider a point in a surface embedded in $\mathbb{R}^3$. We can inspect the curves resulting from the intersection of planes which contain the normal unit vector at that point and the surface itself. At this point, for each plane we fit a circle and compute the inverse of the radius. Principal curvatures, κ_1 and κ_2, at this particular point are the maximum and minimum values the inverse of the radius of all circles fitted this way. This approach, however, is quite cumbersome numerically. Hence we will look in particular at Gaussian curvature, $K = \kappa_1 \kappa_2$, and mean curvature, $H = (\kappa_1 + \kappa_2)/2$. These two quantities can be computed without having to solve an optimisation problem.

The Gauss-Bonnet theorem ensures that the integral of Gaussian curvature over the surface is constant and equal to 4π. Descartes' theorem on total angular defect of polyhedron states that, if the polyhedron has the topology we are using for the tissue in this work, then the sum of angular defects is always equal to 4π. The second theorem can be regarded as a special case of the first, yet it is stated in a discretized form from the outset. By angle defect we mean the angle remaining after flattening the vertex. In other words,

$$4\pi = \sum_{i=1}^{N+M} \left(2\pi - \sum_{j \in \mathcal{T}_i} \theta_{j+1ij} \right) \approx \sum_{i=1}^{N+M} A_i^{\text{mixed}} K\left(\boldsymbol{x}_i\right) \Rightarrow K\left(\boldsymbol{x}_i\right) \approx \frac{2\pi - \sum_{j \in \mathcal{T}_i} \theta_{j+1ij}}{A_i^{\text{mixed}}}. \quad (2.11)$$

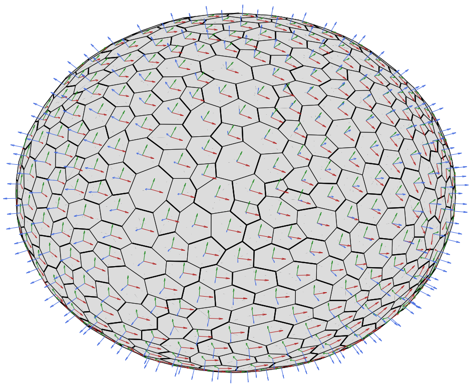

Figure 2.6: For each face of the sample tissue we assign a local projected reference frame which we can use to compute quantities more conveniently expressed in two dimensions. The basis of the reference frame assigned to cell α is given by $\boldsymbol{u}_\alpha$ (red) and $\boldsymbol{v}_\alpha$ (green). The normal vector, $\boldsymbol{w}_\alpha$, (blue) is also represented and can be used if we need to keep the same span between the original and the local reference frames.

In this case we have to use inverse trigonometric functions (such as arccot) to recover angles θ_{j+1ij}.

Mean curvature requires a bit more effort than its Gaussian counterpart. Mean curvature can be written as [121],

$$H\left(\boldsymbol{x}_i\right) = \frac{1}{2}\left(\Delta_S \boldsymbol{x}_i\right) \cdot \boldsymbol{w}_i, \tag{2.12}$$

where Δ_S is the Laplace-Beltrami operator. The Laplace-Beltrami operator is the generalisation of the Laplacian for functions defined on sub-manifolds, such as our two-dimensional spherical surface embedded in three-dimensional Euclidean space. The expression above is true for all points of the surface, not just at the triangulated vertices. We become tethered to the triangulation when we discretize Δ_S. In this case, we use

$$\Delta_S f\left(\boldsymbol{x}_i\right) \approx \frac{\sum_{j\in\mathcal{T}_i}\left(\cot\left(\theta_{ij-1j}\right) + \cot\left(\theta_{jj+1i}\right)\right)\left(f\left(\boldsymbol{x}_i\right) - f\left(\boldsymbol{x}_j\right)\right)}{A_i^{\text{mixed}}}, \tag{2.13}$$

as outlined in [120]. We can now apply the Laplace-Beltrami to each component of the position vector $\boldsymbol{x}_i$ to obtain the vector needed to find the mean curvature with Eq. 2.12. We show an example of mean curvature computation for the same sample tissue in Fig. 2.5.

2.2.2 Projected coordinates

We do not want to constrain our physical models of the cell to three dimensions, where a two-dimensional model would suffice. In order to be able to do this, however, we need to assign each polygon, representing each cell in the tissue, with an intrinsic set of two-dimensional coordinates resulting from a projection onto a best fitting plane.

We deem that the centroid and normal vector of each polygon define a good enough plane to carry out the projection. We just need to establish a vector basis inside the plane to project numerically. We proceed to find a new basis vector by means of a Gram-Schmidt orthonormalisation. We will generally start with the unit vector $\hat{\boldsymbol{e}}_x$, one of our original basis vectors, and compute

$$\boldsymbol{u}_\alpha = \frac{\boldsymbol{u}^*_\alpha}{\|\boldsymbol{u}^*_\alpha\|}, \qquad \boldsymbol{u}^*_\alpha = \hat{\boldsymbol{e}}_x - \left(\hat{\boldsymbol{e}}_x \cdot \boldsymbol{w}_\alpha\right) \boldsymbol{w}_\alpha, \tag{2.14}$$

also called the rejection of $\hat{\boldsymbol{e}}_x$ on $\boldsymbol{w}_\alpha$, which is then normalised. If $\boldsymbol{w}_\alpha = \hat{\boldsymbol{e}}_x$, then we use $\hat{\boldsymbol{e}}_y$ for generating $\boldsymbol{u}_\alpha$ instead. We can now easily compute the last basis vector with

$$\boldsymbol{v}_\alpha = \boldsymbol{w}_\alpha \times \boldsymbol{u}_\alpha. \tag{2.15}$$

We can now write the same position vectors, but in terms of this new rotated basis (Fig. 2.6). Because the basis is orthogonal and normalised we can rewrite the same vector as

$$\boldsymbol{x}_i = \left(\boldsymbol{u}_\alpha \cdot \boldsymbol{x}_i\right) \boldsymbol{u}_\alpha + \left(\boldsymbol{v}_\alpha \cdot \boldsymbol{x}_i\right) \boldsymbol{v}_\alpha + \left(\boldsymbol{w}_\alpha \cdot \boldsymbol{x}_i\right) \boldsymbol{w}_\alpha. \tag{2.16}$$

Projecting is now as simple as ignoring the last term,

$$\boldsymbol{x}^{\text{proj}}_i = \left(\boldsymbol{u}_\alpha \cdot \boldsymbol{x}_i\right) \boldsymbol{u}_\alpha + \left(\boldsymbol{v}_\alpha \cdot \boldsymbol{x}_i\right) \boldsymbol{v}_\alpha = \left(\boldsymbol{u}_\alpha \cdot \boldsymbol{x}_i, \boldsymbol{v}_\alpha \cdot \boldsymbol{x}_i\right) = \left(x^{\text{proj}}_i, y^{\text{proj}}_i\right), \tag{2.17}$$

where we have represented the vector as an ordered pair (x, y) of the new basis.

Finally, we will also center the polygon at the origin. We need, therefore, to compute the centroid of the projected coordinates. For a two-dimensional polygon, the centroid is given by

$$\boldsymbol{C}^{\text{proj}}_\alpha = \frac{1}{6A^{\text{proj}}} \sum_{i \in \mathcal{V}_\alpha} \left(x^{\text{proj}}_i y^{\text{proj}}_{i+1} - x^{\text{proj}}_{i+1} y^{\text{proj}}_i\right) \left(\boldsymbol{x}^{\text{proj}}_i + \boldsymbol{x}^{\text{proj}}_{i+1}\right), \tag{2.18}$$

where the projected area, A^{proj}, is given by the shoelace formula

$$A^{\text{proj}} = \frac{1}{2} \sum_{i \in \mathcal{V}_\alpha} \left(x^{\text{proj}}_i y^{\text{proj}}_{i+1} - x^{\text{proj}}_{i+1} y^{\text{proj}}_i\right). \tag{2.19}$$

These two formulas can be derived by converting the surface integral inside the polygon

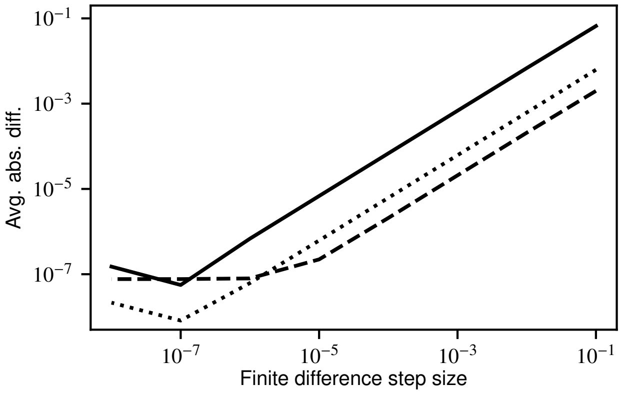

Figure 2.7: Average absolute deviation of the gradient computed analytically *versus* using forward difference scheme with different numerical step sizes (precision) for three different scalar test functions: $\sum_\alpha L_\alpha$ (solid), $\sum_\alpha A_\alpha$ (dashed), $\sum_\alpha \sum_{i\in\mathcal{V}_\alpha} \left(x_i'^2 + y_i'^2\right)$ (dotted). The average absolute difference drops until it reaches a difference within 10^{-7} which is enough precision for most purposes.

to a line integral around it as shown in Appendix A. We use a different letter for the centroid of the projected polygon in order not to conflate with the projection of $\boldsymbol{X}_\alpha$. For each junction, for each cell surrounding the junction, we will keep track of the components

$$\boldsymbol{x}_i' = \boldsymbol{x}_i^{\text{proj}} - \boldsymbol{C}_\alpha^{\text{proj}} = \left(x_i^{1'}, x_i^{2'}\right) = \left(x_i', y_i'\right). \tag{2.20}$$

2.2.3 Differentiating all of the above

As mentioned before, in general, one might want to compute forces acting on junctions. If the mechanical energy is written in terms of these geometrical quantities, the gradient of those is needed. One approach would be to use a simple finite difference scheme and change, ever so slightly, the position of each vertex individually. Numerically, this is not optimal since it means computing all previously mentioned geometric quantities $3N$ times per evaluation. Ideally we would like the analytical expressions for the gradient.

Looking ahead, we will need to integrate auxin transport over time, which would entail a global optimisation procedure at each time step. This is unfeasible since the complexity of a global optimisation can vary up to NP-hard. We can also take advantage of the fact that if we admit we are in a minimum at some point in time, in the next time step we should be close to the minimum already (phase transitions aside), making a local optimisation a better approach. In order to perform a local optimisation, we need to compute the gradient of energy at a specific point in the configuration space. This means that even if in principle someone could reproduce the experiments of this thesis with only the global optimisation, we cannot guarantee that those simulations will be finished in a reasonable amount of time. Since reproducibility is essential, we deem necessary to include the computed gradients in this work. We provide the gradient expressions for all quantities and proofs in Appendix B.

For brevity we will only show a test of the analytical result against a forward finite difference scheme for varying degrees of accuracy (Fig. 2.7). We tested the gradient of the sum of all perimeters, gradient of the sum of all areas, and gradient of the sum of a potential r^2 for each vertex around the centroid of each polygon in local projected coordinates. The numerical result and the analytical one continue to approach each other until an average absolute deviation of the order 10^{-7}. Since this value is still above machine precision, we are safe in assuming that the remnant deviation is due to the compounding round-off errors and errors from Gaussian quadrature for the centroid computation.

2.3 Implementation

A tissue description of this nature is useful especially for studies of epithelial tissue morphogenesis and development. We set our sights in providing an implementation which, not only will it allow us to extend the results of our work and pursue new experiments, but also help just as well in describing tissue mechanics of other biological systems. For instance, the description used here would be very helpful in the context of studying the mechanics of epithelial tissue, especially when considering topological transitions and cell division. The three-dimensional nature of it is necessary to study out-of-plane mechanical instabilities, which are often proposed to be the cause of morphogenesis.

We adopted the Quad-Edge library implemented by Paul Heckbert [122]. It contains all basic functionality as well as iterators and an input/output protocol with the aid of Wavefront .obj files. By wrapping it with the use of Simplified Wrapper and Interface Generator (SWIG) we compiled the C++ source into a python package, allowing us to benefit from the performance of C++ and the potential syntax clarity we can achieve with Python 3. It also allows us to integrate Python software packages seamlessly with the simulations if need be. For instance, plotting will be exclusively dealt with by the Matplotlib package [123].

On top of the Quad-Edge package, we developed surface geometry analysis tools containing all calculations herein as well as the implied required logistics. Being written in C++, the package has decent performance and has been wrapped with SWIG in the same way. A notable feature is the reconciliation of vertex linked-list-like data structure with a contiguous block of adaptable size of all vertex position coordinates. Not only is cell-division already taken into account, it is always ready to be fed to routines for optimisation and solving. To visualise the polygonal mesh we implemented specific routines invoking the Matplotlib package.

Another addition for this package is optimisation tools, since the protocol for accessing vertex coordinate components is already in place. Optimisation procedures are set to be done with the NLopt C++ package [124] with both local and global optimisation algorithms. One can also access coordinate components using the Numpy package [125] in Python 3, in case Python is preferred for coordinate optimisation.

Equipped with the mathematical concept, the formalism, and the numerical implementation of our tissue surface, we are ready to endow it with physical and biological phenomena we propose to study.

Chapter 3

Modelling mechanically regulated auxin transport

Equipped with the geometrical description of the tissue we will, in this chapter, develop mechanical models for the tissue and auxin transport model between cells of the tissue. Depending on the system we intend to model, we might need to make some extra assumptions. In our case, because we intend to model planar systems only, we will designate one cell to be virtual such that we can close the planar graph representation of the tissue. We will call this cell the boundary cell.

The bridge between the geometrical and the biological will be done by mapping tissue surface faces to plant cells, and edges to cell walls. Note that we will always assume each edge contains two cell wall compartments, one facing a different cell. Note that the Quad-Edge data structure is particularly suited for holding this correspondence, since it implies a complete directed graph. We can define that the cell wall data stored in a directed edge pertains to the compartment adjacent to the cell whose face is on the left of the current edge (any side works, so long as we do it consistently).

Plant mechanics is often modelled with the Finite Element Method [34, 46, 126, 127], using mass-spring models [127], or by evolving the system according to a model for mechanical energy [127, 128]. The approach most suitable for the vertex model described in the last chapter is to model each physical phenomenon with a mechanical energy term as a function of tissue coordinates. In the next section we focus on describing how we can use the mechanical energy to arrive at a tissue configuration, and then we will write down, term by term, the mechanical energy of the physical phenomena we want to take into account throughout this work.

By virtue of the cell wall, auxin transport has been successfully modelled with the use of compartment models [34, 73, 78, 89]. These models are based on subdividing space into different compartments with different rules for transport of molecules or other particles between compartments of, typically, spatially homogenous concentration.

3.1 Plant cell mechanical description

In order to model mechanics using a vertex model we are required to, first and foremost, write down the mechanical energy of the tissue. The ground state of the tissue can be obtained by minimisation of this mechanical energy. We will assume this approach to be enough given the difference in typical response time of auxin signaling and the propagation of (over-dampened) mechanical waves. This is reasonable, since auxin metabolism and PIN binding take place in the order of minutes [35].

Although not developed here, an alternative approach is to compute the gradient of energy in order to compute the conservative forces acting on each junction. By endowing the system with a typical response time and inertia to each junction, one could in principle simulate dynamics by integrating the equations of motion of each vertex. In this framework, dissipative forces could be included as an addition to the forces at each junction.

There are two main mechanical phenomena we want to capture with the vertex model. The first is tissue elasticity, and the second is cell turgor. In this category, we could also take into account tissue curvature, junction bending stiffness, gravitic potential, surface tension, cell line tension, or even other external force fields, for instance, as a proxy for simulating application of stress by contact.

Our aim, therefore, is to find the position vectors

$$\boldsymbol{x}_i^* \in \underset{\{\boldsymbol{x}_i\}}{\arg\min}\ \mathcal{H}\left(\{\boldsymbol{x}_i\}\right), \tag{3.1}$$

where $\mathcal{H}$ denotes the Hamiltonian, and $\{\boldsymbol{x}_i\}$ refers to the set of positional vectors that define the geometry of the tissue. We will omit the kinetic terms in the Hamiltonian, since we simply want the state in which the resulting forces vanish. This implies a static that we are dealing with a quasi-static regime [96, 129], the time between successive optimisations is not well defined. The tissue deformation timescale is, therefore, defined by how mechanical parameters vary over time. In the remainder of this section we will describe the terms we choose to include in the Hamiltonian that we will use to describe plant tissue.

3.1.1 Cell-based elastic description

One approach to include elasticity is to confer to each cell domain an energy density based on the shape of the cell. In this case it is much easier to perform the description in the projected local two-dimensional coordinate system. A staple of biological systems is to consider a parabola in the domain of cell area around a target. It works well when we consider a cell membrane where the membrane itself is relatively easy to deform in comparison to compressing the cytoplasm. A phenomenological approach such as this one is more powerful than it might appear at first glance.

In short, the behaviour of observables of a system in stable equilibrium can be compared to an harmonic oscillator for small enough perturbations. In the above description, we used area as an observable around which we Taylor expand an elastic potential, leaving us with two parameters: the equilibrium value of the observable (target area), and the concavity of the potential (bulk modulus). This idea can be generalised to a myriad number of observables.

The advantage of this approach is that one can describe a system around a stable equilibrium point without knowing the exact underlying mechanisms responsible for its stability. After choosing observables, one has only to fit the resulting parameters to empirical data to be able to predict system behaviour. On the other hand, we can only predict the behaviour for small perturbations to the system. Another issue is that the act of choosing observables can be considered a transformation of state space variables and, as such, we have no guarantee of it spanning the whole state space, let alone of it being invertible.

In this system, we need to take into account that it is harder for a plant cell to deform at all due to the existence of cell walls. Instead of choosing cell area as an observable, we base our choice in higher moments of area distribution, specifically in the second moment of area. We focus on the quantity

$$M_\alpha^{\mu'\nu'} = \iint_{S_\alpha} x^{\mu'} x^{\nu'} \mathrm{d}S_\alpha, \tag{3.2}$$

where S_α denotes the projected cell region. Note the expression is written in local projected coordinates and, therefore, centered at the centroid. Note also that μ' and ν' can take two values each, and $M_\alpha^{\mu'\nu'}$ is a symmetric matrix. We will henceforth call the second moment of area with respect to the centroid the shape matrix of the cell. This observable has been used before in a similar context [93].

Much like the shoelace area formula for a two-dimensional polygon, or the similar expression for the centroid, Green's theorem can be used to perform the surface integral as a line integral around the polygon. This simplifies the computation and discretisation necessary for computing Eq. 3.2. With the help of Green's theorem, we are able to write the shape matrix components of cell α,

$$M_\alpha^{x'x'} = \frac{1}{12}\sum_{i\in\mathcal{V}_\alpha}\left(x'_i y'_{i+1} - x'_{i+1} y'_i\right)\left({x'_i}^2 + x'_i x'_{i+1} + {x'_{i+1}}^2\right), \tag{3.3}$$

$$M_\alpha^{y'y'} = \frac{1}{12}\sum_{i\in\mathcal{V}_\alpha}\left(x'_i y'_{i+1} - x'_{i+1} y'_i\right)\left({y'_i}^2 + y'_i y'_{i+1} + {y'_{i+1}}^2\right), \tag{3.4}$$

$$M_\alpha^{x'y'} = M_\alpha^{y'x'} = \frac{1}{24}\sum_{i\in\mathcal{V}_\alpha}\left(x'_i y'_{i+1} - x'_{i+1} y'_i\right)\left(x'_i y'_{i+1} + 2x'_i y'_i + 2x'_{i+1} y'_{i+1} + x'_{i+1} y'_i\right). \tag{3.5}$$

The proof of these expressions can be found in Appendix A. If the cell is not strained, this matrix would be the target shape matrix, ${M_0}_\alpha^{\mu'\nu'}$. Ultimately, the target shape matrix is simply three adjustable parameters.

We will keep the matrix component representation since it emphasises the underlying two-dimensional coordinate system. We will also normalise the difference with the trace of the target shape matrix, such that multiplying by a scalar does not affect energy density. Total mechanical energy is already different when the system is scaled, since the implied domain of integration of energy density is different for the scaled case. With this in mind, the relative deviation from the unperturbed configuration,

$$\tilde{\varepsilon}_\alpha^{\mu'\nu'} = \frac{M_\alpha^{\mu'\nu'} - {M_0}_\alpha^{\mu'\nu'}}{{M_0}_\alpha^{\mu'\mu'}}, \tag{3.6}$$

is our choice of observables.

We will now proceed to write down energy density. With the power to choose any set of observables, we have already forfeited the guarantee of physically meaningful higher order terms. In general, since we have three observables, we would have up to six terms in the potential energy density, one for each possible combination, which we can compactly write down as

$$\psi_\alpha^{\text{elastic}} = \frac{1}{2} C_\alpha^{\mu'\nu'\xi'\eta'}\,\tilde{\varepsilon}_\alpha^{\mu'\nu'}\,\tilde{\varepsilon}_\alpha^{\xi'\eta'}. \tag{3.7}$$

Because we have no higher order terms, we are limited to linear elastic behaviour. Note that the fourth rank tensor introduced to capture all possible constants has symmetry properties leaving us with the aforementioned number of independent components. Another assumption we conjure is homogeneity, which simply results in the independence of $C_\alpha^{\mu'\nu'\xi'\eta'}$ from the coordinates at which we evaluate energy. Lastly, a perhaps more severe assumption is that of isotropy. Taking the general isotropic fourth rank tensor[1], replacing

---

[1] A fourth rank tensor of the form

$$C^{\alpha\beta\mu\nu} = \alpha\delta^{\alpha\beta}\delta^{\mu\nu} + \beta\delta^{\alpha\mu}\delta^{\beta\nu} + \gamma\delta^{\alpha\nu}\delta^{\beta\mu}$$

is invariant under any rotation, i.e, isotropic.

it in the expression for elastic energy density, and using the symmetry of the matrix $\tilde{\varepsilon}_{\alpha}^{\mu'\nu'}$[2], we are left with only two terms,

$$\psi_{\alpha}^{\text{elastic}} = c_{1\alpha}\tilde{\varepsilon}_{\alpha}^{\mu'\nu'}\tilde{\varepsilon}_{\alpha}^{\mu'\nu'} + \frac{c_{2\alpha}}{2}\tilde{\varepsilon}_{\alpha}^{\mu'\mu'}\tilde{\varepsilon}_{\alpha}^{\nu'\nu'}. \tag{3.8}$$

Since we assume an isotropic material at this point, this energy density is unable to capture the mechanical effect of microtubule orientation and polar cellulose deposition. The factor of 1/2 exists solely for the energy density expression to be a direct parallel to the typical expression for the linear elastic homogenous isotropic material.

Being an energy density, we obtain total energy via integration of the projected region and multiply by the height of each cell. Note that not one object in Eq. 3.8 is position dependent, resulting in simply a factor accounting for the volume of the cell. The Hamiltonian term for cell-based elasticity is, therefore,

$$\mathcal{H}^{\text{elastic}} = \sum_{\alpha=1}^{M} A_{\alpha}^{\text{proj}} h \left[c_{1\alpha}\frac{\|M_{\alpha} - M_{0\alpha}\|_F^2}{\operatorname{Tr}^2(M_{0\alpha})} + \frac{c_{2\alpha}}{2}\frac{\operatorname{Tr}^2(M_{\alpha} - M_{0\alpha})}{\operatorname{Tr}^2(M_{0\alpha})} \right], \tag{3.9}$$

where A_{α}^{proj} is the projected area of the cell, h its height, $\|\cdot\|_F$ is the Frobenius norm of a matrix, and $\operatorname{Tr}(\cdot)$ represents the trace of the matrix. Here we have dropped the index notation in favor of matrix notation. Note that this expression is written in terms of projected local coordinates. This implies that in order to compute the gradient of mechanical energy, we make use of the gradient transformation explored in Appendix B. We derive the gradient of the previous expression with regards to the local projected coordinate system in Appendix C.

In order to compare our model with already studied material models, we would like to map our constants $c_{1\alpha}$ and $c_{2\alpha}$ to the moduli generally employed for linear elasticity written in terms of components of the infinitesimal strain tensor. This mapping is explored in Appendix D, where we confirm c_1 to be Lamé's second parameter (μ), also called shear modulus (G), and

$$c_2 = \frac{\lambda - 3\mu}{4}, \qquad \lambda = 3c_1 + 4c_2, \tag{3.10}$$

where λ is Lamé's first parameter. We can transform back and forth to Young's modulus

---

[2] Note that

$$\frac{1}{2}C^{\alpha\beta\mu\nu}\tilde{\varepsilon}^{\alpha\beta}\tilde{\varepsilon}^{\mu\nu},$$

when replacing $C^{\alpha\beta\mu\nu}$, becomes

$$\frac{\alpha}{2}\tilde{\varepsilon}^{\alpha\alpha}\tilde{\varepsilon}^{\beta\beta} + \frac{\beta}{2}\tilde{\varepsilon}^{\alpha\beta}\tilde{\varepsilon}^{\alpha\beta} + \frac{\gamma}{2}\tilde{\varepsilon}^{\alpha\beta}\tilde{\varepsilon}^{\beta\alpha} = \frac{\alpha}{2}\tilde{\varepsilon}^{\alpha\alpha}\tilde{\varepsilon}^{\beta\beta} + \frac{\beta+\gamma}{2}\tilde{\varepsilon}^{\alpha\beta}\tilde{\varepsilon}^{\alpha\beta},$$

because $\tilde{\varepsilon}^{\alpha\beta} = \tilde{\varepsilon}^{\beta\alpha}$.

and Poisson's ratio with

$$c_1 = \frac{E}{2\left(1+\nu\right)}, \qquad c_2 = \frac{E\left(\nu - 3/8\right)}{\left(1+\nu\right)\left(1-2\nu\right)}, \tag{3.11}$$

$$E = c_1\left(3 - \frac{1}{4}\frac{c_1}{c_2+c_1}\right), \qquad \nu = \frac{1}{2}\left(1 - \frac{1}{4}\frac{c_1}{c_2+c_1}\right). \tag{3.12}$$

Note that these relations are valid only if the target shape is proportional to the identity matrix. It also requires small strains, yet we are already under this assumption.

After minimisation of the energy with respect to junction coordinates, we intend to access mechanical quantities such as strain and stress. However, we have only the target shape matrices as a proxy for the rest configuration of the cell. Had we the initial vertex positions, we could, in principle, triangulate the cell and calculate the displacement gradient of each triangle and possibly average it. Stress is also not directly accessible since it is obtained by computing the derivative of energy with respect to strain. We require a reconstruction of strain as a function of the current and target shape matrices. Presented also in Appendix D reconstructed strain for an isotropic rest shape is given by

$$\varepsilon_\alpha = \frac{M_\alpha - M_{0\alpha}}{\mathrm{Tr}\left(M_{0\alpha}\right)} - \frac{1}{4}I\frac{\mathrm{Tr}\left(M - M_{0\alpha}\right)}{\mathrm{Tr}\left(M_{0\alpha}\right)}, \tag{3.13}$$

where I is the identity matrix. Having strain and the correspondence between mechanical parameters, we need only to use the constitutive relations for a linear elastic isotropic material,

$$\sigma_\alpha = 2\mu\varepsilon_\alpha + \lambda I \mathrm{Tr}\left(\varepsilon_\alpha\right). \tag{3.14}$$

Note we are using our strain approximation and the Lamé parameters. In the course of this work we will set c_2 to zero. This implies a Poisson ratio of $\nu = 3/8$, which is relatively close to the incompressible regime ($\nu = 1/2$).

Since the aim is to model mechanical regulation of membrane-bound carriers, we aim to compute strain and stress of specific walls. As it stands, we can compute average strain and stress acting on the whole cell. We compute wall strain by interpolating between adjacent cells. As a first order approximation, we compute the average strain of the two cells surrounding a specific wall. Projecting this tensor along the wall yields longitudinal strain, which we can use to compute wall stress. If we know the constitutive relations for the cell wall we can compute stress directly via strain. Here we will assume that the mechanical properties of all wall compartments surrounding cell α will have mechanical parameters $c_{1\alpha}$ and $c_{2\alpha}$ (or rather, the resulting E_α and ν_α). This is quite the blunt approximation, yet it allows us not to introduce more parameters, and we can neatly write it in terms of projected coordinates, since the corresponding edge lies near the intersection of the two projection planes in question.

3.1.2 Wall-based description

Another possible realisation of elasticity is to consider the walls themselves as one-dimensional rigid rods with wall width, w, and layer height, h. In a simplified scenario such as this, we can frame the elastic energy directly in the infinitesimal deformation framework. With this description, we would need the Young's modulus, E_α, and Poisson ratio, ν_α. We assume all cell wall compartments surrounding a cell have the same mechanical properties.

Let $l_{ij} = l_{ji}$ be the length of the wall compartments that connect vertices i and j. If we assume that there are no residual stresses in the system, then it follows that the rest lengths these two wall compartments are the same, $l_{0ij} = l_{0ji}$. Then, we can assign to both compartments the same longitudinal infinitesimal strain,

$$\varepsilon_{ij} = \varepsilon_{ji} = \frac{l_{ij} - l_{0ij}}{l_{0ij}}. \tag{3.15}$$

We will neglect all other strain components, since we made the assumption of the wall being akin to a rigid rod. This implies we are neglecting the Poisson ratio for each individual wall. Although seemingly drastic, the deformation of the cross-section of the wall is negligible as we are professedly trying to capture the deformation of the cell as a whole. Even if it does affect the strain on walls quantitatively, the qualitative behaviour is the same.

The elastic energy density of a wall compartment adjacent to cell α is simply[3],

$$\psi^{\text{elastic}}_{\alpha\beta} = \frac{1}{2} E_\alpha \left(\frac{l_{\alpha\beta} - l_{0\alpha\beta}}{l_{0\alpha\beta}} \right)^2, \ \beta \in \mathcal{N}_\alpha, \tag{3.16}$$

where we made use of the face-based edge indexing. Here $\alpha\beta$ stands for the edge separating face α and a neighbouring region β. Being an energy density, we are required to integrate over the whole volume in order to obtain the total elastic energy. We will opt for width, w, to be that of a single compartment. Then we can write the respective Hamiltionian term as

$$\mathcal{H}^{\text{elastic}} = \frac{1}{2} \sum_{\alpha=1}^{M} E_\alpha \sum_{\beta \in \mathcal{N}_\alpha} w h l_{0\alpha\beta} \left(\frac{l_{\alpha\beta} - l_{0\alpha\beta}}{l_{0\alpha\beta}} \right)^2. \tag{3.17}$$

This elastic description is very similar to that of [130]. After optimising geometry, we can

---

[3] Here we invoke the linear elastic isotropic homogeneous material energy density,

$$\psi = \mu \varepsilon^{\alpha\beta} \varepsilon^{\alpha\beta} + \frac{\lambda}{2} \left(\varepsilon^{\alpha\alpha} \right)^2,$$

where, for $\nu = 0$, $\lambda = 0$ and $\mu = E/2$, and the only non-zero component of $\varepsilon^{\alpha\beta}$ is tangent to the wall.

infer wall stress in either compartment via the consitutive relation,

$$\sigma_{\alpha\beta} = E_\alpha \varepsilon_{\alpha\beta} \neq E_\beta \varepsilon_{\beta\alpha} = \sigma_{\beta\alpha}. \tag{3.18}$$

Note that with just this term we cannot assign a general rest cell shape. This becomes a problem when looking at high anisotropic cell shapes present in the lateral root system. If we use only this elastic term and turgor pressure, there is no rest state whose configuration resembles empirical root structure observations (for biological values of turgor and stiffness). Because cell growth is wall-specific in the systems we want to probe, we require a wall-based model for mechanics. In order to keep the structure of the root we have, at this point, two options. Either we reduce turgor pressure, relative to wall stiffness, drastically, or we model bending energy at the junctions, in order for the structure to withstand the turgor pressures we want to achieve. We choose the latter, for we cannot rely on the results of the former for long-term dynamical behaviour.

We want to assign a mechanical energy value to the angle between anticlinal walls. Each face in the surface represents a cell of height, h, which we assume to be a prism whose bases are given by the shape of the face. The walls we want to assign bending energy can be, therefore, considered as a shell of the prism that is the cell. We will assume a vanishing cell wall width and disregard walls parallel to the surface. Because the cell is a prism, then curvature does not depend on the height at which it is computed. The Canham-Helfrich bending energy surface density [131] is

$$\varphi^{\text{bending}}(\boldsymbol{x}_i) = \frac{k_1}{2}\left(H(\boldsymbol{x}_i) - H_0(\boldsymbol{x}_i)\right)^2 + k_2 K(\boldsymbol{x}_i). \tag{3.19}$$

For our particular cell wall surface shape we have curvatures $\kappa_1 \neq 0$ around the cell and $\kappa_2 = 0$ along the cell height. Because $H = (\kappa_1 + \kappa_2)/2$ and $K = \kappa_1\kappa_2$, $H = \kappa_1/2$ and $K = 0$. Curvatures κ_1 will be solely defined at the vertices around a particular cell. The discretisation of a surface integral requires that we assign an area to each vertex to perform the integral. We use $h(l_{i-1i} + l_{ii+1})/2$ since it is essentially the Voronoi area around each vertex in the considered manifold. We now have a polygon for which we want to compute curvature at each vertex.

Curvature of a planar curve at point P is usually defined as $1/R$ where R is the radius of a circumference passing through point P and whose tangent at that point is equal to the tangent of the curve at P. An equivalent definition of curvature, yet more useful for our particular application, is the derivative of the tangent angle of the curve with respect to arclength. The variation of arclength with respect to vertex i is simply $(l_{i-1i} + l_{ii+1})/2$, the size of the Voronoi region assigned to i. The variation of tangent angle at vertex i is simply the exterior angle of the polygon at i. Hence, a discrete curvature for a vertex of the polygon is given by

$$\kappa_i = \frac{2\theta_i}{l_{i-1i} + l_{ii+1}}, \tag{3.20}$$

where θ_i is the external angle at vertex i [132]. We consider that there is a rest angle θ_{0i}, such that $\kappa_i - \kappa_{0i} = 2\left(\theta_i - \theta_{0i}\right) / \left(l_{i-1i} + l_{ii+1}\right)$. These formulas were not included in the previous chapter since they are only meaningful on cells of a planar lattice. Using this value to compute mean curvature, plugging it into the energy surface density previously defined yields

$$\varphi^{\text{bending}}\left(\boldsymbol{x}_i\right) = \frac{k_b}{2}\left(\frac{\theta_i - \theta_{0i}}{l_{i-1i} + l_{ii+1}}\right)^2, \tag{3.21}$$

where k_b is the bending constant of this model. We note that a bending modulus such as k_b is often proportional to Young's modulus, for instance, in the bending of beams [133]. If we assume small angle deflections[4], then after summing for all cells and integrating over the surface the Hamiltonian bending term we consider is

$$\mathcal{H}^{\text{bending}} = \frac{1}{2}\sum_{\alpha=1}^{M} k_{b\alpha} h \sum_{i\in\mathcal{V}_\alpha} \frac{1 - \cos\left(\theta_i - \theta_{0i}\right)}{l_{ii-1} + l_{i+1i}}. \tag{3.22}$$

One can also express the same quantity in terms of tangent vectors $\boldsymbol{t}_{i+1i} = \boldsymbol{u}_{i+1i}/l_{i+1i}$,

$$\mathcal{H}^{\text{bending}} = \frac{1}{4}\sum_{\alpha=1}^{M} k_{b\alpha} h \sum_{i\in\mathcal{V}_\alpha} \frac{\left(\boldsymbol{t}_{i+1i} - \boldsymbol{t}_{0i+1i}\right)^2}{l_{ii-1} + l_{i+1i}}, \tag{3.23}$$

where $\boldsymbol{t}_{0i+1i} = \cos\left(\theta_0\right)\boldsymbol{t}_{ii-1} + \sin\left(\theta_0\right) R_i\left(\pi/2\right)\boldsymbol{t}_{ii-1}$, where $R_i\left(\theta\right)$ is the rotation matrix that rotates a vector by θ radians around the normal to the plane that contains the vectors $\boldsymbol{t}_{i+1i}$ and $\boldsymbol{t}_{ii-1}$[5]. Note that we consider a three-dimensional system, despite the representation being two-dimensional. This can be ascertained by the presence of height,

---

[4] Using Taylor series, the cosine can be approximated as $\cos\left(\theta - \theta_0\right) \approx 1 - \frac{1}{2}\left(\theta - \theta_0\right)^2$.

[5] Note that expanding $\boldsymbol{t}_{i+1i}$ in the same basis as $\boldsymbol{t}_{0i+1i}$, yields

$$\boldsymbol{t}_{i+1i} = \cos\left(\theta\right)\boldsymbol{t}_{ii-1} + \sin\left(\theta\right) R_i\left(\pi/2\right)\boldsymbol{t}_{ii-1},$$

meaning that

$$\left(\boldsymbol{t}_{i+1i} - \boldsymbol{t}_{0i+1i}\right)^2 = 2 - 2\boldsymbol{t}_{i+1i}\cdot\boldsymbol{t}_{0i+1i} = 2\left(1 - \left(\cos\left(\theta\right)\cos\left(\theta_0\right) + \sin\left(\theta\right)\sin\left(\theta_0\right)\right)\right) = 2\left(1 - \cos\left(\theta - \theta_0\right)\right).$$

In two-dimensions $R_i\left(\pi/2\right)$ would be the matrix $\left(\begin{smallmatrix} 0 & -1 \\ 1 & 0 \end{smallmatrix}\right)$. In three-dimensions, we need to rotate it around the unit vector,

$$\boldsymbol{k}_i = \frac{\boldsymbol{t}_{ii-1} \times \boldsymbol{t}_{i+1i}}{\|\boldsymbol{t}_{ii-1} \times \boldsymbol{t}_{i+1i}\|},$$

the normal to the plane of the two cell wall tangents in question. Using Rodrigues' formula, the rotation matrix $R_i\left(\pi/2\right)$ is given by

$$R_i\left(\frac{\pi}{2}\right) = I + \sin\left(\frac{\pi}{2}\right)K_i + \left(1 - \cos\left(\frac{\pi}{2}\right)\right)K_i^2 = I + K_i + K_i^2, \qquad K_i = \begin{pmatrix} 0 & -k_i^z & k_i^x \\ k_i^z & 0 & -k_i^y \\ -k_i^x & k_i^y & 0 \end{pmatrix}.$$

h, in the expressions and the factor of $\frac{1}{4}$, since, in the three dimensional case, mean curvature being an average over two different curvatures. Both expressions (Eq. 3.22 and Eq. 3.23) are often employed to model semi-flexible discrete polymer chain mechanics [134–136].

One would expect that the expression for κ_{0i} should contain rest lengths, however, we have shown above how helpful this approximation is for writing down the bending energy. If one considers $\kappa_{0i} = 2\theta_{0i}/\left(l_{0ii-1} + l_{0i+1i}\right)$ instead, the rest angle at a vertex would change based on wall strain of the two adjacent walls. This deflection angle would mean much more had we considered wall bending in each segment. Since the polygon has to remain closed and walls are kept straight, this effect is hampered by the effect of all other vertices also prone to the same angle deflection. Provided wall strain is of the same order of magnitude in all walls surrounding a cell, therefore, if we dismiss bending along wall segments, the approximation $\kappa_{0i} = 2\theta_{0i}/\left(l_{ii-1} + l_{i+1i}\right)$ is not without merit.

Since the elastic and bending terms for the wall-based model, are written in the original coordinate system, the gradient we compute to aid in energy optimisation does not have to be transformed.

3.1.3 Turgor and internal pressure

Having the energy of the material deformations, whether it is cell-based or wall-based, we will also include the turgor pressure as the source of force which knocks our system off of the equilibrium established by the parabolic shapes of the above terms.

The final term we will consider for the mechanical energy is, therefore, the work done by turgor pressure inside each individual cell. This term arrives directly via standard thermodynamics where the change in internal energy is

$$\mathcal{H}^{\text{turgor}} = -\sum_{\alpha=1}^{M} T_\alpha A_\alpha h, \tag{3.24}$$

where T_α is the turgor of cell α. Almost all energetic models of plant tissue include a term analogous to this one, for instance, [127, 130]. Similarly, we could model internal pressure of the tissue, Γ, by using $-\Gamma V$. In the systems here studied through this work we will only use the turgor pressure term.

Note that all terms, regardless of the elastic model chosen, are proportional to height h, so we can remove it from the target function for optimisation.

3.2 Auxin transport compartment model

Equipped with geometric and physical description of the tissue, we are now in position to include the biological features we are interested in and how they interact. Before tackling the expressions for how auxin and PIN evolve, we will describe the representation we opt for and the assumptions therein.

We will assign to each polygonal cell, face of the polyhedron that is the whole tissue, an auxin concentration, a_α. We consider the value of a_α to be a comparison to a basal value and, therefore, adimensional. Using just a single concentration value implies that we are not regarding intracellular auxin gradients [137]. Auxin is a small molecule and, as such, an assumption of immediate mixing is a reasonable one provided cells are not too large. This assumption, however, is brought to its limit in the case of very elongated cells of the root, where one of the dimensions differs from the other two by an order of magnitude. This poses a potential problem in the interpretation of the results of the section of this work performed on the root system, yet will be taken into account when discussing its results.

The auxin field will not be extended to take into account intracellular distribution, nevertheless we will briefly allude to how one could do so. One could discretise the auxin field inside the cell, for instance, by assigning each vertex a cell-specific local auxin concentration, as well as a central value at the cell's centroid. Triangulating the cell from the centroid would yield a lattice and, similar to the setup of a Finite Element Method, write the evolution of auxin using interpolation functions inside each triangle. One would, however, have to distinguish between intracellular diffusion constant and its intercellular counterpart, which ought to be related.

By assuming auxin in the cell compartment only, we are neglecting auxin diffusion between cell walls, as well as the membrane permeability of auxin and protonated auxin [50]. The approach of considering only intercellular auxin and auxin transport from cell to cell has been shown to be sufficient to model empirically observed auxin patterns [70, 73, 78]. Furthermore, a discussion on the importance of apoplastic diffusion of auxin concludes that the presence of influx carriers, and a large cell-cell interface in comparison with apoplast width, decrease the importance of apoplastic diffusion [26]. We will assume, therefore, that our cell-cell interfaces are large enough to neglect apoplastic diffusion of auxin.

The membrane-bound carriers of the PIN family, as the name suggests, bind to the cell membrane and facilitate auxin efflux to its neighbour. We will assign to the wall compartment between cells α and β, in contact with cell α, a PIN density $p_{\alpha\beta}$ which pumps auxin molecules out of cell α in the direction of cell β. Note that $p_{\alpha\beta}$ is normalised to some typical value of PIN wall density and, as such, is adimensional as well. It also means we do not take into account the distribution of PIN density along each wall, opting instead to average over each wall segment.

We will present the models we will be using for auxin transport and PIN binding. Further assumptions, derivation details, equation adimensionalisation and used parameters can be found in Appendix E, the supplementary material to the article presented in the next chapter.

3.2.1 Auxin rate of change

The model for auxin transport we will be using in this work is based on similar models in literature [34, 73, 78, 95]. We will take into account auxin metabolism, since plant cells produce auxin. Auxin decays with some amount of time and, therefore, in the absence of transport, auxin evolves towards a specific value, the basal auxin concentration. We can also choose the units of time such that the auxin decay rate is one per unit time. Auxin diffuses from cell to cell, prompting us to take into account passive transport of auxin. We will simply adapt Fick's law to our current setting. Since PIN works as an auxin efflux carrier, we take active transport into account by a reaction term of auxin with PIN molecules with Michaels-Menten kinetics. We will use units of length L, of the order of the length of a cell wall as observed for the L1 layer of the shoot apical meristem.

The model we use is, under these assumptions,

$$\dot{a}_\alpha = 1 - a_\alpha + \mathcal{D} \sum_{\beta \in \mathcal{N}_\alpha} \frac{l_{\alpha\beta}}{A_\alpha} (a_\beta - a_\alpha) + \mathcal{P} \sum_{\beta \in \mathcal{N}_\alpha} \frac{l_{\alpha\beta}}{A_\alpha} \left(p_{\beta\alpha} \frac{a_\beta}{K + a_\beta} - p_{\alpha\beta} \frac{a_\alpha}{K + a_\alpha} \right), \quad (3.25)$$

where $\mathcal{D}$ translates into the magnitude of diffusion as compared to auxin metabolism, $\mathcal{P}$ similarly defines the strength of active transport, and K is a scaled Michaelis constant. We emphasise that both numbers $\mathcal{P}$ and $\mathcal{D}$ depend on the length scale of the system.

Note that whenever we perform an optimisation of the mechanical energy and cell areas change, so do auxin concentrations. Before optimising geometry we save the quantity $a_\alpha A_\alpha$, and get the new auxin concentration by dividing with the new area of cell α.

3.2.2 PIN binding model

We will base our approach using a simple binding/unbinding reaction for PIN molecules. At this point we will make no assumption for how the binding rates are regulated. We will, however, assume the number of PIN molecules is conserved. If we have a single value of PIN molecules for all cells, there will be a correlation of auxin concentration and cell perimeter. Since it is unknown exactly how PIN production is regulated, we will choose to scale the conserved number of PIN molecules with the perimeter of the cell. Note that with this setup it only makes sense to call PIN molecule number a conserved quantity when disregarding the geometric changes brought upon by optimisation of mechanical energy.

Furthermore, we will assume a time scale separation between PIN binding and auxin transport such that we can use the steady-state solution of PIN density. This assumption is a risky one, given that osmotic treatment experiments show a full recovery time within 30 minutes [35], which, even if faster, would be on a similar time scale as that of auxin transport, in the order of an hour [138]. In the next chapter where we look at the static pattern formation, this effect might influence the trajectory through phase space, yet the pattern characteristics should be largely unaffected. When discussing the dynamical behaviour, however, the abscense of the phase difference between auxin transport and PIN binding will probably result in PIN localisation being a bit more fickle and the accompanying auxin pattern less stable.

Under these assumptions, the adimensional PIN density, $p_{\alpha\beta}$, bound to the cell wall of α, pumping auxin into cell β, is given by

$$p_{\alpha\beta} = \frac{f_{\alpha\beta}}{1 + \sum_{\gamma\in\mathcal{N}_\alpha} \frac{l_{\alpha\gamma}}{L_\alpha} f_{\alpha\gamma}},\ \beta \in \mathcal{N}_\alpha, \tag{3.26}$$

where $f_{\alpha\beta}$ is the ratio between the binding and unbinding rates to a specific wall. If all binding rates are the same, then $p_{\alpha\beta} = \bar{p} = \bar{f}/\left(1+\bar{f}\right)$, implying $a_\alpha = 1\ \forall\alpha$ being a fixed point of Eq. 3.25. Had we chosen to scale the amount of PIN molecules differently, this fixed point would take into account the geometry of the cell. Though it might be interesting to probe how patterns might be affected by such bias on its own, because of the lack of information in this regard, we opt here for scaling available PIN molecules with perimeter due to its simplicity.

To clarify, $p_{\alpha\beta} = 1$ is the density of bound PIN molecules a cell would have if all PIN were bound and all walls had the same binding and unbinding rates. In fact, $\sum_{\beta\in\mathcal{N}_\alpha} l_{\alpha\beta} p_{\alpha\beta}/L_\alpha$ is the fraction of bound PIN molecules for cell α. This means that in a wall of length $l_{\alpha\beta}$, $p_{\alpha\beta}$ can go up to $L_\alpha/l_{\alpha\beta}$, when all PIN molecules are bound to this specific wall.

3.2.3 Boundary conditions

Here we discuss boundary condition details we need to take into account when modelling a fully planar tissue. Note that the topology of the tissue requires it to be a closed surface and, therefore, the domain we intend to simulate on has to be enclosed by what we call boundary faces.

In the case the tissue is embedded in three dimensions without a face of the polyhedron acting as a boundary, then there are no boundary conditions for auxin transport to worry about. All cells have neighbours in all directions and auxin and PIN density rates of change are all well-defined.

However, in this work, the approach is to flatten the tissue with one or more faces serving as the boundary face of the tissue. How we deal with neighbours of these boundary faces is what defines the boundary conditions. We use reflective boundary conditions, such that auxin flowing into neighbours of a boundary face is then repurposed as the auxin flowing in to the same neighbour through the same wall. Mechanically, we assume this cell has no stiffness, no turgor and, hence, no mechanical energy.

We attempt to discern the bulk behaviour of the model from boundary effects by simulating large enough systems. In the lateral root, however, one has to contend with the limited amount of layers the system can have. Therefore, in order to interpret the results in a meaningful matter, we need to be wary of the potential impact of boundary effects on the resulting data.

3.3 Interaction of mechanics and auxin transport

Our aim, ultimately, requires us to model mechanical regulated PIN binding and auxin-mediated cell wall softening. We are looking to probe the pattern formation mechanism further, as well as to predicting what might occur in other tissues of the plant, or under different conditions. The connective models here described are taken from [34], wherein it is proven they allow for pattern formation capabilities.

3.3.1 Mechanical regulation of PIN binding

In accordance with our working hypothesis, we will modulate binding and unbinding rates such that the ratio, $f_{\alpha\beta}$, is promoted to a function of wall compartment stress, $\sigma_{\alpha\beta}$. As has been observed by [35], strain and/or stress seem to upregulate PIN binding and, thus, we use a power law for positive stress,

$$f_{\alpha\beta} = f\left(\sigma_{\alpha\beta}\right) = \begin{cases} \eta\sigma_{\alpha\beta}^{n}, & \sigma_{\alpha\beta} > 0, \\ 0, & \sigma_{\alpha\beta} \leq 0. \end{cases}, \ \beta \in \mathcal{N}_{\alpha}. \tag{3.27}$$

After mechanical energy optimisation, one can compute stress acting on each wall and, thereafter, compute binding rate ratios. We remark once more that wall stress computation differs slightly depending on the model used. Specifically, in the cell-based model, we compute average strain between two cells and project onto their shared wall to obtain its longitudinal strain. Then, wall compartment stress computed via the constitutive relations.

One could easily come up with an analogous model for wall strain by replacing stress with strain in the previous expression. The two formulations were compared in [95] where it was shown that, in general, both models predict very similar qualitative behaviours, provided the mechanical properties of the tissue are isotropic. As mentioned for the mechanical models in this chapter, we focus exclusively on isotropic materials and, as such, we are under a similar regime. One notable exception is the correlation of auxin concentration and PIN polarity.

In the shoot apical meristem, observations show PIN polarity to be correlated with auxin concentration [86, 139], which resembles the results of the strain-based model. Taking into account that PIN expression is positively affected by auxin activity [23], the choice of model is not as clear cut. Moreover, there is evidence of plant cells, in the context of microtubule alignment, being able to read stress in settings where predicted strain and stress directions differ [46, 140].

Bearing in mind the shortcomings of each model, we opt for modelling PIN binding as regulated by stress, as opposed to strain-mediated regulation. Our argument is that it seems less likely that plant cells, at a regulatory level, can distinguish between stress and strain. In Appendix E we compare and discuss the effect of adopting a strain-based approach during pattern formation.

3.3.2 Auxin-mediated cell wall softening

The final piece of the pattern formation puzzle is how auxin affects the perceived stiffness of the cell wall. External application of auxin has been shown to affect cell wall stiffness [43, 44]. In order to capture this phenomenon, we model the Youngs modulus, E, as a function of auxin concentration using the Hill function for a repressor,

$$E\left(a_\alpha\right) = E_{\mathrm{min}} + \frac{E_{\mathrm{max}} - E_{\mathrm{min}}}{1 + a_\alpha^m}, \tag{3.28}$$

where E_{min} and E_{max} are the minimum and maximum stiffness, and m is the Hill exponent. It is useful to rewrite this expression as

$$E\left(a_\alpha\right) = E_0\left(1 + r\frac{1 - a_\alpha^m}{1 + a_\alpha^m}\right), \tag{3.29}$$

where we use the value of Young's modulus for the basal value of auxin, E_0, and the parameter $r = \left(E_{max} - E_{min}\right) / \left(E_{max} + E_{min}\right)$. The preference for this form stems from linear stability analysis, where E_0 has no bearing on pattern formation threshold, whereas $r \in [0, 1[$ encapsulates how disparate are the limit values of stiffness.

Note that, when setting $c_2 = 0$ in the cell-based mechanical model (Poisson's ratio, $\nu = 3/8$), $c_1 = 11E/4 \propto E$. This implies that r would be the same for E and the corresponding c_1 parameter. Similarly, this means that the expression for c_1/c_{10} is the same as the one for E/E_0. We will, henceforth, use stiffness E to refer to c_1 or Young's modulus depending on the model being used. We will take into account the scaling factor of 11/4 when discussing results obtained with the cell-based model.

3.4 Implementation

We implement the model in a partner package to the developed surface analysis tools. In the same way, it is programmed in C++ and then wrapped in Python 3 with SWIG for easy scripting of experimental setups. It uses the geometry optimisation tools established previously, which use the NLopt package.

In order to run the mechanical model in tandem with auxin transport, we perform a time step of a specific time Δt for the auxin transport equation, knocking our system off of equilibrium. This implies that at each auxin time-step an optimisation procedure has to be done. This reinforces the importance of having the gradient computations such that a local – much faster – optimisation can be performed within a reasonable amount of time. After computing the current geometry of the tissue, strain can be measured and used to compute stress and PIN density.

There is no *a priori* way to measure how areas change with a change in auxin concentration, leaving us to correct auxin concentration *a posteriori*, by scaling the resulting auxin as previously mentioned, as an approximation. This approximation can be valid if the area change is relatively small. Therefore, a sufficiently stiff tissue validates this approximation. Later in this work, we model growth in the lateral root system by using the wall-based model for mechanics. Even if one admits the same approximation for auxin affecting area, the same is harder to argue for rest lengths l_0, when these are promoted to time dependent variables. We attempt to solve this by considering smaller time-steps than we would otherwise.

When not considering growth, we will evolve all time-dependent variables using the Runge–Kutta–Fehlberg method (commonly known as RKF45), available in the GNU Scientific Library (GSL) package [141]. We consider geometry fixed between t and $t + \Delta t$ and integrate accordingly. We allow ourselves to do this only because we regard a stiff enough tissue, such that area changes mediated by auxin-mediated cell wall loosening introduce a much smaller contribution to auxin transport than stress-mediated active transport.

Considering mechanically-mediated growth, however, poses a significant problem since assuming a fixed geometry between t and $t + \Delta t$ is antithetical to modelling growth. Multiple evaluations of the rate of change of l_0 in a single time step, without a new optimisation, introduce a systematic bias since, as l_0 grows, wall strain and stress necessarily decrease if we do not allow l to change. For instance, suppose a minimal system composed of one wall being stressed by a fixed value of σ_{ext} undergoes growth. Regardless of the exact stress-or-strain-dependent growth equation, any evaluation at time t will imply a stress/strain release even when we know it ought to remain the same[6]. Any higher order term implemented naïvely (by taking intermediate steps in l_0 without updating l), therefore, prove to be a correction for the evolution of l_0 to a system other than our own. The amount of optimisations necessary skyrocket and makes the simulation unfeasible. Ultimately, we are cornered into using an explicit Euler method when modelling growth.

After evolving all time-dependent quantities until $t+\Delta t$, we can now update the values of stiffness due to cell wall loosening and, in case of a growing tissue, use the new rest configuration parameters for the next optimisation. We then rinse and repeat until a certain amount of time as passed.

---

[6] The wall length that minimises the mechanical energy,

$$\mathcal{H} = \frac{1}{2} E h w l_0 \left(\frac{l - l_0}{l_0} \right)^2 - h w l_0 \sigma_{\text{ext}} \frac{l - l_0}{l_0},$$

is

$$\frac{d\mathcal{H}}{dl} = 0 \Rightarrow l : \sigma_{\text{ext}} = E \frac{l - l_0}{l_0} = \text{constant}, \ \forall E, \, l_0.$$

In this case we know what l ought to be given an l_0. In order to know this in general, an optimisation of mechanical energy has to be made and, therefore, given l and l_0 at time t we cannot estimate l for intermediate steps without further optimisations, limiting us to first order terms.

Chapter 4

Implications of mechanically-regulated PIN regulation

The pattern formation mechanism via mechanically-regulated PIN is as follows. Suppose we have a cell wall composed of two compartments, that share a rest length, we can solve for the stress acting on each compartment as a function of the mechanical properties of each compartment and the average stress acting on the wall (Appendix E). This stress load division implies that the softer cell wall compartment, facing the cell with greater auxin concentration, will be under a lesser amount of stress than the opposite compartment. This effectively allows for an auxin feedback to occur up-the-gradient as shown in [34]. This simple model however does not regard cell geometry, turgor pressure, or any other mechanical input. Herein lies the basis of our exploration. We intend to find out if and what other factors are missing from the stress-load division auxin pattern emergence mechanism.

Turgor pressure generates stress which, under our hypothesis, regulates PIN binding rates. If we consider plasmodesmata to be open we can assume that a turgor pressure difference will decay as a result of water transport. We will, therefore, assume homogenous turgor pressure in the tissue. We note that, for the particular case of homogenous turgor pressure, homogenous mechanical properties, and symmetric tissue architecture, all cell walls will be stressed by the same amount.

A cell in isolation under internal pressure would expand according to its elastic properties. The geometry would be that which optimises the mechanical energy (sum of Eqs. 3.9 and 3.24) for a single cell. In general, the deformed state is different than the isolated case. Even in the simple case of a regular hexagonal lattice this is only the case if all mechanical properties are the same. For instance, stiffness heterogeneities for this lattice imply that not all cells can achieve their optimal configuration simultaneously. If we consider auxin-mediated softening of the mechanical properties of the cell, then auxin patterns will necessarily introduce stiffness heterogeneity. In this chapter we tackle if auxin heterogeneity feedback via modulation of mechanical properties helps, or hinders, auxin pattern formation, in addition to its positive feedback of stress-load division.

We introduce the uncoupled tissue approximation, where we assume an average stress acting on all walls, as a null hypothesis to compare to the auxin transport vertex model described in Chapters 2 and 3. This is analogous to considering the state of the each cell in an isolated context. Cell-cell communication in this setting is purely via stress load division between cell wall compartments. We use the parameters in the table presented in Appendix E.

We first take a look at the mechanical patterning caused by an ablation experiment in order to make sure it captures the general behaviour observed in [34, 46]. We observe a circumferential pattern around the ablated cell, as well as the same tendency of PIN to bind along the same direction. Even if this experiment and result is straightforward, it helps validate the mechanical model being used since it agrees with previously established results [34, 46].

The aproximation requires tuning in regards to the average wall stress. We performed the linear stability analysis of the uncoupled tissue approximation in order to obtain the most unstable wavelengths as well as the conditions for pattern formation (see Appendix E for the derivation). By checking that the formation threshold matches between both models, we validate the fairness of this comparison.

As argued previously, the interpretation of the approximation, the absence of the impact of stiffness variations on the tissue, makes this comparison insightful. PIN polarity measures and auxin spot concentration between the two models varies drastically and consistently. We observe PIN polarity increases drastically if the impact of auxin mediated cell wall loosening is high. When considering tissue-wide mechanical patterns, PIN polarity saturates earlier for the parameter which effectively translates to preception of stress. Furthermore, the wavelength of the auxin pattern is reduced in when considering tissue-wide stress patterning. All these factors result in stronger auxin flows and higher degrees of auxin depletion and accumulation, contributing, we speculate, to a easier establishment of cell fate. We then focus on characterising the emerging mechanical patterns and how they relate to the emerging auxin patterns.

Quantification of stress and auxin pattern features shows that the mechanical modulation not only drives auxin into the auxin spots through stress load division between wall compartments, but also via stress patterning similar to that of the ablation patterns. We observe the tendency for stress to align perpendicular to auxin gradients (around auxin spots) and for cells at the interface of auxin spots to be more stressed than they would otherwise be. We also observe a lower isotropic stress component inside auxin spots due to being constrained.

The effect of noise in mechanical properties was also tested in order to show that introducing mechanical PIN regulation helps further discern cell identity. We decide to promote the parameter base stiffness to a random variable sampled at the beginning of the simulation. We show in Appendix E that this parameter is particularly disruptive to pattern formation, by comparing to a similar variation of the active transport magnitude. We quantify how discernible auxin patterns are by using entropy of the auxin concentration distribution. We observe that, as we increase noise in reference stiffness, entropy increases by a lesser degree when considering tissue-wide patterning than in the approximation. This suggests that the mechanical patterning of the tissue contributes to the robustness of the pattern emergence mechanism.

Lastly, due to its relevance in the current discourse of growth, auxin signalling, and water transport, [51, 52] we tested how auxin correlates with turgor pressure, under different initial conditions. Our model predicts that even if high turgor consistently correlates with auxin concentration, the reverse is not always the case. Turgor decrease cannot necessarily overwrite already existing auxin maxima. Experimentally, this implies that one cannot easily draw conclusions about turgor and, hence, growth rate from the degree of auxin signalling alone.

Our model predicts that a mechanical regulation of auxin transport brings forth the potential for an enhanced mechanical feedback resulting from auxin-mediated stiffness heterogeneity of plant cells in a tissue. This mechanism differs from that of stress load division alone since its effect depends on cell turgor. The same stiffness variation of an auxin spot would result in radial stress patterns under hypertonic conditions.

To make sure the auxin flow enhancement phenomenon observed in this work was not exclusive to the stress-based model, we show in Appendix E the auxin spot characteristics with an analogous strain-based model.

We predict an abrupt pattern emergence where the perception of stress need not be as high than when considering stress-load division alone in order to achieve relatively high values of PIN polarity and auxin concentration. Besides being more efficient under this hypothesis, these patterns are also more robust. We also predict an auxin spot wavelength decrease in all simulated cases.

It is interesting to observe that the stress patterns around auxin spots are the same as predicted by [46] around emerging primordia. This suggests that microtubules may have their orientation pre-patterned by auxin, and then reinforced by tissue shape as growth takes place. Furthermore, the mechanical feedback on growth anisotropy promoting primordium outgrowth is based on the same stress pattern configuration [93]. The predicted mechanical patterns suggest that auxin patterning contributes via growth rate and mechanical patterning alike to the aforementioned feedback mechanisms.

The introduced approximation can also serve as a stand-in for an analogous auxin-concentration-regulated PIN model. It is interesting to observe how prevalent and impactful tissue mechanics are in this setting. We show the increase in efficiency and robustness via communication through mechanics to be quite remarkable. The work here done can be used to corroborate why some plant developmental mechanisms hinge on mechanical communication, instead of using molecular mediators.

Eur. Phys. J. Plus (2021) 136:250
https://doi.org/10.1140/epjp/s13360-021-01204-6

THE EUROPEAN
PHYSICAL JOURNAL PLUS

Regular Article

Tissue-wide integration of mechanical cues promotes effective auxin patterning

João R. D. Ramos[1], **Alexis Maizel**[2], **Karen Alim**[1,3,a]

[1] Max Planck Institute for Dynamics and Self-Organization, Göttingen, Germany
[2] Center for Organismal Studies, University of Heidelberg, Heidelberg, Germany
[3] Physik-Department, Technische Universität München, Munich, Germany

Received: 30 September 2020 / Accepted: 7 February 2021

Abstract New plant organs form by local accumulation of auxin, which is transported by PIN proteins that localize following mechanical stresses. As auxin itself modifies tissue mechanics, a feedback loop between tissue mechanics and auxin patterning unfolds—yet the impact of tissue-wide mechanical coupling on auxin pattern emergence remains unclear. Here, we use a model composed of a vertex model for plant tissue mechanics and a compartment model for auxin transport to explore the collective mechanical response of the tissue to auxin patterns and how it feeds back onto auxin transport. We compare a model accounting for a tissue-wide mechanical integration to a model that regards cells as mechanically isolated. We show that tissue-wide mechanical coupling not only leads to more focused auxin spots via stress redistribution, but that it also mitigates the disruption to patterning when considering noise in the mechanical properties of each cell of the tissue. We find that this mechanism predicts that a local turgor increase correlates with auxin concentration, and yet auxin spots can exist regardless of the exact local turgor distribution.

1 Introduction

Formation of organs entails an effective coordination of local cell growth typically initiated by patterns of one or more morphogenic factors. Understanding how these patterns of morphogenic agents robustly emerge is fundamental for predicting organ morphogenesis. Plants organ formation is interesting from a physical perspective due to the strong mechanical coupling between plant cells, and the fact that growth is driven by changes in the mechanical properties of the cell wall and internal pressure [1–5]. Evidence indicates that the morphogenic factors such as the plant hormone auxin change the mechanics of the tissue [6,7], with implications for the shaping of organs [8,9]. Interestingly, the transporters of auxin respond to mechanical cues [10,11], leading to an intertwining of chemical and mechanical cues.

The phytohormone auxin, Indole-3-Acetic Acid, is the key morphogenic agent in plants. Auxin accumulation drives a wide range of plant developmental processes including, but

---

Electronic supplementary material The online version of this article (https://doi.org/10.1140/epjp/s13360-021-01204-6) contains supplementary material, which is available to authorized users.

---

[a] e-mail: k.alim@tum.de (corresponding author)

not limited to initiation of cell growth, cell division, and cell differentiation [12–14]. Establishment of auxin patterns is ubiquitous in plant organ morphogenesis [15]. The best characterized example is the regular patterns of auxin spots in the outmost epidermal cell layer at the tip of the shoot that prefigures the regular disposition of organs called phyllotactic pattern [16–21]. These auxin accumulation spots mark the location of emerging primordia of new aerial plant organs. Auxin patterns result from the polar distribution of auxin efflux carriers called PIN-FORMED (PINs) [15,16,20,22–24]. Because of its prevalence in plant development, understanding how these auxin patterns emerge has been intensively studied and mathematically modelled. Auxin concentration feedback models [25–29], organize their flow up-the-gradient of auxin concentration, reinforcing auxin maxima. Canalization models, or flux-based models, [30–36] reinforce already existing flows, and, as such, both up-the-gradient and down-the-gradient flows can exist. Some attempts at unifying both mechanisms have been made [35,37–39], yet many conditions have to be imposed to explain, for instance, the fountain-like patterns arising during root development [35,40].

Tissue mechanics has emerged as a potent regulator of plant development [5,41–44]. Plant cells are able to read mechanical stress and respond accordingly, rearranging their microtubules along the main direction of mechanical stresses [41]. Furthermore, PIN1 polarity and microtubules alignment at the shoot apical meristem are correlated [10], suggesting the possibility of PIN localisation being mechanically regulated. This hypothetical coupling between PIN localisation and mechanical cues is theoretically able to predict PIN polarity and density for a wide range of cell wall stress and membrane tension [11]. Such coupling is also supported by several other observations: the physical connection of PINs to the cell wall [45], the change in polarity induced by cell curvature [46], and disorganization of PIN polarity by modification of the cell wall mechanical properties [7].

Auxin can induce remodelling of the cell wall and thus modify its mechanical properties [4,6,7,47]. This may in turn influence PIN localisation and therefore have consequences on the pattern of auxin. Modelling of this feedback in a tissue showed that mechanical stresses can lead to the emergence of a regular phyllotactic auxin pattern by regulating PIN localisation [10]. Although this result shows the importance of local mechanical coupling (Fig. 1) for emergence of auxin patterns, the full extent of the impact of mechanical coupling on pattern emergence remains unclear.

In fact, cell strain is a compromise between its mechanical properties and the restrictions placed upon its shape by the surrounding cells given the condition that the tissue remains connected. In other words, stiffness variations contribute additional terms to tissue strain. In order to explore the effect of the latter, we adapt the model for auxin transport introduced in [10] to a vertex model mechanical description of the tissue, a tissue-wide mechanical model and compare it to a uncoupled tissue approximation with the same auxin transport model but where we prescribe an average stress acting on all cells (Fig. 2).

By comparing both models, we find that due to stress fields arising from mechanical feedback the magnitude of auxin spots is larger for lower stress-PIN coupling, indicating a more efficient transition between low and high auxin regimes and the subsequent potential cell behaviour response. Furthermore, we explore the information content of auxin distributions when noise is considered and show that tissue-wide mechanical coupling improves robustness of auxin patterns.

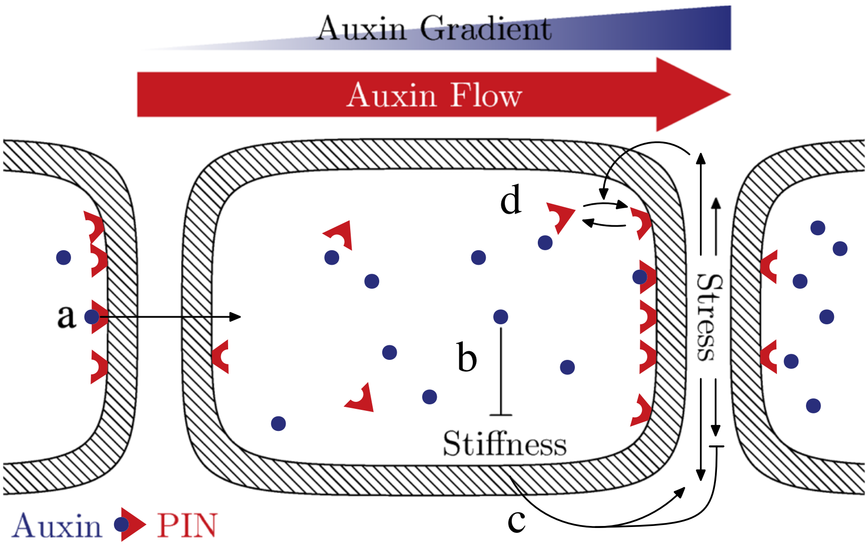

Fig. 1 Schematic representation of the cell–cell feedback mechanism between cell wall loosening via auxin and mechanical control of PIN. (a) Auxin is transported to neighbouring cells via bound PIN efflux carriers. (b) Auxin interacts with the mechanical properties of the cell wall reducing its stiffness. (c) Increasing stiffness of a particular wall component shifts the stress load from the component of its neighbour to itself. (d) Wall stress promotes PIN binding. A difference in auxin, therefore, induces a stress difference between the two compartments separating both cells. This stress difference is such that PIN binds preferentially in the cell with lower auxin concentration, increasing the flow of auxin into the cell with higher auxin concentration

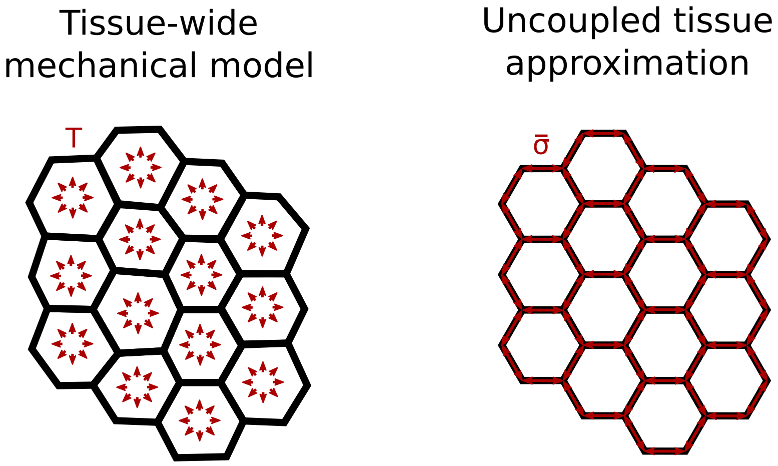

Fig. 2 Schematic difference between the tissue-wide mechanical model (left) and the uncoupled tissue approximation (right). In the tissue-wide mechanical model, turgor pressure, T, and stiffness determine the vertex positions that minimize mechanical energy. Wall strain and stress are then inferred from the mechanical configuration. In the approximation, we prescribe average wall stress, $\bar{\sigma}$, with a static geometry. This approximation disregards the effect of stiffness variations on strain. The prescription of stress in the approximation renders the mechanical interaction to be only between nearest neighbours and uncoupled from all other cells. In the tissue-wide mechanical model, the mechanical state is a function of all cells in the tissue

2 Methods

In order to investigate the interaction between auxin cell wall softening and collective tissue mechanics, we use a vertex model to describe the mechanical behaviour of the tissue and a compartment model to express auxin concentration and transport between adjacent cells.

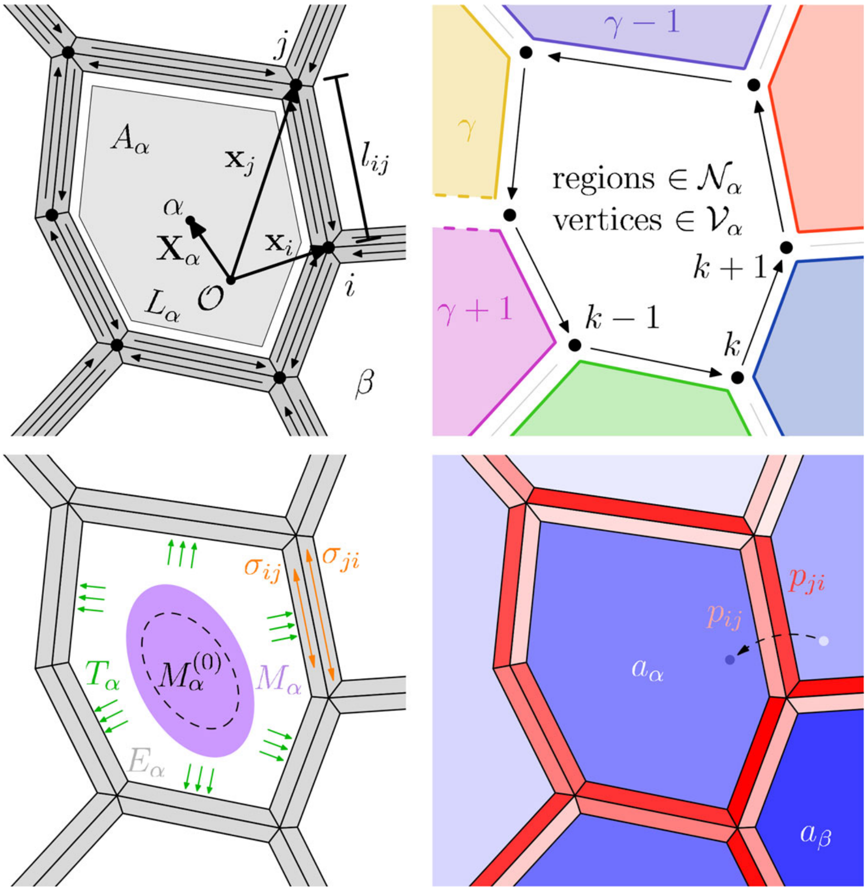

Fig. 3 Vertex model description of a cell as a geometrical, mechanical, and biologically active entity. (top left) A cell α surrounded by its cell walls with centroid $\mathbf{X}_\alpha$, area A_α and perimeter L_α. Vertices i and j have positions $\mathbf{x}_i$ and $\mathbf{x}_j$ and the distance between them is $l_{ij} = l_{ji}$. (top right) Set of surrounding regions, one for each wall, $\mathcal{N}_\alpha$, and set surrounding vertices, $\mathcal{V}_\alpha$, used in the equations of the model. (bottom left) Mechanically, cell α is under turgor pressure T_α, the surrounding wall compartments have stiffness E_α. M_α is the second moment of area of cell α, whereas $M_\alpha^{(0)}$ is that same quantity when the cell is at rest. σ_{ij} refers to the longitudinal stress acting on the compartment of the wall. (bottom right) Cell α has an auxin concentration a_α which is expressed, degraded and transported, both passively and actively. The active component of auxin transport relies on the density of membrane-bound efflux auxin carriers facing a particular wall compartment, p_{ij}

2.1 Geometrical set-up of the tissue

The tissue is described by a tiling of two-dimensional space into M cells surrounded by their cell walls. Walls are represented as edges connecting two vertices each, positioned at $\mathbf{x}_i = (x_i, y_i)$, $i \in [1, N]$. Here, we reserve Latin indices for vertex numbering and Greek ones for cells. Each cell wall segment has two compartments, one facing each cell. Therefore, we represent each cell wall with two edges of opposite direction, one for each compartment. The position of tissue vertices fully define geometrical quantities such as cell areas, A_α, cell perimeters, L_α, wall lengths, $l_{ij} = l_{ji}$, and cell centroids, $\mathbf{X}_\alpha$ (Fig. 3 top left). To simplify notation significantly, we also define for each cell the cyclically ordered set of all vertices around that cell, $\mathcal{V}_\alpha$, arranged counterclockwise (ccw). Hence, we use $\sum_{i \in \mathcal{V}_\alpha}$ to signify the sum over all vertices surrounding cell α with an arbitrary start, where $i+1$ and $i-1$ mean, respectively, the next and previous ccw vertex. Similarly, we introduce $\mathcal{N}_\alpha$ as the cyclically ordered (counterclockwise) set of all neighbouring regions around cell α, one for each edge of α (Fig. 3 top right).

2.2 Tissue mechanics–tissue-wide coupling

Vertex models are a widely employed theoretical approach to describe mechanics of epithelial tissues and morphogenesis [9,48–53]. The essence of vertex models is that cell geometry within a tissue is given as the mechanical equilibrium of the tissue. In the case of plant cells, the shape of a cell is a competition between the turgor pressure, T_α, all cells exert on each other and the cell's resistance to deformation with stiffness, E_α. Strain acting on each cell will be described using the second moment of area of the corresponding cell in reference to its centroid, M_α, whose components are

$$M_{\alpha_{xx}} = \sum_{i\in\mathcal{V}_\alpha} \frac{n_i}{12}\left(x_i'^2 + x_i'x_{i+1}' + x_{i+1}'^2\right), \tag{1}$$

$$M_{\alpha_{yy}} = \sum_{i\in\mathcal{V}_\alpha} \frac{n_i}{12}\left(y_i'^2 + y_i'y_{i+1}' + y_{i+1}'^2\right), \tag{2}$$

$$M_{\alpha_{xy}} = M_{\alpha_{yx}} = \sum_{i\in\mathcal{V}_\alpha} \frac{n_i}{24}\left(x_i'y_{i+1}' + 2x_i'y_i' + 2x_{i+1}'y_{i+1}' + x_{i+1}'y_i'\right), \tag{3}$$

where the primed coordinates represent the translation transformation, $\mathbf{x}_i' = \left(x_i', y_i'\right) = \mathbf{x}_i - \mathbf{X}_\alpha$, and $n_i = x_i'y_{i+1}' - x_{i+1}'y_i'$, $i \in \mathcal{V}_\alpha$. Given a rest shape matrix, $M_\alpha^{(0)}$, we define cell strain as the normalized difference between both matrices,

$$\varepsilon_\alpha = \frac{M_\alpha - M_\alpha^{(0)}}{\mathrm{Tr}\left(M_\alpha^{(0)}\right)}, \tag{4}$$

and stress with $\sigma_\alpha = E_\alpha\varepsilon_\alpha$. Having described the tissue mechanically (Fig. 3 bottom left), we define the energy for a single cell as the sum of work done by turgor pressure and elastic deformation energy, resulting in the tissue mechanical energy,

$$\mathcal{H} = \sum_{\alpha=1}^{M}\left[\frac{1}{2}A_\alpha E_\alpha \frac{\left|\left|M_\alpha - M_\alpha^{(0)}\right|\right|_2^2}{\mathrm{Tr}^2\left(M_\alpha^{(0)}\right)} - A_\alpha T_\alpha\right]. \tag{5}$$

Using this model, we obtain the shape of the tissue by minimizing $\mathcal{H}$ with respect to vertex positions.

After minimizing (Eq. 5), we quantify the stress acting on each wall through the average strain acting on each cell given by (Eq. 4). Assuming that cell wall rest length is the same between two adjacent wall compartments then it follows that they are under the same longitudinal strain, which is, to first approximation, the average between the two cells surrounding them. Therefore, longitudinal average strain acting on a specific wall used here is

$$\bar{\varepsilon}_{\alpha\beta} = \bar{\varepsilon}_{\beta\alpha} \sim \hat{\mathbf{t}}_{\alpha\beta}^T \frac{\varepsilon_\alpha + \varepsilon_\beta}{2}\hat{\mathbf{t}}_{\alpha\beta}, \tag{6}$$

where $\mathbf{t}_{\alpha\beta}$ is a unit vector along the wall separating cell α and cell β. Note that this interpolation assumes a continuous strain field. Then the stresses acting on each compartment are by the constitutive equation of a linear elastic isotropic material with Poisson ratio $\nu = 0$,

$$\sigma_{\alpha\beta} = E_\alpha\bar{\varepsilon}_{\alpha\beta} \neq \sigma_{\beta\alpha} = E_\beta\bar{\varepsilon}_{\beta\alpha}. \tag{7}$$

Note that we are only considering the longitudinal components with regards to the cell wall, which means that $\bar{\varepsilon}_{\alpha\beta}$ and $\sigma_{\alpha\beta}$ are scalar quantities. More details on the mechanical model used can be found in the supporting text. As argued in the supporting material, our choice of $\nu = 0$ does not impact the qualitative behaviour studied here.

2.3 Tissue mechanics–uncoupled tissue approximation

To assess the impact of collective mechanical behaviour within a tissue on auxin pattern self-organization, we approximate the tissue-wide mechanical model to a static tissue geometry where we approximate the effects of turgor pressure of each individual cells in the static tissue by a constant average stress $\bar{\sigma}$ acting on it [10]. Again assuming that both wall compartments have the same rest length, we infer that the stress acting on a particular wall depends only on $\bar{\sigma}$ and the stiffness of the adjacent cells. Effectively, the average longitudinal strain acting on a wall surrounded by cells α and β would simply be

$$\bar{\varepsilon}_{\alpha\beta} = \bar{\varepsilon}_{\beta\alpha} = 2\bar{\sigma} / \left(E_\alpha + E_\beta\right). \tag{8}$$

This way, instead of minimizing the full mechanical model (Eq. 5) given a set of turgor pressures T_α and rest shape matrices $M_\alpha^{(0)}$ we can, in the static tissue, immediately compute stress with Eq. 7 yielding,

$$\sigma_{\alpha\beta} = \frac{2E_\alpha\bar{\sigma}}{E_\alpha + E_\beta}. \tag{9}$$

Interestingly, Eq. 9 is valid for $\nu \neq 0$ as demonstrated in the supporting material.

In order to compare the two models, we choose the value of $\bar{\sigma}$ to be the same as the stress obtained through minimisation of (Eq. 5), for a given set of T_α and $M_\alpha^{(0)}$, with the constraint of the same end geometry.

Note that not only can this approximation be interpreted as the tissue being mechanically coupled only to the nearest neighbours, disregarding the rest of the tissue, (Fig. 2), but also as an analogous non-mechanical auxin concentration feedback model.

2.4 Auxin transport–compartment model

Compartment models for auxin transport are well adapted to the context of plant development, since the prerequisite of a boundary of a plant cell is particularly well defined by courtesy of the cell wall.

Although passive diffusion occurs across cell walls, the dominant players in auxin transport are membrane-bound carriers [22,24]. Namely, efflux transporters of the PIN family are important due to their anisotropic positioning around a cell [16], which leads to a net auxin flow from one cell to the next. Let a_α denote an non-dimensional and normalized average auxin concentration inside cell α. Following the model by [10], which is similar to previous mathematical models [25,26,29], auxin evolves according to auxin metabolism in the cell, passive diffusion between cells and active transport across cell walls via PIN,

$$\begin{aligned}\frac{\mathrm{d}a_\alpha}{\mathrm{d}t} &= \gamma^* - \delta^* a_\alpha + \mathcal{D} \sum_{\beta\in\mathcal{N}_\alpha} W_{\alpha\beta}\left(a_\beta - a_\alpha\right)\\ &\quad + \mathcal{P} \sum_{\beta\in\mathcal{N}_\alpha} W_{\alpha\beta}\left(p_{\beta\alpha}\frac{a_\beta}{K + a_\beta} - p_{\alpha\beta}\frac{a_\alpha}{K + a_\alpha}\right),\end{aligned} \tag{10}$$

where γ^* is the auxin production rate, δ^* is the auxin decay rate, $W_{\alpha\beta} = l_{\alpha\beta}/A_\alpha$, with K, $\mathcal{P}$, and $\mathcal{D}$ as adjustable parameters. $\mathcal{D}$ is the passive permeability of plant cells, whereas $\mathcal{P}$ is permeability of the cell wall due to PIN-mediated transport of auxin, and K is the Michaelis–

Menten constant for the efflux of auxin. More information on how this expression is derived can be found in the supporting text. Although this description ignores the auxin present within the extracellular domain and inside the cell wall, it has been shown that under physiological assumptions, this is a valid approximation [29]. The active transport term depends on the amount of bound PIN in each cell wall,

$$p_{\alpha\beta} = \frac{f_{\alpha\beta}}{1 + \sum_{\gamma \in \mathcal{N}_\alpha} \frac{l_{\alpha\gamma}}{L_\alpha} f_{\alpha\gamma}}, \beta \in \mathcal{N}_\alpha, \tag{11}$$

where $f_{\alpha\beta}, \beta \in \mathcal{N}_\alpha$ expresses the ratio between binding and unbinding rates of a particular wall (Fig. 3 bottom right). Note that $p_{\alpha\beta}$ is different from wall to wall and from cell to cell. This means that in general, $p_{\alpha\beta} \neq p_{\beta\alpha}$, or equivalently, $p_{ij} \neq p_{ji}$. This is consistent with the fact that there are two compartments to a cell wall shared by two adjacent cells. Expression (Eq. 11) is based on the assumption that cell walls around a particular cell compete for the same pool of PIN molecules and that the amount of PIN scales with cell perimeter. This competition has been shown to be important in the polarization of PIN [29]. Alternatively, one could also scale the amount of PIN with cell size or not scale it at all. In the former case, smaller cells would be slightly preferred for auxin accumulation, whereas in the latter, larger cells would be preferred instead. Since we want to study the impact of stress patterns on the tissue, we want to decouple it from this effect as much as possible, choosing instead to scale the amount of PIN with perimeter.

The trivial fixed point of these dynamical equations is given by $a_\alpha = \mu^*/\delta^*, \ \forall\alpha$, which also results in equal PIN density across all walls, provided turgor pressure T_α and stiffness E_α are the same across the tissue.

The feedback between tissue mechanics and auxin pattern unfolds as auxin transport affects tissue mechanics due to auxin, a_α, controlling cell wall stiffness, E_α, and in reverse tissue stress, σ_α, affects auxin transport by regulating PIN binding rates, $f_{\alpha\beta}$, as hypothesized by [10,11].

2.5 Mechanical regulation of PIN binding

According to the hypothesis presented by [10,11], mechanical cues up-regulate PIN binding. The distinction between whether these mechanical cues are strain or stress has been studied recently by [54], yet the exact nature remains unclear. Following the model presented by [10], we model the binding-unbinding ratio, $f_{\alpha\beta}$, as being a power law on positive stress,

$$f_{\alpha\beta} = f\left(\sigma_{\alpha\beta}\right) = \begin{cases} \eta\left(\sigma_{\alpha\beta}\right)^n, & \sigma_{\alpha\beta} > 0, \\ 0, & \sigma_{\alpha\beta} \leq 0, \end{cases} \tag{12}$$

where the stresses, $\sigma_{\alpha\beta}$, follow from tissue mechanics after minimization of the full mechanical model (Eq. 5), or, in the averaged stress approximation, it is the stress load on that particular compartment given by (Eq. 9). Furthermore, n is the exponent of this power law, and η captures the coupling between stress and PIN. Effectively, this mechanical coupling to PIN parameter corresponds to the sensing and subsequent response to stress, loosely translating into how much resources the cell needs to spend for processing stress cues.

2.6 Auxin-mediated cell wall softening

Auxin affects the mechanical properties of a cell wall via methyl esterification of pectin [6,7], resulting in a decrease of the stiffness of the cell wall. We assume that all cell wall

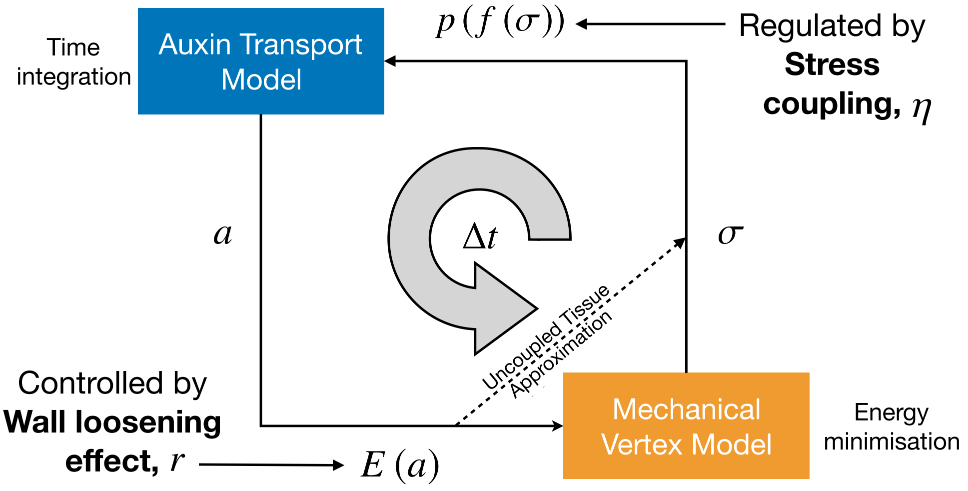

Fig. 4 Schematic representation of the time evolution of the model. From mechanical relaxation of the mechanical model, we calculate PIN densities on each wall via stress. Then we integrate auxin dynamics for a time step and update the stiffness of each cell. This process knocks the system out of the previous mechanical energy minimum, and it has to be relaxed again. Alternatively, we can shortcut energy minimization using the averaged stress approximation for a static tissue. This procedure is repeated until $t = t_{\max}$. The parameters r, wall loosening effect, and η, stress coupling, interface both models and are, therefore, of critical importance to the mechanism studied

compartments surrounding cell α share the same stiffness, E_α. To capture this effect, we model stiffness with a Hill function [10],

$$E_\alpha = E\left(a_\alpha\right) = E_0\left(1 + r\frac{1 - a_\alpha^m}{1 + a_\alpha^m}\right), \tag{13}$$

where $r \in [0, 1[$ which we define as the cell wall loosening effect, m is the Hill exponent of this interaction, and E_0 is the stiffness of the cell walls when its auxin concentration is $a_\alpha = 1$. At low values of auxin, E_α approaches the value $(1 + r)\, E_0$, whereas at high auxin concentration, E_α approaches $(1 - r)\, E_0$. Given a distribution of auxin, we can compute the wall stiffness in (Eq. 5) from (Eq. 13), or the stress acting on a specific compartment in (Eq. 9) for the approximated model.

2.7 Integrating auxin transport and tissue mechanics

At each time step, Δt, starting from an auxin distribution, we compute the stiffness of each cell according to (Eq. 13). Then, with the input of all turgor pressures, we minimize (Eq. 5) to obtain tissue geometry and stresses acting on each wall. Auxin concentration in each cell will evolve according to (Eq. 10), where the active transport term will be regulated by stress according to (Eq. 12) via (Eq. 11). A new auxin distribution will result at the end of this iteration, and we will be ready to take another time step (Fig. 4). We repeat this process until $t = t_{\max}$.

2.8 Implementation

We implemented this model with C++ programming language, where we have used the Quad-Edge data structure for geometry and topology of the tissue [55], implemented in the library Quad-Edge [56]. In order to minimize the mechanical energy of the tissue, we have used a limited-memory Broyden–Fletcher–Goldfarb–Shanno algorithm (L-BFGS) [57, 58], implemented in the library NLopt [59]. For solving the set of ODEs presented in the compartment model, we used the explicit embedded Runge–Kutta–Fehlberg method (often referred to as RKF45) implemented in the GNU Scientific Library (GSL) [60]. We wrapped the resulting classes into a python module with SWIG. For additional details regarding the parameters used for the simulations of the following section, consult Table S1 in the supporting material.

2.9 Observables

In order to quantify the existence of auxin patterns, we compute the difference between an emerging auxin concentration pattern and the trivial steady state of uniform auxin concentration pattern defined as $a_\alpha = \gamma^*/\delta^*,\ \forall\alpha$. To account for a large range of orders of magnitude of auxin concentration, we consider as an order parameter,

$$\varphi = \frac{\left\langle \ln^2\left(a_\alpha\right)\right\rangle_M}{\delta^2 + \left\langle \ln^2\left(a_\alpha\right)\right\rangle_M}, \tag{14}$$

where $\langle\cdot\rangle_M$ denotes an average over all cells within the tissue. This way, $\varphi \approx 0$ means that there are no discernible patterns, whereas $\varphi \approx 1$ implies prominent auxin patterning. The term δ^2 defines the sensitivity of this measure, such that an average deviation of δ yields $\varphi \approx 1/2$ (for small δ). We will choose $\delta = 0.1$, i. e. , a 10% deviation from the trivial steady state.

We also keep track of the average of auxin above basal levels in order to gauge the potential degree of modulation of auxin-mediated cell behaviour.

Furthermore, to characterize cells with regards to PIN localization we introduce the magnitude of the average PIN efflux direction,

$$F_\alpha = \left\| \sum_{i\in\mathcal{V}_\alpha} \frac{l_{ii+1}}{L_\alpha} p_{ii+1}\hat{\mathbf{n}}_{ii+1} \right\|, \tag{15}$$

where $\hat{\mathbf{n}}_{ii+1}$ is the unit vector normal to the wall pointing outwards from α.

Aside from a global measure of auxin patterning, it is also important to locally relate auxin to tissue mechanics. Namely, for auxin we are interested in auxin concentration, a_α, and auxin local gradient, obtained by interpolation,

$$\nabla a_\alpha = \frac{1}{2A^*_\alpha} \sum_{\gamma\in\mathcal{N}_\alpha} \begin{pmatrix} Y'_{\gamma+1} & -Y'_\gamma \\ -X'_{\gamma+1} & X'_\gamma \end{pmatrix} \begin{pmatrix} a_\gamma - a_\alpha \\ a_{\gamma+1} - a_\alpha \end{pmatrix}, \tag{16}$$

where $\mathbf{X}'_\gamma = \left(X'_\gamma, Y'_\gamma\right) = \mathbf{X}_\gamma - \mathbf{X}_\alpha$ and

$$A^*_\alpha = \frac{1}{2} \sum_{\gamma\in\mathcal{N}_\alpha} \left(X'_\gamma Y'_{\gamma+1} - Y'_\gamma X'_{\gamma+1}\right). \tag{17}$$

In fact, the quantity $|\nabla a_\alpha|$ can be used as an indicator of whether there is an interface between auxin spots and the rest of the tissue.

With regards to tissue mechanics, the local quantities we quantify are the isotropic component of stress,

$$P_\alpha = \frac{1}{2}\mathrm{Tr}\left(\sigma_\alpha\right), \tag{18}$$

and the stress deviator tensor projected along the direction of the auxin gradient,

$$D_\alpha = \frac{\nabla a_\alpha^T \sigma_\alpha' \nabla a_\alpha}{|\nabla a_\alpha|^2}, \tag{19}$$

where $\sigma_\alpha' = \sigma_\alpha - I P_\alpha$, and I is the identity matrix. Therefore, P_α is a measure if a cell is being compressed ($P_\alpha < 0$), or pulled apart ($P_\alpha > 0$), and D_α translates into if a cell is more compressed along the auxin gradient than perpendicular to it ($D_\alpha < 0$), or vice-versa ($D_\alpha > 0$).

Finally, to measure the disruption of an auxin pattern we approximate entropy by means of a Riemann sum,

$$S[\Pi] = -\sum_{i=-\infty}^{\infty} \Pi(i\Delta a)\,\Delta a \ln(\Pi(i\Delta a)\,\Delta a), \tag{20}$$

where $\Pi(a)$ is the probability density function of auxin and Δa the partition size. Note that it is only meaningful to compare entropy measures obtained with the same partition size Δa. Here, the probability density function of auxin concentration is obtained by applying a kernel density estimation on the resulting tissue auxin values. Note that $\Pi(a)$ is a continuous function. In order to infer it from simulation data, for each auxin value in the tissue, a_α, we add Kernel functions $K_w(a)$, obeying $\int_{-\infty}^{\infty} K_w(a)da = 1$ and $K_w(a) = K_w(-a)$. Then we can estimate

$$\Pi(a) \sim \frac{1}{M}\sum_{\alpha=1}^{M} K_w(a - a_\alpha), \tag{21}$$

where w is a smoothing parameter defining the width of the Kernel, this parameter is sometimes called bandwidth. This statistical tool is called kernel density estimation (KDE) [61]. We use the Epanechnikov kernel because it is bounded and we can force $\Pi(a) = 0$, $a \leq 0$.

3 Results

3.1 The tissue-wide mechanical model captures stress patterns after ablation

First we verify that the tissue-wide mechanical model captures the expected mechanical behaviour and auxin patterning when a cell is ablated. To model ablation, we set the stiffness of the ablated cell walls to $E_0 = 0$, block all auxin transport to and from it, block PIN transporters of adjacent cells from binding to the shared wall with the ablated cell, and, finally, we lower the turgor pressure to only 10% of the original value. This remnant of pressure represents the surface tension emerging from pressure of the inner layers of the shoot apical meristem acting on a curved surface, as required by the Young–Laplace equation. This is necessary since the model only simulates the epidermal layer in a plane.

We observe that the region neighbouring the ablation site gets depleted of auxin due to PIN binding preferentially to the walls circumferentially aligned around the ablated cell in accordance with the stress principal directions (Fig. 5a). This stress pattern is in agreement with calculations performed by [41] in this setting and PIN aligns according to the ablation experiments in [10].

We also simulated different wound shapes. The resulting stress patterns are shown the supporting material. Stress directions align along the shape of the ablation wound.

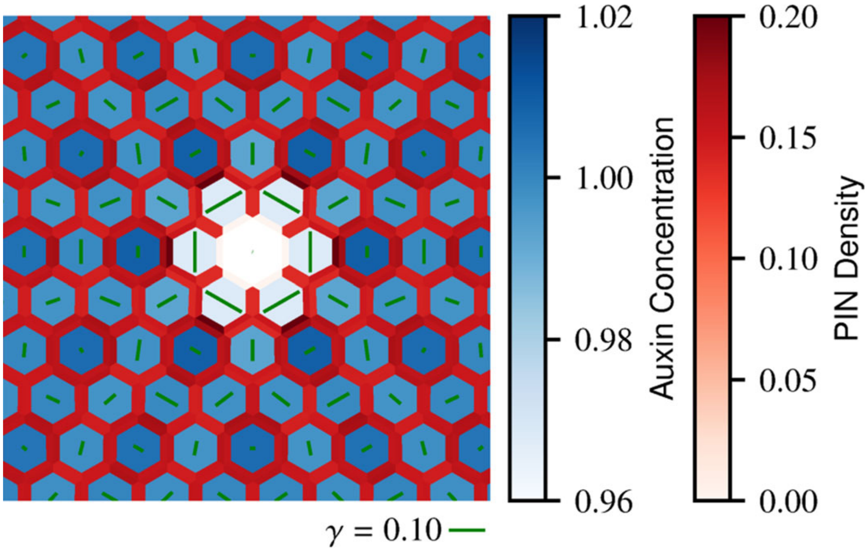

Fig. 5 Tissue-wide mechanical model captures expected stress patterns as well as auxin and PIN distribution after ablation. Green lines represent the magnitude and direction of principal stress, measured $\gamma = \frac{\lambda_+ - \lambda_-}{\lambda_+ + \lambda_-}$, where $\lambda_\pm$ are the largest and lowest eigenvalues of the stress tensor. The ablation perturbs auxin patterning by redirecting PIN. This PIN reorientation coincides with the circumferential stress patterns around the ablation site, as seen in experiments and simulations [10,41].$r = 0.65$ and $\eta = 1.5$

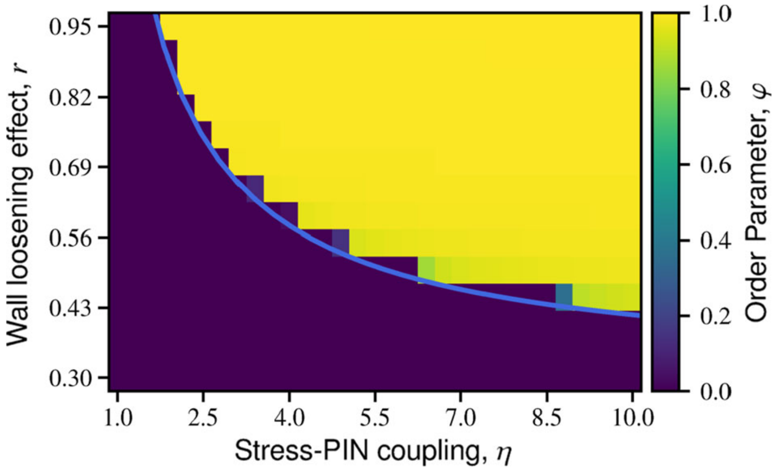

Fig. 6 Simulation results of the order parameter φ, indicator for the existence of auxin patterns, as a function of $r \in [0.30, 0.95]$ and $\eta \in [1.0, 10.0]$ for a model with tissue-wide stress patterning. The simulated tissue is composed of 2977 initially hexagonal cells. The blue line represents the analytically predicted instability for the uncoupled tissue approximation (Eq. 22)

Thus our mechanical model faithfully capture the typical tissue behaviour upon ablation with regards to stress, auxin and PIN transporter patterns.

3.2 Conditions for auxin patterns emergence

The uncoupled tissue approximation allows to analytically compute the conditions for spontaneous auxin pattern emergence in a general regular lattice (Fig. 6). Effectively, for a regular grid, the condition for pattern formation is,

$$\mathcal{M} > \frac{K+1}{W\mathcal{P}} \left[1 + \sqrt{1 + 2W \left(\frac{\mathcal{P}K}{(K+1)^2} + \frac{\mathcal{D}}{p_0} \right)} \right]^2, \tag{22}$$

where $\mathcal{M} = nmr$, $W = 4/\sqrt{3}$ is a geometrical factor specific to the used grid, and $p_0 = f(\bar{\sigma})/(1 + f(\bar{\sigma}))$ (see supporting material for the linear stability analysis details). Equation 22 is the closed form of more general expressions presented by [10,29] tailored to our system and parameters.

To quantify the existence of auxin patterns in the model with tissue-wide stress patterning, we computed the order parameter φ defined in Eq. 14 for simulations with different values of wall loosening effect r and stress coupling η (Fig. 6). These two parameters are conceptually important since the former is the cause for stiffness inhomogeneity of the tissue, and the latter represents a plant cell's sensitivity to mechanical cues.

We observe a very good agreement between the conditions for pattern emergence (Eq. 22) analytically predicted in the case of the uncoupled tissue approximation and the transition of φ in the case of tissue-wide stress patterning (Fig. 6). This means that at the onset of patterns emergence the auxin concentrations are similar enough to make the assumption that the effect of turgor pressure is simply an isotropic stress across the entire tissue, validating the approximation near the transition. This observation is in agreement with the auxin pattern emergence mechanism hypothesis by [10] (Fig. 1). The agreement between the two models does not necessarily apply after patterns emerge. This poses the question of the role of mechanics in potentially enhancing or hindering auxin flows.

3.3 Global mechanical response reinforces PIN polarity

To understand the role of tissue-wide stress patterning on the emergence of PIN-driven auxin patterns, we quantify how PIN rearranges in the model with tissue-wide stress patterning *versus* the uncoupled tissue approximation.

We compute the average PIN efflux direction, i.e., average PIN polarity for each combination of the parameters r (auxin-induced cell wall loosening) and η (coupling of PIN to stress) under the approximated (Fig. 7 top left) and tissue-wide (Fig. 7 top right) stress coupling regimes.

We observe an overall increase in PIN polarity in the tissue-wide stress coupling regime compared with the uncoupled tissue approximation. PIN polarity also becomes more sensitive to r. For very low values of r, tissue stress patterns are slightly detrimental to auxin patterning. These data show that saturation of PIN polarity happens earlier with respect to η for intermediate values of r. For high values of r, we observe a non-monotonic dependence of polarity on η, effectively translating into an optimal value of η.

Visual inspection of the simulations results reveals higher PIN density in proximity of auxin spots and an increase in magnitude of these auxin peaks upon tissue-wide stress patterning (Fig. 7a–d). Moreover, we observe a severe alteration of pattern size and wavelength between both models (Fig. 7 bottom left).

These results show that tissue-wide stress patterning reinforces PIN polarity and that auxin spots are sharper. Next we will quantify how much sharper these auxin spots become.

3.4 Tissue-wide coupling induces efficient emergence of auxin spots

Auxin levels in the shoot apical meristem have been shown to affect cell fate reliably [20], even if the flexibility of the auxin signalling mechanism allows for many potential outcomes [62]. We explore auxin spot concentration achieved by both models in order to gauge the impact of tissue-wide stress patterns on the distinguishability of primordium cells.

For this, we first characterize quantitatively the auxin spot average concentration measured for each simulation of the uncoupled tissue approximation (Fig. 8 left) and tissue-wide

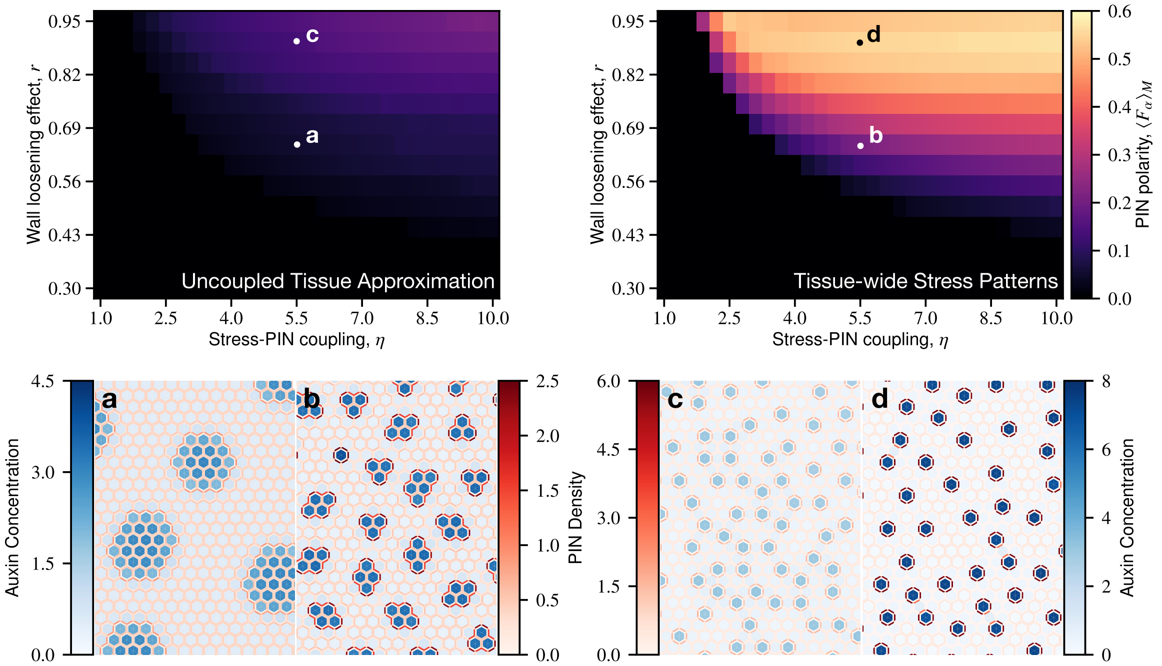

Fig. 7 Quantification of PIN polarity in both models reveals more focused auxin spots due to tissue-wide integration via mechanical coupling. (top) Average magnitude of PIN polarity, $\langle F_\alpha \rangle_M$, as a function of stress-PIN coupling, η, and wall loosening effect, r, for (top left) the uncoupled tissue approximation and (top right) for the tissue-wide stress patterning. PIN polarity magnitude increases when considering the mechanics of the whole tissue, with a particularly strong dependence on the wall loosening affect r of auxin. The labels represent the parameters plotted for (a, b, c, d) comparison between example results of auxin concentration and PIN density of simulations using the uncoupled tissue approximation (a, c) and the tissue-wide stress patterning (b, d), for the same value of $\eta = 5.5$, and $r = 0.65$ (bottom left) or $r = 0.90$ (bottom right). In both instances, we observe that PIN polarity and auxin concentration are higher upon tissue-wide stress patterning (b, d)

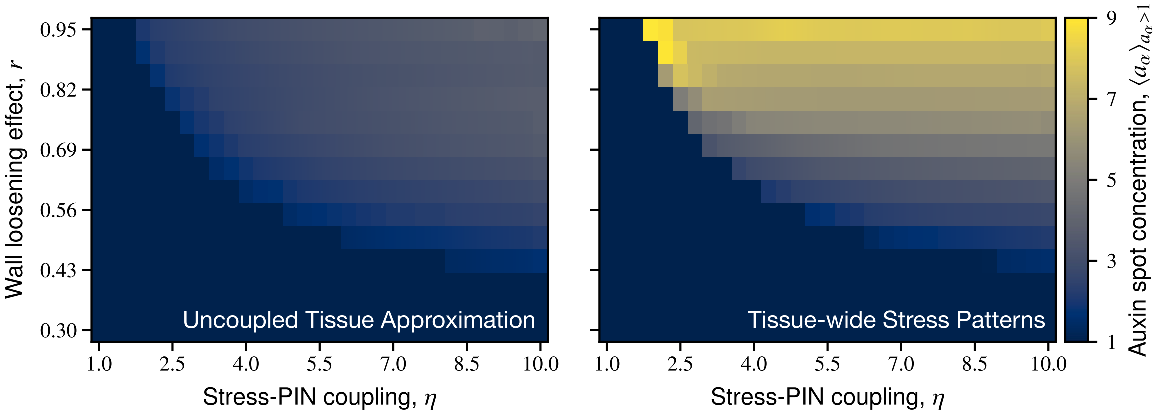

Fig. 8 Characterization of auxin spot concentration reveals more focused auxin spots due to tissue-wide integration via mechanical coupling. Average auxin concentration for cells above basal auxin concentration ($a_\alpha > 1$), for the uncoupled tissue approximation (left), and upon tissue-wide stress patterning (right), as a function of stress-PIN coupling, η, and wall loosening effect, r. Spot auxin concentration increases with both η and r in (left); however, in (right), it increases predominantly with r. For medium to high values of r, auxin concentration jumps to several times immediately after emergence

stress coupling (Fig. 8 right) regimes. We use, as a proxy, the average of cells with auxin concentration $a_\alpha > 1$ to identify auxin spots.

We observe that the dependence on the parameter r recognized for PIN polarity translates into auxin spot concentration. For medium to high values of r, auxin concentration is several

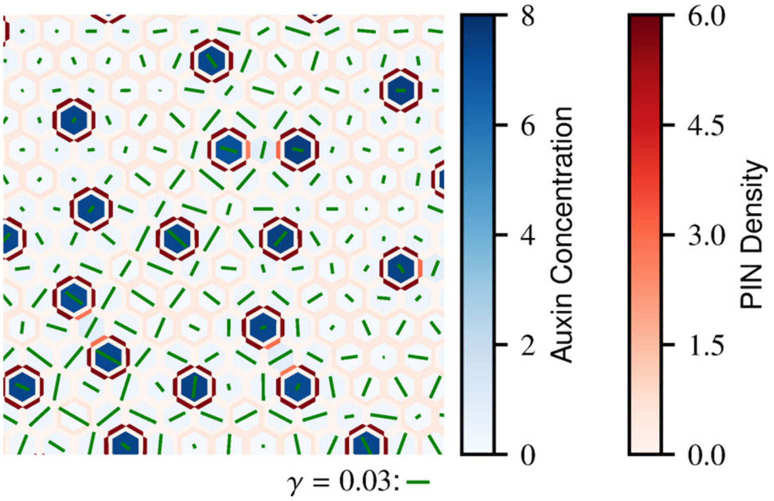

Fig. 9 Map of auxin distribution and PIN density aligns with stress direction. Green lines represent principal direction of stress, measured as $\gamma = \frac{\lambda_+ - \lambda_-}{\lambda_+ + \lambda_-}$, where $\lambda_\pm$ are the largest and lowest eigenvalues of the stress tensor. We observe that stress directions in part congruent with auxin spots. $r = 0.90$ and $\eta = 5.5$

times higher when accounting for tissue-wide behaviour than when considering the uncoupled tissue approximation.

Additionally, at the onset of pattern formation for medium to high values of r, we observe a considerable jump in average auxin spot concentration for a small change in η. This increase in sensitivity to a change in η of the system, under the aforementioned conditions, implies a boost in mechanosensing capabilities when considering tissue-wide stress patterning.

Our results point to stress patterns being responsible for the enhancement of auxin spot concentration and flows. In order to make sure we understand why, we decided to observe and quantify stress patterns and their connection to auxin distribution.

3.5 Part of wall stress within spots is borne by walls at the interface

In order to analyse tissue-wide stress patterns, we choose an example that has simple auxin patterns that allow for a straightforward interpretation. Under this condition, we choose the parameters $r = 0.90$ and $\eta = 5.5$ already presented in Fig. 7d, for which we plot on it a measure of anisotropy along the largest principal stress direction (Fig. 9). Here it becomes apparent that stress patterns are related, even if not absolutely, to auxin spot patterns.

To explore this further, we quantify several local quantities, such as auxin concentration, a_α, auxin gradient norm (Eq. 16), $|\nabla a_\alpha|$, isotropic stress component (Eq. 18), P_α, and deviator stress tensor projection onto auxin gradient (Eq. 19), D_α. For the example mentioned above, we record the histograms of the simultaneous occurrence of the pairs (a_α, P_α) (Fig. 10 top left) and $(|\nabla a_\alpha|, D_\alpha)$ (Fig. 10 top right).

We can section the results according to high or low auxin concentration (Fig. 10 bottom left), and high or low auxin gradient (Fig. 10 bottom right). Here, high auxin cells are a proxy for auxin spot cells, and high auxin gradient cells are a proxy for cells neighbouring auxin spots. Taking into account that in the uncoupled tissue approximation $P_\alpha = \bar{\sigma}$ and $D_\alpha = 0$ by construction, we can get a better picture of tissue-wide stress patterns.

We observe from data (Fig. 10 bottom left) that P_α in cells of auxin spots is lower than in the uncoupled tissue approximation and accompanied by a slight shift in the opposite direction of the P_α of the remaining cells. Additionally, we register a noticeable shift towards negative D_α for high auxin gradient cells (Fig. 10 bottom right).

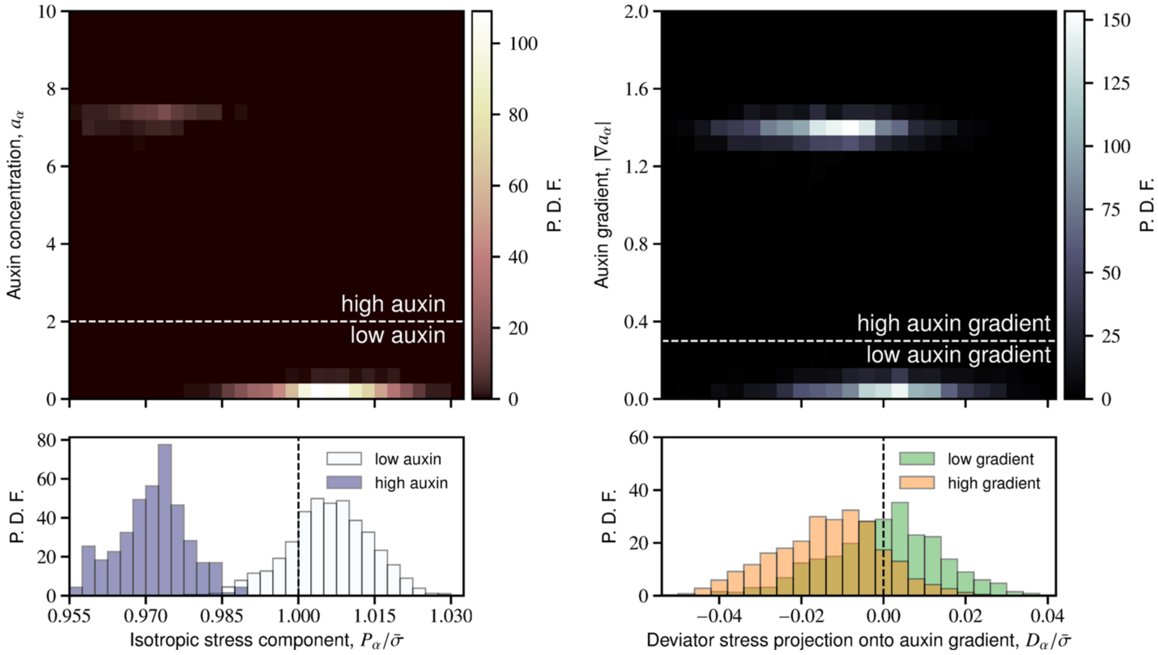

Fig. 10 Stress pattern self-organization concomitant with auxin patterns. Probability density functions (P.D.F.s) of (top left) auxin concentration and isotropic stress component and (top right) auxin gradient magnitude and deviator stress tensor projection onto auxin gradient. In each case, we can identify two populations of cells: high and low auxin concentration (bottom left), and high and low auxin gradient (bottom right). (bottom left), since $P_\alpha = \bar{\sigma}$ signifies the stress that would be expected in the uncoupled tissue approximation, high auxin concentration cell expansion is constrained by the remaining cells which are, in turn, under a larger amount of stress. On the other hand (bottom right) we observe that the auxin spot neighbours have, on average, negative values of D_α, indicating that the largest principal stress direction is perpendicular to auxin gradients, i.e., circumferentially aligned around auxin spots, as suggested by Fig. 9. $r = 0.90$ and $\eta = 5.5$

Taken together, these data suggests that cell walls at the interface of a spot are under a larger amount of stress whereas the cells within auxin spots have decreased stress. This leads to reinforced polar auxin transport towards the spot and hence higher auxin concentration. The lower isotropic stress component inside the auxin spot suggests that the diffusive term inside auxin spots increases in importance relative to the active transport term.

3.6 Tissue-wide stress coupling mitigates disruption by noise

Up until now, our simulations were performed on hexagonal tissues in the absence of noise. This also raises the question of how tissue-wide stress patterns impact pattern emergence robustness against noise.

In plant tissue as any biological entity, noise prevails. As such cells within a tissue differ in their mechanical parameters. In order to inspect how parameter noise disrupts pattern emergence, we choose to sample reference stiffness, E_0, from a normal distribution for each cell. As outlined in the supplementary material, we expect this parameter to be the most disruptive to the active term and it is reasonable to assume it changes from cell to cell. We then simulate the resulting tissue with the uncoupled tissue approximation and tissue-wide stress coupling.

We simulate tissues with $r = 0.65$ and $\eta = 5.5$ for both models by promoting E_0 to a random variable sampled from Gaussian distribution with mean $\bar{E_0} = 300$ MPa and standard deviation of $\alpha \bar{E_0}$, $\alpha \in \{0.03, 0.06, 0.09, 0.12, 0.15\}$, where α is the noise strength. For each value of α, five simulations were performed per model. We fit the resulting auxin distributions

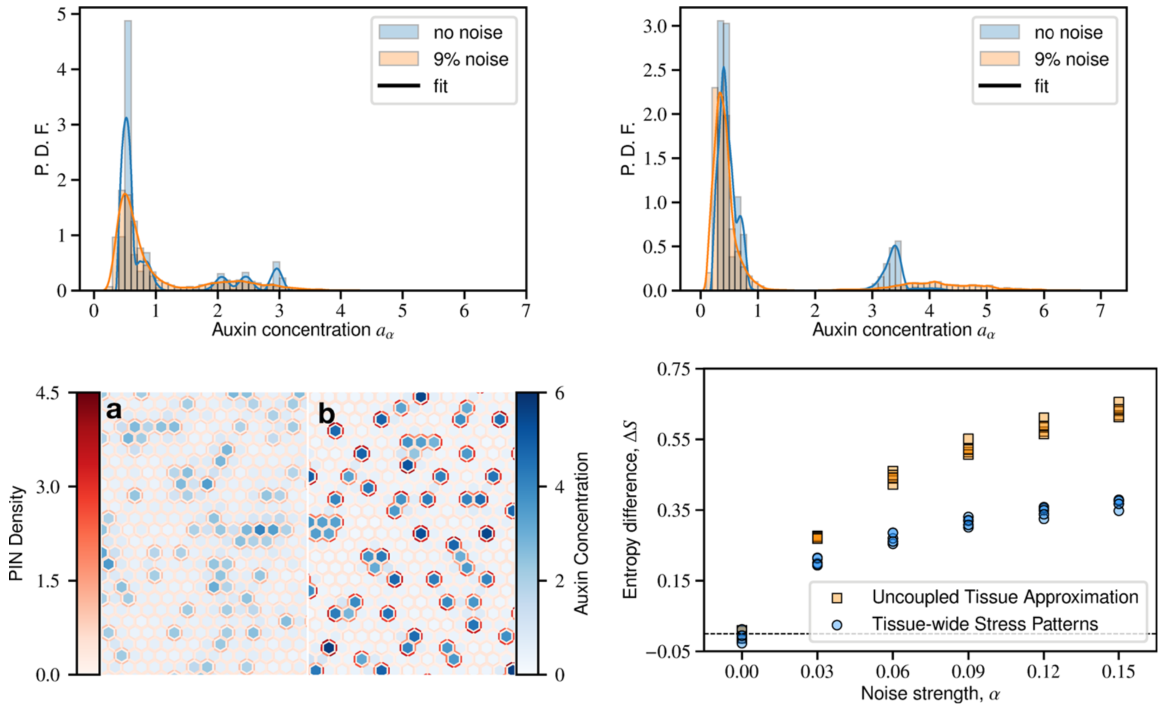

Fig. 11 Impact of noise in reference stiffness in the auxin concentration distributions for the uncoupled tissue approximation and upon tissue-wide coupling reveals robustness of auxin patterns due to tissue-wide integration. For a given noise strength, auxin concentration probability density functions (P.D.F.s) are extracted from simulation results by means of a kernel density estimation for the uncoupled tissue approximation (top left) and when considering tissue-wide stress patterns (top right). The simulated tissues have $r = 0.65$ and $\eta = 5.5$. For both models, we observe broadening of the distributions when considering noise. In each instance, the fit appears to be adequate for describing the resulting auxin concentration. (bottom left) Examples of the resulting patterns in the uncoupled tissue approximation (a) and in the case of tissue-wide stress patterns (b) for a noise strength of 9%. Even though patterns are heavily disrupted, we can still discern more clearly high auxin concentration spikes upon tissue-wide coupling. (bottom right) Entropy difference between the resulting distributions for a given noise strength and in the absence of noise. In the presence of tissue-wide stress patterns disruption of tissue patterning is consistently lower than in the uncoupled tissue approximation

to a probability density function (Fig. 11 top left and top right). We observe that noise in reference stiffness impacts the patterning behaviour in a severe manner (Fig. 11 bottom left). Yet, with tissue-wide stress coupling spots of noticeable auxin accumulation are preserved.

In order to quantify the disruption, we compute the entropy (Eq. 20) of a fitted auxin probability density function by means of a kernel density estimation on the resulting auxin distributions. The kernel used for all fits was the Epanechnikov kernel with a bandwidth of about 0.202. This number arises in the rule-of-thumb estimate for the Gaussian kernel for the sample size and dimension of this system. The partition size used for the numerical approximation of the entropy is the same for all instances. Afterwards, we measure the entropy difference between the expected auxin distribution for each value of α, of each model and for all simulations (Fig. 11 bottom right). The reference entropy is taken to be the average of the uncoupled tissue approximation at $\alpha = 0$. We can infer from these results that tissue-wide coupling helps to rescue auxin accumulation spots despite its heavy disruption in comparison to the uncoupled tissue approximation.

3.7 High turgor preferred but not required for sustaining auxin maxima

It is of interest to the experimental community at this point in time how auxin spots and turgor pressure correlates [63,64]. To explore how the the tissue-wide mechanical model

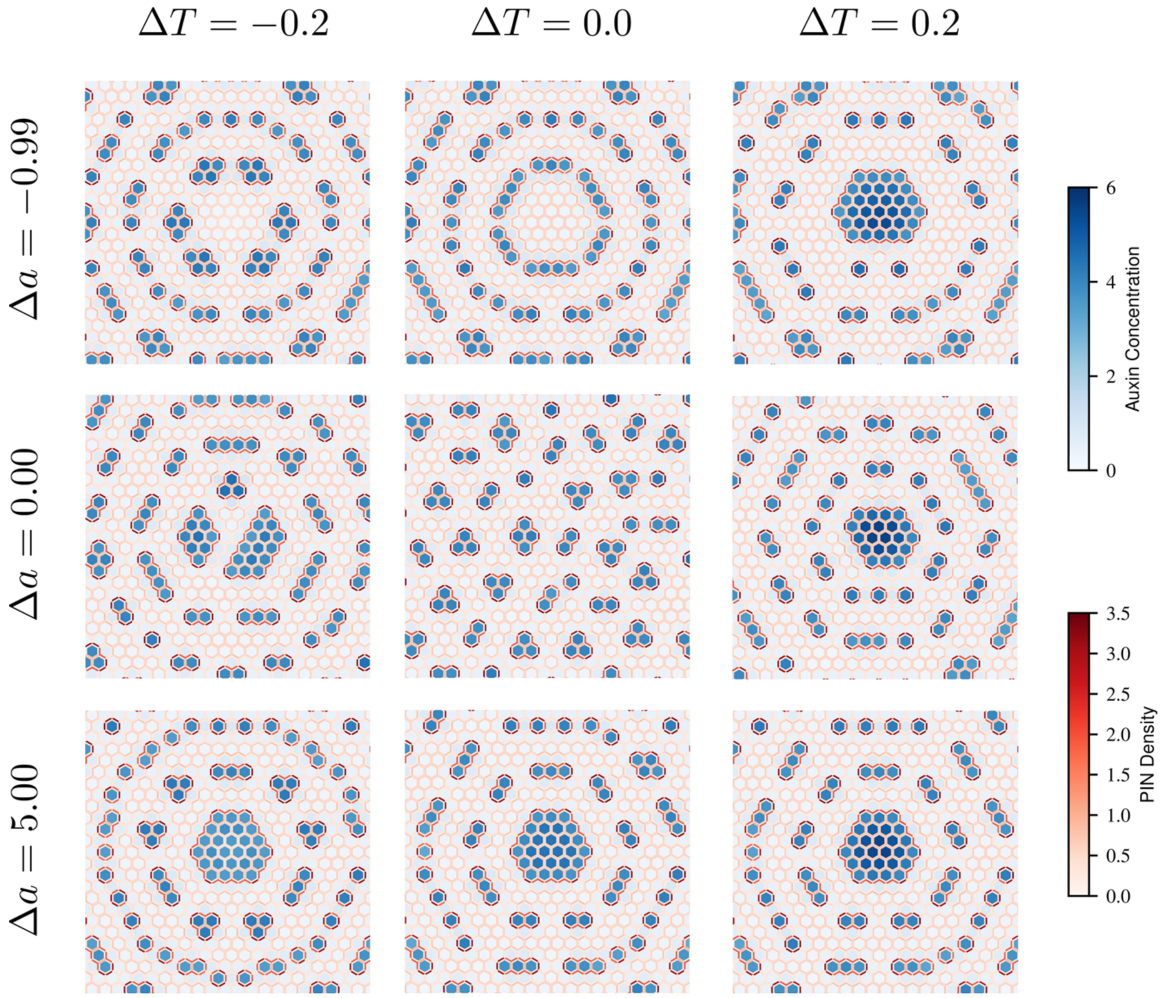

Fig. 12 Simulations of auxin patterning with the tissue-wide mechanical model when considering a local turgor increase (right column), decrease (left column), or constant (middle column), and a prior high (bottom row), low (top row), or constant (middle row) initial auxin concentration. Units of ΔT are MPa. We used $\eta = 10$ and $r = 0.65$ for all simulations. Even if high turgor predicts an auxin maximum, it becomes unclear what might happen with low turgor. The tissue-wide mechanical model seems to preserve already existing auxin maxima

responds to local turgor variations, we probe what happens when patterns emerge with a local increase or decrease in turgor. Since stress is tied to active auxin flow, the results are prone to be affected by prior auxin concentration distribution. Hence, we test the several turgor scenarios as well as initial auxin concentration. We added a contribution to turgor of $\Delta T e^{-\frac{x^2+y^2}{2\sigma}}$, where $\Delta T \in \{-0.2, 0.0, 0.2\}$ MPa and $\sigma = 2L$. For initial auxin concentration, we used the same form with the same σ, yet the largest deviations are $\Delta a \in \{-0.99, 0.00, 5.00\}$. To be sure we are well within the pattern formation regime of the model for low pressure, we used the stress-PIN coupling value of $\eta = 10$ and $r = 0.65$.

Regardless of initial auxin concentration, for high turgor, we observe an auxin maximum predictably emerges correlated with a turgor maximum (Fig. 12 right column). Nevertheless, if an initial auxin concentration exists, we also predict that the spot remains regardless of whether this position is a turgor minimum or not (Fig. 12 bottom row). Low turgor regions can still exhibit patterns adding to the complexity of this simple measure (Fig. 12 middle row, left).

From these data, we can conclude is that developmental history is as important as turgor pressure for predicting auxin maxima positioning. We can predict high turgor leads to auxin accumulation, yet low turgor gives us little insight on auxin distribution. We can also predict that a high auxin concentration region.

4 Discussion

Here, we used a model composed of a vertex model for plant tissue mechanics, and a compartment model for auxin transport to uncover the role of tissue-wide mechanical coupling on auxin redistribution. We first verified that the tissue-wide mechanical model successfully captures the behaviour of plant tissue upon ablation experiments and the conditions for emergence of auxin patterns. We then compared the behaviour of our model featuring tissue-wide mechanical coupling to an approximation which regards cells as mechanically isolated. We observe the emergence of focused auxin spots with high auxin concentration when tissue-wide mechanical coupling is implemented. Notably, depending on the parameters of the tissue-wide stress model, auxin spot concentration is more sensitive to stress than what could be predicted from the approximation. We observe that tissue-wide mechanical effects unaccounted for by the approximation have a positive impact on PIN polarity. Furthermore, we show that stress patterning of the tissue mitigates the disruption caused by noise, increasing robustness of the system. Finally, we observe auxin concentration correlating with high local turgor pressure. This behaviour coexists with the possibility of having auxin maxima anti-correlating with turgor.

The auxin-induced cell wall loosening effect (r parameter in this work) is an important determinant of the feedback of auxin on tissue mechanics. The range of values of r for which substantial pattern focusing occurs is around $r \sim 0.60$ and above in our model. This translates into a variation of stiffness from a minimum value $E_{\min}$ up to $E_{\max} = 4E_{\min}$ (see supplementary material). Although high, this range is within biological expectation and supported by AFM measurements on auxin treated tissues [7] and comparable to previous simulations of this mechanism [10] where $E_{\max}/E_{\min} = 5$ which translates into $r = 2/3$.

Comparison of the tissue-wide stress patterning case to the uncoupled tissue approximation reveals that auxin spot concentration has a very steep transition in the former case (Fig. 8). This results in a several-fold increase in auxin concentration at values of η close to the threshold for pattern formation. What was once a relatively subtle graded response of auxin spot concentration on stress behaves now as an on-off switch by virtue of tissue mechanical relaxation. Since the mechanical perturbations being highlighted through the comparison are purely passive, this improvement in sensing comes at no additional cost for the plant and therefore has the potential to increase efficiency.

In the present work, we explored the parameter space (η, r) exclusively. We observe consistently that pattern wavelengths shorten from the uncoupled tissue approximation and the tissue-wide coupling model. It would be interesting to systematically probe the diversity of patterns and how they change upon tissue-wide mechanical coupling. For our simulations, we used the parameters n, m, K from [10], parameters on which we have little empirical information. Yet, the sensitivity analysis from [29] suggests that n and K especially should affect patterning the most. We speculate the parameter m, specific to wall loosening, to be of similar importance. We expect that a study focusing on these three parameters would yield more interesting patterns shapes.

This work focused exclusively in the hypothesis that PIN is mechanically regulated. However, competing chemical feedback mechanisms have been proposed. Recently, mechanics and ARF-mediated PIN expression have been modelled together by [40] and show promising pattern formation capabilities. Other factors we have not taken into account is the family of auxin importers of the AUX family, which have been shown to be present in the epidermal layer of the shoot apical meristem [16]. Auxin binding proteins have also been hypothesized to promote auxin flow polarization [65]. Another observed interaction is cytokinin action controlling PIN polarity during lateral root formation [66].

The PIN regulation used in the auxin transport compartment model was specifically stress-based. In the supplementary text, we show results using strain-based PIN binding instead. We observe the same overall auxin spot focusing behaviour. It is still unclear whether the PIN density change due to mechanics is a result of strain or stress [11]. In fact, this question has been tackled recently by [54] concluding that in most simulated experiments both strain and stress-based models behave similarly. A notable exception is the experimentally observed correlation of PIN polarity and auxin concentration [37,67]. On one hand, this observation is not captured by the stress-based PIN binding model. On the other hand, available experimental data and simulations suggest stress sensing being easier to explain [54]. Furthermore, the polarity difference could be rescued by the observation that ARF-mediated PIN expression is higher at the tip of the primordium [68].

The specific distribution of emergent stress patterns is remarkable in the sense that it coincides with the shape-induced stress patterns, as indicated by microtubule orientation, around the tip of the primordium as it emerges from the meristem [41]. Therefore, tissue-wide stress patterning sets the stage for primordium outgrowth by focusing efficiently auxin, forming local circumferential stress that in turn may re-orient microtubules and prefigure the shape of the primordium. This process could, in turn, be capable of reinforcing auxin transport to the tip of the newly forming organ. Yet, quantifying this requires further modelling. Therefore, it would be interesting to include auxin transport in already existing models for primordium outgrowth [8,9].

Even though the analysed numerical simulations were limited to noise in the parameter E_0, it showcases the power of the aforementioned auxin peak focusing that happens upon tissue-wide mechanical coupling. In this instance, we show here the power of tissue-wide stress patterns to mitigate the information loss due to noise by inspecting entropy of auxin concentration distribution. This result, especially when paired with the increase in sensitivity mentioned above, is indeed remarkable. This is due to the fact that in a wide range of optimized systems, biological or otherwise, robustness and efficiency are thought to be in opposition to each other, as illustrated, for example, by [69]. This is because robustness is usually brought upon by additional systems which would be considered clutter by a system geared towards efficiency. This opens a novel line of argumentation in the discourse of the evolution of mechanical signalling in multicellular organisms.

Lastly, we probed the behaviour of the used tissue-wide mechanical model when faced with local turgor variations. Our results indicate that once established auxin spots can endure low turgor scenarios, even if they would prefer high turgor regions all else being equal. Maintaining a turgor pressure difference for so long, however, might not be feasible for the plant. To answer how this setting could be achieved would require modelling water transport between plant cells along the lines of [63]. Nevertheless, our model can explain, at least in part, why these two quantities do not correlate in a straightforward manner.

5 Conclusion

Even though the mechanisms by which PIN preferentially associate with stressed cell walls is unclear, here we show that there are substantial advantages by intertwining tissue-wide mechanics and auxin patterning. Even if auxin patterning is possible by chemical processes and local mechanical coupling, tissue-wide mechanics may provide a way for patterning to still occur at a lower energy cost for the tissue. Moreover, this process can also provide robustness to the patterning, factoring in tissue-wide stress pattern, a sort of proprioceptive mechanism.

Acknowledgements This work was supported by the Max Planck Society and the Deutsche Forschungsgemeinschaft via DFG-FOR2581.

Author contributions JRDR, AM and KA designed research. JRDR performed the research. JRDR, AM and KA wrote the article.

Funding This work has been Funded by Deutsche Forschungsgemeinschaft via FOR-2581 (P1, P6).

Data availibility The data that support the findings of this study are available from the corresponding author upon request.

Compliance with ethical standards

Conflict of interest The authors decalre that they have no conflict of interest.

Code availibility The code used to produce the data of this study are available from the corresponding author upon request.

References

1. J.A. Lockhart, An analysis of irreversible plant cell elongation. J. Theor. Biol. **8**, 264–275 (1965)
2. J.K.E. Ortega, Augmented growth equation for cell wall expansion. Plant Physiol. **79**, 318–320 (1985)
3. D. Cosgrove, Biophysical control of plant cell growth. Ann. Rev. Plant Physiol. **37**, 377–405 (1986)
4. A. Geitmann, J.K. Ortega, Mechanics and modeling of plant cell growth. Trends Plant Sci. **14**, 467–478 (2009)
5. O. Hamant, J. Traas, The mechanics behind plant development. New Phytol. **185**, 369–385 (2010)
6. A. Peaucelle, S.A. Braybrook, L. Le Guillou, E. Bron, C. Kuhlemeier, H. Höfte, Pectin-induced changes in cell wall mechanics underlie organ initiation in arabidopsis. Curr. Biol. **21**, 1720–1726 (2011)
7. S.A. Braybrook, A. Peaucelle, Mechano-chemical aspects of organ formation in *Arabidopsis thaliana*: the relationship between auxin and pectin. PLoS ONE **8**, e57813 (2013)
8. F. Boudon, J. Chopard, O. Ali, B. Gilles, O. Hamant, A. Boudaoud, J. Traas, C. Godin, A computational framework for 3D mechanical modeling of plant morphogenesis with cellular resolution. PLoS Comput. Biol. **11**, e1003950 (2015)
9. J. Khadka, J.-D. Julien, K. Alim, Feedback from tissue mechanics self-organizes efficient outgrowth of plant organ. Biophys. J . **117**, 1995–2004 (2019)
10. M.G. Heisler, O. Hamant, P. Krupinski, M. Uyttewaal, C. Ohno, H. Jönsson, J. Traas, E.M. Meyerowitz, Alignment between PIN1 polarity and microtubule orientation in the shoot apical meristem reveals a tight coupling between morphogenesis and auxin transport. PLoS Biol. **8**, e1000516 (2010)
11. N. Nakayama, R.S. Smith, T. Mandel, S. Robinson, S. Kimura, A. Boudaoud, C. Kuhlemeier, Mechanical regulation of auxin-mediated growth. Curr. Biol. **22**, 1468–1476 (2012)
12. W.D. Teale, I.A. Paponov, K. Palme, Auxin in action: signalling, transport and the control of plant growth and development. Nat. Rev. Mol. Cell Biol. **7**, 847–859 (2006)
13. S. Vanneste, J. Friml, Auxin: a trigger for change in plant development. Cell **136**, 1005–1016 (2009)

14. M. Sassi, T. Vernoux, Auxin and self-organization at the shoot apical meristem. J. Exp. Bot. **64**, 2579–2592 (2013)
15. E. Benková, M. Michniewicz, M. Sauer, T. Teichmann, D. Seifertová, G. Jürgens, J. Friml, Local, efflux-dependent auxin gradients as a common module for plant organ formation. Cell **115**, 591–602 (2003)
16. D. Reinhardt, E.-R. Pesce, P. Stieger, T. Mandel, K. Baltensperger, M. Bennett, J. Traas, J. Friml, C. Kuhlemeier, Regulation of phyllotaxis by polar auxin transport. Nature **426**(6964), 255–60 (2003)
17. P.B. de Reuille, I. Bohn-Courseau, K. Ljung, H. Morin, N. Carraro, C. Godin, J. Traas, Computer simulations reveal properties of the cell-cell signaling network at the shoot apex in Arabidopsis. Proc. Nat. Acad. Sci. **103**, 1627–1632 (2006)
18. D. Reinhardt, T. Mandel, C. Kuhlemeier, Auxin regulates the initiation and radial position of plant lateral organs. Plant Cell **12**, 507 (2000)
19. R.S. Smith, The role of auxin transport in plant patterning mechanisms. PLoS Biol. **6**, e323 (2008)
20. T. Vernoux, F. Besnard, J. Traas, Auxin at the shoot apical meristem. Cold Spring Harb. Perspect. Biol. **2**, a001487–a001487 (2010)
21. S. Robinson, A. Burian, E. Couturier, B. Landrein, M. Louveaux, E.D. Neumann, A. Peaucelle, A. Weber, N. Nakayama, Mechanical control of morphogenesis at the shoot apex. J. Exp. Bot. **64**, 4729–4744 (2013)
22. J. Petrasek, PIN proteins perform a rate-limiting function in cellular auxin efflux. Science **312**, 914–918 (2006)
23. J. Wisniewska, Polar PIN localization directs auxin flow in plants. Science **312**, 883–883 (2006)
24. J. Petrasek, J. Friml, Auxin transport routes in plant development. Development **136**, 2675–2688 (2009)
25. H. Jonsson, M.G. Heisler, B.E. Shapiro, E.M. Meyerowitz, E. Mjolsness, An auxin-driven polarized transport model for phyllotaxis. Proc. Nat. Acad. Sci. **103**, 1633–1638 (2006)
26. R.S. Smith, S. Guyomarc'h, T. Mandel, D. Reinhardt, C. Kuhlemeier, P. Prusinkiewicz, A plausible model of phyllotaxis. Proc. Nat. Acad. Sci. **103**, 1301–1306 (2006)
27. R.M. Merks, Y. Van de Peer, D. Inzé, G.T. Beemster, Canalization without flux sensors: a traveling-wave hypothesis. Trends Plant Sci. **12**, 384–390 (2007)
28. A.C. Newell, P.D. Shipman, Z. Sun, Phyllotaxis: cooperation and competition between mechanical and biochemical processes. J. Theor. Biol. **251**, 421–439 (2008)
29. P. Sahlin, B. Söderberg, H. Jönsson, Regulated transport as a mechanism for pattern generation: capabilities for phyllotaxis and beyond. J. Theor. Biol. **258**, 60–70 (2009)
30. T. Sachs, Polarity and the induction of organized vascular tissues. Ann. Bot. **33**, 263–275 (1969)
31. G.J. Mitchison, A model for vein formation in higher plants, in *Proceedings of the Royal Society of London. Series B. Biological Sciences*, vol. 207, pp. 79–109 (1980)
32. F.G. Feugier, A. Mochizuki, Y. Iwasa, Self-organization of the vascular system in plant leaves: inter-dependent dynamics of auxin flux and carrier proteins. J. Theor. Biol. **236**, 366–375 (2005)
33. F.G. Feugier, Y. Iwasa, How canalization can make loops: a new model of reticulated leaf vascular pattern formation. J. Theor. Biol. **243**, 235–244 (2006)
34. H. Fujita, A. Mochizuki, Pattern formation of leaf veins by the positive feedback regulation between auxin flow and auxin efflux carrier. J. Theor. Biol. **241**, 541–551 (2006)
35. S. Stoma, M. Lucas, J. Chopard, M. Schaedel, J. Traas, C. Godin, Flux-based transport enhancement as a plausible unifying mechanism for auxin transport in meristem development. PLoS Comput. Biol. **4**, e1000207 (2008)
36. K. Alim, E. Frey, Quantitative predictions on auxin-induced polar distribution of PIN proteins during vein formation in leaves. Eur. Phys. J. E **33**, 165–173 (2010)
37. E.M. Bayer, R.S. Smith, T. Mandel, N. Nakayama, M. Sauer, P. Prusinkiewicz, C. Kuhlemeier, Integration of transport-based models for phyllotaxis and midvein formation. Genes Dev. **23**, 373–384 (2009)
38. M. Cieslak, A. Runions, P. Prusinkiewicz, Auxin-driven patterning with unidirectional fluxes. J. Exp. Bot. **66**, 5083–5102 (2015)
39. Y. Hayakawa, M. Tachikawa, A. Mochizuki, Mathematical study for the mechanism of vascular and spot patterns by auxin and pin dynamics in plant development. J. Theor. Biol. **365**, 12–22 (2015)
40. H.R. Allen, M. Ptashnyk, Mathematical modelling of auxin transport in plant tissues: flux meets signalling and growth. Bull. Math. Biol. **82**, 1–35 (2020)
41. O. Hamant, M.G. Heisler, H. Jonsson, P. Krupinski, M. Uyttewaal, P. Bokov, F. Corson, P. Sahlin, A. Boudaoud, E.M. Meyerowitz, Y. Couder, J. Traas, Developmental patterning by mechanical signals in arabidopsis. Science **322**, 1650–1655 (2008)
42. O. Hamant, E.S. Haswell, Life behind the wall: sensing mechanical cues in plants. BMC Biol. **15**, 59 (2017)
43. O. Hamant, D. Inoue, D. Bouchez, J. Dumais, E. Mjolsness, Are microtubules tension sensors? Nat. Commun. **10**, 2360 (2019)

44. M. Uyttewaal, A. Burian, K. Alim, B. Landrein, D. Borowska-Wykręt, A. Dedieu, A. Peaucelle, M. Ludynia, J. Traas, A. Boudaoud, D. Kwiatkowska, O. Hamant, Mechanical stress acts via katanin to amplify differences in growth rate between adjacent cells in arabidopsis. Cell **149**, 439–451 (2012)
45. E. Feraru, M.I. Feraru, J. Kleine-Vehn, A. Martinière, G. Mouille, S. Vanneste, S. Vernhettes, J. Runions, J. Friml, PIN polarity maintenance by the cell wall in arabidopsis. Curr. Biol. **21**, 338–343 (2011)
46. H. Li, D. Lin, P. Dhonukshe, S. Nagawa, D. Chen, J. Friml, B. Scheres, H. Guo, Z. Yang, Phosphorylation switch modulates the interdigitated pattern of PIN1 localization and cell expansion in Arabidopsis leaf epidermis, in *Cell Research*, vol. 21, pp. 970–978 (2011)
47. P.J. Overvoorde, Functional genomic analysis of the AUXIN/INDOLE-3-ACETIC ACID gene family members in *Arabidopsis thaliana*. Plant Cell Online **17**, 3282–3300 (2005)
48. D.B. Staple, R. Farhadifar, J.C. Röper, B. Aigouy, S. Eaton, F. Jülicher, Mechanics and remodelling of cell packings in epithelia. Eur. Phys. J. E **33**, 117–127 (2010)
49. Y. Li, H. Naveed, S. Kachalo, L.X. Xu, J. Liang, Mechanisms of regulating cell topology in proliferating epithelia: impact of division plane, mechanical forces, and cell memory. PLoS ONE **7**, e43108 (2012)
50. G. Trichas, A.M. Smith, N. White, V. Wilkins, T. Watanabe, A. Moore, B. Joyce, J. Sugnaseelan, T.A. Rodriguez, D. Kay, R.E. Baker, P.K. Maini, S. Srinivas, Multi-cellular rosettes in the mouse visceral endoderm facilitate the ordered migration of anterior visceral endoderm cells. PLoS Biol. **10**, e1001256 (2012)
51. N. Murisic, V. Hakim, I.G. Kevrekidis, S.Y. Shvartsman, B. Audoly, From discrete to continuum models of three-dimensional deformations in epithelial sheets. Biophys. J . **109**, 154–163 (2015)
52. M. Osterfield, X. Du, T. Schüpbach, E. Wieschaus, S.Y. Shvartsman, Three-dimensional epithelial morphogenesis in the developing drosophila egg. Dev. Cell **24**, 400–410 (2013)
53. S. Alt, P. Ganguly, G. Salbreux, Vertex models: from cell mechanics to tissue morphogenesis. Philos. Trans. R. Soc. B Biol. Sci. **372**, 20150520 (2017)
54. J.-D. Julien, A. Pumir, A. Boudaoud, Strain- or stress-sensing in mechanochemical patterning by the phytohormone auxin. bioRxiv **81**, 3342–3361 (2019)
55. L. Guibas, J. Stolfi, Primitives for the manipulation of general subdivisions and the computation of voronoi. ACM Trans. Graph. **4**, 74–123 (1985)
56. P. Heckbert, Quad-edge data structure library. http://www.cs.cmu.edu/afs/andrew/scs/cs/15-463/2001/pub/src/a2/cell/
57. J. Nocedal, Updating quasi-Newton matrices with limited storage. Math. Comput. **35**, 773 (1980)
58. D.C. Liu, J. Nocedal, On the limited memory BFGS method for large scale optimization. Math. Program. **45**, 503–528 (1989)
59. S.G. Johnson, The nlopt nonlinear-optimization package. http://github.com/stevengj/nlopt
60. M. Galassi et al., *Gnu Scientific Library Reference Manual*, 3rd edn. (Network Theory Ltd., Surrey, 2009).
61. S. Weglarczyk, Kernel density estimation and its application. ITM Web Conf. **23**, 00037 (2018)
62. O. Leyser, Auxin signaling. Plant Physiol. **176**, 465–479 (2018)
63. Y. Long, I. Cheddadi, G. Mosca, V. Mirabet, M. Dumond, A. Kiss, J. Traas, C. Godin, A. Boudaoud, Cellular heterogeneity in pressure and growth emerges from tissue topology and geometry. Curr. Biol. **30**(8), 1504-1516.e8 (2020)
64. I. Cheddadi, M. Génard, N. Bertin, C. Godin, Coupling water fluxes with cell wall mechanics in a multicellular model of plant development. PLOS Comput. Biol. **15**, 1–16 (2019)
65. M. Adamowski, J. Friml, PIN-dependent auxin transport: action, regulation, and evolution. Plant Cell Online **27**, 20–32 (2015)
66. P. Marhavý, J. Duclercq, B. Weller, E. Feraru, A. Bielach, R. Offringa, J. Friml, C. Schwechheimer, A. Murphy, E. Benková, Cytokinin controls polarity of PIN1-dependent auxin transport during lateral root organogenesis. Curr. Biol. **24**, 1031–1037 (2014)
67. D.L. O'Connor, A. Runions, A. Sluis, J. Bragg, J.P. Vogel, P. Prusinkiewicz, S. Hake, A division in pin-mediated auxin patterning during organ initiation in grasses. PLOS Comput. Biol. **10**, 1–14 (2014)
68. M.G. Heisler, C. Ohno, P. Das, P. Sieber, G.V. Reddy, J.A. Long, E.M. Meyerowitz, Patterns of auxin transport and gene expression during primordium development revealed by live imaging of the arabidopsis inflorescence meristem. Curr. Biol. **15**, 1899–1911 (2005)
69. G. Peng, S.-Y. Tan, J. Wu, P. Holme, Trade-offs between robustness and small-world effect in complex networks. Sci. Rep. **6**, 37317 (2016)

Chapter 5

From lateral root founder cell identity to a primordium proper

We have peered into the complexity of mechanical regulation of PIN in an abstracted setting. There, we have documented how mechanical regulation of PIN binding modulates the auxin patterning mechanism via the interaction of tissue turgidity and auxin-mediated mechanical heterogeneities. We are, at this point, equipped with a powerful description of plant tissue mechanics and mechanically-regulated auxin transport. We will try, in the course of this chapter, to apply this model in a novel setting, namely the lateral root formation (LRF). This will enable us to judge how feasible this regulatory mechanism is or in which way it fails to capture empirical observations.

First we will introduce the biological processes underpinning formation of the lateral root, emphasising the initial stages. We focus our attention to the LRF system from founder cell (FC) identity establishment until the first anticlinal cell division. Next we will discuss how we adapt our current formulation of plant mechanics and auxin transport, as well as how to include growth. Afterwards, we will discuss the consequences of growth, assuming a constant auxin distribution. We will also discuss what factors we observe to contribute to the maintenance of auxin in the primed pericycle (founder) cells, in the absence of growth. Lastly, we will include all processes at once in order to observe how these interact with each other dynamically, as well as the consequence for lateral root formation during this stage. We will discuss results following their exposition in the course of this chapter.

5.1 Biological overview of lateral root formation

The whole process of lateral root formation is characterised by an extraordinary degree of mechanical interactions between cells [97, 142]. Pericycle cells are primed to initiate

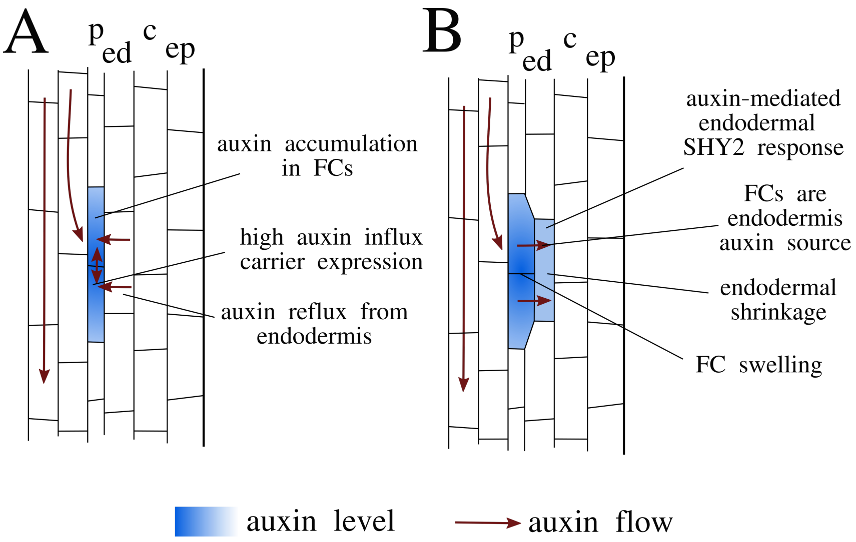

Figure 5.1: Schematic of the auxin concentration and flows during LRF from the (A) pericycle cell priming, in which the affected cells will develop into FCs, until (B) before the first round of cell divisions. Auxin accumulates in the primed cells due to auxin flows from the vasculature, endodermal reflux and high auxin influx carrier expression. After a while endodermal auxin response unleashes the SHY2 mechanism leading to intense cell wall remodelling of the endodermis, after which the FCs swell outwards. The represented layers are vasculature layers, the pericycle (p), the endodermis (ed), the cortex (c) and the epidermis (ep). To the left of the represented region is the center of the root and to the right we have its surface.

the lateral root primordium (LRP) when displaying high degree of auxin response [22, 25] (Fig. 5.1 A). After mechanical remodelling of the overlaying layer by endodermal auxin response, the founder cells are allowed to pursue growth [101] (Fig. 5.1 B). After FC swelling, FCs start dividing marking the lateral root initiation (LRI). Cell division and growth takes place in the newly formed LRP. A new auxin gradient is established within the primordium towards the outer layers [22]. The LRP continues to grow and divide traversing layer after layer until it emerges as a new functional lateral root [97, 142].

As already established throughout Chapter 1, auxin patterns preceding plant morphogenesis, and organogenesis thereafter, are a result of auxin transport. This system, LRF, is remarkable for the dynamic rearrangement of auxin flows. As a first example we have carrier-mediated auxin accumulation in the lateral root FCs resembling auxin spot patterns [100, 143]. At later stages, as cell division takes place, the established auxin gradient implies a PIN polarity shift towards the LRP tip [22]. Later still, the LRP auxin transport route resembles that of the root meristem with fountain-like polar auxin flows [22]. Therefore, not only is LRF an interesting system to study auxin transport in general, but also, due to its close coupling to mechanics, a prime system to test the hypothesis of mechanically-regulated auxin transport.

Related to how the LRP is initiated in the pericycle layer and needs to traverse several layers until it emerges, this specific system has a myriad of specific geometrical and mechanical characteristics. In the differentiation zone of the root tissue, where FC identity is acquired [144], plant cells are highly anisotropic. Root cell aspect ratio can easily reach the order of 10 to 1 [145]. This anisotropy is a result of the strong microtubule polarity present in stems [45, 46].

Plant cell stiffness is different from layer to layer. The internal layers are in general stiffer as indicated by recent measurements using Brillouin microscopy complemented by atomic force microscopy comparisons [146]. There is some debate about what exactly Brillouin microscopy measures [147, 148], namely if it conflates cell wall stiffness with water content of plant cells. Vasculature cells being stiffer is also in line with the observation that xylem cell walls contain lignin [149], a class of polymers contributing to the structural stability of wood. From these data we can have a rough picture of how cell wall stiffness changes from xylem cells up to the epidermis, even if there are measurement details which are not entirely clear.

Another important factor to take note of is water transport in the root during LRF. As the LRP develops, the symplastic connections between LRP and the surrounding tissue are progressively impaired [150]. Blocking water transport from the LRP helps maintain cell turgor difference between the inside and outside the primordium. A higher turgor pressure inside the LRP would explain the direction of growth when taking into account the difference in stiffness between layers. Before the first round of cell-divisions, however, FCs seem to still be symplastically connected to their neighbours. Furthermore, aquaporin expression, both in the LRP and the overlaying tissue, has been shown to be regulated by auxin via ARF7 and critical to lateral root emergence [65]. The capacity for FCs to sustain turgor differences with their neighbourhood seems unlikely, yet the possibility of transient turgor differences is still within expectation.

Our scope lies within the timeframe after lateral root FCs have been primed to start LRF up to the first round of cell divisions. We will cover the factors underpinning FC selection as well as the necessary FC swelling that happens right before the first anticlinal cell divisions. This choice is precipitated by the mechanical remodelling and auxin patterns exhibited during this time, as we will shortly describe.

5.1.1 Founder cell selection

Founder cells are the cells whose lineage comprises the whole LRP after initiation takes place. FC identity is tied to strong auxin response [22, 25, 151], suggesting high auxin concentration. Specifically, degradation of the Aux/IAA family member IAA14, and subsequent ARF7 and ARF19 function, has been shown to be necessary for LRF [152]. Another hint that suggests very high auxin concentration is the high expression of the AUX1 auxin importers [143, 151]. We can observe some consistent features of LRF, such as FCs emerge in the pericycle layer, LRPs appear to inhibit presence of others around it, and LRPs usually initiate on the convex side of a curved root [98, 145, 153]. There is evidence to suggest that similarly to phyllotaxis, LRP spacing is a result of emergent auxin maxima [144, 154]. Modelling of auxin transport has been widely employed in predicting LRI positioning [144].

The mechanical aspects of this process, however, should not go understated. Auxin accumulation and LRI has been induced by manual bending alone [151]. This work also tracked PIN localisation, finding it to play a role in directing auxin flow towards the LRI site upon bending, gravitropic or manual. Furthermore, polar auxin flows from the endodermis to the FCs has been shown to aid LRF [100]. The hypothesis of mechanically-regulated PIN binding seems to have the potential to seamlessly combine the LRI curvature preference observation with the auxin patterning framework.

5.1.2 Founder cell swelling

After FC specification by high auxin signalling, these cells start swelling towards the endodermis, acquiring a somewhat trapezoidal shape. The growth direction implied is very different from the typical continued elongation of cells in the root system. Curiously, this growth is localised towards the center of the lateral root FCs. This different growth direction suggests a mechanical alteration of the LRI region which we will proceed to explore.

Endodermal auxin response has been shown to be critical to successful LRF [67, 101, 155]. The SHORT HYPOCOTYL 2 (SHY2) gene encodes IAA3, from the Aux/IAA family, and shown to affect multiple auxin-dependent responses [155]. Exploration of auxin sources during LRF showed a prominent role of the auxin influx carrier LAX3, itself auxin-inducible, during lateral root emergence [67]. Although LAX3 is expressed in the cortical and epidermal layers at a later stage, it was also shown that endodermal auxin-dependent SHY2 response affects expression of several cell wall remodelling genes. Afterwards, SHY2 was shown to be crucial for LRF [101]. Not only was it shown that the absence of SHY2 response blocked FC swelling completely, but it also made it impossible to execute the first round of cell divisions. Auxin-mediated aquaporin expression [65] could also contribute to differences in mechanical behaviour by the endodermis at this stage, namely the shrinkage of the endodermis upon FC swelling [101]. It is still unclear if the transport mechanism of auxin from the FCs to the endodermis is simply diffusion, or if it is carrier-mediated.

The placement of the first round of cell division is tightly regulated to be asymmetric. Disruption of cytoskeleton elements, including microtubules, affects the placement of divisions and the morphology of the primordium [156]. Curiously, before division FC microtubules are aligned along the root instead of perpendicular to it. After the first cell division of FCs, microtubules align perpendicular to the root, albeit slightly more disorganised in the central region of the LRP. This same cell division has been shown to be dependent on EXPANSIN A1 (EXPA1), a cell wall remodelling enzyme [157]. Lower levels of EXPA1 resulted in overall wider percicycle width. The loss of localised pericycle radial growth disrupted cell division patterns. This reinforces, once again the tight link between morphology and growth. Also, this implies that the radial growth of the shared interface between founder cells is no coincidence.

During LRF, the traversal of the endodermis is a major milestone of LRF. The Casparian strip is strengthened barrier intersecting half-way through the endodermis [158]. It almost seems to merge all endodermal cell walls severely limiting apoplastic transport. It suggests that endodermal mechanical remodelling is extremely severe. When comparing the surface view of the emerging primordium [101], the endodermal layer is deformed such that it tightly constrains the LRP whereas some gaps might exist during the emergence from the epidermal layer.

5.2 Adapting the mechanically-regulated auxin transport to LRI

As we intend to model LRF after establishment of FC identity up to right before the first round of cell divisions, we will want to implement some of the features described earlier in this chapter. First we will go over some assumptions on the model as established in Chapter 3. Next we will introduce a cell wall growth model and have it be explicitly auxin-dependent, as auxin is a major growth hormone. Finally we will discuss the implementation of influx carriers.

Layer dependent stiffness will have an impact in the direction of auxin efflux. The xylem cells, given their composition and measurements, are noticeably stiffer than the remaining outer layers. It would be somewhat reasonable to assume a radial decay of stiffness, or, at the very least, a drop from the xylem to the surrounding pericycle layer. This drop in base stiffness will taken into account by having the parameter E_0 be layer dependent. Note that, depending on the value of the wall loosening parameter, r, auxin reflux from the endodermis to the pericycle layer may become extremely hard due to how stress load division between compartments behaves. We note that layer-dependent stiffness implies some degree of PIN polarity bias.

We will assume that FC identity is already established. Although we will characterise what mechanical signals would help PIN to stabilise auxin accumulation in the FCs, we will model auxin influx carriers to have degree of realistic robustness to the FC stability. Modelling of FC selection should take into account the auxin flows from the root meristem.

Although it falls outside our scope, this has been done by, for instance, [159]. We will single out two adjacent pericycle cells and assume expression of AUX1 carriers in only those FCs. This also raises the question if the description of mechanically-regulated auxin transport should be above or below criticality of pattern formation. We will curb the pattern formation capabilities of the model until an auxin maximum in the FCs is stable, and interpret our results as perturbations to the already present auxin flows from the root to the shoot.

Since we intend on growing individual walls, we will use a cell wall based mechanical description. We will use cell turgor of 0.65MPa [160] and a wall with of $w = 0.08$ (L). Above the epidermis we will guess the pressure to be around atmospheric pressure, $\sim$ 0.1MPa. A simple mechanical relaxation with only the elasticity model yields unrealistic cell geometries unless extreme boundary conditions are used. Cells expand isotropically resulting in a tendency of junction angles as close to $2\pi/3$ as enabled by the remaining structure. These geometries resemble soap froth, yet we know the root system has a very well defined cell anisotropy. Interestingly, it also resembles cell geometries resulting from oryzalin treatments to depolymerise microtubules [130]. Therefore, we also use the cell wall bending model so as to keep geometries realistic. We also note that the bending modulus of a material is proportional to its Young's modulus. We will, however treat these as independent parameters since our justification for using this model in this tissue is phenomenological, and we already suspect different microscopic phenomena to contribute to these two effective parameters in different ways.

5.2.1 Modelling cell wall growth

Plant cell growth models emerged as being rate equations on cell volume for elongating cells [40–42]. These early models write down relative volume change as being proportional to the combined contribution of hydrostatic pressure and osmotic pressure [40–42], what we denote as cell turgor. It was also introduced a yield value of turgor below which no growth would take place to account for an elastic and a plastic regime [41]. We also note that there is a necessary dependence of volume change, hydrostatic pressure, and solute concentration. It becomes even more complex when considering neighbouring cells where differences in hydrostatic pressure result in water transport feeding back to all of the above. As a general behaviour as growth takes place cell turgor tends to decrease [42].

Our tissue description, however, is not particularly well-suited for evolving a rate of change in volume since our optimisation variables are vertex positions. One option, without resorting to other models, could be computing what volume each cell should have in the next step based on these models and introduce an Hamiltonian term punishing deviations from the expected volume change. Our approach, is to try to translate these models into rates of change of rest cell wall rest length, l_0. We require that this model fulfils the general observed features of plant growth – a yield value of strain or stress and growth, or relative growth, proportional to strain or stress.

Our approach to describing cell wall rheology will be similar to those of [51, 130]. We will model the wall as a Maxwell material such that growth is stress driven. As in [130], we develop a model based on the behaviour of a Maxwell material and focus on the rate of change of the relative irreversible (rest) wall length as proportional to wall stress. We will use φ as the extensibility of this cell wall element as the reciprocal of viscosity. Then, we introduce a yield value of strain as is the case in [51]. Given a wall of length l, rest length l_0, stiffness E, extensibility φ, and yield strain Y, at time t, we evolve rest length l_0 as

$$\frac{\dot{l_0}}{l_0} = \begin{cases} E\varphi\left(\dfrac{l-l_0}{l_0} - Y\right), & \dfrac{l-l_0}{l_0} > Y, \\ 0, & \dfrac{l-l_0}{l_0} \leq Y. \end{cases} \tag{5.1}$$

We note, however, that we are using a single value of stiffness and extensibility, yet we have two compartments, one facing each cell, with different mechanical properties (Fig. 5.2). We have to decide on how to couple the two adjacent Maxwell material compartments. We have implicitly assumed Y to be the same between two adjacent compartments. Another detail is that auxin is also a growth hormone in more ways than simple stiffness modulation, hence we expect extensibility to be a function of auxin concentration in the surrounding cells. For the growth simulations in this chapter we will keep $Y = 0.05$.

We first assume that the value of rest length is shared between compartments. Recall this as the same assumption underlying stress-load division. Differences in rest length between compartments would retain residual amounts of stress. It might be interesting to understand how auxin mechanical modulation affects memory formation by residual stresses in this setting, yet we will avoid breaking the rest length assumption. We will model both compartments connected in parallel yet the viscous elements will both be in parallel with a single plastic element such that irreversible length remains well-defined and the same between compartments. Luckily, this assumption allows us to treat the overall wall by an equivalent Maxwell element. All we have to do is find how extensibility is coupled in such a model. Stress would couple in exactly the same way. Taking into account wall compartment cross-section we need only to average stiffness between compartments as we did to find out stress load division in Appendix E. Above threshold, the viscous elements are in parallel with each other, yet in series with the parallel springs. As we did with the equivalent elastic element, we deduce the equivalent viscous element[1]. We will

---

[1] Let a viscous element have extensibility φ^* and be under stress σ. Its strain rate is given by $\dot{\varepsilon} = \varphi^* \sigma$. Now consider two parallel compartments of half the cross section with different extensibilities φ_1 and φ_2. Stress is divided as $\sigma = (\sigma_1 + \sigma_2)/2$ when accounting for cross-section difference between

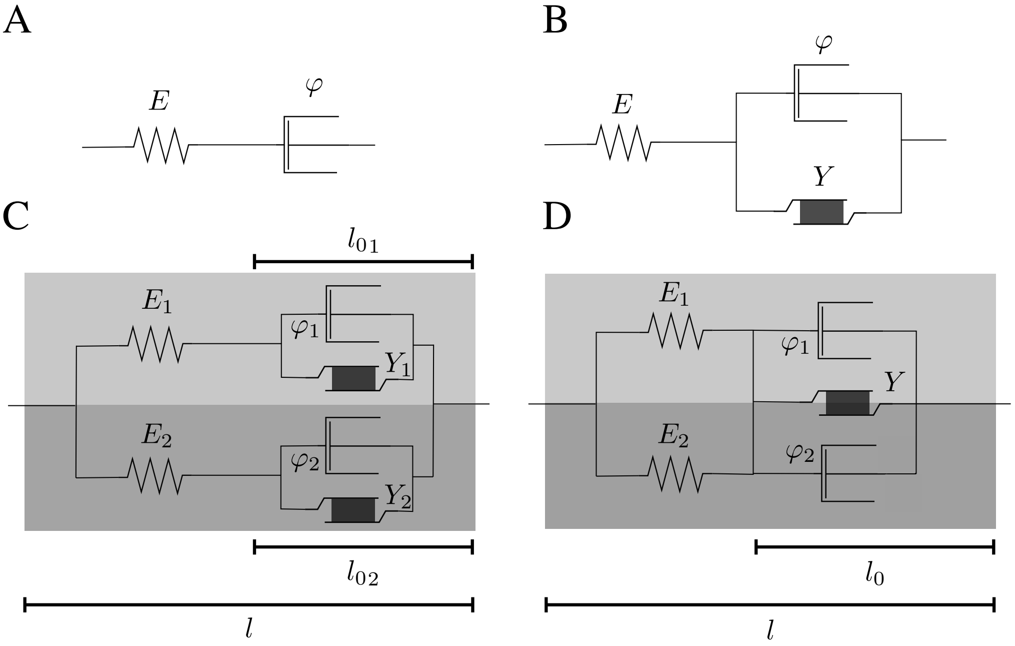

Figure 5.2: Rheological models allowing for growth and how to couple them across two adjacent cell wall compartments. (A) A typical Maxwell material with elastic modulus E and $1/\varphi$ viscosity, where we refer to φ as extensibility. (B) One can create a plastic yield such that above such of a value Y of strain (or stress) the irreversible length starts extending. Below this threshold, the material behaves as elastic. (C) Parallel coupling between two simple viscoelastoplastic materials can be used to represent how stress relaxes in each compartment of the cell wall with a single value of length, l. Unfortunately, this model is quite complicated as is and stress load division is already under the assumption of a single rest length. Here we cannot as readily assign a single irreversible length to the whole wall without time integration of the viscoelastoplastic ODEs. (D) Our approximation assumes a single plastic element. The joining of the two branches here means we can separate the elastic behaviour from the viscous one and, therefore, the whole wall behaves as an element of B with equivalent elasticity modulus and equivalent extensibility.

use for walls between cells α and β,

$$\bar{E}_{\alpha\beta} = \frac{E_\alpha + E_\beta}{2} \qquad \bar{\varphi}_{\alpha\beta} = \frac{2\varphi_\alpha\varphi_\beta}{\varphi_\alpha + \varphi_\beta}, \tag{5.2}$$

where E_α is the auxin-dependent stiffness of compartment facing cell α and, similarly, φ_α is the extensibility of cell walls around cell α. We will use a linear relationship between extensibility and auxin with proportionality constant g. Auxin is always positive and so is extensibility.

---

each compartment and the wall as a whole. Strain rate is the same in each parallel viscous element, $\dot{\varepsilon} = \sigma_1\varphi_1 = \sigma_2\varphi_2$. This implies $\sigma = (1 + \varphi_1/\varphi_2)\,\sigma_1/2$, since $\sigma_2 = \varphi_1\sigma_1/\varphi_2$. Substituting $\dot{\varepsilon} = \varphi_1\sigma_1$ back in the equivalent extensibility expression yields, $\varphi^*\,(1 + \varphi_1/\varphi_2)\,\sigma_1/2 = \varphi_1\sigma_1$. The equality is verified when $\varphi^* = 2\varphi_1\varphi_2/\,(\varphi_1 + \varphi_2)$.

5.2.2 Maintenance of auxin and PIN patterns

As previously established, we intend to model LRF from the establishment of FC identity. We will select two adjacent pericycle cells as LRP FCs at the start of each simulation. These cells will have high initial auxin concentration. Perturbations to mechanically-regulated auxin transport, however, have the potential to drain the FC cells of auxin entirely. In line with empirical observations we will implement auxin-dependent influx carrier expression and transport.

We will adopt the AUX1 carrier expression model similar to [145],

$$q_\alpha = \frac{{a_\alpha}^4}{1 + {a_\alpha}^4}. \tag{5.3}$$

Note again that we consider AUX1 expression in the selected FCs only. Using the half value at $a = 1$ is in line with the previously used value for the cell wall loosening expression, as both are a result of auxin signalling [32, 161]. Even though we know that ARF and Aux/IAA content may imply different auxin perception for different response types, we have no reason to make any assumption in any which way. Note that these carriers have been observed to bind isotropically around the cell. We can, therefore, assume that the density of bound carriers at the wall to be proportional to q_α. Just as in the case of PIN, we also have to consider the volume and surface area of the cell. Consistent with this formulation, in the LRP FCs we add a new term to the auxin transport equation,

$$\dot{a}_\alpha^{(\mathrm{FC})} = \dot{a}_\alpha + \mathcal{Q} \sum_{\beta \in \mathcal{N}_\alpha} \frac{l_{\alpha\beta}}{A_\alpha} \left(q_\alpha \frac{a_\beta}{K_{\mathrm{AUX1}} + a_\beta} - q_\beta \frac{a_\alpha}{K_{\mathrm{AUX1}} + a_\alpha} \right), \tag{5.4}$$

where we assume Michaelis-Menten kinetics, implying a saturation of activity of influx carriers. We choose $K_{\mathrm{AUX1}} = 1$, as we did for PIN-mediated efflux. The parameter $\mathcal{Q}$ denotes the magnitude of auxin influx permeability when compared to auxin turnover rate. We use a permeability of $\mathcal{Q} = 10\mathcal{P}$ to ensure influx dominates. Note that even at this high level of influx, we observe that, depending on stress patterns, PIN can still override this effect (not shown). This expression is also a particular case of the transport equation used in [73].

We also expect the mechanically-regulated PIN binding to help accumulate auxin in the FCs due to its up-the-gradient typical behaviour. Many mechanical perturbations to FCs will inadvertently help auxin accumulation, such as turgor pressure, tension in periclinal walls, softening of FCs. In a later section we will explore which perturbations we expect to help auxin accumulation in LRP FCs. The main disruptive factor in keeping FCs filled with auxin, initially at least, is the stress patterns of the specific architecture of the tissue, diffusion, and auxin turnover rate.

5.3 Lateral root founder cell swelling

In this section we will concern ourselves with localised growth characteristic of lateral root FC swelling. Namely, we will focus on answering if localised growth happens, under what conditions is it possible to happen, and if the model we have is enough to capture that LRP shapes empirically observed.

Since we already assume lateral root FC phenotype of two initial pericycle cells, we already expect high auxin content and signalling during growth and auxin-dependent mechanical remodelling of the endodermis. In a first approach, we can take advantage of this by not simulating auxin transport and keeping high auxin concentration in the LRP FCs.

The mechanical and growth models are already complex enough to warrant exploration on their own. In fact, the rheological assumptions made when conceptualising the model already gives us some insight into the early stage LRF system itself, namely that we already expect growth to be localised in the FC shared wall.

Next, we will examine the impact of mechanical variables on growth rate, as well as analyse the shape of the growing FCs. We find that bending modulus has a disproportionate impact and that a drop in endodermal bending modulus can be enough to unleash FC swelling.

5.3.1 Rheological assumptions imply FC localised growth

We will first take a few steps back and reinterpret the result for extensibility coupling in the context of lateral root FC swelling. As FCs display high auxin signalling, we assume a higher extensibility than the surrounding cells, showing little auxin signalling. The assumption $\varphi^{\text{FC}} \gg \varphi^{\text{non-FC}}$ implies three different cell wall growth rates based on each possible interface. They are $\bar{\varphi}^{\text{FC/FC}} = \varphi^{\text{FC}}$, $\bar{\varphi}^{\text{FC/non-FC}} = 2\varphi^{\text{non-FC}}$, and $\bar{\varphi}^{\text{non-FC/non-FC}} = \varphi^{\text{non-FC}}$. We expect that, if growth takes place it will be necessarily localised to the FC shared walls, since $\bar{\varphi}^{\text{FC/FC}} \gg \bar{\varphi}^{\text{non-FC/any}}$.

This behaviour is also encouraging for the validity of the growth model since it can also explain the necessity of a FC/FC cell interface for any morphological change to take place. Throughout the study of LRI, a commonly observed feature is that of multiple pericycle FCs, implying the existance of such interface, involved in LRI [25, 97–99, 162–164].

This mechanism for localised growth makes it noteworthy to recall the observation that loss of EXPA1 activity results in a wider overall pericycle layer width and disrupts the localised swelling preceding the first round of cell divisions [157]. Our results suggest auxin response could be to repress the activity of EXPA1 in the pericycle layer, directly or otherwise. Then again, competition with other redundant processes might be involved in this pericycle expansion, or lack thereof, rendering our remarks as an hypothesis to be tested rather than evidence of any kind.

Next we will probe how growth is affected by mechanical parameters of the lattice.

5.3.2 Bending stiffness poses a severe obstacle to growth

Since we are waiving the auxin transport simulation for now, we can run the growth model for a long time without too much effort. We are going to tackle how growth is affected by cell turgor and cell wall mechanical properties. Specifically, we are looking for clues as to what may be happening mechanically upon endodermal auxin response via SHY2.

In this first approach we will affect the entire lattice we use to represent the root. During these simulations, pericycle cells we choose to be FCs will have auxin $a = 10$ throughout the simulation, and the remaining cells will have auxin at a fixed value close to zero (10^{-12}). We will keep track of the rest length and current length of the shared wall between adjacent pericycle FCs, as this is the only wall capable of growing due to how extensibility couples.

We will use a control simulation with $E_0 = 300\,\mathrm{MPa}$, $k_b = 600\,\mathrm{MPa}$, and $T = 0.65\,\mathrm{MPa}$. The final rest length of the shared wall by the FCs seems to be decreased by lattice stiffness (Fig. 5.3 top). Cell turgor increases the final length linearly (Fig. 5.3 center). The range of values of length and rest length permitted by a change in bending modulus is much broader (Fig. 5.3 bottom). For low values of bending modulus, rest length increases drastically. At high values, however, the wall can barely manage to grow at all.

A decrease in base stiffness, E_0, seems to ever so slightly help growth in the long-term. Our results suggest that an endodermal drop in stiffness can only barely help FC swelling. We note that the different values of initial rest length for different stiffness are a result of setting a base isotropic stress in the lattice. This base stress is needed to represent the stress acting on the periclinal walls which would, otherwise, have near zero (or even negative) stress due to the constraints of boundary conditions. We add a base stress $\sigma_0 = 20\,\mathrm{MPa}$ to all walls which, for $E = 300\,\mathrm{MPa}$, is just above yield strain.

Cell turgor increases the final length of the FC shared wall linearly. We note that we are affecting the whole lattice and, as such, we expect the effect of exclusive turgor increase in the lateral root FCs to yield a more pronounced growth than presented here, as the remaining cells would not be pushing back as strongly. Nevertheless, knowing that the FCs are not symplastically isolated from the rest of the tissue at this point, a sustained value of FC turgor around 150% of base cell turgor is very unlikely as water transport

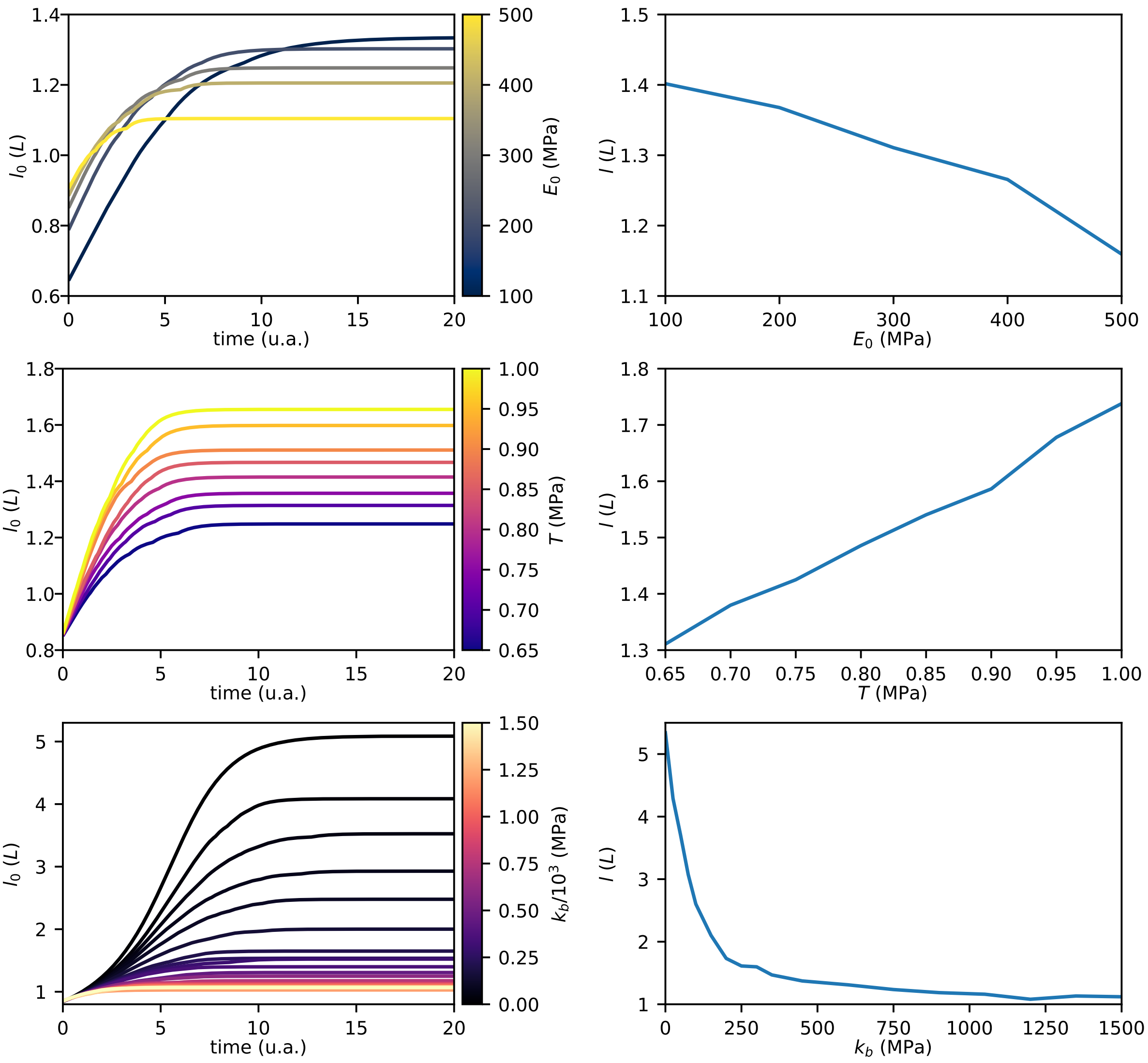

Figure 5.3: Growth of the wall shared by FCs depends on the mechanical properties of the lattice. Namely, (top) stiffness, (middle) cell turgor, and (bottom) bending modulus. Simulation results for (left) rest length as a function of time and for different mechanical properties and (right) final length of the FC shared wall as a function of mechanical properties. Only one parameter was varied at one time keeping all other parameters at the default values of $E_0 = 300\,\mathrm{MPa}$, $T = 0.65\,\mathrm{MPa}$, and $k_b = 600\,\mathrm{MPa}$.

would quickly ensue. Unfortunately, it is extremely difficult to measure cell turgor for cells not at the surface of the plant (where one could in principle use AFM). Because of the ever changing mechanical properties of the tissue during this stage, predicting turgor based on cell shape may be just as difficult.

The severe endodermal cell shape deformities observed when traversing this specific layer [101] suggest stiffness and bending modulus to be a main contributing factor to this process. Here we confirm the suspicions of bending modulus, as this parameter stands out as being a major determinant of growth. Recall that, even if we are varying bending modulus and stiffness independently, bending modulus is proportional to stiffness. A

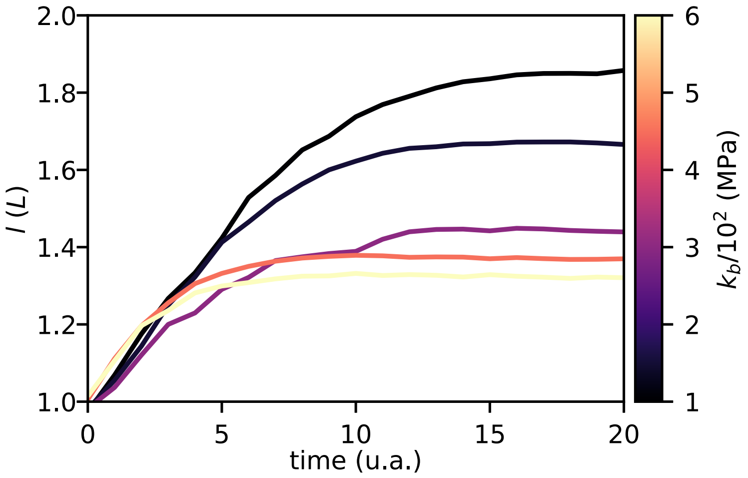

Figure 5.4: Simulated length of the FC shared wall over time and for different values of bending modulus of the FCs and overlaying endodermis. High values of bending modulus cluster at relatively low values of length. As bending modulus increases, the end values of length increase non-linearly.

sharp decrease in this parameter has the potential to explain a sudden swelling of the lateral root FCs. We note, however, that these results were obtained by affecting the whole lattice. In the next section we will try to uncover if and how the bending modulus findings translate into a local perturbation at the FCs and overlaying endodermis, and if this perturbation is capable of unleashing FC swelling.

5.3.3 Turgor difference is not required for FC swelling

In this section, we focus back onto the mechanical properties of the lateral root FCs and the overlaying endodermal cells. We will use a default value of $k_b = 600\,\text{MPa}$ for the lattice and for FCs and the overlaying endodermal cells we will assign a varying value $k_b = k_b^{\text{SHY2}}$. We will also consider auxin concentration to be $a = 1$ in the endodermal cells overlaying the lateral root FCs.

We will focus on the current length of the wall shared between FCs as this observable can be measured empirically. We can still observe a non-linear effect of bending modulus on the final length of the shared anticlinal wall (Fig. 5.4). The final values, in this case, are much lower than when we affect the whole lattice, as would be expected.

Even though growth happens in all cases, the final shape of the FCs is quite different between different values of k_b^{SHY2} (Fig. 5.5). At high values, FC shape remains close to the initial one and no directed growth towards the endodermis is predicted. For low values, the FCs acquire a trapezoid shape, where localised growth happens towards the endodermis.

We also measured the area of the overlaying endodermis and FCs before and after

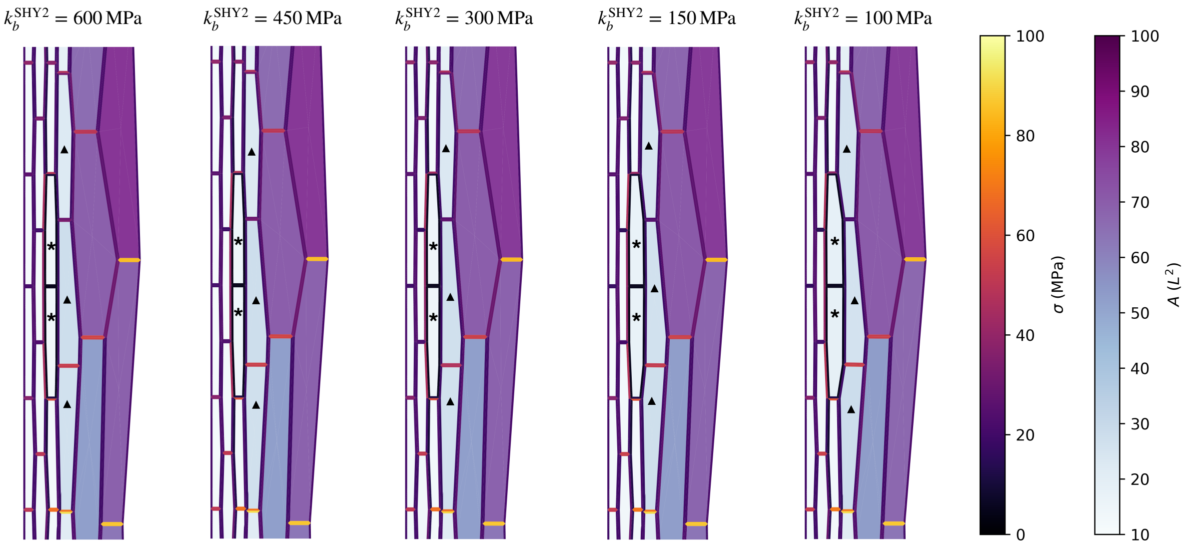

Figure 5.5: Simulation results of lateral root FC swelling morphology, cell area, and wall stress, for different values of k_b^{SHY2}. Lateral root FCs (marked with $*$) and overlaying endodermal cells (marked with ▲) have their bending modulus affected. As bending modulus decreases, FCs acquire different morphologies.

the simulation as a function of bending stiffness of the FCs and overlaying endodermis (Fig. 5.6). We found that endodermal cells and founder cells do not decrease in volume during growth. Because the lattice can freely expand towards the outer layers, the endodermis does not need to shrink in order for the swelling to take place. Observations of endodermal shrinkage may, therefore, point towards turgor playing a role at this stage, even if here we have shown it is not strictly required for lateral root FC swelling.

From these data we infer that it is possible to obtain the swelled FC shape by manipulating mechanical properties of the FCs and overlaying endodermal cells. Strikingly, by introducing the bending energy term we are able to explain why no growth takes place despite there being enough cell turgor. In fact, the case where the bending modulus does not change ($k_b^{\mathrm{SHY2}} = 600\,\mathrm{MPa}$) can be understood as a proxy for the *shy2* mutant that displays little to no mechanical remodelling, at least under the current understanding of this process. Our results predict no localised growth of this mutant in agreement with experiments [101].

We note also that wall stress, measured with $\sigma = E(l - l_0)/l_0$, is heavily dependent on the architecture of the tissue in question. Walls perpendicular to the surface have generally higher stress. Since we show stress after growth takes place, the strain acting on the wall between the FCs drops until 5%, the value of yield strain, as stress is released through growth. Furthermore, we note that tissue geometry for $k_b = 600\,\mathrm{MPa}$ to be somewhat aberrant, especially in the cortex and epidermis. For the next section, we will ramp up the default value of $k_b = 1050\,\mathrm{MPa}$ to combat the high turgor. We expect that

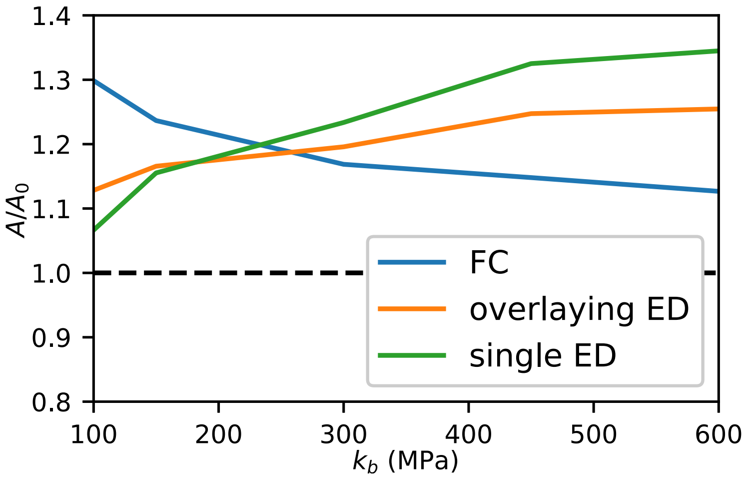

Figure 5.6: Final cell area relative to initial cell area of FCs (blue), the endodermal cells overlaying the FCs (orange), and just the middle endodermal cell (green), as a fuction of bending modulus of these cells. We observe than no shrinking occurred since all values are greater than 1.0. We note that experimental results suggest endodermal shrinkage during lateral root founder swelling [101].

using this default value of bending modulus in this particular experiment would simply make growth differences more pronounced.

Finally, our results show endodermal deformation but not shrinkage during the studied process. Because we allow the lattice to expand outwards, growth simply pushes the overlaying layers ever so slightly. Even though a stiffer plant surface has the potential to explain how the endodermis can shrink at this stage, it is not possible to ascertain its effect without further numerical modelling. This is because, even if it may provide a barrier that forces the endodermis to shrink upon FC swelling, it also affects FC growth and so this explanation becomes harder to parse. Another possible explanation for endodermal shrinkage is the hypothesis that turgor is decreased in the overlaying endodermis. Not only could this explain the shrinkage, but also enhance swelling. Nevertheless, as is a recurring motif throughout this chapter, cell turgor differences are hard to justify before symplastic isolation of the LRP at later stages. In this case, however, we have an expanding cell underneath which we set to have constant turgor. This constant turgor can only happen if water is flowing into the FCs as they expand. The high degree of mechanical remodelling combined with water flowing out of the endodermis also has the potential to explain a volume change such as the endodermal shrinkage proposed by [101]. Further modelling of water transport in this setting may help elucidate exactly how the endodermal shrinkage may occur.

So long as the auxin concentration is maintained high in the FCs and, at a certain point, exists in the endodermis for a long enough time to trigger SHY2 response impacting mechanical properties of the endodermis, we predict lateral root FC swelling takes place.

5.4 Mechanical PIN regulation during LRF

Having elucidated the requirements for lateral root founder swelling, we now reintroduce auxin transport. Before committing to a full-fledged LRI model we first take a look at the auxin transport model in isolation, with the newly included auxin importers. After checking out how mechanics would affect auxin accumulation in FCs, we will then proceed to investigate whether the addition of growth potentiates any new auxin flow behaviour.

As we set out to test the hypothesis of mechanical regulation of auxin flows, we intend now to explore how auxin concentration in lateral root FCs responds to different mechanical perturbations. We expect to find parameter regions where mechanically-regulated PIN aids accumulation if only because of its usual up-the-gradient behaviour.

Because of high cell anisotropy and pressure boundary conditions, the discrepancy between stress of the short walls in the same layer and the longer walls in between layers is wide (Fig. 5.5). Since empirically we observe auxin flows across layers [100, 151], to explore how these can arise with the hypothesis highlighted in this work we will also explore the impact of the amount of stress acting on walls parallel to the surface.

The difference of stress from layer to layer implies that patterning will most likely occur in the cortex and epidermis. Since no auxin-response is observed in these three layers at this stage, and PIN patterning herein found is better captured with canalisation models, we choose to increase diffusion of auxin in these two layers enough such that no patterns can develop. To couple diffusivity of two cell walls of each of those cells, we use a wall-specific diffusion strength $\mathcal{D}_{\alpha\beta} = 2\mathcal{D}_{\alpha}\mathcal{D}_{\beta}/\left(\mathcal{D}_{\alpha} + \mathcal{D}_{\beta}\right), \beta \in \mathcal{N}_{\alpha}$ in the transport equation. This expression captures some of the expected behaviour, such as if auxin cannot diffuse through one of the compartments, then there is no diffusion across cells possible. Another option would be to freeze auxin concentration at low levels in those two layers. It seems reasonable from a biological perspective that these layers act as a sink, yet dismissing a significant portion of cells in an already small lattice (along one of its dimensions) is concerning regarding boundary effects. Furthermore, auxin is still flowing through those cells and PIN can, in principle at least, redirect that flow into the simulated region of the tissue. Short of simulating the flows from the root meristem to the shoot apical meristem, there is little room for avoiding such drastic measures. To ensure no patterns emerge we increase diffusion strength of auxin tenfold in the cortex and epidermis.

5.4.1 Mechanically-regulated PIN binding can explain response to curvature

In this section we will go over a relatively simple experiment. We run the auxin transport model while affecting the lattice or FCs of some perturbations. We will change cell turgor, FC PIN availability, and stress of cell walls parallel to the surface. By comparing with a control simulation with only auxin importers, we will be able to predict the impact o efflux mediated transport in this system.

For these simulations, we pick the value of stress-PIN coupling $\eta = 0.0001$. In the context of the parameter exploration of Chapter 4 this value would be comparable to 6.4. This comparison is not entirely fair due to the variations in stress from wall to wall, but gives us a rough estimate where to explore. This value can be obtained by taking base wall stress used in previous simulations of about $\sigma_0 = 20\,\mathrm{MPa}$ and comparing it with the computed value in the table of Appendix E of about $\bar{\sigma} \approx 0.5\,\mathrm{MPa}$, taking into account the power-law with exponent $n = 3$. Pattern formation threshold is also different due to changes in cell geometry where the ratio of area to perimeter is vastly different than that of the regular hexagonal lattice.

By comparing with a control experiment with only auxin importers, we will be able to gather some insight into which perturbations we expect to increase FC auxin levels, helping auxin accumulation, and by how much relative to each other. We will, for now, disable cell wall growth and focus solely on auxin accumulation. We start by simulating auxin accumulation with only auxin influx carriers until $t = 0.10$ (which, with the parameters from the table in Appendix E would be 6 min). We note that the high parameter for influx carrier active transport requires us to decrease time step and so simulations become more expensive. Being a compromise between precision and computational cost, we found it to be enough time to draw conclusions about impact on accumulation (Fig. 5.7 A). This will, at least, allow us to get a rough idea of the relative impact of each perturbation. Initially, auxin concentration of FCs is at $a = 15$, which is subject to change due to the initial geometry optimisation procedure. We will denote $\bar{a}_0^{\mathrm{FC}}$ as the value of average FC auxin concentration at $t = 0.1$ when considering auxin influx alone.

Now, we include mechanically-regulated PIN binding, vary mechanical quantities, and measure the resulting auxin concentration at the same time point (Fig. 5.7 B). Instead of adding an isotropic stress to all walls, we set initial rest lengths of the tissue such that the average stress on walls is $\mathbf{t}^{\mathrm{T}} \left(\begin{smallmatrix} \sigma_0 & 0 \\ 0 & \bar{\sigma}_p \end{smallmatrix}\right) \mathbf{t}$ where $\mathbf{t}$ is a tangent to some wall (the x-axis here lies towards the surface and the y-axis along the root). Because the root architecture has a high impact on wall stress of walls normal to the surface, we quantified stress in order to account for any potential bias in the interpretation of the results (Fig.5.7 C).

Via simulating auxin transport of the tissue, we find that the parameter $\bar{\sigma}_p$ alters

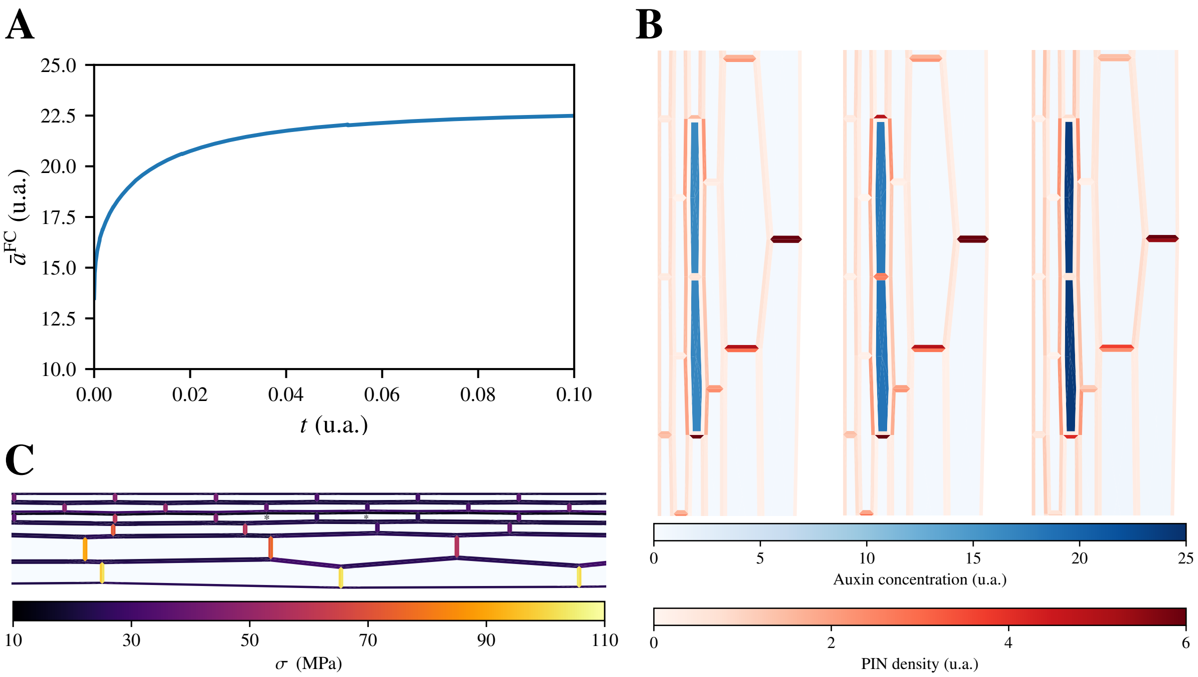

Figure 5.7: Simulation setup details and examples. (A) Average FC auxin concentration for a simulation where we deactivated active auxin efflux. We observe that the total time of the simulation is enough to estimate auxin concentration levels in the FCs. (B) Example simulations at $t = 0.1$ when activating PIN-mediated auxin flux. From left to right: no extra perturbation, increase in FC turgor pressure to $T = 1.0\,\mathrm{MPa}$, and $\bar{\sigma}_p = 30\,\mathrm{MPa}$. (C) Cell wall stress on the tissue when all cells have auxin $a = 1$. The FCs selected are marked with $*$. We can see a slight bias in wall stress in one of the walls of the FC and an adjacent pericycle cell. This effect is also visible in B where the pericycle cell below has always larger PIN density.

drastically the effect of mechanically-regulated PIN on auxin accumulation (Fig. 5.8 Left). Surprisingly, mechanical regulation of PIN binding can have a detrimental effect if $\bar{\sigma}_p$ is not high enough. If mechanical regulation of PIN binding is prevalent in this system, then flows from the endodermis and the inner vasculature seem to play an important role in maintaining FC fate. Auxin reflux from the endodermis as observed by [100] can be explained via this mechanism alone, though it is to be expected from the up-the-gradient nature of the auxin transport model in this setting.

We also decided to test other perturbations to FCs. We altered added turgor as it is still unclear if there are transient turgor differences between FCs than their non-primed neighbours. As auxin is accumulating in the FCs, we cannot dismiss the possibility that cell turgor is increasing faster than water is able to flow out. We find that FC turgor contributes positively to accumulation and it is even capable of rescuing, in part, the negative effects of low $\bar{\sigma}_p$ (Fig. 5.8 Right). This is expected as the cell walls surrounding the FCs are more strained and therefore flows are higher, but also stress on the shared wall increases driving auxin flows from one FC to the other instead of out from the auxin maxima, because of competition for a shared PIN pool. Continuous increase in turgor

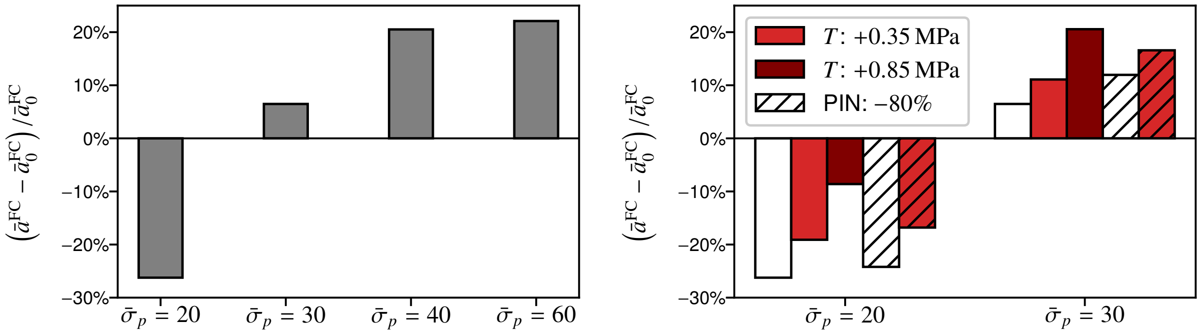

Figure 5.8: Effect of mechanically-regulated PIN binding relative to the case without auxin exporters for different mechanical perturbations by simulating auxin transport until $t = 0.1$. (Left) Changing initial stress on walls parallel to the surface, $\bar{\sigma}_p$, is a major factor in the effectiveness of auxin accumulation in the FCs. (Right) Effects of perturbation to FC turgor, T, and FC PIN availability. The white bars represent the absence of other perturbations (same results as on the left) for side-by-side comparison.

leads to very significant increases in FC auxin accumulation.

Next we decided to change the availability of PIN in the FCs. Reducing the number of efflux carriers exporting auxin out of the FCs necessarily contributes to accumulation. The question, however, is by how much, relatively speaking. In the low $\bar{\sigma}_p$ regime, the effect of reducing the amount of available PIN to only 20% of its initial value is negligible (Fig. 5.8 Right). At $\bar{\sigma}_p$, however, it becomes of the same order of a $\sim$ 50% increase in turgor. We then combined the effects of increasing turgor and decreasing PIN to see if these two perturbations compounded on each other significantly. From these data, it seems they do not.

The strong dependence on stress of walls parallel to the surface is intriguing. As mentioned, mechanically-regulated PIN binding emphasises the role of the endodermis in auxin reflux as well as auxin flows from the vasculature. In fact, if low enough, the plant would be better off not including mechanical cues into its efflux carrier polarity regulation, when considering only their role in accumulation. Considering the two extremes of a negilgible value and an infinite value, we have the $\bar{\sigma}_p$ parameter controls where PIN is bound. A shift in PIN polarity from walls perpendicular to the surface to the LRP tip was shown to happen to LRF during latter stages and is tied to the presence of cytokinin in the LRP [165]. It would be interesting to reexamine the mechanical state of the lateral root in those experiments via segmentation, and check if there is a significant correlation between strain or stress and how PIN polarity is shifting. It would also be interesting to revisit lateral root FC swelling upon changes of $\bar{\sigma}_p$.

Another reason why the dependence on $\bar{\sigma}_p$ is fascinating, is what it predicts about curvature. Some models have shown the impact of curvature on positioning of FCs based on geometry [145]. It is shown experimentally that the convex side of the root is correlated with FC positioning [151, 153]. Bending a beam slightly is to imply a positive strain along the beam axis on the convex side and a negative strain on the concave one. If we assume we are on the convex side of the root bend, we expect larger stresses along the root provided no variation of mechanical properties. This comparison becomes a bit less straightforward when we consider the individual walls and turgor as opposed to a beam composed of a single material, but the argument remains the same. We expect an increase in curvature, therefore, to increase $\bar{\sigma}_p$ on the convex side and consequently help FC auxin accumulation. This behaviour is inline with experimental observations. The concave side would be affected by a contraction implying auxin efflux between layers to be heavily impaired. Having predicted what happens upon a manual bending of an unbent root, the mechanical state of the walls might change if walls are allowed to relax through growth. It would be insightful to model the stress distribution resulting from cell turgor across a curved portion of the root that is no longer growing. Nevertheless, FC selection happens relatively early and the assumption that the tissue is fully mature is not entirely applicable regardless. Note that curvature would imply a gradient of this directional stress towards the surface. Even if one considers mechanically regulated PIN binding in the cortex and epidermis, due to the highly stressed walls perpendicular to the surface, the effect of this stress gradient would be less noticeable.

Turgor was increased by an almost unreasonable amount and only then were the effects on the same scale as $\bar{\sigma}_p$. It is very unlikely that biologically, cell turgor will be as high as this in the FCs. All perturbations presented have the potential of having larger effects if we reduce auxin active influx strength, of which we are uncertain. These results however, allows us to observe how strong these responses are relative to each other. We note also that we found that lowering auxin influx strength, $\mathcal{Q}$ can result in the auxin maxima to either form elsewhere due to architecture or simply fail to maintain itself and fading out. In both cases, the assumed auxin maxima vanishes over time. Then again, the value was picked precisely on the assumption that it does not. Nevertheless, another promising way to expand this study is in trying to figure out the shape of the curve defining the threshold for auxin maxima sustenance in the parameter space $(\mathcal{Q}, T, \bar{\sigma}_p)$.

Because architecture influences stress heavily, as seen by simulations of growth, it will be insightful to study mechanical regulation of PIN binding in the context of FC selection, namely if FC positioning correlates with pericycle wall strain as necessitated by root architecture. To do that, it would be useful to include the root meristem and a layer specific auxin transport properties in accordance with other models attempting the same [144]. Because we want to impose the least amount of layer-specific constraints, so as to test the impact of mechanics on auxin flows in different tissues, we will forego this undertaking.

Even though these results would benefit from refinement, we are confident that are representative of the ones we would obtain by running the program for a longer time, and

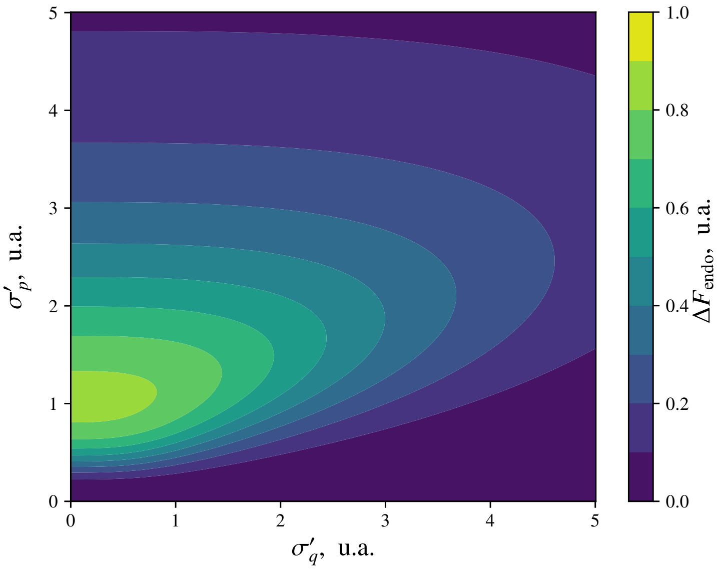

Figure 5.9: Approximate polarity shift towards endodermis after stress relaxation of FC shared wall (Eq. 5.6) as a function of stress of the wall facing the adjacent pericycle cell, σ'_q, and stress of the wall shared with the endodermis, σ'_p. We used $\chi = 10$ and $\sigma'_{sw} = 5$.

of the trends we would observe by improving parameter resolution. We have shown that stress of walls parallel to the surface plays a defining role in the impact of mechanically-regulated PIN binding during auxin accumulation. Introducing the dynamic element of cell wall growth brings a different way to perturb the system mechanically.

5.4.2 PIN-growth dynamics can explain endodermal auxin presence

We intend to predict what happens to auxin transport if the shared cell wall grows as is the case with the growth model we introduced. As observed for the growth model, the shared wall will relax its stress while growing. If the stress of the shared wall is dominating PIN binding, then auxin flows happen from FC to FC and do not hinder auxin accumulation. If this wall were to undergo stress relaxation, then FC PIN carriers can redirect to another wall. Flows back to the vasculature are unlikely especially since we used stiffer walls for the vasculature by default and, by stress load division, are biased one-way.

Upon stress relaxation of the FC shared wall, what happens to PIN polarity depends on the stress distribution around the FC. In order to estimate how PIN reacts, we will compute the PIN polarity measure,

$$\mathbf{F} = \sum_{\beta \in \mathcal{N}_{\mathrm{FC}}} \frac{l_{\mathrm{FC}\,\beta}}{L_{\mathrm{FC}}} p_{\mathrm{FC}\,\beta} \mathbf{n}_{\mathrm{FC}\,\beta}, \tag{5.5}$$

where the basis is defined with the x-axis towards the surface and the y-axis towards the neighbouring FC, $\mathbf{n}_{\mathrm{FC}\,\beta}$ is the normal to the wall separating the FC and cell β and it points outwards from the FC. If bending modulus is high enough, we can approximate the cell by a rectangle. Let χ be the aspect ratio of the cell $\chi > 1$. Then we have l/L can have the values $(2(\chi+1))^{-1}$ or $\chi(2(\chi+1))^{-1}$. We define $\sigma_{\mathrm{ref}} = E_0(1-r)Y$, the value of expected stress after full relaxation of the shared FC wall. Let σ_p denote the stress of the wall compartment of FC adjacent to the endodermis, σ_q the stress on the FC wall facing its non-FC percicycle layer neighbour, and σ_{sw} be the stress of the shared FC wall. We will neglect stress towards the vasculature. Let $\sigma'_p = \sigma_p/\sigma_{\mathrm{ref}}$, $\sigma'_q = \sigma_q/\sigma_{\mathrm{ref}}$, and $\sigma'_{sw} = \sigma_{sw}/\sigma_{\mathrm{ref}}$. We also assume all PIN is bound, which is effectively the limit $\eta \to \infty$. If we start with an initial stress σ_{sw} in the shared wall and it relaxes until it reaches the threshold at σ_{ref}, then we can compute the endodermal component of the polarity shift as

$$\begin{aligned}\Delta F_{\mathrm{endo}} = \frac{\chi}{2(\chi+1)} &\left(\frac{2(\chi+1)\,{\sigma'_p}^n}{1+{\sigma'_q}^n+\chi{\sigma'_p}^n} - \frac{2(\chi+1)\,{\sigma'_p}^n}{{\sigma'_{sw}}^n+{\sigma'_q}^n+\chi{\sigma'_p}^n} \right) \\ &= \chi{\sigma'_p}^n \left(\frac{1}{1+{\sigma'_q}^n+\chi{\sigma'_p}^n} - \frac{1}{{\sigma'_{sw}}^n+{\sigma'_q}^n+\chi{\sigma'_p}^n} \right), \end{aligned} \tag{5.6}$$

where we made use of Eq. 3.26 and Eq.3.27. The condition $\Delta F_{\mathrm{endo}} > 0$, meaning an increase in polarity towards the endodermis, is fulfilled when $\sigma'_{sw} > 1$. In other words, as long as growth happens we expect endodermal PIN polarity to shift towards the endodermis. Of course this expression is an approximation that relies on stresses on other walls to not change as much as the growing FC shared wall. This expression can be visualised in Fig. 5.9 for values of σ'_p and σ'_q below the initial stress of the shared wall, such that PIN is initially directed from one FC to the other. We observe that there is a region where PIN polarity changes substantially. As the shared wall stress and σ'_q approach each other this polarity shift continues to drop. There is also an optimal value of σ'_p above which the endodermal polarity shift starts decreasing, meaning we cannot simply increase $\bar{\sigma}_p$ indefinitely.

In regards to determining stress, for now $\bar{\sigma}_p$, and by extensions σ'_p, is a free parameter and we do not know what value it should take unless we model mechanics more thoroughly. The influence of architecture on FC selection definitely comes into play as it directly determines stress of walls perpendicular to the surface. Our guess is that FCs would select for high shared wall stress as it would have the least efflux-mediated leakage, under the mechanically-regulated PIN binding hypothesis. Without explicit modelling of FC emergence, we cannot be certain of the relationship between the two. When we account for auxin-mediated cell wall loosening, the stress of the shared wall can decrease drastically depending on the value of r. On the other hand, auxin depletion in the neighbouring pericycle cell would imply low stress in the same wall facing the FC via stress-load division. Note that FC turgor favours stress in the shared FC walls.

If there is no high shared wall stress, then cell wall growth and, by extension, stress relaxation predict no changes to PIN polarity. If there is high shared wall stress, then stress relaxation via cell wall growth can bind towards the endodermis as seen in the analytical approach. In our lattice and for our choice of FCs, we have higher wall stress between one FC and an adjacent pericycle cell (Fig. 5.7 C). In order to be able to observe a growth-related PIN polarity shift towards the endodermis, we will have to increase FC turgor so as to increase the difference between σ'_{sw} and σ'_q.

As a proof of principle that this is the case we will simulate PIN polarity shift towards the endodermis. To ensure the shared wall is stressed and dominates PIN binding we chose $T = 1.0\,\text{MPa}$. We can then increase $\bar{\sigma}_p$ until it is lower than the shared wall stress yet higher than the cell walls between FCs and the adjacent pericycle cells. We chose a value of $\bar{\sigma}_p = 60\,\text{MPa}$ which, after stress load division roughly translates to $\sigma'_p = 4$ ($E_0 = 300\,\text{MPa}$, $r = 2/3$, and $Y = 0.05$). Unfortunately, the value of σ'_p has to be this high to distinguish PIN density in the wall shared with the endodermis and the wall shared with the adjacent pericycle. Increasing bending modulus to $k_b = 1500\,\text{MPa}$ helps clarify how cell turgor will impact cell wall stress[2]. To make PIN polarity shifts drastic we bump stress-PIN coupling all the way up to $\eta = 5.0$.

We show that it is possible to find parameter regions where growth induces a PIN polarity shift toward the endodermis is possible via simulation (Fig. 5.10). Because higher cell turgor would result in aberrant cell shapes (as it overpowers the bending term), the PIN reorientation observed was unfortunately minimal. These results may benefit from

---

[2] If the cell cannot bend as much, we can approximate the anisotropic root cells by a rectangle. Consider a rectangle with sides p and q, $p > q$. The Hamiltonian, disregarding the bending term since $\theta = \theta_0$ for all angles of the polygon, can be written as

$$\mathcal{H} = Ewp_0\left(\frac{p-p_0}{p_0}\right)^2 + Ewq_0\left(\frac{q-q_0}{q_0}\right)^2 - Tpq.$$

The we find that a variation of energy upon a change of ∂p or ∂q, and setting it to zero so as to search for an energy minimum, imply,

$$2Ew\frac{p-p_0}{p_0} = Tq \qquad\qquad 2Ew\frac{q-q_0}{q_0} = Tp,$$

i.e.

$$\sigma_p = E\frac{p-p_0}{p_0} = \frac{Tq}{2w} < \frac{Tp}{2w} = E\frac{q-q_0}{q_0} = \sigma_q.$$

Meaning stress on the shorter walls generated by turgor is larger than on longer walls in rectangles. This is also explains why pressurising a rectangle would deform it into a square. Furthermore, we expect the shared wall to have a higher tension as there is a contribution from each of the surrounding cells.

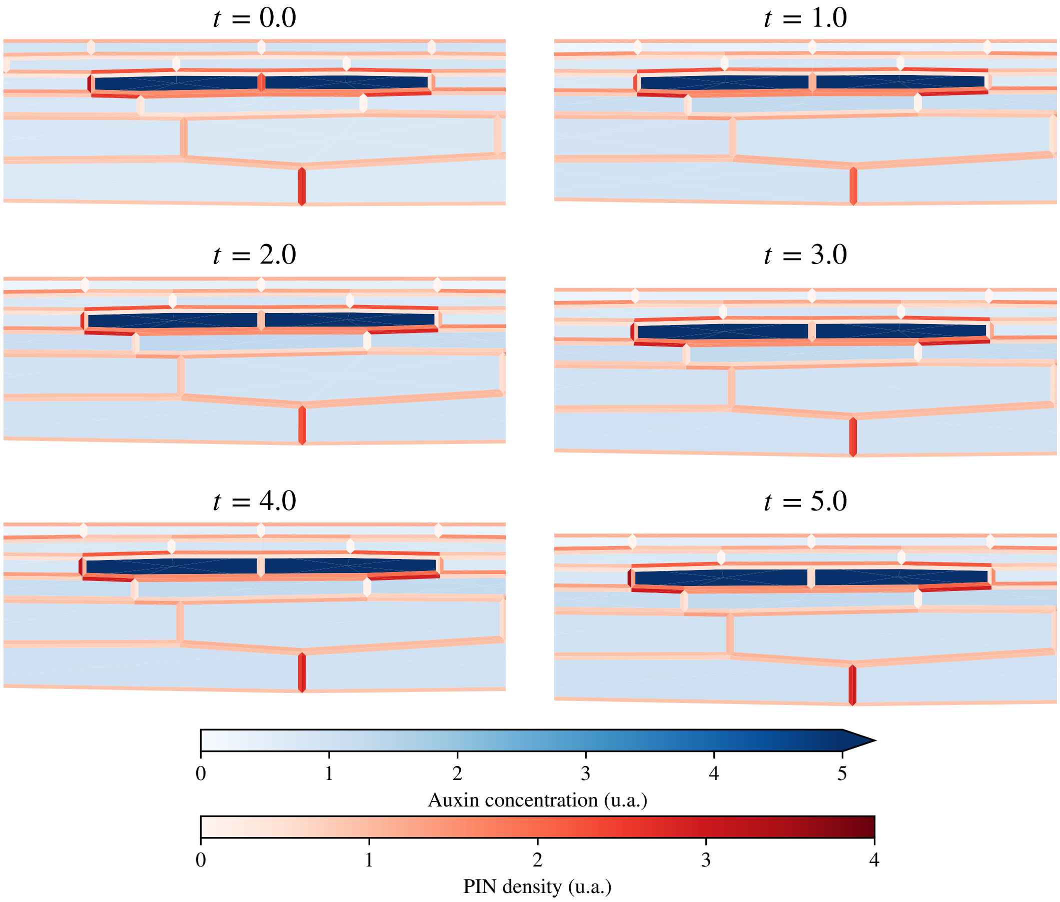

Figure 5.10: Growth can change FC PIN polarity orientation towards the endodermis. Simulation results for a simulation with $k_b = 1500\,\text{MPa}$, $T = 1.0$ in FCs, $\eta = 5.0$, and $\bar{\sigma}_p = 60\,\text{MPa}$. By inspecting the simulation at different time points, we observe that the shared FC wall is the FC wall with largest PIN density initially. By $t = 1.0$ we already observe that growth causes relaxation of that wall and, depending on the stress distribution, what before was a flow from a FC to another is now from FCs to the endodermis. Because auxin is not zero in all cells that are not FCs, there is growth throughout the rest of the lattice.

choose FCs whose shared wall has highest stress. Assuming cell turgor cannot change in FCs, then we can only answer if this is feasible from a biological perspective once we analyse mechanically-regulated FC selection and its correlation with shared wall stress. As it stands we can only state that this is a possibility arising from this hypothesis and motivate the a new experiment. A FC PIN polarity shift towards the endodermis has not been observed experimentally. It may very well be that it is impossible for biologically relevant parameters and its absence tells us little about the overall mechanism. Although there is a slight increase in endodermal auxin overlaying the FCs, we also have to take into account for the likely overestimation of influx carriers derived from how the value of parameter $\mathcal{Q}$ was set.

It may also be the case that a drop in FC influx carriers can explain a transient increase in endodermal auxin by diffusion, which could also explain the SHY2 response. There might be endodermal influx carriers yet to be discovered which could also explain this phenomenon. PIN carriers at the cortex might also play a role in endodermal auxin presence.

It is also a concern that experimentally, auxin concentration is not what is usually tracked but rather auxin response (DR5). Their relationship is assumed nonlinear, and it was recently shown to be as such [166]. Therefore, the whole section on auxin transport of this chapter has to be filtered through the possibility that auxin concentration changes might ultimately not be empirically perceivable.

To summarise, the stress-coupling PIN hypothesis opens up the possibility of stress relaxation of the shared wall, when swelling has yet to take place, to be able to redirect auxin flows from the FCs to the endodermis, which could, in turn, unleash the auxin-dependent endodermal SHY2 response.

Chapter 6

Conclusion and outlook

As it stands, mechanisms underlying plant development can only be unveiled by the inclusive consideration of mechanics. In this work, we inspect the hypothesis that mechanical forces acting on plant tissue impact auxin flows during developmental patterning of different plant organs. Namely, we study unique features of the patterning mechanism this hypothesis allows for, as well as predict the impact of the same interaction during the development of the lateral root.

In order to accomplish this, we set forth a mathematical description of plant tissue with a vertex model. We were able to conceptualise and develop analytical and computational tools to perform geometrical analysis of the tissue. The developed package is not strictly for plant tissue and can be adapted to many other contexts in developmental biology as it is readily extendible. This package also includes differentiation so as to improve geometrical optimisation of the tissue, and as a stepping stone towards simulating dynamics. We adopted a quasi-static approach to modelling cell elasticity and cell turgor using the established framework. Furthermore, we also included a bending energy description to accompany a simple wall-based elastic model. Having described mechanics, we adopted and adapted previous auxin transport models to our particular mathematical description of the tissue. Lastly, the interactions between auxin transport and mechanics were introduced – auxin-mediated cell wall softening and mechanically-regulated auxin efflux carrier binding.

The mechanism for auxin pattern formation of this hypothesis is sufficiently explained [34], yet it does not account for seemingly subtle effects we found to be understated. Namely, the interaction of turgor and stiffness gradients generates mechanical patterns from auxin patterns with the capacity for enhancing the already accounted for feedback based on cell wall rheology. Not only did auxin patterns become sharper, but also more robust to noise in the parameter defining cell stiffness at basal auxin levels. Lastly, considering the puzzling nature of spatial correlations of cell turgor, cell growth, and auxin response, we predict that, even if turgor correlates with auxin maxima, the reciprocal is not necessarily verified.

Next we turn our attention to the system of LRF, specifically to the events after FC establishment and leading up to the first round of cell divisions. The specificity demands that we adapt the model to this setting. In this work, we chose to account for growth and auxin influx carriers in addition to what was previously modeled. The addition of, effectively, two models is quite cumbersome as the number of parameters we are required to choose increases with it. The growth model, in particular, brought with it enough complexity to warrant an analysis on its own. Using the wall-based elasticity model and bending energy term along with growth of rest lengths proved insightful as to the nature of, and the mechanical requirements for, lateral root FC swelling. By studying the auxin transport model in this setting, and without growth, we explored how auxin accumulation in the FCs is affected by several different perturbations. Most interesting of which is the disproportionate effect of tension of periclinal walls due in part to its potential role in endodermal auxin reflux. Based on these data, we speculate a mechanism for explaining endodermal auxin reponses which we argue analytically and provide a proof of concept for via numerics.

The mechanism by which developmental patterns in plants emerge is still far from understood. Although computer models can help filter hypotheses before they set off to the chopping block that is empirical testing, this process relies on quantification of observables and validation of assumptions. In regards to auxin, a major obstacle to overcome is to experimentally distinguish auxin concentration from auxin response. There is, however, some encouraging developments in regards to methods for detecting auxin [166, 167]. Quantification of auxin spatio-temporal distribution at the shoot apical meristem was recently obtained [166] and will, certainly, contribute to refinement of auxin transport models. Furthermore, new insights regarding effects of auxin in PIN endocytosis are challenging a portion of existing auxin transport models [168].

Measurement of mechanical properties and cell turgor continues to be a challenge, which is prone to cause issues in verification of predictions herein made. Knowing the mechanical state of the tissue generally requires aid from computer models and, even good mechanical descriptions fall into the pitfall of having to assume cell turgor. Some recent efforts have been done in order to attempt to model plant tissue development taking into account water transport of the tissue [51, 52]. The falsification of growth and auxin transport models may very well require precise measurements of such quantities. Recent efforts in image segmentation improvements [169] inspire hope that, perhaps at some point, changes in mechanical states can be inferred with enough precision to validate, or falsify, assumptions made throughout all of plant development models.

From a theoretical point of view, it may be interesting to continue exploring the diversity of patterns possible with the mechanical PIN binding mechanism tested throughout this work. Specifically, it would be insightful to check what happens when changing the exponents associated with wall loosening and relative PIN binding rates, as well as the Michaelis constant for active auxin efflux. Power law exponents, Hill coefficients, and auxin concentration at half the response in feedback and transport have been shown to be particularly sensitive parameters [73]. It would also be interesting to see how different patterns respond to tissue-wide stress patterns. Just as we have observed shorter wavelengths in auxin spots, different patterns might respond differently to tissue-wide stress patterns or even, in extreme cases, cease to be stable altogether. Another question that is worth tackling is what conditions have to be met for the mechanically-regulated auxin transport model to behave as a canalisation model. Even if a stress gradient can in principle explain it, it will be worth exploring if such a setting is reasonably found in the relevant plant tissues. Another candidate is the existance of internal auxin gradients which may help carve the mechanical property distribution required for such a behaviour. Another promising, yet often overlooked, feature of auxin transport is the apoplastic diffusion of auxin. By introducing both transcriptional and nontranscriptional auxin responses in this setup it could be possible to understand which is more likely to be involved in mechanically-regulated auxin transport.

As foreshadowed by the choice of a three-dimensional mathematical description and the inclusion of curvature computations, a direction to take this work forward could be outside the plane. Specifically, since the auxin spots are a characteristic of shoot apical meristematic tissue, modelling the L1 layer embedded in three dimensions might bring consequences to auxin spot size and pattern wavelength which were not taken into account. In keeping with the tight link of auxin, cell growth, and mechanical properties, it would also be extremely interesting to probe how primordium outgrowth would affect the surrounding auxin patterns. Namely, if the hypothesis we have is sufficient for proper organ placement. With access to spatio-temporal auxin distributions opens up the possibility to test the same models in regards to primordium outgrowth timing. Interestingly, a very recent study manages to change shoot apical meristem cell size [170] and could, in principle, provide an interesting test case for the studied mechanism.

On the subject of growth and auxin transport, implementation of cell division and cell cycle might be required for comparable spatio-temporal patterning conditions. Plant development of tissue in different geometrical settings might necessitate the inclusion of stress dependent microtubule orientation and anisotropic growth. Microtubule orientation will inevitably introduce anisotropy in mechanical properties of the cells. The analysis done on the infinitesimal strain tensor estimation from the second moment of area (Appendix D) enables us to approximate anisotropic rest shape stress and build anisotropic constitutive relations to that end. Including mechanical feedback of microtubule orientations has the potential to dramatically change what we might predict from auxin transport models. Primordium outgrowth timing will almost surely change [93].

Another avenue along which to travel could be in trying to implement a water transport model alongside the auxin transport model and mechanical PIN binding model. Differences in concentration of solute and geometry will inherently affect turgor and might result in phenomena not yet accounted for. With water flow and turgor, we can also tie it back to cell growth and, effectively, extend the approach taken by, for instance, [51] to include auxin transport and PIN binding. In the immediate future, however, it may be rash to start including too many effects as the dimensions of the parameter space one would have to search increases disproportionately.

Just as we have tried to approach the system of LRF, because most plant developmental systems are auxin-dependent [22], modelling different tissues could help testing auxin transport models and PIN regulatory models. Numerical simulations of these systems may help inform if some shared feature between systems has to be revised or, alternatively, what components of the model are more likely to be tissue specific. Furthermore, tissues of elongated cells will most likely benefit from the modelling of internal auxin gradients as it may be crucial for determining the auxin transport mechanism. Since other hormones interfere with auxin signaling, it may prove insightful to include, for instance, cytokinin in models as this hormone has been shown to affect PIN polarity during LRF [165].

Following through with LRF and emergence might be another worthwhile endeavour. Namely, understanding what mechanical constraints are required for the mechanically-regulated PIN binding hypothesis resulting in the emergence of fountain-like patterns. Another curious phenomenon is the robust establishment of an auxin gradient towards the tip of the LRP. Alternatively, instead of continuing forward with the LRF stages, one could also turn to the emergence of primed pericycle cells via auxin transport. Despite having to model the root meristem, modelling mechanical regulation of PIN would prove insightful as mechanics play a major role in FC positioning [151]. Another major issue it would address is in clarifying the role of plant tissue architecture and how it relates to the emerging founder cells. This particular insight is of such importance that it may affect how to interpret the results we obtained in the previous chapter.

In order to corroborate the findings regarding lateral root FC swelling, it would be interesting to probe the details of the remodelling triggered by auxin via SHY2. Namely, to find out if and how FC swelling can be rescued by altering endodermal mechanics or cell wall composition. Another key insight necessary for this particular clarification is the relation between the several cell wall components to the bending modulus parameter used here. This connection would be best expressed in the scope of statistical mechanics of cross-linking filaments and would necessarily call for a completely different approach. An effective rheological behaviour of the wall could, in principle, be achieved by doing so and, by the same token, validation of the assumptions made when modelling growth could be tested.

Although theoretical and numerical data was provided to show how the ingredients explored in this work are suficient to explain endodermal auxin responses, it is still unclear if the phenomenon described is possible in the LRF system. Evidently, as more empirical data becomes available we can narrow down the window of uncertainty. The results presented in this work still require a great deal of polish in order to ascertain this mechanism's likelyhood. If possible to prove it at least unlikely, then the lack of evidence for it will not falsify mechanically-regulated auxin transport in this setting. On a more positive note, we have an hypothesis to test.

Although the geometrical description was fully realised, computations of derivatives of differential geometric quantities are still to be implemented in code. Namely, we still have to implement derivatives of curvatures, mixed Voronoi region area, and normals, with respect to vertex positions. Since it is not a focus of our particular work, and since all systems we have dealt with are described as planar, it is also not a main concern here. The structure used, however, is particularly suited for modelling two-dimensional apical tissue surfaces embedded in three-dimensions. If accounting for cell divisions and topological transitions of the tissue, we can promptly adapt a vertex model to many animal systems, for instance drosophilla embryogenesis. Hence, we have a strong incentive to implement and distribute the polygonal mesh analysis code, which we already took steps to make it a python package and, therefore, straightforward to distribute. Specifically, the computation of gradients is of particular usefulness for inspecting dynamics of such systems.

The concept of mechanical regulation of tissue shape posited when introducing plant development is not only true, but also ubiquitous to the extent that there is seemingly no seam along which to tear its composing mechanisms apart. The move away from an abstracted setting elucidated this by providing more questions than answers. Plant development remains a fascinating example of coordinated growth responses to mechanical cues with capacity to generate a large range of shape diversity. Just as interesting is the key role auxin plays at the center of it all. The sheer amount of processes auxin is involved in renders any attempt at quantifying its effects lacking in some way. Mechanically-regulated auxin transport hypothesis remains a contender, yet the behaviour overlap with other models make it extremely difficult to distinguish and, ultimately, to quantify its prevalence.

Bibliography

[1] Paul Martin and Susan M. Parkhurst. “Parallels between tissue repair and embryo morphogenesis”. In: *Development* 131.13 (July 2004), pp. 3021–3034. DOI: `10.1242/dev.01253` (page 5).

[2] Setsuo Hirohashi and Yae Kanai. “Cell adhesion system and human cancer morphogenesis”. In: *Cancer Science* 94.7 (2003), pp. 575–581. DOI: `10.1111/j.1349-7006.2003.tb01485.x` (page 5).

[3] Huawei Qu, Hongya Fu, Zhenyu Han, and Yang Sun. “Biomaterials for bone tissue engineering scaffolds: a review”. In: *RSC Adv.* 9 (45 2019), pp. 26252–26262. DOI: `10.1039/C9RA05214C` (page 5).

[4] Soroosh Derakhshanfar, Rene Mbeleck, Kaige Xu, Xingying Zhang, Wen Zhong, and Malcolm Xing. “3D bioprinting for biomedical devices and tissue engineering: A review of recent trends and advances”. In: *Bioactive Materials* 3.2 (2018), pp. 144–156. ISSN: 2452-199X. DOI: `10.1016/j.bioactmat.2017.11.008` (page 5).

[5] Rebekah M. Samsonraj, Michael Raghunath, Victor Nurcombe, James H. Hui, Andre J. van Wijnen, and Simon M. Cool. “Concise Review: Multifaceted Characterization of Human Mesenchymal Stem Cells for Use in Regenerative Medicine”. In: *STEM CELLS Translational Medicine* 6.12 (2017), pp. 2173–2185. DOI: `10.1002/sctm.17-0129` (page 5).

[6] Reza Mohammadinejad, Anuj Kumar, Marziyeh Ranjbar-Mohammadi, Milad Ashrafizadeh, Sung Soo Han, Gilson Khang, and Ziba Roveimiab. “Recent Advances in Natural Gum-Based Biomaterials for Tissue Engineering and Regenerative Medicine: A Review”. In: *Polymers* 12.1 (2020). ISSN: 2073-4360. DOI: `10.3390/polym12010176` (page 5).

[7] Pinak Samal, Clemens van Blitterswijk, Roman Truckenmüller, and Stefan Giselbrecht. “Grow with the Flow: When Morphogenesis Meets Microfluidics”. In: *Advanced Materials* 31.17 (2019), p. 1805764. DOI: `10.1002/adma.201805764` (page 5).

[8] Takahiro Yamaguchi, Hirokazu Tsukaya, Hironori Fujita, Kenji Fukushima, Mitsuyasu Hasebe, and Masayoshi Kawaguchi. “Oriented cell division shapes carnivorous pitcher leaves of Sarracenia purpurea”. In: *Nature Communications* 6.1 (2015), pp. 1–10. DOI: `10.1038/ncomms7450` (page 6).

[9] A.M. Turing. “The chemical basis of morphogenesis”. In: *Bulletin of Mathematical Biology* 52.1 (1990), pp. 153–197. ISSN: 0092-8240. DOI: `doi.org/10.1016/S0092-8240(05)80008-4` (page 6).

[10] Michael E. Cates and Julien Tailleur. “Motility-Induced Phase Separation”. In: *Annual Review of Condensed Matter Physics* 6.1 (2015), pp. 219–244. DOI: `10.1146/annurev-conmatphys-031214-014710` (page 6).

[11] B. I. Shraiman. “Mechanical feedback as a possible regulator of tissue growth”. In: *Proceedings of the National Academy of Sciences USA* 102.9 (Mar. 2005), pp. 3318–3323. ISSN: 0027-8424. DOI: `10.1073/pnas.0404782102` (page 6).

[12] D. B. Staple, R. Farhadifar, J. C. Röper, B. Aigouy, S. Eaton, and F. Jülicher. “Mechanics and remodelling of cell packings in epithelia”. In: *The European Physical Journal E* 33.2 (Oct. 2010), pp. 117–127. ISSN: 1292-8941. DOI: `10.1140/epje/i2010-10677-0` (pages 6, 19).

[13] Yingzi Li, Hammad Naveed, Sema Kachalo, Lisa X. Xu, and Jie Liang. “Mechanisms of Regulating Cell Topology in Proliferating Epithelia: Impact of Division Plane, Mechanical Forces, and Cell Memory”. In: *PLoS ONE* 7.8 (Aug. 2012). Ed. by Che John Connon, e43108. ISSN: 1932-6203. DOI: `10.1371/journal.pone.0043108` (pages 6, 19).

[14] Chii J. Chan, Carl-Philipp Heisenberg, and Takashi Hiiragi. “Coordination of Morphogenesis and Cell-Fate Specification in Development”. In: *Current Biology* 27.18 (Sept. 2017), R1024–R1035. ISSN: 09609822. DOI: `10.1016/j.cub.2017.07.010` (page 6).

[15] Ottoline Leyser. “Auxin Signaling”. In: *Plant Physiology* 176.1 (Jan. 2018), pp. 465–479. ISSN: 0032-0889. DOI: `10.1104/pp.17.00765` (pages 7, 10, 13).

[16] Jodi L Stewart and Jennifer L Nemhauser. “Do Trees Grow on Money? Auxin as the Currency of the Cellular Economy”. In: *Cold Spring Harbor Perspectives in Biology* 2.2 (Feb. 2010), a001420–a001420. ISSN: 1943-0264. DOI: `10.1101/cshperspect.a001420` (pages 7, 9, 10).

[17] Steffen Vanneste and Jiří Friml. “Auxin: A Trigger for Change in Plant Development”. In: *Cell* 136.6 (Mar. 2009), pp. 1005–1016. ISSN: 00928674. DOI: `10.1016/j.cell.2009.03.001` (page 7).

[18] William D. Teale, Ivan A. Paponov, and Klaus Palme. “Auxin in action: signalling, transport and the control of plant growth and development”. In: *Nature Reviews Molecular Cell Biology* 7.11 (Nov. 2006), pp. 847–859. ISSN: 1471-0072. DOI: `10.1038/nrm2020` (pages 7, 9, 10).

[19] Didier Reinhardt, Eva-Rachele Pesce, Pia Stieger, Therese Mandel, Kurt Baltensperger, Malcolm Bennett, Jan Traas, Jiří Friml, and Cris Kuhlemeier. “Regulation of phyllotaxis by polar auxin transport.” In: *Nature* 426.6964 (2003), pp. 255–60. ISSN: 1476-4687. DOI: `10.1038/nature02081` (page 7).

[20] Teva Vernoux, Fabrice Besnard, and Jan Traas. "Auxin at the Shoot Apical Meristem". In: *Cold Spring Harbor Perspectives in Biology* 2.4 (Apr. 2010), a001487–a001487. ISSN: 1943-0264. DOI: `10.1101/cshperspect.a001487` (page 7).

[21] Massimiliano Sassi and Teva Vernoux. "Auxin and self-organization at the shoot apical meristem". In: *Journal of Experimental Botany* 64.9 (June 2013), pp. 2579–2592. ISSN: 1460-2431. DOI: `10.1093/jxb/ert101` (page 7).

[22] Eva Benková, Marta Michniewicz, Michael Sauer, Thomas Teichmann, Daniela Seifertová, Gerd Jürgens, and Jiři Friml. "Local, Efflux-Dependent Auxin Gradients as a Common Module for Plant Organ Formation". In: *Cell* 115.5 (Nov. 2003), pp. 591–602. ISSN: 00928674. DOI: `10.1016/S0092-8674(03)00924-3` (pages 7, 11, 80, 81, 108).

[23] Marcus G. Heisler, Carolyn Ohno, Pradeep Das, Patrick Sieber, Gonehal V. Reddy, Jeff A. Long, and Elliot M. Meyerowitz. "Patterns of Auxin Transport and Gene Expression during Primordium Development Revealed by Live Imaging of the Arabidopsis Inflorescence Meristem". In: *Current Biology* 15.21 (Nov. 2005), pp. 1899–1911. DOI: `10.1016/j.cub.2005.09.052` (pages 7, 11, 49).

[24] Richard S Smith. "The Role of Auxin Transport in Plant Patterning Mechanisms". In: *PLoS Biology* 6.12 (Dec. 2008), e323. ISSN: 1545-7885. DOI: `10.1371/journal.pbio.0060323` (page 7).

[25] Joseph G. Dubrovsky, Michael Sauer, Selene Napsucialy-Mendivil, Maria G. Ivanchenko, Jiří Friml, Svetlana Shishkova, John Celenza, and E. Benkova. "Auxin acts as a local morphogenetic trigger to specify lateral root founder cells". In: *Proceedings of the National Academy of Sciences USA* 105.25 (June 2008), pp. 8790–8794. ISSN: 0027-8424. DOI: `10.1073/pnas.0712307105` (pages 7, 9, 80, 81, 88).

[26] Eric M. Kramer and Malcolm J. Bennett. "Auxin transport: a field in flux". In: *Trends in Plant Science* 11.8 (Aug. 2006), pp. 382–386. ISSN: 13601385. DOI: `10.1016/j.tplants.2006.06.002` (pages 7, 11, 45).

[27] J. Petrasek and J. Friml. "Auxin transport routes in plant development". In: *Development* 136.16 (Aug. 2009), pp. 2675–2688. ISSN: 0950-1991. DOI: `10.1242/dev.030353` (pages 7, 11).

[28] J. Van Overbeek. "Auxins". In: *The Botanical Review* 25.2 (Apr. 1959), pp. 269–350. DOI: `10.1007/bf02860041` (page 7).

[29] Terry L. Root, Jeff T. Price, Kimberly R. Hall, Stephen H. Schneider, Cynthia Rosenzweig, and J. Alan Pounds. "Fingerprints of global warming on wild animals and plants". In: *Nature* 421.6918 (Jan. 2003), pp. 57–60. DOI: `10.1038/nature01333` (page 7).

[30] Léna Beauzamy, Naomi Nakayama, and Arezki Boudaoud. "Flowers under pressure: ins and outs of turgor regulation in development". In: *Annals of Botany* 114.7 (Nov. 2014), pp. 1517–1533. ISSN: 0305-7364. DOI: `10.1093/aob/mcu187` (pages 7, 9).

[31] Valeria Hernandez-Hernandez, Mariana Benítez, and Arezki Boudaoud. "Interplay between turgor pressure and plasmodesmata during plant development". In: *Journal of experimental botany* 71 (Sept. 2019). DOI: `10.1093/jxb/erz434` (pages 7, 9).

[32] Mateusz Majda and Stéphanie Robert. "The Role of Auxin in Cell Wall Expansion". In: *International Journal of Molecular Sciences* 19.4 (Mar. 2018), p. 951. ISSN: 1422-0067. DOI: `10.3390/ijms19040951` (pages 7, 10, 11, 87).

[33] Sarah Robinson, Agata Burian, Etienne Couturier, Benoit Landrein, Marion Louveaux, Enrique D. Neumann, Alexis Peaucelle, Alain Weber, and Naomi Nakayama. "Mechanical control of morphogenesis at the shoot apex". In: *Journal of Experimental Botany* 64.15 (Nov. 2013), pp. 4729–4744. ISSN: 1460-2431. DOI: `10.1093/jxb/ert199` (pages 7, 15).

[34] Marcus G. Heisler, Olivier Hamant, Pawel Krupinski, Magalie Uyttewaal, Carolyn Ohno, Henrik Jönsson, Jan Traas, and Elliot M. Meyerowitz. "Alignment between PIN1 Polarity and Microtubule Orientation in the Shoot Apical Meristem Reveals a Tight Coupling between Morphogenesis and Auxin Transport". In: *PLoS Biology* 8.10 (Oct. 2010). Ed. by Ottoline Leyser, e1000516. ISSN: 1545-7885. DOI: `10.1371/journal.pbio.1000516` (pages 7, 14–16, 35, 46, 48, 53, 54, 105).

[35] Naomi Nakayama, Richard S Smith, Therese Mandel, Sarah Robinson, Seisuke Kimura, Arezki Boudaoud, and Cris Kuhlemeier. "Mechanical regulation of auxin-mediated growth." In: *Current Biology* 22.16 (Aug. 2012), pp. 1468–1476 (pages 7, 14, 36, 47, 48).

[36] Kelly Houston, Matthew R. Tucker, Jamil Chowdhury, Neil Shirley, and Alan Little. "The Plant Cell Wall: A Complex and Dynamic Structure As Revealed by the Responses of Genes under Stress Conditions". In: *Frontiers in Plant Science* 7 (2016), p. 984. ISSN: 1664-462X. DOI: `10.3389/fpls.2016.00984` (page 8).

[37] Logan Bashline, Lei Lei, Shundai Li, and Ying Gu. "Cell Wall, Cytoskeleton, and Cell Expansion in Higher Plants". In: *Molecular Plant* 7.4 (Apr. 2014), pp. 586–600. DOI: `10.1093/mp/ssu018` (page 8).

[38] Amir J. Bidhendi and Anja Geitmann. "Relating the mechanics of the primary plant cell wall to morphogenesis". In: *Journal of Experimental Botany* 67.2 (Jan. 2016), pp. 449–461. ISSN: 0022-0957. DOI: `10.1093/jxb/erv535` (pages 8, 11).

[39] Anja Geitmann and Joseph K.E. Ortega. "Mechanics and modeling of plant cell growth". In: *Trends in Plant Science* 14.9 (Sept. 2009), pp. 467–478. ISSN: 13601385. DOI: `10.1016/j.tplants.2009.07.006` (pages 8, 11).

[40] James A. Lockhart. "An analysis of irreversible plant cell elongation". In: *Journal of Theoretical Biology* 8.2 (Mar. 1965), pp. 264–275. ISSN: 00225193. DOI: `10.1016/0022-5193(65)90077-9` (pages 8, 84).

[41] J. K. E. Ortega. "Augmented Growth Equation for Cell Wall Expansion". In: *Plant Physiology* 79.1 (Sept. 1985), pp. 318–320. ISSN: 0032-0889. DOI: `10.1104/pp.79.1.318` (pages 8, 84).

[42] Daniel Cosgrove. "Biophysical Control of Plant Cell Growth". In: *Annual Review of Plant Physiology* 37.1 (June 1986), pp. 377–405. ISSN: 0066-4294. DOI: `10.1146/annurev.pp.37.060186.002113` (pages 8, 84).

[43] Siobhan A. Braybrook and Alexis Peaucelle. "Mechano-Chemical Aspects of Organ Formation in Arabidopsis thaliana: The Relationship between Auxin and Pectin". In: *PLoS ONE* 8.3 (Mar. 2013). Ed. by Markus Grebe, e57813. ISSN: 1932-6203. DOI: `10.1371/journal.pone.0057813` (pages 8, 11, 49).

[44] Alexis Peaucelle, Siobhan A. Braybrook, Laurent Le Guillou, Emeric Bron, Cris Kuhlemeier, and Herman Höfte. "Pectin-Induced Changes in Cell Wall Mechanics Underlie Organ Initiation in Arabidopsis". In: *Current Biology* 21.20 (Oct. 2011), pp. 1720–1726. ISSN: 09609822. DOI: `10.1016/j.cub.2011.08.057` (pages 8, 11, 49).

[45] Olivier Hamant and Jan Traas. "The mechanics behind plant development". In: *New Phytologist* 185.2 (Jan. 2010), pp. 369–385. ISSN: 0028646X. DOI: `10.1111/j.1469-8137.2009.03100.x` (pages 8, 81).

[46] O. Hamant, M. G. Heisler, H. Jonsson, P. Krupinski, M. Uyttewaal, P. Bokov, F. Corson, P. Sahlin, A. Boudaoud, E. M. Meyerowitz, Y. Couder, and J. Traas. "Developmental Patterning by Mechanical Signals in Arabidopsis". In: *Science* 322.5908 (Dec. 2008), pp. 1650–1655. ISSN: 0036-8075. DOI: `10.1126/science.1165594` (pages 8, 14, 35, 49, 54, 55, 81).

[47] Christophe Maurel, Yann Boursiac, Doan-Trung Luu, Véronique Santoni, Zaigham Shahzad, and Lionel Verdoucq. "Aquaporins in Plants". In: *Physiological Reviews* 95.4 (2015), pp. 1321–1358. DOI: `10.1152/physrev.00008.2015` (page 9).

[48] Thorsten Seidel, Michéle Siek, Berenice Marg, and Karl-Josef Dietz. "Chapter Two - Energization of Vacuolar Transport in Plant Cells and Its Significance Under Stress". In: ed. by Kwang W. Jeon. Vol. 304. International Review of Cell and Molecular Biology. Academic Press, 2013, pp. 57–131. DOI: `10.1016/B978-0-12-407696-9.00002-6` (page 9).

[49] Haiwen Zhang, Fu-Geng Zhao, Ren-Jie Tang, Yuexuan Yu, Jiali Song, Yuan Wang, Legong Li, and Sheng Luan. "Two tonoplast MATE proteins function as turgor-regulating chloride channels in Arabidopsis". In: *Proceedings of the National Academy of Sciences USA* 114.10 (2017), E2036–E2045. ISSN: 0027-8424. DOI: `10.1073/pnas.1616203114` (page 9).

[50] J. A. Raven. "Transport of Indoleacetic Acid in Plant Cells in Relation to pH and Electrical Potential Gradients, and its Significance for Polar IAA Transport". In: *The New Phytologist* 74.2 (1975), pp. 163–172. ISSN: 0028646X, 14698137 (pages 9, 11, 45).

[51] Yuchen Long, Ibrahim Cheddadi, Gabriella Mosca, Vincent Mirabet, Mathilde Dumond, Annamaria Kiss, Jan Traas, Christophe Godin, and Arezki Boudaoud. "Cellular Heterogeneity in Pressure and Growth Emerges from Tissue Topology and Geometry". In: *Current Biology* 30.8 (2020), 1504–1516.e8. ISSN: 0960-9822. DOI: `10.1016/j.cub.2020.02.027` (pages 9, 55, 85, 106, 108).

[52] Ibrahim Cheddadi, Michel Génard, Nadia Bertin, and Christophe Godin. "Coupling water fluxes with cell wall mechanics in a multicellular model of plant development". In: *PLOS Computational Biology* 15.6 (June 2019), pp. 1–16. DOI: `10.1371/journal.pcbi.1007121` (pages 9, 55, 106).

[53] Didier Reinhardt, Therese Mandel, and Cris Kuhlemeier. "Auxin Regulates the Initiation and Radial Position of Plant Lateral Organs". In: *The Plant Cell* 12.4 (Apr. 2000), p. 507. ISSN: 10404651. DOI: `10.2307/3871065` (pages 9, 12, 13).

[54] C. Alex Esmon, Ullas V. Pedmale, and Emmanuel Liscum. "Plant tropisms: providing the power of movement to a sessile organism". In: *The International Journal of Developmental Biology* 49.5-6 (2005), pp. 665–674. DOI: `10.1387/ijdb.052028ce` (page 10).

[55] John M. Christie and Angus S. Murphy. "Shoot phototropism in higher plants: New light through old concepts". In: *American Journal of Botany* 100.1 (2013), pp. 35–46. DOI: `10.3732/ajb.1200340` (page 10).

[56] ROBYN M. PERRIN, LI-SEN YOUNG, U.M. NARAYANA MURTHY, BENJAMIN R. HARRISON, YAN WANG, JESSICA L. WILL, and PATRICK H. MASSON. "Gravity Signal Transduction in Primary Roots". In: *Annals of Botany* 96.5 (July 2005), pp. 737–743. ISSN: 0305-7364. DOI: `10.1093/aob/mci227` (page 10).

[57] Yasushi Shimizu-Mitao and Tatsuo Kakimoto. "Auxin Sensitivities of All Arabidopsis Aux/IAAs for Degradation in the Presence of Every TIR1/AFB". In: *Plant and Cell Physiology* 55.8 (May 2014), pp. 1450–1459. ISSN: 0032-0781. DOI: `10.1093/pcp/pcu077` (page 10).

[58] Paul J Overvoorde. "Functional Genomic Analysis of the AUXIN/INDOLE-3-ACETIC ACID Gene Family Members in Arabidopsis thaliana". In: *The Plant Cell Online* 17.12 (Dec. 2005), pp. 3282–3300. ISSN: 1040-4651. DOI: `10.1105/tpc.105.036723` (page 10).

[59] Ivan A. Paponov, Martina Paponov, William Teale, Margit Menges, Sohini Chakrabortee, James A.H. Murray, and Klaus Palme. "Comprehensive Transcriptome Analysis of Auxin Responses in Arabidopsis". In: *Molecular Plant* 1.2 (Mar. 2008), pp. 321–337. ISSN: 16742052. DOI: `10.1093/mp/ssm021` (pages 10, 11).

[60] B A McClure, G Hagen, C S Brown, M A Gee, and T J Guilfoyle. "Transcription, organization, and sequence of an auxin-regulated gene cluster in soybean." In: *The Plant Cell* 1.2 (Feb. 1989), pp. 229–239. ISSN: 1040-4651. DOI: `10.1105/tpc.1.2.229` (page 10).

[61] S. Abel and A. Theologis. “Early Genes and Auxin Action”. In: *Plant Physiology* 111.1 (May 1996), pp. 9–17. ISSN: 0032-0889. DOI: `10.1104/pp.111.1.9` (page 10).

[62] A. M. Jones. “Auxin-Dependent Cell Expansion Mediated by Overexpressed Auxin-Binding Protein 1 ”. In: *Science* 282.5391 (Nov. 1998), pp. 1114–1117. ISSN: 0036-8075. DOI: `10.1126/science.282.5391.1114` (page 10).

[63] Alexandre Tromas, Nils Braun, Philippe Muller, Tatyana Khodus, Ivan A. Paponov, Klaus Palme, Karin Ljung, Ji-Young Lee, Philip Benfey, James A. H. Murray, Ben Scheres, and Catherine Perrot-Rechenmann. “The AUXIN BINDING PROTEIN 1 Is Required for Differential Auxin Responses Mediating Root Growth”. In: *PLOS ONE* 4.9 (Sept. 2009), pp. 1–11. DOI: `10.1371/journal.pone.0006648` (page 10).

[64] Gabriele B. Monshausen, Nathan D. Miller, Angus S. Murphy, and Simon Gilroy. “Dynamics of auxin-dependent Ca2+ and pH signaling in root growth revealed by integrating high-resolution imaging with automated computer vision-based analysis”. In: *The Plant Journal* 65.2 (2011), pp. 309–318. DOI: `10.1111/j.1365-313X.2010.04423.x` (page 10).

[65] Benjamin Péret, Guowei Li, Jin Zhao, Leah R. Band, Ute Voß, Olivier Postaire, Doan-Trung Luu, Olivier Da Ines, Ilda Casimiro, Mikaël Lucas, Darren M. Wells, Laure Lazzerini, Philippe Nacry, John R. King, Oliver E. Jensen, Anton R. Schäffner, Christophe Maurel, and Malcolm J. Bennett. “Auxin regulates aquaporin function to facilitate lateral root emergence”. In: *Nature Cell Biology* 14.10 (Oct. 2012), pp. 991–998. ISSN: 1465-7392. DOI: `10.1038/ncb2573` (pages 11, 81, 82).

[66] Yaodong Yang, Ulrich Z. Hammes, Christopher G. Taylor, Daniel P. Schachtman, and Erik Nielsen. “High-Affinity Auxin Transport by the AUX1 Influx Carrier Protein”. In: *Current Biology* 16.11 (June 2006), pp. 1123–1127. ISSN: 09609822. DOI: `10.1016/j.cub.2006.04.029` (page 11).

[67] Kamal Swarup, Eva Benková, Ranjan Swarup, Ilda Casimiro, Benjamin Péret, Yaodong Yang, Geraint Parry, Erik Nielsen, Ive De Smet, Steffen Vanneste, Mitch P. Levesque, David Carrier, Nicholas James, Vanessa Calvo, Karin Ljung, Eric Kramer, Rebecca Roberts, Neil Graham, Sylvestre Marillonnet, Kanu Patel, Jonathan D.G. Jones, Christopher G. Taylor, Daniel P. Schachtman, Sean May, Goran Sandberg, Philip Benfey, Jiri Friml, Ian Kerr, Tom Beeckman, Laurent Laplaze, and Malcolm J. Bennett. “The auxin influx carrier LAX3 promotes lateral root emergence”. In: *Nature Cell Biology* 10.8 (Aug. 2008), pp. 946–954. ISSN: 1465-7392. DOI: `10.1038/ncb1754` (pages 11, 82).

[68] J. Petrasek. “PIN Proteins Perform a Rate-Limiting Function in Cellular Auxin Efflux”. In: *Science* 312.5775 (May 2006), pp. 914–918. ISSN: 0036-8075. DOI: `10.1126/science.1123542` (page 11).

[69] Justyna Wisniewska. "Polar PIN Localization Directs Auxin Flow in Plants". In: *Science* 312.5775 (May 2006), pp. 883–883. ISSN: 0036-8075. DOI: `10.1126/science.1121356` (page 11).

[70] P. B. de Reuille, I. Bohn-Courseau, K. Ljung, H. Morin, N. Carraro, C. Godin, and J. Traas. "Computer simulations reveal properties of the cell-cell signaling network at the shoot apex in Arabidopsis". In: *Proceedings of the National Academy of Sciences USA* 103.5 (Jan. 2006), pp. 1627–1632. ISSN: 0027-8424. DOI: `10.1073/pnas.0510130103` (pages 11, 45).

[71] Richard S Smith, S. Guyomarc'h, Therese Mandel, Didier Reinhardt, Cris Kuhlemeier, and Przemyslaw Prusinkiewicz. "A plausible model of phyllotaxis". In: *Proceedings of the National Academy of Sciences USA* 103.5 (Jan. 2006), pp. 1301–1306. ISSN: 0027-8424. DOI: `10.1073/pnas.0510457103` (page 13).

[72] Neha Bhatia, Behruz Bozorg, André Larsson, Carolyn Ohno, Henrik Jönsson, and Marcus G. Heisler. "Auxin Acts through MONOPTEROS to Regulate Plant Cell Polarity and Pattern Phyllotaxis". In: *Current Biology* 26.23 (Dec. 2016), pp. 3202–3208. ISSN: 09609822. DOI: `10.1016/j.cub.2016.09.044` (page 13).

[73] Patrik Sahlin, Bo Söderberg, and Henrik Jönsson. "Regulated transport as a mechanism for pattern generation: Capabilities for phyllotaxis and beyond". In: *Journal of Theoretical Biology* 258.1 (May 2009), pp. 60–70. ISSN: 00225193. DOI: `10.1016/j.jtbi.2009.01.019` (pages 13, 16, 19, 35, 45, 46, 87, 107).

[74] K. van Berkel, R. J. de Boer, B. Scheres, and K. ten Tusscher. "Polar auxin transport: models and mechanisms". In: *Development* 140.11 (June 2013), pp. 2253–2268. ISSN: 0950-1991. DOI: `10.1242/dev.079111` (page 13).

[75] T. Sachs. "Polarity and the Induction of Organized Vascular Tissues". In: *Annals of Botany* 33.2 (Mar. 1969), pp. 263–275. ISSN: 1095-8290. DOI: `10.1093/oxfordjournals.aob.a084281` (page 13).

[76] Maciek Adamowski and Jiří Friml. "PIN-Dependent Auxin Transport: Action, Regulation, and Evolution". In: *The Plant Cell Online* 27.1 (Jan. 2015), pp. 20–32. ISSN: 1040-4651. DOI: `10.1105/tpc.114.134874` (page 13).

[77] Tomasz Paciorek, Eva Zažímalová, Nadia Ruthardt, Jan Petrášek, York-Dieter Stierhof, Jürgen Kleine-Vehn, David A. Morris, Neil Emans, Gerd Jürgens, Niko Geldner, and Jiří Friml. "Auxin inhibits endocytosis and promotes its own efflux from cells". In: *Nature* 435.7046 (June 2005), pp. 1251–1256. ISSN: 0028-0836. DOI: `10.1038/nature03633` (page 13).

[78] H. Jonsson, M. G. Heisler, B. E. Shapiro, E. M. Meyerowitz, and E. Mjolsness. "An auxin-driven polarized transport model for phyllotaxis". In: *Proceedings of the National Academy of Sciences USA* 103.5 (Jan. 2006), pp. 1633–1638. ISSN: 0027-8424. DOI: `10.1073/pnas.0509839103` (pages 13, 35, 45, 46).

[79] Roeland M.H. Merks, Yves Van de Peer, Dirk Inzé, and Gerrit T.S. Beemster. "Canalization without flux sensors: a traveling-wave hypothesis". In: *Trends in*

Plant Science 12.9 (Sept. 2007), pp. 384–390. ISSN: 13601385. DOI: `10.1016/j.tplants.2007.08.004` (page 13).

[80] Alan C Newell, Patrick D Shipman, and Zhiying Sun. "Phyllotaxis: Cooperation and competition between mechanical and biochemical processes". In: *Journal of Theoretical Biology* 251.3 (Apr. 2008), pp. 421–439. ISSN: 00225193. DOI: `10.1016/j.jtbi.2007.11.036` (page 13).

[81] G. J. Mitchison. "A model for vein formation in higher plants". In: *Proceedings of the Royal Society of London. Series B. Biological Sciences* 207.1166 (Feb. 1980), pp. 79–109. ISSN: 2053-9193. DOI: `10.1098/rspb.1980.0015` (page 13).

[82] Francois G. Feugier, A. Mochizuki, and Y. Iwasa. "Self-organization of the vascular system in plant leaves: Inter-dependent dynamics of auxin flux and carrier proteins". In: *Journal of Theoretical Biology* 236.4 (Oct. 2005), pp. 366–375. ISSN: 00225193. DOI: `10.1016/j.jtbi.2005.03.017` (page 13).

[83] Hironori Fujita and Atsushi Mochizuki. "Pattern formation of leaf veins by the positive feedback regulation between auxin flow and auxin efflux carrier". In: *Journal of Theoretical Biology* 241.3 (Aug. 2006), pp. 541–551. ISSN: 00225193. DOI: `10.1016/j.jtbi.2005.12.016` (page 13).

[84] Szymon Stoma, Mikael Lucas, Jérôme Chopard, Marianne Schaedel, Jan Traas, and Christophe Godin. "Flux-Based Transport Enhancement as a Plausible Unifying Mechanism for Auxin Transport in Meristem Development". In: *PLoS Computational Biology* 4.10 (Oct. 2008). Ed. by Jason A. Papin, e1000207. ISSN: 1553-7358. DOI: `10.1371/journal.pcbi.1000207` (pages 13, 14).

[85] K. Alim and E. Frey. "Quantitative predictions on auxin-induced polar distribution of PIN proteins during vein formation in leaves". In: *The European Physical Journal E* 33.2 (Oct. 2010), pp. 165–173. ISSN: 1292-8941. DOI: `10.1140/epje/i2010-10604-5` (page 13).

[86] Emmanuelle M. Bayer, Richard S. Smith, Therese Mandel, Naomi Nakayama, Michael Sauer, Przemyslaw Prusinkiewicz, and Cris Kuhlemeier. "Integration of transport-based models for phyllotaxis and midvein formation". In: *Genes & Development* 23.3 (Feb. 2009), pp. 373–384. ISSN: 0890-9369. DOI: `10.1101/gad.497009` (pages 14, 19, 49).

[87] Mikolaj Cieslak, Adam Runions, and Przemyslaw Prusinkiewicz. "Auxin-driven patterning with unidirectional fluxes". In: *Journal of Experimental Botany* 66.16 (Aug. 2015), pp. 5083–5102. ISSN: 0022-0957. DOI: `10.1093/jxb/erv262` (page 14).

[88] Yoshinori Hayakawa, Masashi Tachikawa, and Atsushi Mochizuki. "Mathematical study for the mechanism of vascular and spot patterns by auxin and pin dynamics in plant development". In: *Journal of Theoretical Biology* 365 (Jan. 2015), pp. 12–22. ISSN: 00225193. DOI: `10.1016/j.jtbi.2014.09.039` (page 14).

[89] Henry R. Allen and Mariya Ptashnyk. "Mathematical Modelling of Auxin Transport in Plant Tissues: Flux Meets Signalling and Growth". In: *Bulletin of Mathe-*

matical Biology 82.2 (Jan. 2020). DOI: `10.1007/s11538-019-00685-y` (pages 14, 19, 35).

[90] Olivier Hamant and Elizabeth S. Haswell. "Life behind the wall: sensing mechanical cues in plants". In: *BMC Biology* 15.1 (Dec. 2017), p. 59. ISSN: 1741-7007. DOI: `10.1186/s12915-017-0403-5` (page 14).

[91] Olivier Hamant, Daisuke Inoue, David Bouchez, Jacques Dumais, and Eric Mjolsness. "Are microtubules tension sensors?" In: *Nature Communications* 10.1 (Dec. 2019), p. 2360. ISSN: 2041-1723. DOI: `10.1038/s41467-019-10207-y` (page 14).

[92] Magalie Uyttewaal, Agata Burian, Karen Alim, Benoît Landrein, Dorota Borowska-Wykrt, Annick Dedieu, Alexis Peaucelle, Michał Ludynia, Jan Traas, Arezki Boudaoud, Dorota Kwiatkowska, and Olivier Hamant. "Mechanical Stress Acts via Katanin to Amplify Differences in Growth Rate between Adjacent Cells in Arabidopsis". In: *Cell* 149.2 (Apr. 2012), pp. 439–451. ISSN: 00928674. DOI: `10.1016/j.cell.2012.02.048` (page 14).

[93] Jason Khadka, Jean-Daniel Julien, and Karen Alim. "Feedback from Tissue Mechanics Self-Organizes Efficient Outgrowth of Plant Organ". In: *Biophysical Journal* 117.10 (Nov. 2019), pp. 1995–2004. DOI: `10.1016/j.bpj.2019.10.019` (pages 14, 37, 55, 107).

[94] J. Kleine-Vehn, F. Huang, S. Naramoto, J. Zhang, M. Michniewicz, R. Offringa, and J. Friml. "PIN Auxin Efflux Carrier Polarity Is Regulated by PINOID Kinase-Mediated Recruitment into GNOM-Independent Trafficking in Arabidopsis". In: *The Plant Cell* 21.12 (Dec. 2009), pp. 3839–3849. ISSN: 1040-4651. DOI: `10.1105/tpc.109.071639` (page 14).

[95] Jean-Daniel Julien, Alain Pumir, and Arezki Boudaoud. "Strain- or Stress-sensing in mechanochemical patterning by the phytohormone auxin". In: *bioRxiv* (2019). DOI: `10.1101/582551` (pages 15, 46, 49).

[96] Silvanus Alt, Poulami Ganguly, and Guillaume Salbreux. "Vertex models: from cell mechanics to tissue morphogenesis". In: *Philosophical Transactions of the Royal Society B: Biological Sciences* 372.1720 (May 2017), p. 20150520. ISSN: 0962-8436. DOI: `10.1098/rstb.2015.0520` (pages 16, 19, 36).

[97] Amaya Vilches-Barro and Alexis Maizel. "Talking through walls: Mechanisms of lateral root emergence in Arabidopsis thaliana". In: *Current Opinion in Plant Biology* 23.May (2015), pp. 31–38. ISSN: 13695266. DOI: `10.1016/j.pbi.2014.10.005` (pages 17, 79, 80, 88).

[98] Marta Laskowski. "Lateral root initiation is a probabilistic event whose frequency is set by fluctuating levels of auxin response". In: *Journal of Experimental Botany* 64.9 (June 2013), pp. 2609–2617. ISSN: 1460-2431. DOI: `10.1093/jxb/ert155` (pages 17, 82, 88).

[99] Benjamin Péret, Bert De Rybel, Ilda Casimiro, Eva Benková, Ranjan Swarup, Laurent Laplaze, Tom Beeckman, and Malcolm J. Bennett. "Arabidopsis lateral

root development: an emerging story". In: *Trends in Plant Science* 14.7 (July 2009), pp. 399–408. ISSN: 13601385. DOI: `10.1016/j.tplants.2009.05.002` (pages 17, 88).

[100] Peter Marhavý, Marleen Vanstraelen, Bert De Rybel, Ding Zhaojun, Malcolm J. Bennett, Tom Beeckman, and Eva Benková. "Auxin reflux between the endodermis and pericycle promotes lateral root initiation". In: *The EMBO Journal* 32.1 (Nov. 2012), pp. 149–158. ISSN: 0261-4189. DOI: `10.1038/emboj.2012.303` (pages 17, 80, 82, 94, 96).

[101] J. E. M. Vermeer, D. von Wangenheim, M. Barberon, Y. Lee, E. H. K. Stelzer, A. Maizel, and N. Geldner. "A Spatial Accommodation by Neighboring Cells Is Required for Organ Initiation in Arabidopsis". In: *Science* 343.6167 (Jan. 2014), pp. 178–183. ISSN: 0036-8075. DOI: `10.1126/science.1245871` (pages 17, 80, 82, 83, 90, 92, 93).

[102] P. Van Liedekerke, M. M. Palm, N. Jagiella, and D. Drasdo. "Simulating tissue mechanics with agent-based models: concepts, perspectives and some novel results". In: *Computational Particle Mechanics* 2.4 (Nov. 2015), pp. 401–444. DOI: `10.1007/s40571-015-0082-3` (page 19).

[103] Yang Jiao and Salvatore Torquato. "Emergent Behaviors from a Cellular Automaton Model for Invasive Tumor Growth in Heterogeneous Microenvironments". In: *PLOS Computational Biology* 7.12 (Dec. 2011), pp. 1–14. DOI: `10.1371/journal.pcbi.1002314` (page 19).

[104] Jan Poleszczuk and Heiko Enderling. "A High-Performance Cellular Automaton Model of Tumor Growth with Dynamically Growing Domains". In: *Applied Mathematics* 05.01 (2014), pp. 144–152. DOI: `10.4236/am.2014.51017` (page 19).

[105] Maurício Moreira-Soares, Rita Coimbra, Luís Rebelo, João Carvalho, and Rui D. M. Travasso. "Angiogenic Factors produced by Hypoxic Cells are a leading driver of Anastomoses in Sprouting Angiogenesis–a computational study". In: *Scientific Reports* 8.1 (June 2018). DOI: `10.1038/s41598-018-27034-8` (page 19).

[106] David Zwicker, Johannes Baumgart, Stefanie Redemann, Thomas Müller-Reichert, Anthony A. Hyman, and Frank Jülicher. "Positioning of Particles in Active Droplets". In: *Phys. Rev. Lett.* 121 (15 Oct. 2018), p. 158102. DOI: `10.1103/PhysRevLett.121.158102` (page 19).

[107] Michael R. Tonks and Larry K. Aagesen. "The Phase Field Method: Mesoscale Simulation Aiding Material Discovery". In: *Annual Review of Materials Research* 49.1 (2019), pp. 79–102. DOI: `10.1146/annurev-matsci-070218-010151` (page 19).

[108] Tsuyoshi Hirashima, Elisabeth G. Rens, and Roeland M. H. Merks. "Cellular Potts modeling of complex multicellular behaviors in tissue morphogenesis". In: *Development, Growth & Differentiation* 59.5 (2017), pp. 329–339. DOI: `10.1111/dgd.12358` (page 19).

[109] András Szabó and Roeland M. Merks. “Cellular Potts Modeling of Tumor Growth, Tumor Invasion, and Tumor Evolution”. In: *Frontiers in Oncology* 3 (2013), p. 87. ISSN: 2234-943X. DOI: `10.3389/fonc.2013.00087` (page 19).

[110] René F. M. van Oers, Elisabeth G. Rens, Danielle J. LaValley, Cynthia A. Reinhart-King, and Roeland M. H. Merks. “Mechanical Cell-Matrix Feedback Explains Pairwise and Collective Endothelial Cell Behavior In Vitro”. In: *PLOS Computational Biology* 10.8 (Aug. 2014), pp. 1–14. DOI: `10.1371/journal.pcbi.1003774` (page 19).

[111] Elisabeth G. Rens and Roeland M.H. Merks. “Cell Shape and Durotaxis Explained from Cell-Extracellular Matrix Forces and Focal Adhesion Dynamics”. In: *iScience* 23.9 (2020), p. 101488. ISSN: 2589-0042. DOI: `10.1016/j.isci.2020.101488` (page 19).

[112] Néstor Sepúlveda, Laurence Petitjean, Olivier Cochet, Erwan Grasland-Mongrain, Pascal Silberzan, and Vincent Hakim. “Collective Cell Motion in an Epithelial Sheet Can Be Quantitatively Described by a Stochastic Interacting Particle Model”. In: *PLOS Computational Biology* 9.3 (Mar. 2013), pp. 1–12. DOI: `10.1371/journal.pcbi.1002944` (page 19).

[113] Julien Delile, Matthieu Herrmann, Nadine Peyriéras, and René Doursat. “A cell-based computational model of early embryogenesis coupling mechanical behaviour and gene regulation”. In: *Nature Communications* 8.1 (Jan. 2017). DOI: `10.1038/ncomms13929` (page 19).

[114] Sebastian A Sandersius and Timothy J Newman. “Modeling cell rheology with the Subcellular Element Model”. In: *Physical Biology* 5.1 (Apr. 2008), p. 015002. DOI: `10.1088/1478-3975/5/1/015002` (page 19).

[115] T. J. Newman. “Modeling Multicellular Systems Using Subcellular Elements”. In: *Mathematical Biosciences & Engineering* 2.3 (2005), pp. 613–624 (page 19).

[116] Georgios Trichas, Aaron M. Smith, Natalia White, Vivienne Wilkins, Tomoko Watanabe, Abigail Moore, Bradley Joyce, Jacintha Sugnaseelan, Tristan A. Rodriguez, David Kay, Ruth E. Baker, Philip K. Maini, and Shankar Srinivas. “Multi-Cellular Rosettes in the Mouse Visceral Endoderm Facilitate the Ordered Migration of Anterior Visceral Endoderm Cells”. In: *PLoS Biology* 10.2 (Feb. 2012). Ed. by Charles D. Little, e1001256. ISSN: 1545-7885. DOI: `10.1371/journal.pbio.1001256` (page 19).

[117] Nebojsa Murisic, Vincent Hakim, Ioannis G. Kevrekidis, Stanislav Y. Shvartsman, and Basile Audoly. “From Discrete to Continuum Models of Three-Dimensional Deformations in Epithelial Sheets”. In: *Biophysical Journal* 109.1 (July 2015), pp. 154–163. ISSN: 00063495. DOI: `10.1016/j.bpj.2015.05.019` (page 19).

[118] Miriam Osterfield, XinXin Du, Trudi Schüpbach, Eric Wieschaus, and Stanislav Y. Shvartsman. “Three-Dimensional Epithelial Morphogenesis in the Developing

Drosophila Egg". In: *Developmental Cell* 24.4 (Feb. 2013), pp. 400–410. ISSN: 15345807. DOI: `10.1016/j.devcel.2013.01.017` (page 19).

[119] Leonidas Guibas and Jorge Stolfi. "Primitives for the Manipulation of General Subdivisions and the Computation of Voronoi". In: *ACM Trans. Graph.* 4.2 (Apr. 1985), pp. 74–123. ISSN: 0730-0301. DOI: `10.1145/282918.282923` (page 20).

[120] Mark Meyer, Mathieu Desbrun, Peter Schröder, and Alan H. Barr. "Discrete Differential-Geometry Operators for Triangulated 2-Manifolds". In: *Mathematics and Visualization*. Springer Berlin Heidelberg, 2003, pp. 35–57. DOI: `10.1007/978-3-662-05105-4_2` (pages 26, 27, 30).

[121] Achim Guckenberger, Marcel P. Schraml, Paul G. Chen, Marc Leonetti, and Stephan Gekle. "On the bending algorithms for soft objects in flows". In: *Computer Physics Communications* 207 (Oct. 2016), pp. 1–23. ISSN: 00104655. DOI: `10.1016/j.cpc.2016.04.018` (pages 26, 30).

[122] P. Heckbert. *Quad-Edge Data Structure Library.* URL: `http://www.cs.cmu.edu/afs/andrew/scs/cs/15-463/2001/pub/src/a2/cell/` (page 33).

[123] J. D. Hunter. "Matplotlib: A 2D graphics environment". In: *Computing in Science & Engineering* 9.3 (2007), pp. 90–95. DOI: `10.1109/MCSE.2007.55` (page 33).

[124] S. G. Johnson. *The NLopt nonlinear-optimization package.* URL: `http://github.com/stevengj/nlopt` (page 34).

[125] Charles R. Harris, K. Jarrod Millman, Stéfan J van der Walt, Ralf Gommers, Pauli Virtanen, David Cournapeau, Eric Wieser, Julian Taylor, Sebastian Berg, Nathaniel J. Smith, Robert Kern, Matti Picus, Stephan Hoyer, Marten H. van Kerkwijk, Matthew Brett, Allan Haldane, Jaime Fernández del Río, Mark Wiebe, Pearu Peterson, Pierre Gérard-Marchant, Kevin Sheppard, Tyler Reddy, Warren Weckesser, Hameer Abbasi, Christoph Gohlke, and Travis E. Oliphant. "Array programming with NumPy". In: *Nature* 585 (2020), pp. 357–362. DOI: `10.1038/s41586-020-2649-2` (page 34).

[126] Frédéric Boudon, Jérôme Chopard, Olivier Ali, Benjamin Gilles, Olivier Hamant, Arezki Boudaoud, Jan Traas, and Christophe Godin. "A Computational Framework for 3D Mechanical Modeling of Plant Morphogenesis with Cellular Resolution". In: *PLoS Computational Biology* 11.1 (Jan. 2015). Ed. by Stanislav Shvartsman, e1003950. ISSN: 1553-7358. DOI: `10.1371/journal.pcbi.1003950` (page 35).

[127] Gabriella Mosca, Milad Adibi, Soeren Strauss, Adam Runions, Aleksandra Sapala, and Richard S. Smith. "Modeling Plant Tissue Growth and Cell Division". In: *Mathematical Modelling in Plant Biology.* Springer International Publishing, 2018, pp. 107–138. DOI: `10.1007/978-3-319-99070-5_7` (pages 35, 44).

[128] Roeland M.H. Merks, Michael Guravage, Dirk Inzé, and Gerrit T.S. Beemster. "VirtualLeaf: An Open-Source Framework for Cell-Based Modeling of Plant Tissue Growth and Development". In: *Plant Physiology* 155.2 (Feb. 2011), pp. 656–666. ISSN: 0032-0889. DOI: `10.1104/pp.110.167619` (page 35).

[129] Alexander G. Fletcher, Miriam Osterfield, Ruth E. Baker, and Stanislav Y. Shvartsman. “Vertex Models of Epithelial Morphogenesis”. In: *Biophysical Journal* 106.11 (June 2014), pp. 2291–2304. DOI: `10.1016/j.bpj.2013.11.4498` (page 36).

[130] F Corson, O Hamant, S Bohn, J Traas, A Boudaoud, and Y Couder. “Turning a plant tissue into a living cell froth through isotropic growth”. In: *Proceedings of the National Academy of Sciences USA* 106.21 (May 2009), pp. 8453–8458. ISSN: 0027-8424. DOI: `10.1073/pnas.0812493106` (pages 41, 44, 84, 85).

[131] H.J. Deuling and W. Helfrich. “Red blood cell shapes as explained on the basis of curvature elasticity”. In: *Biophysical Journal* 16.8 (1976), pp. 861–868. ISSN: 0006-3495. DOI: `10.1016/S0006-3495(76)85736-0` (page 42).

[132] Juliá Cufı, Agustı Reventó, and Carlos J. RodrÍz. “Curvature for Polygons”. In: *The American Mathematical Monthly* 122.4 (2015), p. 332. DOI: `10.4169/amer.math.monthly.122.04.332` (page 43).

[133] L D Landau, L. P. Pitaevskii, A. M. Kosevich, and E.M. Lifshitz. *Theory of Elasticity*. Dec. 2012. ISBN: 9780080570693 (page 43).

[134] Jan Kierfeld, Krzysztof Baczynski, Petra Gutjahr, and Reinhard Lipowsky. “Semiflexible Polymers and Filaments: From Variational Problems to Fluctuations”. In: *AIP Conference Proceedings* 1002 (Apr. 2008), p. 151. DOI: `10.1063/1.2918091` (page 44).

[135] J. Kierfeld, O. Niamploy, V. Sa-yakanit, and R. Lipowsky. “Stretching of semiflexible polymers with elastic bonds”. In: *The European Physical Journal E* 14.1 (May 2004), pp. 17–34. DOI: `10.1140/epje/i2003-10089-3` (page 44).

[136] L. Livadaru, R. R. Netz, and H. J. Kreuzer. “Stretching Response of Discrete Semiflexible Polymers”. In: *Macromolecules* 36.10 (Apr. 2003), pp. 3732–3744. DOI: `10.1021/ma020751g` (page 44).

[137] Eric M. Kramer. “Computer models of auxin transport: a review and commentary”. In: *Journal of Experimental Botany* 59.1 (Apr. 2007), pp. 45–53. ISSN: 0022-0957. DOI: `10.1093/jxb/erm060` (page 45).

[138] Eric M. Kramer and Ethan M. Ackelsberg. “Auxin metabolism rates and implications for plant development”. In: *Frontiers in Plant Science* 6.March (Mar. 2015), pp. 1–8. ISSN: 1664-462X. DOI: `10.3389/fpls.2015.00150` (page 47).

[139] Devin L. O’Connor, Adam Runions, Aaron Sluis, Jennifer Bragg, John P. Vogel, Przemyslaw Prusinkiewicz, and Sarah Hake. “A Division in PIN-Mediated Auxin Patterning during Organ Initiation in Grasses”. In: *PLOS Computational Biology* 10.1 (Jan. 2014), pp. 1–14. DOI: `10.1371/journal.pcbi.1003447` (page 49).

[140] Behruz Bozorg, Pawel Krupinski, and Henrik Jönsson. “Stress and Strain Provide Positional and Directional Cues in Development”. In: *PLOS Computational Biology* 10.1 (Jan. 2014), pp. 1–13. DOI: `10.1371/journal.pcbi.1003410` (page 49).

[141] M. Galassi et al. *GNU Scientific Library Reference Manual (3rd Ed.)* URL: `https://www.gnu.org/software/gsl/` (page 50).

[142] Dorothee Stoeckle, Martha Thellmann, and Joop EM Vermeer. “Breakout — lateral root emergence in Arabidopsis thaliana”. In: *Current Opinion in Plant Biology* 41 (Feb. 2018), pp. 67–72. ISSN: 13695266. DOI: `10.1016/j.pbi.2017.09.005` (pages 79, 80).

[143] Alan Marchant, Rishikesh Bhalerao, Ilda Casimiro, Jan Eklöf, Pedro J. Casero, Malcolm Bennett, and Goran Sandberg. “AUX1 Promotes Lateral Root Formation by Facilitating Indole-3-Acetic Acid Distribution between Sink and Source Tissues in the Arabidopsis Seedling”. In: *The Plant Cell* 14.3 (Mar. 2002), pp. 589–597. ISSN: 1040-4651. DOI: `10.1105/tpc.010354` (pages 80, 81).

[144] Marta Laskowski and Kirsten H. ten Tusscher. “Periodic Lateral Root Priming: What Makes It Tick?” In: *The Plant Cell* 29.3 (Mar. 2017), pp. 432–444. ISSN: 1040-4651. DOI: `10.1105/tpc.16.00638` (pages 81, 82, 98).

[145] Marta Laskowski, Verônica A Grieneisen, Hugo Hofhuis, Colette A. ten Hove, Paulien Hogeweg, Athanasius F. M Marée, and Ben Scheres. “Root System Architecture from Coupling Cell Shape to Auxin Transport”. In: *PLoS Biology* 6.12 (Dec. 2008). Ed. by Detlef Weigel, e307. ISSN: 1545-7885. DOI: `10.1371/journal.pbio.0060307` (pages 81, 82, 87, 97).

[146] Marketa Samalova, Kareem Elsayad, Alesia Melnikava, Alexis Peaucelle, Evelina Gahurova, Jaromir Gumulec, Ioannis Spyroglou, Elena V. Zemlyanskaya, Elena V. Ubogoeva, and Jan Hejatko. “Expansin-controlled cell wall stiffness regulates root growth in Arabidopsis”. In: *bioRxiv* (2020). DOI: `10.1101/2020.06.25.170969` (page 81).

[147] Robert Prevedel, Alba Diz-Muñoz, Giancarlo Ruocco, and Giuseppe Antonacci. “Brillouin microscopy: an emerging tool for mechanobiology”. In: *Nature Methods* 16.10 (Sept. 2019), pp. 969–977. DOI: `10.1038/s41592-019-0543-3` (page 81).

[148] Pei-Jung Wu, Irina V. Kabakova, Jeffrey W. Ruberti, Joseph M. Sherwood, Iain E. Dunlop, Carl Paterson, Peter Török, and Darryl R. Overby. “Water content, not stiffness, dominates Brillouin spectroscopy measurements in hydrated materials”. In: *Nature Methods* 15.8 (July 2018), pp. 561–562. DOI: `10.1038/s41592-018-0076-1` (page 81).

[149] Eleftheria Roumeli, Leah Ginsberg, Robin McDonald, Giada Spigolon, Rodinde Hendrickx, Misato Ohtani, Taku Demura, Guruswami Ravichandran, and Chiara Daraio. “Structure and Biomechanics during Xylem Vessel Transdifferentiation in Arabidopsis thaliana”. In: *Plants* 9.12 (2020). ISSN: 2223-7747. DOI: `10.3390/plants9121715` (page 81).

[150] Yoselin Benitez-Alfonso, Christine Faulkner, Ali Pendle, Shunsuke Miyashima, Ykä Helariutta, and Andrew Maule. “Symplastic Intercellular Connectivity Regulates Lateral Root Patterning”. In: *Developmental Cell* 26.2 (July 2013), pp. 136–147. ISSN: 15345807. DOI: `10.1016/j.devcel.2013.06.010` (page 81).

[151] Franck Anicet Ditengou, William D. Teale, Philip Kochersperger, Karl Andreas Flittner, Irina Kneuper, Eric van der Graaff, Hugues Nziengui, Francesco Pinosa, Xugang Li, Roland Nitschke, Thomas Laux, and Klaus Palme. "Mechanical induction of lateral root initiation in Arabidopsis thaliana". In: *Proceedings of the National Academy of Sciences USA* 105.48 (2008), pp. 18818–18823. ISSN: 0027-8424. DOI: `10.1073/pnas.0807814105` (pages 81, 82, 94, 98, 108).

[152] Hidehiro Fukaki, Yoko Nakao, Yoko Okushima, Athanasios Theologis, and Masao Tasaka. "Tissue-specific expression of stabilized SOLITARY-ROOT/IAA14 alters lateral root development in Arabidopsis". In: *The Plant Journal* 44.3 (2005), pp. 382–395. DOI: `10.1111/j.1365-313X.2005.02537.x` (page 81).

[153] Ive De Smet, Takuya Tetsumura, Bert De Rybel, Nicolas Frei dit Frey, Laurent Laplaze, Ilda Casimiro, Ranjan Swarup, Mirande Naudts, Steffen Vanneste, Dominique Audenaert, Dirk Inzé, Malcolm J. Bennett, and Tom Beeckman. "Auxin-dependent regulation of lateral root positioning in the basal meristem of Arabidopsis". In: *Development* 134.4 (Feb. 2007), pp. 681–690. ISSN: 0950-1991. DOI: `10.1242/dev.02753` (pages 82, 98).

[154] Jaimie M. Van Norman, Wei Xuan, Tom Beeckman, and Philip N. Benfey. "To branch or not to branch: the role of pre-patterning in lateral root formation". In: *Development* 140.21 (Nov. 2013), pp. 4301–4310. ISSN: 0950-1991. DOI: `10.1242/dev.090548` (page 82).

[155] Qing Tian, Nicholas J. Uhlir, and Jason W. Reed. "Arabidopsis SHY2/IAA3 Inhibits Auxin-Regulated Gene Expression". In: *The Plant Cell* 14.2 (2002), pp. 301–319. ISSN: 1040-4651. DOI: `10.1105/tpc.010283` (page 82).

[156] Amaya Vilches Barro, Dorothee Stöckle, Martha Thellmann, Paola Ruiz-Duarte, Lotte Bald, Marion Louveaux, Patrick von Born, Philipp Denninger, Tatsuaki Goh, Hidehiro Fukaki, Joop E.M. Vermeer, and Alexis Maizel. "Cytoskeleton Dynamics Are Necessary for Early Events of Lateral Root Initiation in Arabidopsis". In: *Current Biology* 29.15 (Aug. 2019), 2443–2454.e5. DOI: `10.1016/j.cub.2019.06.039` (page 82).

[157] Priya Ramakrishna, Paola Ruiz Duarte, Graham A. Rance, Martin Schubert, Vera Vordermaier, Lam Dai Vu, Evan Murphy, Amaya Vilches Barro, Kamal Swarup, Kamaljit Moirangthem, Bodil Jørgensen, Brigitte van de Cotte, Tatsuaki Goh, Zhefeng Lin, Ute Voß, Tom Beeckman, Malcolm J. Bennett, Kris Gevaert, Alexis Maizel, and Ive De Smet. "EXPANSIN A1-mediated radial swelling of pericycle cells positions anticlinal cell divisions during lateral root initiation". In: *Proceedings of the National Academy of Sciences USA* 116.17 (2019), pp. 8597–8602. ISSN: 0027-8424. DOI: `10.1073/pnas.1820882116` (pages 83, 88).

[158] Sadaf Naseer, Yuree Lee, Catherine Lapierre, Rochus Franke, Christiane Nawrath, and Niko Geldner. "Casparian strip diffusion barrier in Arabidopsis is made of a lignin polymer without suberin". In: *Proceedings of the National Academy of*

Sciences USA 109.25 (2012), pp. 10101–10106. ISSN: 0027-8424. DOI: `10.1073/pnas.1205726109` (page 83).

[159] Thea van den Berg and Kirsten H. ten Tusscher. “Lateral Root Priming Synergystically Arises from Root Growth and Auxin Transport Dynamics”. In: *bioRxiv* (2018). DOI: `10.1101/361709` (page 84).

[160] Sergey N. Shabala and Roger R. Lew. “Turgor Regulation in Osmotically Stressed Arabidopsis Epidermal Root Cells. Direct Support for the Role of Inorganic Ion Uptake as Revealed by Concurrent Flux and Cell Turgor Measurements”. In: *Plant Physiology* 129.1 (May 2002), pp. 290–299. ISSN: 0032-0889. DOI: `10.1104/pp.020005` (page 84).

[161] Marta Laskowski, Steven Biller, Ken Stanley, Tymoteusz Kajstura, and Reeta Prusty. “Expression Profiling of Auxin-treated Arabidopsis Roots: Toward a Molecular Analysis of Lateral Root Emergence”. In: *Plant and Cell Physiology* 47.6 (June 2006), pp. 788–792. ISSN: 0032-0781. DOI: `10.1093/pcp/pcj043` (page 87).

[162] Ive De Smet. “Lateral root initiation: one step at a time”. In: *New Phytologist* 193.4 (2012), pp. 867–873. DOI: `10.1111/j.1469-8137.2011.03996.x` (page 88).

[163] Joseph G. Dubrovsky, Thomas L. Rost, Adán Colón-Carmona, and Peter Doerner. “Early primordium morphogenesis during lateral root initiation in Arabidopsis thaliana”. In: *Planta* 214.1 (Nov. 2001), pp. 30–36. DOI: `10.1007/s004250100598` (page 88).

[164] Ilda Casimiro, Tom Beeckman, Neil Graham, Rishikesh Bhalerao, Hanma Zhang, Pedro Casero, Goran Sandberg, and Malcolm J. Bennett. “Dissecting Arabidopsis lateral root development”. In: *Trends in Plant Science* 8.4 (2003), pp. 165–171. ISSN: 1360-1385. DOI: `10.1016/S1360-1385(03)00051-7` (page 88).

[165] Peter Marhavý, Jérôme Duclercq, Benjamin Weller, Elena Feraru, Agnieszka Bielach, Remko Offringa, Jiří Friml, Claus Schwechheimer, Angus Murphy, and Eva Benková. “Cytokinin Controls Polarity of PIN1-Dependent Auxin Transport during Lateral Root Organogenesis”. In: *Current Biology* 24.9 (May 2014), pp. 1031–1037. ISSN: 09609822. DOI: `10.1016/j.cub.2014.04.002` (pages 97, 108).

[166] Carlos S Galvan-Ampudia, Guillaume Cerutti, Jonathan Legrand, Géraldine Brunoud, Raquel Martin-Arevalillo, Romain Azais, Vincent Bayle, Steven Moussu, Christian Wenzl, Yvon Jaillais, Jan U Lohmann, Christophe Godin, and Teva Vernoux. “Temporal integration of auxin information for the regulation of patterning”. In: *eLife* 9 (May 2020). Ed. by Jürgen Kleine-Vehn and Christian S Hardtke, e55832. ISSN: 2050-084X. DOI: `10.7554/eLife.55832` (pages 103, 106).

[167] Ole Herud-Sikimić, Andre C. Stiel, Martina Kolb, Sooruban Shanmugaratnam, Kenneth W. Berendzen, Christian Feldhaus, Birte Höcker, and Gerd Jürgens. “A biosensor for the direct visualization of auxin”. In: *Nature* 592.7856 (Apr. 2021), pp. 768–772. DOI: `10.1038/s41586-021-03425-2` (page 106).

[168] Kirsten H ten Tusscher. “What remains of the evidence for auxin feedback on PIN polarity patterns?” In: *Plant Physiology* (Mar. 2021). ISSN: 0032-0889. DOI: `10.1093/plphys/kiab118` (page 106).

[169] Adrian Wolny, Lorenzo Cerrone, Athul Vijayan, Rachele Tofanelli, Amaya Vilches Barro, Marion Louveaux, Christian Wenzl, Sören Strauss, David Wilson-Sánchez, Rena Lymbouridou, Susanne S Steigleder, Constantin Pape, Alberto Bailoni, Salva Duran-Nebreda, George W Bassel, Jan U Lohmann, Miltos Tsiantis, Fred A Hamprecht, Kay Schneitz, Alexis Maizel, and Anna Kreshuk. “Accurate and versatile 3D segmentation of plant tissues at cellular resolution”. In: *eLife* 9 (July 2020). DOI: `10.7554/elife.57613` (page 106).

[170] Marco D’Ario, Rafael Tavares, Katharina Schiessl, Bénédicte Desvoyes, Crisanto Gutierrez, Martin Howard, and Robert Sablowski. “Cell size controlled in plants using DNA content as an internal scale”. In: *Science* 372.6547 (2021), pp. 1176–1181. ISSN: 0036-8075. DOI: `10.1126/science.abb4348` (page 107).

Appendix A

Shoelace formulas

Here we will provide a small overview of how to derive the expressions used for area, centroid, and second moment of area of a two-dimensional polygon. The idea is to use Green's theorem in order turn surface integrals into line integrals. We will concern ourselves with cases where the integration surface region is a simply connected one. By definition, the three quantities we want are

$$A_\alpha = \iint\limits_{S_\alpha} \mathrm{d}S_\alpha, \qquad C^\mu_\alpha = \frac{1}{A}\iint\limits_{S_\alpha} x^\mu \mathrm{d}S_\alpha, \qquad M^{\mu\nu}_\alpha = \iint\limits_{S_\alpha} x^\mu x^\nu \mathrm{d}S_\alpha. \tag{A.1}$$

Because we are dealing with a polygon, the curve around it, ∂S_α, is discretised by default and easy to parametrise. This means that a line integral of the form

$$\oint\limits_{\partial S_\alpha} \boldsymbol{F}(\boldsymbol{x}) \cdot d\boldsymbol{l} = \sum_{i\in\mathcal{V}_\alpha} \int\limits_{t|\boldsymbol{x}_i(t)=\boldsymbol{x}_i}^{t|\boldsymbol{x}_i(t)=\boldsymbol{x}_{i+1}} \boldsymbol{F}(t) \cdot \frac{\mathrm{d}\boldsymbol{x}_i(t)}{\mathrm{d}t}\mathrm{d}t. \tag{A.2}$$

The parametrisation chosen here is

$$\boldsymbol{x}_i = \frac{\boldsymbol{x}_{i+1} + \boldsymbol{x}_i}{2} + t\frac{\boldsymbol{x}_{i+1} - \boldsymbol{x}_i}{2}, \; t \in [-1, 1[\,, \tag{A.3}$$

and hence the line integral above becomes,

$$\oint\limits_{\partial S_\alpha} \boldsymbol{F}(\boldsymbol{x}) \cdot d\boldsymbol{l} = \frac{1}{2}\sum_{i\in\mathcal{V}_\alpha} \int\limits_{-1}^{1} \boldsymbol{F}(t) \cdot (\boldsymbol{x}_{i+1} - \boldsymbol{x}_i)\,\mathrm{d}t. \tag{A.4}$$

Green's theorem states

$$\oint\limits_{\partial S} \boldsymbol{F} \cdot \mathrm{d}\boldsymbol{l} = \iint\limits_{S} \left(\frac{\partial F^y}{\partial x} - \frac{\partial F^x}{\partial y}\right)\mathrm{d}S, \tag{A.5}$$

where F^x and F^y are the x and y components of vector field $\boldsymbol{F}$. The question now becomes, for each of the quantities we set out to compute, what is the vector field we use such that we are performing the correct surface integral.

Area

For area we will choose the field $F^x = -y/2$ and $F^y = x/2$. This choice ensures the integrand of the surface integral to be equal to 1. The integral, therefore, is

$$\begin{aligned}A_\alpha = \frac{1}{4}\sum_{i\in\mathcal{V}_\alpha}\int_{-1}^{1}\Bigg[-\left(\frac{y_{i+1}+y_i}{2}+t\frac{y_{i+1}-y_i}{2}\right)(x_{i+1}-x_i)+ \\ \left(\frac{x_{i+1}+x_i}{2}+t\frac{x_{i+1}-x_i}{2}\right)(y_{i+1}-y_i)\Bigg]\,\mathrm{d}t,\end{aligned} \quad \text{(A.6)}$$

Note that all odd powers of t integrated in the bounds $[-1,1[$ vanish by symmetry. Rearranging the remaining terms, we get

$$A_\alpha = \frac{1}{8}\sum_{i\in\mathcal{V}_\alpha}\int_{-1}^{1}\left[2x_iy_{i+1}-2x_{i+1}y_i\right]\mathrm{d}t = \frac{1}{2}\sum_{i\in\mathcal{V}_\alpha}\left[x_iy_{i+1}-x_{i+1}y_i\right]. \quad \text{(A.7)}$$

This is often called the shoelace formula.

Centroid

We will use $F^x = 0$ and $F^y = x^2/2$ for computing the x component of C^μ_α. Hence,

$$\begin{aligned}C^x_\alpha &= \frac{1}{16A}\sum_{i\in\mathcal{V}_\alpha}\int_{-1}^{1}\left(x_{i+1}+x_i+t\left(x_{i+1}-x_i\right)\right)^2\left(y_{i+1}-y_i\right)\mathrm{d}t \\ &= \frac{1}{24A}\sum_{i\in\mathcal{V}_\alpha}\left[3\left(x_{i+1}^2+x_i^2+2x_ix_{i+1}\right)\left(y_{i+1}-y_i\right)+\left(x_{i+1}^2-2x_ix_{i+1}+x_i^2\right)\left(y_{i+1}-y_i\right)\right] \\ &= \frac{1}{6A}\sum_{i\in\mathcal{V}_\alpha}\left[x_iy_{i+1}\left(x_i+x_{i+1}\right)-x_{i+1}y_i\left(x_{i+1}+x_i\right)+x_{i+1}^2y_{i+1}-x_i^2y_i\right] \\ &= \frac{1}{6A}\sum_{i\in\mathcal{V}_\alpha}\left[x_iy_{i+1}-x_{i+1}y_i\right]\left(x_i+x_{i+1}\right),\end{aligned} \quad \text{(A.8)}$$

where the term $x_i^2y_i$ is the same as $x_{i+1}^2y_{i+1}$, since our sum is cyclic and has an arbitrary starting point. To find the y component we can use $F^x = 0$ and $F^y = xy$ instead. We get

$$
\begin{aligned}
C_\alpha^y = \frac{1}{8A} \sum_{i\in\mathcal{V}_\alpha} \int_{-1}^{1} \left(x_{i+1} + x_i + t\left(x_{i+1} - x_i\right)\right)\left(y_{i+1} + y_i + t\left(y_{i+1} - y_i\right)\right)\left(y_{i+1} - y_i\right) \mathrm{d}t \\
= \frac{1}{12A} \sum_{i\in\mathcal{V}_\alpha} \left[3\left(x_{i+1} + x_i\right)\left(y_{i+1}^2 - y_i^2\right) + \left(x_{i+1} - x_i\right)\left(y_{i+1}^2 - 2y_i y_{i+1} + y_i^2\right)\right] \\
= \frac{1}{6A} \sum_{i\in\mathcal{V}_\alpha} \left[x_i y_{i+1} - x_{i+1} y_i\right]\left(y_{i+1} + y_i\right). \quad \text{(A.9)}
\end{aligned}
$$

Second moment of area

Lastly, we will have to compute the three independent components of the second moment of area. Starting with the xx component, we use $F^x = 0$ and $F^y = x^3/3$. Then, we can write

$$
\begin{aligned}
M_\alpha^{xx} = \frac{1}{48} \sum_{i\in\mathcal{V}_\alpha} \int_{-1}^{1} \left(x_{i+1} + x_i + t\left(x_{i+1} - x_i\right)\right)^3 \left(y_{i+1} - y_i\right) \mathrm{d}t \\
= \frac{1}{24} \sum_{i\in\mathcal{V}_\alpha} \left(y_{i+1} - y_i\right)\left(x_{i+1} + x_i\right)\left[\left(x_{i+1} + x_i\right)^2 + \left(x_{i+1} - x_i\right)^2\right] \\
= \frac{1}{12} \sum_{i\in\mathcal{V}_\alpha} \left(y_{i+1} - y_i\right)\left(x_{i+1}^3 + x_{i+1}^2 x_i + x_{i+1} x_i^2 + x_i^3\right) \\
= \frac{1}{12} \sum_{i\in\mathcal{V}_\alpha} \left[x_i y_{i+1} - x_{i+1} y_i\right]\left(x_{i+1}^2 + x_{i+1} x_i + x_i^2\right). \quad \text{(A.10)}
\end{aligned}
$$

With $F^x = -y^3/3$ and $F^y = 0$ instead, we can simply swap x with y and flip the sign, yielding

$$
\begin{aligned}
M_\alpha^{yy} = -\frac{1}{48} \sum_{i\in\mathcal{V}_\alpha} \int_{-1}^{1} \left(y_{i+1} + y_i + t\left(y_{i+1} - y_i\right)\right)^3 \left(x_{i+1} - x_i\right) \mathrm{d}t \\
= \frac{1}{12} \sum_{i\in\mathcal{V}_\alpha} \left[x_i y_{i+1} - x_{i+1} y_i\right]\left(y_{i+1}^2 + y_{i+1} y_i + y_i^2\right). \quad \text{(A.11)}
\end{aligned}
$$

For the last independent component, we can use $F^x = 0$ and $F^y = x^2 y/2$. We can write

$$\begin{aligned}
M_\alpha^{xy} &= \frac{1}{32}\sum_{i\in\mathcal{V}_\alpha}\int_{-1}^{1}\left(x_{i+1}+x_i+t\left(x_{i+1}-x_i\right)\right)^2\left(y_{i+1}+y_i+t\left(y_{i+1}-y_i\right)\right)\left(y_{i+1}-y_i\right)\mathrm{d}t \\
&= \frac{1}{24}\sum_{i\in\mathcal{V}_\alpha}\left[2\left(y_{i+1}^2-y_i^2\right)\left(x_{i+1}^2+x_i^2+x_{i+1}x_i\right)+\left(x_{i+1}^2-x_i^2\right)\left(y_{i+1}^2-2y_{i+1}y_i+y_i^2\right)\right] \\
&= \frac{1}{24}\sum_{i\in\mathcal{V}_\alpha}\left[x_iy_{i+1}\left(x_iy_{i+1}+2x_iy_i+2x_{i+1}y_{i+1}\right)-x_{i+1}y_i\left(x_{i+1}y_i+2x_iy_i+2x_{i+1}y_{i+1}\right)\right] \\
&= \frac{1}{24}\sum_{i\in\mathcal{V}_\alpha}\left[x_iy_{i+1}-x_{i+1}y_i\right]\left(x_iy_{i+1}+2x_iy_i+2x_{i+1}y_{i+1}+x_{i+1}y_i\right), \qquad \text{(A.12)}
\end{aligned}$$

where to obtain the last expression we added and subtracted the term $x_iy_ix_{i+1}y_{i+1}$.

Appendix B

Differentiation of geometrical features

In this section we will derive and express the gradient of geometrical features presented in chapter 2 with respect to vertex coordinates. These formulas are crucial for fast local optimisation, extensively used throughout this work. Also, during this exercise extensive use will be made of Einstein summation convention on upper indices. Sums on lower indices will be made explicit, since these refer to faces or vertices. Upper indices will have values $1, 2, 3$ representing each component in three-dimensional space.

We will introduce the Kronecker delta for components,

$$\delta^{\alpha\beta} = \begin{cases} 1, & \alpha = \beta, \\ 0, & \alpha \neq \beta, \end{cases} \tag{B.1}$$

as well as an analogous Kronecker delta for junctions, δ_{ij}. This will be useful as all gradients eventually boil down to expressions containing,

$$\frac{\partial x_i^\alpha}{\partial x_j^\beta} = \delta^{\alpha\beta}\delta_{ij}. \tag{B.2}$$

Another useful tool we will not shy away from using is the Levi-Civita symbol,

$$\varepsilon^{\lambda\mu\nu} = \begin{cases} 1, & (\lambda, \mu, \nu) \text{ is a cyclic permutation of } (1, 2, 3), \\ -1, & (\lambda, \mu, \nu) \text{ is an anticyclic permutation of } (1, 2, 3), \\ 0, & \lambda = \mu,\ \mu = \nu, \text{ or } \nu = \lambda, \end{cases} \tag{B.3}$$

which will helps us describe cross products component-wise as

$$(\boldsymbol{a} \times \boldsymbol{b})^\lambda = \varepsilon^{\lambda\mu\nu} a^\mu b^\nu. \tag{B.4}$$

Other properties include, but are not limited to,

$$\varepsilon^{\lambda\mu\nu} = \varepsilon^{\mu\nu\lambda} = \varepsilon^{\nu\lambda\mu} = -\varepsilon^{\lambda\nu\mu} = -\varepsilon^{\nu\mu\lambda} = -\varepsilon^{\mu\lambda\nu}, \tag{B.5}$$

and

$$\varepsilon^{\lambda\mu\nu}\varepsilon^{\nu\alpha\beta} = \delta^{\alpha\lambda}\delta^{\beta\mu} - \delta^{\alpha\mu}\delta^{\beta\lambda}. \tag{B.6}$$

Furthermore, two recurring patterns which will be useful to call upon is the gradient of the norm of a vector,

$$\frac{\partial \left\|\boldsymbol{u}\right\|}{\partial x_j^\beta} = \frac{\partial \left(\sqrt{u^\alpha u^\alpha}\right)}{\partial x_j^\beta} = \frac{u^\alpha}{\sqrt{u^\gamma u^\gamma}} \frac{\partial u^\alpha}{\partial x_j^\beta}, \tag{B.7}$$

and the gradient of a normalisation procedure,

$$\frac{\partial \tilde{\boldsymbol{u}}}{\partial x_j^\beta} = \frac{\partial \left(\boldsymbol{u}/\left\|\boldsymbol{u}\right\|\right)}{\partial x_j^\beta} = \frac{\partial \left(u^\alpha/\sqrt{u^\gamma u^\gamma}\right)}{\partial x_j^\beta} = \frac{1}{\sqrt{u^\gamma u^\gamma}} \left(\frac{\partial u^\alpha}{\partial x_j^\beta} - \tilde{u}^\alpha \tilde{u}^\lambda \frac{\partial u^\lambda}{\partial x_j^\beta}\right). \tag{B.8}$$

Lastly, a quantity which appears recurrently is the norm of the cross-product. First we note that any cross-product can be written as a product of a matrix and a vector, as such,

$$\varepsilon^{\gamma\mu\nu} a^\mu b^\nu = K^{\gamma\nu} b^\nu. \tag{B.9}$$

The matrix K is often called the cross product matrix. When differentiating the norm, we get a term such as,

$$\partial \left\|\boldsymbol{a} \times \boldsymbol{b}\right\| = \frac{\boldsymbol{a} \times \boldsymbol{b}}{\left\|\boldsymbol{a} \times \boldsymbol{b}\right\|} \cdot \partial \left(\boldsymbol{a} \times \boldsymbol{b}\right) = \frac{\varepsilon^{\gamma\mu\nu} a^\mu b^\nu}{\left\|\boldsymbol{a} \times \boldsymbol{b}\right\|} \varepsilon^{\gamma\xi\eta} \left(b^\eta \partial a^\xi + a^\xi \partial b^\eta\right). \tag{B.10}$$

If we identify the first factor as a normal unit vector $\boldsymbol{k}$ to the plane spanned by $\boldsymbol{a}$ and $\boldsymbol{b}$, then we can write,

$$\partial \left\|\boldsymbol{a} \times \boldsymbol{b}\right\| = \varepsilon^{\eta\gamma\xi} k^\gamma \left(b^\eta \partial a^\xi + a^\xi \partial b^\eta\right) = K^{\eta\xi} \left(b^\eta \partial a^\xi + a^\xi \partial b^\eta\right). \tag{B.11}$$

Adapting to our geometrical setup we will define for vertices,

$$K_{ijk}^{\mu\nu} = \frac{\varepsilon^{\gamma\lambda\rho} \left(x_j^\lambda - x_i^\lambda\right) \left(x_k^\rho - x_i^\rho\right) \varepsilon^{\mu\gamma\nu}}{\left\|\left(\boldsymbol{x}_j - \boldsymbol{x}_i\right) \times \left(\boldsymbol{x}_k - \boldsymbol{x}_i\right)\right\|}, \tag{B.12}$$

as well as with respect to a centroid, $\boldsymbol{X}_\alpha$,

$$K_{\alpha i i+1}^{\mu\nu} = \frac{\varepsilon^{\gamma\lambda\rho} \left(x_i^\lambda - X_\alpha^\lambda\right) \left(x_{i+1}^\rho - X_\alpha^\rho\right) \varepsilon^{\mu\gamma\nu}}{\left\|\left(\boldsymbol{x}_i - \boldsymbol{X}_\alpha\right) \times \left(\boldsymbol{x}_{i+1} - \boldsymbol{X}_\alpha\right)\right\|} = \varepsilon^{\mu\gamma\nu} \frac{n_i^\gamma}{2a_i}, \tag{B.13}$$

B.1 Geometrical quantities

We will go through most quantities defined in Section 2.2. Unfortunately, curvature and mixed Voronoi region area, circumcenter, and normal unit vector become difficult to compute and implement. Since we are not dealing with these quantities in the results of this work, we were not compelled to derive them at this point in time. It will be useful to get these ones down when moving to three-dimensions and is, therefore, an immediate goal for the outlook of this work.

Segment length and polygon perimeter

Since,

$$l_{ij} = \|\boldsymbol{x}_i - \boldsymbol{x}_j\| = \sqrt{\left(x_i^\alpha - x_j^\alpha\right)\left(x_i^\alpha - x_j^\alpha\right)}, \tag{B.14}$$

by differentiating with respect to x_k^β, we obtain,

$$\frac{\partial l_{ij}}{\partial x_k^\beta} = \frac{x_i^\alpha - x_j^\alpha}{l_{ij}}\left(\frac{\partial x_i^\alpha}{\partial x_k^\beta} - \frac{\partial x_j^\alpha}{\partial x_k^\beta}\right) = \frac{x_i^\beta - x_j^\beta}{l_{ij}}\left(\delta_{ik} - \delta_{jk}\right). \tag{B.15}$$

Furthermore, the gradient of the perimeter of cell α is given by

$$L_\alpha = \sum_{i\in\mathcal{V}_\alpha} l_{i+1i}, \tag{B.16}$$

which when differentiating yields

$$\frac{\partial L_\alpha}{\partial x_j^\beta} = \sum_{i\in\mathcal{V}_\alpha}\frac{\partial l_{i+1i}}{\partial x_j^\beta} = \sum_{i\in\mathcal{V}_\alpha}\frac{x_{i+1}^\beta - x_i^\beta}{l_{i+1i}}\left(\delta_{i+1j} - \delta_{ij}\right) = \frac{x_j^\beta - x_{j-1}^\beta}{l_{jj-1}} - \frac{x_{j+1}^\beta - x_j^\beta}{l_{j+1j}}, \tag{B.17}$$

if $j \in \mathcal{V}_\alpha$, otherwise it would be null. In order to avoid repeating this caveat over and over again, we will assume henceforth that the differentiation is only done with respect to vertices pertaining to the particular quantity being differentiated.

Centroid

This is where we pay the price for the restrictions we placed upon ourselves when attempting to define a centroid of a polygon embedded in three-dimensional space. Starting from,

$$\boldsymbol{X}_\alpha = \frac{\sum_{i\in\mathcal{V}_\alpha} l_{i+1i}\int_{-1}^{1} C_i\left(t\right)\mathrm{d}t}{2L_\alpha}, \tag{B.18}$$

by differentiation, becomes

$$\begin{aligned}\frac{\partial X_\alpha^\beta}{\partial x_j^\gamma} &= \frac{\sum_{i\in\mathcal{V}_\alpha} l_{i+1i}\int_{-1}^{1}\frac{\partial C_i^\beta(t)}{\partial x_j^\gamma}\mathrm{d}t}{2L_\alpha} + \frac{\sum_{i\in\mathcal{V}_\alpha}\frac{\partial l_{i+1i}}{\partial x_j^\gamma}\int_{-1}^{1} C_i^\beta\left(t\right)\mathrm{d}t}{2L_\alpha} - \frac{X_\alpha^\beta}{L_\alpha}\frac{\partial L_\alpha}{\partial x_j^\gamma}\\ &= \frac{\sum_{i\in\mathcal{V}_\alpha} l_{i+1i}\int_{-1}^{1}\frac{\partial C_i^\beta(t)}{\partial x_j^\gamma}\mathrm{d}t}{2L_\alpha} + \frac{1}{2L_\alpha}\left\{\frac{x_j^\gamma - x_{j-1}^\gamma}{l_{jj-1}}\int\limits_{-1}^{1}\left[C_{j-1}^\beta\left(t\right) - X_\alpha^\beta\right]\mathrm{d}t\right.\\ &\qquad\left. - \frac{x_{j+1}^\gamma - x_j^\gamma}{l_{j+1j}}\int\limits_{-1}^{1}\left[C_j^\beta\left(t\right) - X_\alpha^\beta\right]\mathrm{d}t\right\}, \end{aligned}\tag{B.19}$$

where we notice that $\partial l_{i+1i}/\partial x_j^\beta$ inside the sum selects for the same terms as $\partial L_\alpha/\partial x_j^\beta$. For the first term, we need to go back to the definition

$$C_i^\beta\left(t\right) = \frac{\sum_{j\in\mathcal{V}_\alpha} A_{ij}\left(t\right) C_{ij}^\beta\left(t\right)}{\sum_{j\in\mathcal{V}_\alpha} A_{ij}\left(t\right)}, \tag{B.20}$$

and differentiate in a similar fashion to before,

$$\frac{\partial C_i^\beta\left(t\right)}{\partial x_k^\gamma} = \frac{\sum_{j\in\mathcal{V}_\alpha} A_{ij}\left(t\right)\frac{\partial C_{ij}^\beta(t)}{\partial x_k^\gamma}}{\sum_{j\in\mathcal{V}_\alpha} A_{ij}\left(t\right)} + \frac{\sum_{j\in\mathcal{V}_\alpha}\frac{\partial A_{ij}(t)}{\partial x_k^\gamma}\left[C_{ij}^\beta\left(t\right) - C_i^\beta\left(t\right)\right]}{\sum_{j\in\mathcal{V}_\alpha} A_{ij}\left(t\right)}. \tag{B.21}$$

The similarity between both expressions arises due to both being averages. Now we tackle,

$$C_{ij}^\beta\left(t\right) = \frac{x_i^\beta\left(t\right) + x_j^\beta + x_{j+1}^\beta}{3}, \qquad A_{ij}\left(t\right) = \frac{1}{2}\sqrt{\xi_{ij}^\beta\left(t\right)\xi_{ij}^\beta\left(t\right)}, \tag{B.22}$$

$$\xi_{ij}^\beta\left(t\right) = \varepsilon^{\beta\mu\nu}\left(x_j^\mu - x_i^\mu\left(t\right)\right)\left(x_{j+1}^\nu - x_i^\nu\left(t\right)\right) \qquad x_i^\beta\left(t\right) = \frac{x_{i+1}^\beta + x_i^\beta}{2} + t\frac{x_{i+1}^\beta - x_i^\beta}{2}, \tag{B.23}$$

from which we will start proverbially hitting chain rule bedrock.

Since $A_{ij}\left(t\right)$ is simply one half the norm of $\xi_{ij}^\beta\left(t\right)$,

$$\frac{\partial A_{ij}\left(t\right)}{\partial x_k^\gamma} = \frac{\xi_{ij}^\beta\left(t\right)}{4A_{ij}\left(t\right)}\frac{\partial \xi_{ij}^\beta\left(t\right)}{\partial x_k^\gamma}. \tag{B.24}$$

We now proceed from the bottom up,

$$\frac{\partial x_i^\beta\left(t\right)}{\partial x_k^\gamma} = \delta^{\beta\gamma}\left(\frac{1+t}{2}\delta_{i+1k} + \frac{1-t}{2}\delta_{ik}\right), \tag{B.25}$$

$$\frac{\partial \xi^{\beta}_{ij}\left(t\right)}{\partial x^{\gamma}_{k}} = \varepsilon^{\beta\mu\nu}\left(\delta^{\mu\gamma}\left[\delta_{jk} - \frac{1+t}{2}\delta_{i+1k} - \frac{1-t}{2}\delta_{ik}\right]\left[x^{\nu}_{j+1} - x^{\nu}_{i}\left(t\right)\right]\right.$$
$$\left. + \delta^{\nu\gamma}\left[x^{\mu}_{j} - x^{\mu}_{i}\left(t\right)\right]\left[\delta_{j+1k} - \frac{1+t}{2}\delta_{i+1k} - \frac{1-t}{2}\delta_{ik}\right]\right),$$

where we can now make use of the antisymmetry of the Levi-Civita symbol to contract the Kronecker deltas, rename dummy indices, and rewrite

$$\frac{\partial \xi^{\beta}_{ij}\left(t\right)}{\partial x^{\gamma}_{k}} = \varepsilon^{\beta\gamma\nu}\left(\delta_{jk}\left[x^{\nu}_{j+1} - x^{\nu}_{i}\left(t\right)\right] - \delta_{j+1k}\left[x^{\nu}_{j} - x^{\nu}_{i}\left(t\right)\right]\right.$$
$$\left. - \left[\frac{1+t}{2}\delta_{i+1k} + \frac{1-t}{2}\delta_{ik}\right]\left[x^{\nu}_{j+1} - x^{\nu}_{j}\right]\right). \quad \text{(B.26)}$$

To complete the expression of $\partial A_{ij}\left(t\right)/\partial x^{\gamma}_{k}$, it will facilitate writing if we reintroduce

$$u^{\nu}_{ji}\left(t\right) = x^{\nu}_{j} - x^{\nu}_{i}\left(t\right), \qquad u^{\nu}_{kj} = x^{\nu}_{k} - x^{\nu}_{j}. \quad \text{(B.27)}$$

The expression becomes,

$$\frac{\partial A_{ij}\left(t\right)}{\partial x^{\gamma}_{k}} = \frac{\varepsilon^{\gamma\nu\beta}}{4A_{ij}\left(t\right)}\left(\delta_{jk}u^{\nu}_{j+1i}\left(t\right) - \delta_{j+1k}u^{\nu}_{ji}\left(t\right)\right.$$
$$\left. - \left[\frac{1+t}{2}\delta_{i+1k} + \frac{1-t}{2}\delta_{ik}\right]u^{\nu}_{j+1j}\right)\xi^{\beta}_{ij}\left(t\right). \quad \text{(B.28)}$$

We will use the cross product with a unit vector shorthand, $K^{\gamma\nu}_{ijj+1}\left(t\right) = \varepsilon^{\gamma\beta\nu}\xi^{\beta}_{ij}\left(t\right)/\left(2A_{ij}\left(t\right)\right)$, in the expressions to follow.

The gradient of the centroids $C_{ij}\left(t\right)$ is much simpler,

$$\frac{\partial C^{\beta}_{ij}\left(t\right)}{\partial x^{\beta}_{k}} = \frac{\delta^{\beta\gamma}}{3}\left(\frac{1+t}{2}\delta_{i+1k} + \frac{1-t}{2}\delta_{ik} + \delta_{jk} + \delta_{j+1k}\right). \quad \text{(B.29)}$$

We can now go back to $C^{\beta}_{i}\left(t\right)$,

$$\frac{\partial C^{\beta}_{i}\left(t\right)}{\partial x^{\gamma}_{k}} = \delta^{\beta\gamma}\left[\left(\delta_{i+1k}\frac{1+t}{6} + \delta_{ik}\frac{1-t}{6}\right) + \frac{A_{ik}\left(t\right) + A_{ik-1}\left(t\right)}{3\sum_{j\in\mathcal{V}_{\alpha}}A_{ij}\left(t\right)}\right]$$
$$+\frac{1}{2}\left(\sum_{j\in\mathcal{V}_{\alpha}}A_{ij}\left(t\right)\right)^{-1}\left(\left[\frac{1+t}{2}\delta_{i+1k} + \frac{1-t}{2}\delta_{ik}\right]\sum_{j\in\mathcal{V}_{\alpha}}K^{\gamma\mu}_{ijj+1}\left(t\right)u^{\mu}_{j+1j}\left[C^{\beta}_{ij}\left(t\right) - C^{\beta}_{i}\left(t\right)\right]\right.$$
$$\left. - K^{\gamma\mu}_{ikk+1}\left(t\right)u^{\mu}_{k+1i}\left(t\right)\left[C^{\beta}_{ik}\left(t\right) - C^{\beta}_{i}\left(t\right)\right] + K^{\gamma\mu}_{ik-1k}\left(t\right)u^{\mu}_{k-1i}\left(t\right)\left[C^{\beta}_{ik-1}\left(t\right) - C^{\beta}_{i}\left(t\right)\right]\right). \quad \text{(B.30)}$$

Albeit hectic, we would now replace this expression in the centroid. We first note that we will use Gaussian quadrature on all non-immediate integrals in the resulting expression.

This means that we prefer the sum in i to be inside the integral, and all Kronecker deltas resolved. Then we will be left with several integrand functions of polygon geometry which can be evaluated at any t in order to perform the quadrature. The difference between each $C_{ij}^{\beta}(t)$ and the average value $C_i^{\beta}(t)$ shows up quite a bit, as well as in its analogous expression regarding $C_i^{\beta}(t)$ and $\boldsymbol{X}_{\alpha}^{\beta}$. We will abbreviate this difference with $\Delta C_{ij}(t)^{\beta}$ and $\Delta C_i(t)^{\beta}$, respectivelly. Hopefully we can simplify it ever so slightly. We will proceed term by term in $\partial C_i^{\beta}(t)/\partial x_k^{\gamma}$. For the first term, the corresponding term in $\partial X_{\alpha}^{\beta}/\partial x_j^{\gamma}$ becomes

$$\frac{\delta^{\beta\gamma}}{6L_{\alpha}}\left(l_{jj-1}+l_{j+1j}\right),$$

since the integral is immediate and the Kronecker delta makes short work of the summation in i. The second term is

$$\frac{\delta^{\beta\gamma}}{6L_{\alpha}}\int_{-1}^{1}\sum_{i\in\mathcal{V}_{\alpha}}l_{ii+1}\frac{A_{ij}(t)+A_{ij-1}(t)}{\sum_{k\in\mathcal{V}_{\alpha}}A_{ik}(t)}\mathrm{d}t.$$

In the next term, we end up swapping one sum for another, yielding

$$\frac{1}{8L_{\alpha}}\int_{-1}^{1}\sum_{l=-1}^{0}\frac{l_{j+1+l\,j+l}\left[1+(-1)^{l}t\right]}{\sum_{k\in\mathcal{V}_{\alpha}}A_{j+l\,k}(t)}\sum_{i\in\mathcal{V}_{\alpha}}K_{j+l\,ii+1}^{\gamma\mu}(t)\,u_{i+1i}^{\mu}\Delta C_{j+l\,i}^{\beta}(t)\,\mathrm{d}t,$$

where we renamed dummy indices and introduced a new sum to encapsulate both terms.We will do the same with the next and final terms, resulting in

$$\frac{1}{4L_{\alpha}}\int_{-1}^{1}\sum_{k=-1}^{0}(-1)^{k+1}\sum_{i\in\mathcal{V}_{\alpha}}l_{ii+1}\frac{K_{i\,j+k\,j+k+1}^{\gamma\mu}(t)\,u_{j+2k+1\,i}^{\mu}(t)\,\Delta C_{i\,j+k}^{\beta}(t)}{\sum_{l\in\mathcal{V}_{\alpha}}A_{i\,j+k}(t)}\mathrm{d}t$$

Finally, going back to the centroid gradient expression, we can rewrite it as

$$\begin{aligned}\frac{\partial X_{\alpha}^{\beta}}{\partial x_j^{\gamma}}=\frac{\delta^{\beta\gamma}}{6L_{\alpha}}&\left(l_{jj-1}+l_{j+1j}+\int_{-1}^{1}\sum_{i\in\mathcal{V}_{\alpha}}l_{i+1i}\frac{A_{ij}(t)+A_{ij-1}(t)}{\sum_{k\in\mathcal{V}_{\alpha}}A_{ik}(t)}\mathrm{d}t\right)\\&+\frac{1}{2L_{\alpha}}\sum_{k=-1}^{0}\left(\frac{l_{j+1+k\,j+k}}{4}\int_{-1}^{1}\frac{1+(-1)^{k}t}{\sum_{l\in\mathcal{V}_{\alpha}}A_{j+k\,l}(t)}\sum_{i\in\mathcal{V}_{\alpha}}K_{j+k\,ii+1}^{\gamma\mu}(t)\,u_{i+1i}^{\mu}\Delta C_{j+k\,i}^{\beta}(t)\,\mathrm{d}t\right.\\&\qquad+(-1)^{k+1}\left[\frac{1}{2}\int_{-1}^{1}\sum_{i\in\mathcal{V}_{\alpha}}l_{i+1i}\frac{K_{i\,j+k\,j+k+1}^{\gamma\mu}(t)\,u_{j+2k+1\,i}^{\mu}(t)\,\Delta C_{i\,j+k}^{\beta}(t)}{\sum_{l\in\mathcal{V}_{\alpha}}A_{i\,j+k}(t)}\mathrm{d}t\right.\\&\qquad\qquad\left.\left.+\frac{u_{j+1+k\,j+k}^{\gamma}}{l_{j+1+k\,j+k}}\int_{-1}^{1}\Delta C_{j+k}^{\beta}(t)\,\mathrm{d}t\right]\right).\end{aligned}\tag{B.31}$$

Area

Having the centroid defined, and now the centroid gradient, it becomes quite straightforward to compute area gradient. Starting from the expressions of area, now written component-wise as

$$A_\alpha = \sum_{i\in\mathcal{V}_\alpha} a_i = \frac{1}{2}\sum_{i\in\mathcal{V}_\alpha}\sqrt{n_i^\gamma n_i^\gamma} \qquad\qquad n_i^\gamma = \varepsilon^{\gamma\mu\nu}\left(x_i^\mu - X_\alpha^\mu\right)\left(x_{i+1}^\nu - X_\alpha^\nu\right), \tag{B.32}$$

we first note that it is just a norm of a vector and write

$$\frac{\partial A_\alpha}{\partial x_j^\beta} = \frac{1}{2}\sum_{i\in\mathcal{V}_\alpha}\frac{n_i^\gamma}{\sqrt{n_i^\lambda n_i^\lambda}}\frac{\partial n_i^\gamma}{\partial x_j^\beta}. \tag{B.33}$$

As for n_i^γ, we make use of the fact we know the centroid gradient and use the chain rule,

$$\begin{aligned}
\frac{\partial n_i^\gamma}{\partial x_j^\beta} &= \left(\frac{\partial n_i^\gamma}{\partial x_j^\beta}\right)_{\boldsymbol{X}_\alpha} + \sum_{k\in\mathcal{V}_\alpha}\frac{\partial x_k^\eta}{\partial x_j^\beta}\frac{\partial X_\alpha^\xi}{\partial x_k^\eta}\frac{\partial n_i^\gamma}{\partial X_\alpha^\xi} = \left(\frac{\partial n_i^\gamma}{\partial x_j^\beta}\right)_{\boldsymbol{X}_\alpha} + \frac{\partial X_\alpha^\xi}{\partial x_j^\beta}\frac{\partial n_i^\gamma}{\partial X_\alpha^\xi}\\
&= \varepsilon^{\gamma\mu\nu}\left(\delta_{ij}\delta^{\beta\mu}\left(x_{i+1}^\nu - X_\alpha^\nu\right) + \delta_{i+1j}\delta^{\beta\nu}\left(x_i^\mu - X_\alpha^\mu\right) - \frac{\partial X_\alpha^\xi}{\partial x_j^\beta}\delta^{\xi\mu}\left(x_{i+1}^\nu - x_i^\nu\right)\right)\\
&= \varepsilon^{\gamma\beta\nu}\left(\delta_{ij}\left(x_{i+1}^\nu - X_\alpha^\nu\right) - \delta_{i+1j}\left(x_i^\nu - X_\alpha^\nu\right)\right) - \varepsilon^{\gamma\mu\nu}\frac{\partial X_\alpha^\mu}{\partial x_j^\beta}\left(x_{i+1}^\nu - x_i^\nu\right).
\end{aligned} \tag{B.34}$$

Replacing back onto $\partial A_\alpha/\partial x_j^\beta$ yields

$$\frac{\partial A_\alpha}{\partial x_j^\beta} = \frac{\varepsilon^{\beta\nu\gamma}}{2}\left[\frac{\left(x_{j+1}^\nu - X_\alpha^\nu\right)n_j^\gamma}{\sqrt{n_j^\lambda n_j^\lambda}} + \frac{\left(x_{j-1}^\nu - X_\alpha^\nu\right)n_{j-1}^\gamma}{\sqrt{n_{j-1}^\lambda n_{j-1}^\lambda}}\right] - \frac{\varepsilon^{\mu\nu\gamma}}{2}\frac{\partial X_\alpha^\mu}{\partial x_j^\beta}\sum_{i\in\mathcal{V}_\alpha}\frac{u_{i+1i}^\nu n_i^\gamma}{\sqrt{n_i^\lambda n_i^\lambda}}. \tag{B.35}$$

This expression can be rewritten in a more compact form when using the matrix K as defined earlier. Hence, we can also write,

$$\frac{\partial A_\alpha}{\partial x_j^\beta} = \frac{1}{2}\left[K_{\alpha jj+1}^{\beta\nu}\left(x_{j+1}^\nu - X_\alpha^\nu\right) + K_{\alpha j-1j}^{\beta\nu}\left(x_{j-1}^\nu - X_\alpha^\nu\right) - \frac{\partial X_\alpha^\mu}{\partial x_j^\beta}\sum_{i\in\mathcal{V}_\alpha}K_{\alpha ii+1}^{\mu\nu}u_{i+1i}^\nu\right]. \tag{B.36}$$

Normal unit vector

The expression for the normal unit vector,

$$w_\alpha^\gamma = \frac{N_\alpha^\gamma}{\sqrt{N_\alpha^\lambda N_\alpha^\lambda}}, \qquad\qquad N_\alpha^\gamma = \sum_{i\in\mathcal{V}_\alpha}\varepsilon^{\gamma\mu\nu}x_i^\mu x_{i+1}^\nu, \tag{B.37}$$

can be differentiated by invoking the derivative of a normalisation procedure, as well as comparing the terms of the sum in N_α^γ with that of vectors n_i^γ. We have,

$$\frac{\partial N_\alpha^\gamma}{\partial x_j^\beta} = \sum_{i\in\mathcal{V}_\alpha} \varepsilon^{\gamma\mu\nu}\left(\delta^{\mu\beta}\delta_{ij}x_{i+1}^\nu + \delta^{\nu\beta}\delta_{i+1j}x_i^\mu\right) = \varepsilon^{\gamma\beta\nu}u_{j+1j-1}^\nu, \tag{B.38}$$

and

$$\frac{\partial w_\alpha^\gamma}{\partial x_j^\beta} = \frac{1}{\sqrt{N_\alpha^\lambda N_\alpha^\lambda}}\left(\frac{\partial N_\alpha^\gamma}{\partial x_j^\beta} - w_\alpha^\gamma w_\alpha^\mu \frac{\partial N_\alpha^\mu}{\partial x_j^\beta}\right) = \\ \frac{1}{\sqrt{N_\alpha^\lambda N_\alpha^\lambda}}\left(\varepsilon^{\gamma\beta\nu}u_{j+1j-1}^\nu + w_\alpha^\gamma \varepsilon^{\beta\mu\nu} w_\alpha^\mu u_{j+1j-1}^\nu\right). \tag{B.39}$$

Volume

The expression for the volume gradient becomes relatively simple when using the results above, since volume is computed with,

$$V = \sum_{\alpha=1}^{M} v_\alpha, \qquad\qquad v_\alpha = \frac{1}{6}N_\alpha^\gamma X_\alpha^\gamma. \tag{B.40}$$

We start by working the terms v_α,

$$\frac{\partial v_\alpha}{\partial x_j^\beta} = \frac{1}{6}\left(\frac{\partial N_\alpha^\gamma}{\partial x_j^\beta}X_\alpha^\gamma + N_\alpha^\gamma\frac{\partial X_\alpha^\gamma}{\partial x_j^\beta}\right) = \frac{1}{6}\left(\varepsilon^{\beta\nu\gamma}u_{j+1j-1}^\nu X_\alpha^\gamma + N_\alpha^\gamma \frac{\partial X_\alpha^\gamma}{\partial x_j^\beta}\right). \tag{B.41}$$

For the total volume gradient with respect to vertex j we then have to sum these contributions for each of the surrounding faces, i.e.,

$$\frac{\mathrm{d}V}{\mathrm{d}x_j^\beta} = \sum_{\alpha\in\mathcal{N}_j}\frac{\partial v_\alpha}{\partial x_j^\beta}. \tag{B.42}$$

We could perform a similar operation in regards to obtain total surface area gradient from face area, A_α.

Mixed Voronoi Area

From this section onwards we will consider the triangulated surface only. A useful quantity to track is the cross product between two of the sides of the triangle ijk,

$$m_{ijk}^\gamma = \varepsilon^{\gamma\mu\nu}u_{ji}^\mu u_{ki}^\nu, \tag{B.43}$$

i.e., the cross product of position of j with position of k, relative to i. Note that the vectors m^{γ}_{ijk} are the same upon a cyclic permutation of the indices, since they refer to the same direction and area. The cotangent of an angle can be rewritten, using the inner and cross products, as

$$\cot\left(\theta_{ijk}\right) = \frac{u^{\gamma}_{kj} u^{\gamma}_{ij}}{\sqrt{m^{\mu}_{jki} m^{\mu}_{jki}}} = \frac{\|\boldsymbol{u}_{kj}\| \, \|\boldsymbol{u}_{ij}\| \cos\left(\theta_{ijk}\right)}{\|\boldsymbol{u}_{kj}\| \, \|\boldsymbol{u}_{ij}\| \sin\left(\theta_{ijk}\right)} \tag{B.44}$$

Recall the mixed Voronoi area of a triangle is

$$A^{\text{mixed}}_{ijk} = \begin{cases} \dfrac{\sqrt{m^{\gamma}_{ijk} m^{\gamma}_{ijk}}}{4}, & u^{\mu}_{ji} u^{\mu}_{ki} \leq 0, \\ \dfrac{\sqrt{m^{\gamma}_{ijk} m^{\gamma}_{ijk}}}{8}, & u^{\mu}_{kj} u^{\mu}_{ij} u^{\nu}_{ik} u^{\nu}_{jk} \leq 0, \\ A^{\text{Voronoi}}_{ijk}, & \text{otherwise}, \end{cases} \tag{B.45}$$

where the three expressions correspond to the area of the mixed region assigned to an obtuse angle, an acute angle of an obtuse triangle, and any angle of an acute triangle, respectively. The Voronoi region area in the third expression is,

$$A^{\text{Voronoi}}_{ijk} = \frac{u^{\mu}_{ki} u^{\mu}_{ki} \cot\left(\theta_{ijk}\right) + u^{\mu}_{ji} u^{\mu}_{ji} \cot\left(\theta_{jki}\right)}{8} \tag{B.46}$$

For each triangulated vertex, we then sum over all triangles around it,

$$A^{\text{mixed}}_{i} = \sum_{j \in \mathcal{T}_i} A^{\text{mixed}}_{ijj+1}. \tag{B.47}$$

We will make extensive use of the area of the whole triangle ijk, A_{ijk}. We have

$$A_{kij} = A_{jki} = A_{ijk} = \frac{1}{2}\sqrt{m^{\gamma}_{ijk} m^{\gamma}_{ijk}}, \tag{B.48}$$

since the area is the same regardless where at which vertex we center the cross product. The gradient of the area is,

$$\begin{aligned} \frac{\partial A_{ijk}}{\partial x^{\beta}_{l}} = \frac{1}{2} \frac{m^{\gamma}_{ijk}}{2A_{ijk}} \frac{\partial m^{\gamma}_{ijk}}{\partial x^{\beta}_{l}} &= \frac{1}{2} \frac{m^{\gamma}_{ijk}}{2A_{ijk}} \varepsilon^{\gamma\mu\beta} \left(\left(\delta_{kl} - \delta_{il}\right) u^{\mu}_{ji} - \left(\delta_{jl} - \delta_{il}\right) u^{\mu}_{ki} \right) \\ &= \frac{1}{2} K^{\beta\mu}_{ijk} \left(\delta_{il} u^{\mu}_{kj} + \delta_{jl} u^{\mu}_{ik} + \delta_{kl} u^{\mu}_{ji} \right), \end{aligned} \tag{B.49}$$

where in the last line we used the definition of the cross product matrix K. Note that $K^{\beta\mu}_{ijk}$ has the same symmetry properties as m^{γ}_{ijk} does. In the above expression we can combine any cyclic permutation in the indexation of K with any other cyclic permutation of the indices of A to suit a particular situation. With this, the obtuse triangle case is essentially done. Furthermore, the gradient of the cotangent is

$$\frac{\partial \cot\left(\theta_{ijk}\right)}{\partial x_l^\beta} = \frac{1}{2A_{ijk}}\left(\left(\delta_{kl} - \delta_{jl}\right) u_{ij}^\beta + \left(\delta_{il} - \delta_{jl}\right) u_{kj}^\beta - 2\cot\left(\theta_{ijk}\right)\frac{\partial A_{ijk}}{\partial x_l^\beta}\right) \tag{B.50}$$

We can now differentiate the Voronoi region area,

$$\begin{aligned}\frac{\partial A_{ijk}^{\text{Voronoi}}}{\partial x_l^\beta} = \frac{1}{8}\Bigg[& 2u_{ki}^\beta \cot\left(\theta_{ijk}\right)\left(\delta_{kl} - \delta_{il}\right) + 2u_{ji}^\beta \cot\left(\theta_{jki}\right)\left(\delta_{jl} - \delta_{il}\right) \\ + \frac{1}{2A_{ijk}}\Bigg[& u_{ki}^\mu u_{ki}^\mu \left[u_{ij}^\beta\left(\delta_{kl} - \delta_{jl}\right) + u_{kj}^\beta\left(\delta_{il} - \delta_{jl}\right)\right] + u_{ji}^\mu u_{ji}^\mu \left[u_{jk}^\beta\left(\delta_{il} - \delta_{kl}\right) + u_{ik}^\beta\left(\delta_{jl} - \delta_{kl}\right)\right] \\ & - 2\frac{\partial A_{ijk}}{\partial x_l^\beta}\left[u_{ki}^\mu u_{ki}^\mu \cot\left(\theta_{ijk}\right) + u_{ji}^\beta u_{ji}^\beta \cot\left(\theta_{jki}\right)\right]\Bigg]\Bigg].\end{aligned} \tag{B.51}$$

We note the last term contains the Voronoi region area once again. We unfold the first two contangents an rearrange terms, yielding

$$\begin{aligned}\frac{\partial A_{ijk}^{\text{Voronoi}}}{\partial x_l^\beta} = \frac{1}{16A_{ijk}}\Bigg[& \delta_{il}\left(2u_{kj}^\mu\left(u_{ik}^\mu u_{ji}^\beta - u_{ij}^\mu u_{ki}^\beta\right) + u_{kj}^\beta\left(u_{ki}^\mu u_{ki}^\mu - u_{ji}^\mu u_{ji}^\mu\right)\right) \\ & + \delta_{jl}\left(2u_{ji}^\beta u_{ik}^\mu\left(u_{jk}^\mu + u_{ik}^\mu\right) + u_{ik}^\beta\left(u_{ki}^\mu u_{ki}^\mu + u_{ji}^\mu u_{ji}^\mu\right)\right) \\ & + \delta_{kl}\left(2u_{ki}^\beta u_{ij}^\mu\left(u_{kj}^\mu + u_{ij}^\mu\right) + u_{ij}^\beta\left(u_{ki}^\mu u_{ki}^\mu + u_{ji}^\mu u_{ji}^\mu\right)\right)\Bigg] \\ & - \frac{A_{ijk}^{\text{Voronoi}}}{2A_{ijk}} K_{ijk}^{\beta\mu}\left(\delta_{il} u_{kj}^\mu + \delta_{jl} u_{ik}^\mu + \delta_{kl} u_{ji}^\mu\right),\end{aligned} \tag{B.52}$$

where we made liberal use of $u_{jk}^\alpha = u_{ji}^\alpha + u_{ik}^\alpha$ and $u_{ji}^\alpha = -u_{ij}^\alpha$. The total mixed region area gradient for vertex i can be done by summing over the adjacent triangles. Since the expression for the area of each triangle may vary, we cannot assume a general form for the summation.

Mixed Voronoi region intersection point

As stated in the main text, it is useful to determine exactly where the perpendicular bisectors of a triangle intersect, so that we can give shape to the mixed region. This will be required to differentiate the vertex normals. The intersection coordinates, $x^{*\gamma}$, depend on if the triangle is obtuse or not, and is

$$x^{*\gamma}_{ijk} = \begin{cases} \dfrac{x^\gamma_j + x^\gamma_k}{2}, & u^\mu_{ji} u^\mu_{ki} \leq 0, \\ \dfrac{x^\gamma_k + x^\gamma_i}{2}, & u^\mu_{kj} u^\mu_{ij} \leq 0, \\ \dfrac{x^\gamma_i + x^\gamma_j}{2}, & u^\nu_{ik} u^\nu_{jk} \leq 0, \\ x^{\text{circ}\gamma}_{ijk}, & \text{otherwise,} \end{cases} \tag{B.53}$$

where $x^{\text{circ}\gamma}_{ijk}$ is the circumcenter of the triangle ijk given by,

$$x^{\text{circ}\gamma}_{ijk} = x^\gamma_i + \frac{K^{\gamma\mu}_{ijk}}{2A_{ijk}} \left(u^\mu_{ji} u^\lambda_{ki} u^\lambda_{ki} - u^\mu_{ki} u^\lambda_{ji} u^\lambda_{ji} \right). \tag{B.54}$$

This form emphasises the position of vertex i. We can get a more symmetric form for it by asserting that the intersection point would be the same regardless of which vertex we use for computing the expression above. Therefore,

$$x^{\text{circ}\gamma}_{ijk} = \frac{1}{3} \left(x^{\text{circ}\gamma}{}_{ijk} + x^{\text{circ}\gamma}{}_{jki} + x^{\text{circ}\gamma}{}_{kij} \right), \tag{B.55}$$

leading to

$$x^{\text{circ}\gamma}_{ijk} = \frac{x^\gamma_i + x^\gamma_j + x^\gamma_k}{3} + \frac{K^{\gamma\mu}_{ijk}}{6A_{ijk}} \left(u^\mu_{ki} u^\lambda_{ki} u^\lambda_{ki} + u^\mu_{ij} u^\lambda_{ij} u^\lambda_{ij} + u^\mu_{jk} u^\lambda_{jk} u^\lambda_{jk} \right), \tag{B.56}$$

where we identify the centroid of the triangle,

$$C_{ijk}{}^\gamma = \frac{x^\gamma_i + x^\gamma_j + x^\gamma_k}{3}, \tag{B.57}$$

and we will define the vector

$$B^\mu_{ijk} = u^\mu_{ki} u^\lambda_{ki} u^\lambda_{ki} + u^\mu_{ij} u^\lambda_{ij} u^\lambda_{ij} + u^\mu_{jk} u^\lambda_{jk} u^\lambda_{jk}, \tag{B.58}$$

which will be helpful later and is symmetric upon cyclic permutation of vertices.

The obtuse case is immediate and, hence, we will only worry about differentiating $x^{\text{circ}\gamma}{}_{ijk}$. Recall

$$K^{\gamma\mu}_{ijk} = \frac{\varepsilon^{\gamma\nu\mu} m^\nu_{ijk}}{2A_{ijk}}, \qquad A_{ijk} = \frac{1}{2}\sqrt{m^\gamma_{ijk} m^\gamma_{ijk}}, \qquad m^\nu_{ijk} = \varepsilon^{\nu\xi\eta} u^\xi_{ji} u^\eta_{ki}. \tag{B.59}$$

These expressions were heavily used in the last section. We just need the gradient of $K^{\gamma\mu}_{ijk}$.

To summarize, because

$$\frac{\partial m^{\gamma}_{ijk}}{\partial x^{\beta}_{l}} = \varepsilon^{\gamma\beta\mu}\left(\delta_{il}u^{\mu}_{jk} + \delta_{jl}u^{\mu}_{ki} + \delta_{kl}u^{\mu}_{ij}\right), \tag{B.60}$$

we have

$$\begin{aligned}\frac{\partial K^{\mu\nu}_{ijk}}{\partial x^{\beta}_{l}} &= \frac{\varepsilon^{\mu\gamma\nu}}{2A_{ijk}}\left(\frac{\partial m^{\gamma}_{ijk}}{\partial x^{\beta}_{l}} - \frac{m^{\gamma}_{ijk}}{A_{ijk}}\frac{\partial A_{ijk}}{\partial x^{\beta}_{l}}\right)\\ &= \frac{1}{2A_{ijk}}\left(\delta^{\beta\nu}\delta^{\mu\eta} - \delta^{\beta\mu}\delta^{\nu\eta} - K^{\mu\nu}_{ijk}K^{\beta\eta}_{ijk}\right)\left(\delta_{il}u^{\eta}_{jk} + \delta_{jl}u^{\eta}_{ki} + \delta_{kl}u^{\eta}_{ij}\right). \end{aligned} \tag{B.61}$$

We can write

$$\begin{aligned}\frac{\partial x^{\mathrm{circ}\gamma}_{ijk}}{\partial x^{\beta}_{l}} &= \delta^{\beta\gamma}\frac{\delta_{il}+\delta_{jl}+\delta_{kl}}{3} + \frac{1}{6A_{ijk}}\frac{\partial K^{\gamma\mu}_{ijk}}{\partial x^{\beta}_{l}}B^{\mu}_{ijk} - \frac{x^{\mathrm{circ}\gamma}_{ijk} - C_{ijk}{}^{\gamma}}{A_{ijk}}\frac{\partial A_{ijk}}{\partial x^{\beta}_{l}}\\ &\quad + \frac{K^{\gamma\mu}_{ijk}}{6A_{ijk}}\Bigg[\delta_{il}\left(2u^{\beta}_{ij}u^{\mu}_{ij} - 2u^{\beta}_{ki}u^{\mu}_{ki} + \delta^{\beta\mu}\left(u^{\lambda}_{ij}u^{\lambda}_{ij} - u^{\lambda}_{ki}u^{\lambda}_{ki}\right)\right)\\ &\quad + \delta_{jl}\left(2u^{\beta}_{jk}u^{\mu}_{jk} - 2u^{\beta}_{ij}u^{\mu}_{ij} + \delta^{\beta\mu}\left(u^{\lambda}_{jk}u^{\lambda}_{jk} - u^{\lambda}_{ij}u^{\lambda}_{ij}\right)\right)\\ &\quad + \delta_{kl}\left(2u^{\beta}_{ki}u^{\mu}_{ki} - 2u^{\beta}_{jk}u^{\mu}_{jk} + \delta^{\beta\mu}\left(u^{\lambda}_{ki}u^{\lambda}_{ki} - u^{\lambda}_{jk}u^{\lambda}_{jk}\right)\right)\Bigg]. \end{aligned} \tag{B.62}$$

The second term contains a diagonal term and one with the derivative of area. We distribute $K^{\gamma\mu}_{ijk}$ in the last term. We group what we can, leading to

$$\begin{aligned}\frac{\partial x^{\mathrm{circ}\gamma}_{ijk}}{\partial x^{\beta}_{l}} &= \delta^{\beta\gamma}\left(\frac{\delta_{il}+\delta_{jl}+\delta_{kl}}{3} - \frac{B^{\mu}_{ijk}}{12A^{2}_{ijk}}\left(\delta_{il}u^{\mu}_{jk} + \delta_{jl}u^{\mu}_{ki} + \delta_{kl}u^{\mu}_{ij}\right)\right)\\ &\quad + \left(\frac{B^{\beta}_{ijk}\delta^{\gamma\eta}}{12A^{2}_{ijk}} - \frac{x^{\mathrm{circ}\gamma}_{ijk} - C_{ijk}{}^{\gamma}}{A_{ijk}}K^{\beta\eta}_{ijk}\right)\left(\delta_{il}u^{\eta}_{jk} + \delta_{jl}u^{\eta}_{ki} + \delta_{kl}u^{\eta}_{ij}\right)\\ &\quad + \frac{1}{6A_{ijk}}\Bigg[\delta_{il}\left(2K^{\gamma\mu}_{ijk}\left(u^{\beta}_{ij}u^{\mu}_{ij} - u^{\beta}_{ki}u^{\mu}_{ki}\right) + K^{\gamma\beta}_{ijk}\left(u^{\lambda}_{ij}u^{\lambda}_{ij} - u^{\lambda}_{ki}u^{\lambda}_{ki}\right)\right)\\ &\quad + \delta_{jl}\left(2K^{\gamma\mu}_{ijk}\left(u^{\beta}_{jk}u^{\mu}_{jk} - u^{\beta}_{ij}u^{\mu}_{ij}\right) + K^{\gamma\beta}_{ijk}\left(u^{\lambda}_{jk}u^{\lambda}_{jk} - u^{\lambda}_{ij}u^{\lambda}_{ij}\right)\right)\\ &\quad + \delta_{kl}\left(2K^{\gamma\mu}_{ijk}\left(u^{\beta}_{ki}u^{\mu}_{ki} - u^{\beta}_{jk}u^{\mu}_{jk}\right) + K^{\gamma\beta}_{ijk}\left(u^{\lambda}_{ki}u^{\lambda}_{ki} - u^{\lambda}_{jk}u^{\lambda}_{jk}\right)\right)\Bigg]. \end{aligned} \tag{B.63}$$

Vertex normal unit vector

As described in Chapter 2, we now use the path around the mixed region of a vertex with the same equation used for each face. We need to keep in mind that for each neighbouring triangulated vertex, we can potentially have one more point to worry about, the circumcenter. With this in mind, we write the expression,

$$M_i^\gamma = \sum_{j \in \mathcal{T}_i} \varepsilon^{\gamma\mu\nu} \left(\frac{x_i^\mu + x_j^\mu}{2} x^{*\nu}_{ijj+1} + x^{*\mu}_{ijj+1} \frac{x_i^\nu + x_{j+1}^\nu}{2} \right) = \frac{1}{2} \sum_{j \in \mathcal{T}_i} \varepsilon^{\gamma\mu\nu} x^{*\mu}_{ijj+1} u^\nu_{j+1j}. \tag{B.64}$$

Note that if the triangle is obtuse at j or $j+1$, one of the term disappears since the positions merge. Since the expression ultimately depends on the case at hand, we are limited on how much we can simplify.

The gradient is,

$$\frac{\partial M_i^\gamma}{\partial x_l^\beta} = \frac{1}{2} \sum_{j \in \mathcal{T}_i} \varepsilon^{\gamma\mu\nu} \frac{\partial x^{*\mu}_{ijj+1}}{\partial x_l^\beta} u^\nu_{j+1j} + \frac{\varepsilon^{\gamma\beta\mu}}{2} \left(x^{*\mu}_{ill+1} - x^{*\mu}_{il-1l} \right). \tag{B.65}$$

What we need, however, is the normalised quantity

$$w_i^\gamma = \frac{M_i^\gamma}{\sqrt{M_i^\lambda M_i^\lambda}}. \tag{B.66}$$

For this we just have to apply the derivative of a normalised quantity defined at the beginning of this appendix,

$$\frac{\partial w_i^\gamma}{\partial x_l^\beta} = \frac{1}{\sqrt{M_i^\nu M_i^\nu}} \left(\frac{\partial M_i^\gamma}{\partial x_l^\beta} - w_i^\gamma w_i^\mu \frac{\partial M_i^\mu}{\partial x_l^\beta} \right). \tag{B.67}$$

Tissue curvature

In a way, the last three sections are building up to be able to differentiate curvature. We start by writing down Gaussian curvature,

$$K\left(\boldsymbol{x}_i\right) = K_i = \frac{2\pi - \sum_{j \in \mathcal{T}_i} \theta_{j+1ij}}{A_i^{\text{mixed}}}. \tag{B.68}$$

We note that we can write

$$\theta_{j+1ij} = \operatorname{arccot}\left(\cot\left(\theta_{j+1ij}\right)\right), \tag{B.69}$$

where the cotangent was extensively used in computing the Voronoi region area and its gradient. Using the chain rule, we have

$$\begin{aligned}\frac{\partial \theta_{j+1ij}}{\partial x_l^{\beta}} &= -\frac{1}{1+\cot^2\left(\theta_{j+1ij}\right)}\frac{\partial \cot\left(\theta_{j+1ij}\right)}{\partial x_l^{\beta}} \\ &= -\frac{1}{1+\cot^2\left(\theta_{j+1ij}\right)}\frac{1}{2A_{ijj+1}}\left(\left(\delta_{jl}-\delta_{il}\right)u_{j+1i}^{\beta}+\left(\delta_{j+1l}-\delta_{il}\right)u_{ji}^{\beta}-2\cot\left(\theta_{j+1ij}\right)\frac{\partial A_{ijj+1}}{\partial x_l^{\beta}}\right).\end{aligned} \tag{B.70}$$

Therefore,

$$\begin{aligned}\frac{\partial K_i}{\partial x_l^{\beta}} = \frac{1}{A_i^{\text{mixed}}}\sum_{j\in\mathcal{T}_i}\frac{1}{1+\cot^2\left(\theta_{j+1ij}\right)}\frac{1}{2A_{ijj+1}}&\left(\delta_{jl}u_{j+1i}^{\beta}+\delta_{j+1l}u_{ji}^{\beta}-\delta_{il}\left(u_{j+1i}^{\beta}+u_{ji}^{\beta}\right)\right. \\ &\left.+\cot\left(\theta_{j+1ij}\right)K_{ijj+1}^{\beta\eta}\left(\delta_{il}u_{jj+1}^{\eta}+\delta_{jl}u_{j+1i}^{\eta}+\delta_{j+1l}u_{ij}^{\eta}\right)\right)-\frac{K_i}{A_i^{\text{mixed}}}\frac{\partial A_i^{\text{mixed}}}{\partial x_l^{\beta}}.\end{aligned} \tag{B.71}$$

If one assumes l to be either i or $\in \mathcal{T}_i$, we can separate between the term in δ_{il} and $1-\delta_{il}$ for the terms relating to δ_{jl} and δ_{j+1l}. This procedure results in

$$\begin{aligned}\frac{\partial K_i}{\partial x_l^{\beta}} =& \frac{\delta_{il}}{A_i^{\text{mixed}}}\sum_{j\in\mathcal{T}_i}\frac{\cot\left(\theta_{ijj+1}\right)-u_{j+1i}^{\beta}-u_{ji}^{\beta}}{2A_{ijj+1}\left(1+\cot^2\left(\theta_{j+1ij}\right)\right)}-\frac{K_i}{A_i^{\text{mixed}}}\frac{\partial A_i^{\text{mixed}}}{\partial x_l^{\beta}} \\ &+\frac{1-\delta_{il}}{A_i^{\text{mixed}}}\left(\frac{u_{l+1i}^{\beta}+\cot\left(\theta_{l+1il}\right)K_{ill+1}^{\beta\mu}u_{l+1i}^{\mu}}{2A_{ill+1}\left(1+\cot^2\left(\theta_{l+1il}\right)\right)}+\frac{u_{l-1i}^{\beta}+\cot\left(\theta_{lil-1}\right)K_{il-1l}^{\beta\mu}u_{il-1}^{\mu}}{2A_{il-1l}\left(1+\cot^2\left(\theta_{lil-1}\right)\right)}\right)\end{aligned} \tag{B.72}$$

As for mean curvature,

$$H\left(\boldsymbol{x}_i\right)=H_i=\frac{1}{2}\Delta_S x_i^{\mu}w_i^{\mu}, \tag{B.73}$$

where

$$\Delta_S x_i^{\mu} \approx \frac{\sum_{j\in\mathcal{V}_i}\left(\cot\left(\theta_{jj+1i}\right)+\cot\left(\theta_{ij-1j}\right)\right)\left(x_i^{\mu}-x_j^{\mu}\right)}{A_i^{\text{mixed}}}. \tag{B.74}$$

We can separate terms just as above and substitute all quantities we need, resulting in

$$
\begin{aligned}
\frac{\partial \Delta_S x_i^\mu}{\partial x_l^\beta} = \frac{\delta^{\beta\mu}}{A_i^{\text{mixed}}} &\left(\delta_{il} \sum_{j \in \mathcal{T}_i} \left[\cot\left(\theta_{ij-1j}\right) + \cot\left(\theta_{jj+1i}\right) \right] - \left[1 - \delta_{il}\right] \left[\cot\left(\theta_{il-1l}\right) + \cot\left(\theta_{il-1l}\right) \right] \right) \\
+ \frac{\delta_{il}}{A_i^{\text{mixed}}} \sum_{j \in \mathcal{T}_i} u_{ij}^\mu &\left[\frac{u_{jj+1}^\beta - \cot\left(\theta_{jj+1i}\right) K_{ijj+1}^{\beta\nu} u_{j+1j}^\nu}{2A_{ijj+1}} + \frac{u_{jj-1}^\beta - \cot\left(\theta_{ij-1j}\right) K_{ij-1j}^{\beta\nu} u_{jj-1}^\nu}{2A_{ij-1j}} \right] \\
+ \frac{1 - \delta_{il}}{A_i^{\text{mixed}}} &\left[u_{il}^\mu \left(\frac{u_{il+1}^\beta - \cot\left(\theta_{ll+1li}\right) K_{il-1l}^{\beta\nu} u_{il+1}^\nu}{2A_{ill+1}} + \frac{u_{il-1}^\beta - \cot\left(\theta_{il-1l}\right) K_{il-1l}^{\beta\nu} u_{l-1i}^\nu}{2A_{il-1l}} \right) \right. \\
&\left. - u_{il-1}^\mu \frac{u_{l-1l}^\beta + u_{il}^\beta + \cot\left(\theta_{l-1li}\right) K_{il-1l}^{\beta\nu} u_{l-1i}^\nu}{2A_{il-1l}} - u_{il+1}^\mu \frac{u_{il}^\beta + u_{l+1l}^\beta + \cot\left(\theta_{ill+1}\right) K_{ill+1}^{\beta\nu} u_{il+1}^\nu}{2A_{ill+1}} \right] \\
&- \frac{\Delta_S x_i^\mu}{A_i^{\text{mixed}}} \frac{\partial A_i^{\text{mixed}}}{\partial x_l^\beta}. \qquad \text{(B.75)}
\end{aligned}
$$

Where we would only have

$$
\frac{\partial H_i}{\partial x_l^\beta} = \frac{1}{2} w_i^\mu \frac{\partial \Delta_S x_i^\mu}{\partial x_l^\beta} + \frac{1}{2} \Delta_S x_i^\mu \frac{\partial w_i^\mu}{\partial x_l^\beta} \qquad \text{(B.76)}
$$

left to compute.

B.2 Projected coordinate system gradient transformation

This section will focus on figuring out the gradient of a function of projected coordinates in the original reference frame. Recall we performed two transformations consecutively. The first is a rotation to the reference frame where the normal unit vector to a face, w_α^μ, defines the $\hat{\boldsymbol{e}}_{z'}$ direction. The second was a translation to the projected centroid, $C_\alpha^{\text{proj}\mu'}$. In short, we intend to compute for each face,

$$
\frac{\partial f}{\partial x_i^\mu} = \sum_{j \in \mathcal{V}_\alpha} \frac{\partial x_j^{\text{proj}\nu''}}{\partial x_i^\mu} \frac{\partial f}{\partial x_j^{\text{proj}\nu''}} = \sum_{j \in \mathcal{V}_\alpha} \frac{\partial x_j^{\text{proj}\nu''}}{\partial x_i^\mu} \sum_{k \in \mathcal{V}_\alpha} \frac{\partial x_k^{\xi'}}{\partial x_j^{\text{proj}\nu''}} \frac{\partial f}{\partial x_k^{\xi'}}. \qquad \text{(B.77)}
$$

We will start by differentiating

$$x_i^{\mu'} = x_i^{\mathrm{proj}\,\mu''} - C_\alpha^{\mathrm{proj}\,\mu''}, \tag{B.78}$$

$$C_\alpha^{\mathrm{proj}\,x''} = \frac{1}{6A_\alpha^{\mathrm{proj}}} \sum_{i\in\mathcal{V}_\alpha} \left(x_i^{\mathrm{proj}} y_{i+1}^{\mathrm{proj}} - x_{i+1}^{\mathrm{proj}} y_i^{\mathrm{proj}}\right) \left(x_i^{\mathrm{proj}} + x_{i+1}^{\mathrm{proj}}\right), \tag{B.79}$$

$$C_\alpha^{\mathrm{proj}\,y''} = \frac{1}{6A_\alpha^{\mathrm{proj}}} \sum_{i\in\mathcal{V}_\alpha} \left(x_i^{\mathrm{proj}} y_{i+1}^{\mathrm{proj}} - x_{i+1}^{\mathrm{proj}} y_i^{\mathrm{proj}}\right) \left(y_i^{\mathrm{proj}} + y_{i+1}^{\mathrm{proj}}\right), \tag{B.80}$$

$$A_\alpha^{\mathrm{proj}} = \frac{1}{2} \sum_{i\in\mathcal{V}_\alpha} \left(x_i^{\mathrm{proj}} y_{i+1}^{\mathrm{proj}} - x_{i+1}^{\mathrm{proj}} y_i^{\mathrm{proj}}\right). \tag{B.81}$$

Starting with,

$$\frac{\partial A_\alpha^{\mathrm{proj}}}{\partial x_j^{\mathrm{proj}}} = \frac{1}{2} \sum_{i\in\mathcal{V}_\alpha} \left(\delta_{ij} y_{i+1}^{\mathrm{proj}} - \delta_{i+1j} y_{i+1}^{\mathrm{proj}}\right) = \frac{y_{j+1}^{\mathrm{proj}} - y_{j-1}^{\mathrm{proj}}}{2}, \quad \frac{\partial A_\alpha^{\mathrm{proj}}}{\partial y_j^{\mathrm{proj}}} = -\frac{x_{j+1}^{\mathrm{proj}} - x_{j-1}^{\mathrm{proj}}}{2}, \tag{B.82}$$

we then proceed to differentiating the centroid,

$$\frac{\partial C_\alpha^{\mathrm{proj}\,x''}}{\partial x_j^{\mathrm{proj}}} = \frac{y_{j+1}^{\mathrm{proj}} - y_j^{\mathrm{proj}}}{2A^{\mathrm{proj}}} \left(\frac{2x_j^{\mathrm{proj}} + x_{j+1}^{\mathrm{proj}}}{3} - C_\alpha^{\mathrm{proj}\,x''}\right) + \frac{y_j^{\mathrm{proj}} - y_{j-1}^{\mathrm{proj}}}{2A^{\mathrm{proj}}} \left(\frac{2x_j^{\mathrm{proj}} + x_{j-1}^{\mathrm{proj}}}{3} - C_\alpha^{\mathrm{proj}\,x''}\right), \tag{B.83}$$

$$\frac{\partial C_\alpha^{\mathrm{proj}\,x''}}{\partial y_j^{\mathrm{proj}}} = \frac{x_j^{\mathrm{proj}} - x_{j+1}^{\mathrm{proj}}}{2A_\alpha^{\mathrm{proj}}} \left(\frac{2x_j^{\mathrm{proj}} + x_{j+1}^{\mathrm{proj}}}{3} - C_\alpha^{\mathrm{proj}\,x''}\right) + \frac{x_{j-1}^{\mathrm{proj}} - x_j^{\mathrm{proj}}}{2A_\alpha^{\mathrm{proj}}} \left(\frac{2x_j^{\mathrm{proj}} + x_{j-1}^{\mathrm{proj}}}{3} - C_\alpha^{\mathrm{proj}\,x''}\right), \tag{B.84}$$

$$\frac{\partial C_\alpha^{\mathrm{proj}\,y''}}{\partial x_j^{\mathrm{proj}}} = \frac{y_{j+1}^{\mathrm{proj}} - y_j^{\mathrm{proj}}}{2A^{\mathrm{proj}}} \left(\frac{2y_j^{\mathrm{proj}} + y_{j+1}^{\mathrm{proj}}}{3} - C_\alpha^{\mathrm{proj}\,y''}\right) + \frac{y_j^{\mathrm{proj}} - y_{j-1}^{\mathrm{proj}}}{2A^{\mathrm{proj}}} \left(\frac{2y_j^{\mathrm{proj}} + y_{j-1}^{\mathrm{proj}}}{3} - C_\alpha^{\mathrm{proj}\,y''}\right), \tag{B.85}$$

$$\frac{\partial C_\alpha^{\mathrm{proj}\,y''}}{\partial y_j^{\mathrm{proj}}} = \frac{x_j^{\mathrm{proj}} - x_{j+1}^{\mathrm{proj}}}{2A^{\mathrm{proj}}} \left(\frac{2y_j^{\mathrm{proj}} + y_{j+1}^{\mathrm{proj}}}{3} - C_\alpha^{\mathrm{proj}\,y''}\right) + \frac{x_{j-1}^{\mathrm{proj}} - x_j^{\mathrm{proj}}}{2A^{\mathrm{proj}}} \left(\frac{2y_j^{\mathrm{proj}} + y_{j-1}^{\mathrm{proj}}}{3} - C_\alpha^{\mathrm{proj}\,y''}\right). \tag{B.86}$$

Notice that these expression can be written in terms of the local projected coordinate system. Thus they can be written as

$$\frac{\partial A_\alpha^{\mathrm{proj}}}{\partial x_j^{\mathrm{proj}}} = \frac{y'_{j+1} - y'_{j-1}}{2}, \qquad \frac{\partial A_\alpha^{\mathrm{proj}}}{\partial y_j^{\mathrm{proj}}} = -\frac{x'_{j+1} - x'_{j-1}}{2}, \tag{B.87}$$

and

$$\frac{\partial C_\alpha^{\mathrm{proj}x''}}{\partial x_j^{\mathrm{proj}}} = \frac{y'_{j+1} - y'_j}{2A^{\mathrm{proj}}}\frac{2x'_j + x'_{j+1}}{3} + \frac{y'_j - y'_{j-1}}{2A^{\mathrm{proj}}}\frac{2x'_j + x'_{j-1}}{3}, \tag{B.88}$$

$$\frac{\partial C_\alpha^{\mathrm{proj}x''}}{\partial y_j^{\mathrm{proj}}} = \frac{x'_j - x'_{j+1}}{2A^{\mathrm{proj}}}\frac{2x'_j + x'_{j+1}}{3} + \frac{x'_{j-1} - x'_j}{2A^{\mathrm{proj}}}\frac{2x'_j + x'_{j-1}}{3}, \tag{B.89}$$

$$\frac{\partial C_\alpha^{\mathrm{proj}y''}}{\partial x_j^{\mathrm{proj}}} = \frac{y'_{j+1} - y'_j}{2A^{\mathrm{proj}}}\frac{2y'_j + y'_{j+1}}{3} + \frac{y'_j - y'_{j-1}}{2A^{\mathrm{proj}}}\frac{2y'_j + y'_{j-1}}{3}, \tag{B.90}$$

$$\frac{\partial C_\alpha^{\mathrm{proj}y''}}{\partial x_j^{\mathrm{proj}}} = \frac{x'_j - x'_{j+1}}{2A^{\mathrm{proj}}}\frac{2y'_j + y'_{j+1}}{3} + \frac{x'_{j-1} - x'_j}{2A^{\mathrm{proj}}}\frac{2y'_j + y'_{j-1}}{3}. \tag{B.91}$$

All that is left is the transformation itself,

$$\frac{\partial x_i^{\mu'}}{\partial x_j^{\mathrm{proj}\nu''}} = \delta_{ij}\delta^{\mu'\nu''} - \frac{\partial C_\alpha^{\mathrm{proj}\mu''}}{\partial x_j^{\mathrm{proj}\nu''}}, \tag{B.92}$$

hence,

$$\frac{\partial f}{\partial x_i^\mu} = \sum_{j\in\mathcal{V}_\alpha}\frac{\partial x_j^{\mathrm{proj}\nu''}}{\partial x_i^\mu}\left[\frac{\partial f}{\partial x_j^{\nu'}} - \frac{\partial C_\alpha^{\mathrm{proj}\xi''}}{\partial x_j^{\mathrm{proj}\nu''}}\sum_{k\in\mathcal{V}_\alpha}\frac{\partial f}{\partial x_k^{\xi'}}\right]. \tag{B.93}$$

Now we consider the rotation from the original reference frame to the one where the fitted plane to a particular face lies on the $x''\mathcal{O}y''$ plane. We have

$$x_i^{\mathrm{proj}} = u_\alpha^\mu x_i^\mu, \qquad y_i^{\mathrm{proj}} = v_\alpha^\mu x_i^\mu, \tag{B.94}$$

$$u_\alpha^\mu = \frac{u^{*\mu}_\alpha}{\sqrt{u^{*\lambda}_\alpha u^{*\lambda}_\alpha}}, \qquad v_\alpha^\mu = \varepsilon^{\mu\xi\eta}w_\alpha^\xi u_\alpha^\eta, \tag{B.95}$$

$$u^{*\mu}_\alpha = \delta^{\mu\sigma} - w_\alpha^\sigma w_\alpha^\mu, \tag{B.96}$$

where σ is the index of the chosen basis unit vector used to start the Gram-Schimdt orthonormalisation (usually $\sigma = 1$). Note that we already explored the expresison and gradient of the face normal unit vector, w_α^μ. It is relatively straightforward to obtain

$$\frac{\partial u^{*\mu}_\alpha}{\partial x_j^\beta} = -w_\alpha^\sigma\frac{\partial w_\alpha^\mu}{\partial x_j^\beta} - \frac{\partial w_\alpha^\sigma}{\partial x_j^\beta}w_\alpha^\mu, \tag{B.97}$$

$$\frac{\partial u_\alpha^\mu}{\partial x_j^\beta} = \frac{1}{\sqrt{u^{*\lambda}_\alpha u^{*\lambda}_\alpha}}\left(-w_\alpha^\sigma\frac{\partial w_\alpha^\mu}{\partial x_j^\beta} - \frac{\partial w_\alpha^\sigma}{\partial x_j^\beta}w_\alpha^\mu + u_\alpha^\mu u_\alpha^\nu w_\alpha^\sigma\frac{\partial w_\alpha^\nu}{\partial x_j^\beta}\right), \tag{B.98}$$

$$\frac{\partial v_\alpha^\mu}{\partial x_j^\beta} = \varepsilon^{\mu\xi\eta}\left(\frac{\partial w_\alpha^\xi}{\partial x_j^\beta}u_\alpha^\eta - \frac{w_\alpha^\xi w_\alpha^\sigma}{\sqrt{u^{*\lambda}_\alpha u^{*\lambda}_\alpha}}\frac{\partial w_\alpha^\eta}{\partial x_j^\beta}\right) + \frac{w_\alpha^\sigma v_\alpha^\mu u_\alpha^\nu}{\sqrt{u^{*\lambda}_\alpha u^{*\lambda}_\alpha}}\frac{\partial w_\alpha^\nu}{\partial x_j^\beta}, \tag{B.99}$$

$$\frac{\partial x_i^{\text{proj}}}{\partial x_j^\beta} = \delta_{ij} u_\alpha^\beta + x_i^\mu \frac{\partial u_\alpha^\mu}{\partial x_j^\beta}, \qquad \frac{\partial y_i^{\text{proj}}}{\partial x_j^\beta} = \delta_{ij} v_\alpha^\beta + x_i^\mu \frac{\partial v_\alpha^\mu}{\partial x_j^\beta}, \tag{B.100}$$

where some simplifications took place because the three basis vectors are orthogonal. We can merge both expressions if we construct the matrix L such that $L_\alpha^{1\nu} = u_\alpha^\nu$ and $L_\alpha^{2\nu} = v_\alpha^\nu$ (and even $L_\alpha^{3\nu} = w_\alpha^\nu$ if one desires to store the z-coordinate after rotation, instead of projecting immediately). We can rewrite the expressions above as

$$\frac{\partial x_i^{\text{proj}\gamma''}}{\partial x_j^\beta} = \delta_{ij} L_\alpha^{\gamma\beta} + x_i^\mu \frac{\partial L_\alpha^{\gamma\mu}}{\partial x_j^\beta}. \tag{B.101}$$

Going back to the gradient transformation, using this matrix leaves us with

$$\begin{aligned}\frac{\partial f}{\partial x_i^\mu} = \sum_{j\in\mathcal{V}_\alpha} \left(\delta_{ji} L_\alpha^{\nu\mu} + x_i^\gamma \frac{\partial L_\alpha^{\nu\gamma}}{\partial x_j^\mu}\right) &\left[\frac{\partial f}{\partial x_j^{\nu'}} - \frac{\partial C_\alpha^{\text{proj}\xi''}}{\partial x_j^{\text{proj}\nu''}} \sum_{k\in\mathcal{V}_\alpha} \frac{\partial f}{\partial x_k^{\xi'}}\right] \\ &= L_\alpha^{\nu\mu} \frac{\partial f}{\partial x_i^{\mu'}} + x_i^\gamma \sum_{j\in\mathcal{V}_\alpha} \frac{\partial L_\alpha^{\nu\gamma}}{\partial x_j^\mu} \frac{\partial f}{\partial x_j^{\nu'}} \\ &- \left(L_\alpha^{\nu\mu} \frac{\partial C_\alpha^{\text{proj}\xi''}}{\partial x_i^{\text{proj}\nu''}} + x_i^\gamma \sum_{j\in\mathcal{V}_\alpha} \frac{\partial L_\alpha^{\nu\mu}}{\partial x_j^\mu} \frac{\partial C_\alpha^{\text{proj}\xi''}}{\partial x_j^{\text{proj}\nu''}}\right) \left[\sum_{k\in\mathcal{V}_\alpha} \frac{\partial f}{\partial x_k^{\xi'}}\right].\end{aligned} \tag{B.102}$$

Now, given a function of local projected coordinates of face α, we can translate the gradient of that function with respect to the local projected coordinates to the gradient with respect to the actual vertex coordinates. We also note that all terms can be computed with access only to the initial frame of reference and the projected coordinates after translation to the projected centroid. The intermediate coordinates need not be stored.

Appendix C

Conservative mechanical forces

In this chapter we will derive the gradient of all mechanical energy terms introduced in Section 3.1. This is effectively computing conservative mechanical forces (save for a minus sign) acting on the tissue. We will proceed term by term. We will make heavy use of the notation and results presented in Appendix B.

Cell-based elastic energy

Since we are setting $c_2 = 0$, the expression of elastic energy for cell α is

$$\mathcal{H}_\alpha^{\text{elastic}} = A_\alpha^{\text{proj}} h c_{1\alpha} \frac{\left\| M_\alpha - M_{0\alpha} \right\|_F^2}{\operatorname{Tr}^2\left(M_{0\alpha}\right)}. \tag{C.1}$$

We will differentiate with respect to the local projected coordinate system and transform back with Eq. B.102. Then, for each vertex, we have to sum all contributions to this term from all adjacent cells,

$$\frac{d\mathcal{H}^{\text{elastic}}}{dx_j^\beta} = \sum_{\alpha \in \mathcal{N}_j} \frac{\partial \mathcal{H}_\alpha^{\text{elastic}}}{\partial x_j^\beta}. \tag{C.2}$$

Written component-wise, the partial derivative in the local projected frame of reference is

$$\frac{\partial \mathcal{H}_\alpha^{\text{elastic}}}{\partial x_j^{\beta'}} = \frac{\mathcal{H}_\alpha^{\text{elastic}}}{A_\alpha^{\text{proj}}} \frac{\partial A_\alpha^{\text{proj}}}{\partial x_j^{\beta'}} + 2 A_\alpha^{\text{proj}} h c_{1\alpha} \frac{M_\alpha^{\mu'\nu'} - {M_0}_\alpha^{\mu'\nu'}}{\left({M_0}_\alpha^{\eta'\eta'}\right)^2} \frac{\partial M_\alpha^{\mu'\nu'}}{\partial x_j^{\beta'}}. \tag{C.3}$$

The first term can be immediately computed, since we have access to the projected area gradient through Eq. B.87.

We can rewrite the shape matrix in terms of components of local projected coordinates,

$$M_\alpha^{\mu'\nu'} = \frac{1}{24} \sum_{i \in \mathcal{V}_\alpha} \varepsilon^{3'\xi'\eta'} x_i^{\xi'} x_{i+1}^{\eta'} \left(S_i^{\mu'\nu'} + S_i^{\nu'\mu'} \right), \tag{C.4}$$

where

$$S_i^{\mu'\nu'} = x_i^{\mu'} x_i^{\nu'} + x_i^{\mu'} x_{i+1}^{\nu'} + x_{i+1}^{\mu'} x_{i+1}^{\nu'}. \tag{C.5}$$

The cross product differentiation is

$$\frac{\partial \varepsilon^{3'\mu'\nu'} x_i^{\mu'} x_{i+1}^{\nu'}}{\partial x_j^{\beta'}} = \varepsilon^{3'\beta'\nu'} \left(\delta_{ij} x_{i+1}^{\nu'} - \delta_{i+1j} x_i^{\nu'} \right). \tag{C.6}$$

The remaining factor becomes

$$\begin{aligned} \frac{\partial \left(S_i^{\mu'\nu'} + S_i^{\nu'\mu'} \right)}{\partial x_j^{\beta'}} &= \delta_{ij} \left[\delta^{\mu'\beta'} \left(2x_i^{\nu'} + x_{i+1}^{\nu'} \right) + \delta^{\nu'\beta'} \left(2x_i^{\mu'} + x_{i+1}^{\mu'} \right) \right] \\ &\quad + \delta_{i+1j} \left[\delta^{\mu'\beta'} \left(2x_{i+1}^{\nu'} + x_i^{\nu'} \right) + \delta^{\nu'\beta'} \left(2x_{i+1}^{\mu'} + x_i^{\mu'} \right) \right]. \end{aligned} \tag{C.7}$$

Using the derivative of the product, the shape matrix gradient is

$$\begin{aligned} \frac{\partial M_\alpha^{\mu'\nu'}}{\partial x_j^{\beta'}} = \frac{1}{24} \Big[& \varepsilon^{3'\xi'\eta'} x_j^{\xi'} x_{j+1}^{\eta'} \left(\delta^{\mu'\beta'} \left(2x_j^{\nu'} + x_{j+1}^{\nu'} \right) + \delta^{\nu'\beta'} \left(2x_j^{\mu'} + x_{j+1}^{\mu'} \right) \right) \\ & + \varepsilon^{3'\xi'\eta'} x_{j-1}^{\xi'} x_j^{\eta'} \left(\delta^{\mu'\beta'} \left(2x_j^{\nu'} + x_{j-1}^{\nu'} \right) + \delta^{\nu'\beta'} \left(2x_j^{\mu'} + x_{j-1}^{\mu'} \right) \right) \\ & + \varepsilon^{3'\beta'\eta'} \left(x_{j+1}^{\eta'} \left(S_j^{\mu'\nu'} + S_j^{\nu'\mu'} \right) - x_{j-1}^{\eta'} \left(S_{j-1}^{\mu'\nu'} + S_{j-1}^{\nu'\mu'} \right) \right) \Big]. \end{aligned} \tag{C.8}$$

Although the previous expression encapsulates all terms, we will unpack all six ($M_\alpha^{\mu'\nu'}$ is symmetric) relevant expressions,

$$\begin{aligned} \frac{\partial M_\alpha^{x'x'}}{\partial x_j'} = \frac{1}{12} \Big[& \left(x_j' y_{j+1}' - x_{j+1}' y_j' \right) \left(2x_j' + x_{j+1}' \right) + \left(x_{j-1}' y_j' - x_j' y_{j-1}' \right) \left(2x_j' + x_{j-1}' \right) \\ & + y_{j+1}' \left({x_j'}^2 + x_j' x_{j+1}' + {x_{j+1}'}^2 \right) - y_{j-1}' \left({x_{j-1}'}^2 + x_{j-1}' x_j' + {x_j'}^2 \right) \Big], \end{aligned} \tag{C.9}$$

$$\frac{\partial M_\alpha^{x'x'}}{\partial y_j'} = \frac{1}{12} \left[x_{j-1}' \left({x_{j-1}'}^2 + x_{j-1}' x_j' + {x_j'}^2 \right) - x_{j+1}' \left({x_j'}^2 + x_j' x_{j+1}' + {x_{j+1}'}^2 \right) \right], \tag{C.10}$$

$$\begin{aligned} \frac{\partial M_\alpha^{y'y'}}{\partial y_j'} = \frac{1}{12} \Big[& \left(x_j' y_{j+1}' - x_{j+1}' y_j' \right) \left(2y_j' + y_{j+1}' \right) + \left(x_{j-1}' y_j' - x_j' y_{j-1}' \right) \left(2y_j' + y_{j-1}' \right) \\ & - x_{j+1}' \left({y_j'}^2 + y_j' y_{j+1}' + {y_{j+1}'}^2 \right) + x_{j-1}' \left({y_{j-1}'}^2 + y_{j-1}' y_j' + {y_j'}^2 \right) \Big], \end{aligned} \tag{C.11}$$

$$\frac{\partial M_\alpha^{y'y'}}{\partial x'_j} = \frac{1}{12}\left[y'_{j+1}\left({y'_j}^2 + y'_j y'_{j+1} + {y'_{j+1}}^2\right) - y'_{j-1}\left({y'_{j-1}}^2 + y'_{j-1}y'_j + {y'_j}^2\right)\right], \tag{C.12}$$

$$\begin{aligned}\frac{\partial M_\alpha^{x'y'}}{\partial x'_j} = \frac{1}{12}&\left[y'_j\left(x'_j y'_{j+1} - x'_{j+1}y'_j + x'_{j-1}y'_j - x'_j y'_{j-1}\right)\right.\\ &\left.+y'_{j+1}\left(x'_j y'_{j+1} + x'_j y'_j + x'_{j+1}y'_{j+1}\right) - y'_{j-1}\left(x'_{j-1}y'_{j-1} + x'_j y'_j + x'_j y'_{j-1}\right)\right],\end{aligned} \tag{C.13}$$

$$\begin{aligned}\frac{\partial M_\alpha^{x'y'}}{\partial y'_j} = \frac{1}{12}&\left[x'_j\left(x'_j y'_{j+1} - x'_{j+1}y'_j + x'_{j-1}y'_j - x'_j y'_{j-1}\right)\right.\\ &\left.-x'_{j+1}\left(x'_j y'_j + x'_{j+1}y'_{j+1} + x'_{j+1}y'_j\right) + x'_{j-1}\left(x'_{j-1}y'_j + x'_{j-1}y'_{j-1} + x'_j y'_j\right)\right].\end{aligned} \tag{C.14}$$

Wall-based elastic energy

In comparison, the wall-based elastic term is much simpler and requires no transformation. Since stiffness might be cell dependent, we will derive the gradient of elastic energy of cell walls surrounding cell α,

$$\mathcal{H}_\alpha^{\text{elastic}} = \frac{1}{2}E_\alpha wh \sum_{i\in\mathcal{V}_\alpha} l_{0i+1i}\left(\frac{l_{i+1i} - l_{0i+1i}}{l_{0i+1i}}\right)^2. \tag{C.15}$$

Note that here we are using vertex-based indexing for cell walls. After differentiation, it becomes

$$\frac{\partial \mathcal{H}_\alpha^{\text{elastic}}}{\partial x_j^\beta} = E_\alpha wh \sum_{i\in\mathcal{V}_\alpha} \varepsilon_{i+1i}\frac{\partial l_{ii+1}}{\partial x_j^\beta} = E_\alpha wh\left(\varepsilon_{jj-1}t_{jj-1}^\beta - \varepsilon_{j+1j}t_{j+1j}^\beta\right), \tag{C.16}$$

where ε_{i+1i} is longitudinal wall strain and we introduce the wall unit tangent vectors $t_{ji}^\mu = u_{ji}^\mu / l_{ji}$ which will be useful for the bending energy term. All that is left is to add, for each junction, all contributions from the surrounding cells,

$$\frac{d\mathcal{H}^{\text{elastic}}}{dx_j^\beta} = \sum_{\alpha\in\mathcal{N}_j} \frac{\partial \mathcal{H}_\alpha^{\text{elastic}}}{\partial x_j^\beta}. \tag{C.17}$$

Wall-based bending energy

Recall the bending energy for cell α,

$$\mathcal{H}_\alpha^{\text{bending}} = \frac{1}{4}k_{b\alpha}E_\alpha h \sum_{i\in\mathcal{V}_\alpha} \frac{\left(\boldsymbol{t}_{i+1i} - \boldsymbol{t}_{0i+1i}\right)^2}{l_{i+1i} + l_{ii-1}}, \tag{C.18}$$

where we used the version with wall tangents to avoid using inverse trigonometric functions later on. Note that $\boldsymbol{t}_{0i+1i} = \boldsymbol{t}_{0i+1i}(\theta_0)$, and is expressed as

$$t_{0}{}_{i+1i}^{\mu} = \cos(\theta_0)\, t_{ii-1}^{\mu} + \sin(\theta_0)\, R_i^{\mu\nu}\left(\frac{\pi}{2}\right) t_{ii-1}^{\nu}, \tag{C.19}$$

where R_i is the rotation matrix,

$$R_i^{\mu\nu}\left(\frac{\pi}{2}\right) = \delta^{\mu\nu} + K_i^{\mu\nu} + K_i^{\mu\gamma}K_i^{\gamma\nu}, \qquad\qquad K_i^{\mu\nu} = \varepsilon^{\mu\nu\gamma}k_i^{\gamma}, \tag{C.20}$$

around the unit vector,

$$k_i^{\gamma} = \frac{\varepsilon^{\gamma\xi\eta}t_{ii-1}^{\xi}t_{i+1i}^{\eta}}{\|\boldsymbol{t}_{ii-1} \times \boldsymbol{t}_{i+1i}\|}. \tag{C.21}$$

If $\boldsymbol{t}_{i+1i}$ and $\boldsymbol{t}_{ii-1}$ are colinear we continue to previous edges, for instance, $\boldsymbol{t}_{i-1i-2}$, until we find another edge that, along with $\boldsymbol{t}_{i+1i}$, spans a plane for which we can compute k_i^{γ}. For most cases, considering the previous edge is sufficient, and so we will assume k_i^{γ} is always well-defined. We can rewrite the rotation matrix simply as,

$$R_i^{\mu\nu}\left(\frac{\pi}{2}\right) = k_i^{\mu}k_i^{\nu} + \varepsilon^{\mu\nu\gamma}k_i^{\gamma}, \tag{C.22}$$

by contracting the Levi-Civita symbols in the third term. Because k_i^{ν} is normal to t_{ii-1}^{ν}, it follows that

$$t_{0}{}_{i+1i}^{\mu} = \cos(\theta_0)\, t_{ii-1}^{\mu} + \sin(\theta_0)\, \varepsilon^{\mu\nu\gamma}t_{ii-1}^{\nu}k_i^{\gamma}. \tag{C.23}$$

Up until now, this description is valid for any collection of cell walls in three-dimensional space. Another possible approach is to use the cell normal unit vector w_{α}^{μ} instead of k_i^{μ}, effectively treating the bending term in the projected coordinate system. As mentioned before, we are interested in using the bending term exclusively for planar systems. In the plane, the vector k_i^{μ} is simply the unit vector normal to the plane and is kept constant and is the same for all vertices, for all faces.

We will require

$$\frac{\partial t_{i+1i}^{\mu}}{\partial x_j^{\beta}} = \frac{\delta_{i+1j} - \delta_{ij}}{l_{i+1i}}\left(\delta^{\mu\beta} - t_{i+1i}^{\mu}t_{i+1i}^{\nu}\right) = \left(\delta_{i+1j} - \delta_{ij}\right)\Omega_i^{\mu\beta}. \tag{C.24}$$

The derivative of the target tangent is,

$$\begin{aligned}\frac{\partial t_{0}{}_{i+1i}^{\mu}}{\partial x_j^{\beta}} &= \cos(\theta_0)\frac{\partial t_{ii-1}^{\mu}}{\partial x_j^{\beta}} + \sin(\theta_0)\left(\varepsilon^{\gamma\mu\nu}k_i^{\gamma}\frac{\partial t_{ii-1}^{\nu}}{\partial x_j^{\beta}} + \varepsilon^{\gamma\mu\nu}\frac{\partial k_i^{\gamma}}{\partial x_j^{\beta}}t_{ii-1}^{\nu}\right)\\ &= \left(\delta_{ij} - \delta_{i-1j}\right)\left[\cos(\theta_0)\,\Omega_{i-1}^{\mu\beta} + \sin(\theta_0)\,\varepsilon^{\gamma\mu\nu}k_i^{\gamma}\Omega_{i-1}^{\nu\beta}\right]\\ &= \left(\delta_{ij} - \delta_{i-1j}\right)\left[\cos(\theta_0)\,\delta^{\mu\nu} + \sin(\theta_0)\,\varepsilon^{\gamma\mu\nu}k_i^{\gamma}\right]\Omega_{i-1}^{\nu\beta}\\ &= \left(\delta_{ij} - \delta_{i-1j}\right)A_{0}{}_i^{\mu\nu}\Omega_{i-1}^{\nu\beta}.\end{aligned} \tag{C.25}$$

Now,

$$\frac{\partial \mathcal{H}_\alpha^{\text{bending}}}{\partial x_j^\beta} = \frac{1}{4} k_{b\alpha} E_\alpha h \sum_{i\in\mathcal{V}_\alpha} \left\{ \frac{t^\mu_{i+1i} - t_0{}^\mu_{i+1i}}{l_{i+1i}+l_{ii-1}} \left[2\left(\frac{\partial t^\mu_{i+1i}}{\partial x_j^\beta} - \frac{\partial t_0{}^\mu_{i+1i}}{\partial x_j^\beta} \right) \right.\right.$$
$$\left.\left. - \frac{t^\mu_{i+1i} - t_0{}^\mu_{i+1i}}{l_{i+1i}+l_{ii-1}} \left(\frac{\partial l_{i+1i}}{\partial x_j^\beta} + \frac{\partial l_{ii-1}}{\partial x_j^\beta} \right) \right] \right\}, \quad \text{(C.26)}$$

which we can rewrite as,

$$\frac{\partial \mathcal{H}_\alpha^{\text{bending}}}{\partial x_j^\beta} = \frac{1}{4} k_{b\alpha} E_\alpha h \sum_{k=0}^{1} \left\{ (-1)^k \left[2\Omega^{\nu\beta}_{j-1+k} \left(\frac{\Delta t^\nu_{j-1+k}}{l_{j-1+k}+l_{j-2+k}} - \frac{\Delta t^\mu_{j+k}}{l_{j+k}+l_{j-1+k}} A_0{}^{\mu\nu}_{j+k} \right) \right.\right.$$
$$\left.\left. - t^\beta_{j-1+k} \left(\frac{{\Delta t_{j+k}}^2}{l_{j+k}+l_{j-1+k}} + \frac{{\Delta t_{j-1+k}}^2}{l_{j-1+k}+l_{j-2+k}} \right) \right] \right\}, \quad \text{(C.27)}$$

where, to simplify notation we used $l_i = l_{i+1i}$, $t_i^\mu = t^\mu_{i+1i}$, and $\Delta t_i^\mu = t^\mu_{i+1i} - t_0{}^\mu_{i+1i}$.

Turgor and internal pressure gradients

Having the expressions for the area and volume gradients, these derivatives are quite straightforward. For turgor,

$$\mathcal{H}_\alpha^{\text{turgor}} = -T_\alpha A_\alpha h, \quad \text{(C.28)}$$

the total derivative with respect to one of the junctions becomes,

$$\frac{d\mathcal{H}^{\text{turgor}}}{dx_j^\beta} = \sum_{\alpha\in\mathcal{N}_j} \frac{\partial \mathcal{H}_\alpha^{\text{turgor}}}{\partial x_j^\beta} = -h \sum_{\alpha\in\mathcal{N}_j} T_\alpha \frac{\partial A_\alpha}{\partial x_j^\beta}, \quad \text{(C.29)}$$

where we have already computed the area gradient in Eq. B.36.

The expression for a volume term of the form $-PV$ would use the gradient of the volume instead (Eq.B.42).

Appendix D

Rheology of the cell-based elastic model

In accordance to the model presented in Section 3.1.1 the elastic energy density is given by

$$\psi = c_1 \frac{M^{\mu\nu} - M_0^{\mu\nu}}{M_0^{\alpha\alpha}} \frac{M^{\mu\nu} - M_0^{\mu\nu}}{M_0^{\beta\beta}} + \frac{c_2}{2} \frac{M^{\mu\mu} - M_0^{\mu\mu}}{M_0^{\nu\nu}} \frac{M^{\alpha\alpha} - M_0^{\alpha\alpha}}{M_0^{\beta\beta}}, \tag{D.1}$$

where the upper indices signify components and we use Einstein notation of implicitly summing over repeated indices. The matrices two-dimensional matrices M and M_0 correspond to the second moment of area of the projection of a cell on plane fitted to the cell's three-dimensional representation, and its target value. With this setup, we will have access only to the current configuration, from which we can compute the shape matrix, M, and its target value, M_0. In this section we attempt to answer how, from M and M_0 we can retrieve average strain acting on the cell, the corresponding stress (the constitutive relation), and how can we compare c_1 and c_2 to other typical mechanical parameters such as the Lamé parameters, or the more commonly used Young's modulus and Poisson ratio.

The infinitesimal strain tensor, as it is defined, is the symmetric part of the gradient of the displacement vector field describing the difference in position between each volume element of a rest configuration and its current position in the deformed configuration. We make note, at this point, that having only M and M_0 prohibits us from uniquely defining a rotation and a strain simultaneously, in general. For example, if we let M_0 be diagonal and anisotropic, and obtain M by rotating it $\pi/2$ radians, we could obtain the same end shape matrix, M, by appropriately contracting and stretching space along the cartesian axes. By using the infinitesimal strain theory to describe deformations, we already concede to the assumption of small strains and to the assumption that M and M_0 are not connected by a rotation.

A strain of $\varepsilon^{\mu\nu}$ implies that the material being deformed, apart from rotation and translation, is locally under the effect of the linear transformation $\Lambda^{\mu\nu} = \delta^{\mu\nu} + \varepsilon^{\mu\nu}$[1]. Now, we turn our focus to the shape matrix, which is simply the second moment of area of a polygon whose centroid coincides with the origin,

$$M^{\mu\nu} = \iint_S x^\mu x^\nu \mathrm{d}x^\mu \mathrm{d}x^\nu, \tag{D.3}$$

where S here represents the points inside the cell. Under a linear transformation, $x^{\mu'} = \Lambda^{\mu'\nu} x^\nu$,

$$\begin{aligned} M^{\mu'\nu'} = \iint_{S'} x^{\mu'} x^{\nu'} \mathrm{d}x^{\mu'} \mathrm{d}x^{\nu'} &= \iint_S \Lambda^{\mu'\mu} x^\mu \Lambda^{\nu'\nu} x^\nu \det(\Lambda)\, \mathrm{d}x^\mu \mathrm{d}x^\nu \\ &= \Lambda^{\mu'\mu} \Lambda^{\nu'\nu} \det(\Lambda)\, M^{\mu\nu}. \end{aligned} \tag{D.4}$$

We make the assumption that an average strain is acting on the polygon such that M_0 transforms into M, implying

$$M^{\mu\nu} = \det(I + \varepsilon) \left(\delta^{\mu\alpha} + \varepsilon^{\mu\alpha}\right) \left(\delta^{\nu\beta} + \varepsilon^{\nu\beta}\right) M_0^{\alpha\beta}, \tag{D.5}$$

where I is the identity matrix. Note that $\det(I + \varepsilon) = 1 + \mathrm{Tr}(\varepsilon) + \det(\varepsilon)$. Under the small strain assumption we will discard terms of order $\mathcal{O}(\varepsilon^2)$ and higher, resulting in the equation,

$$M^{\mu\nu} - M_0^{\mu\nu} = \mathrm{Tr}(\varepsilon)\, M_0^{\mu\nu} + \varepsilon^{\mu\alpha} M_0^{\alpha\nu} + \varepsilon^{\nu\beta} M_0^{\mu\beta}. \tag{D.6}$$

To aid this computation we introduce the transformation of symmetric 2×2 matrices to vectors in $\mathbb{R}^3$

$$\begin{aligned} A = \begin{pmatrix} A^{xx} & A^{xy} \\ A^{yx} & A^{yy} \end{pmatrix} = A^1 \begin{pmatrix} \frac{\sqrt{2}}{2} & 0 \\ 0 & \frac{\sqrt{2}}{2} \end{pmatrix} + A^2 \begin{pmatrix} \frac{\sqrt{2}}{2} & 0 \\ 0 & -\frac{\sqrt{2}}{2} \end{pmatrix} + A^3 \begin{pmatrix} 0 & \frac{\sqrt{2}}{2} \\ \frac{\sqrt{2}}{2} & 0 \end{pmatrix} \\ = A^1 \mathbf{e}_1 + A^2 \mathbf{e}_2 + A^3 \mathbf{e}_3. \end{aligned} \tag{D.7}$$

Although we have the freedom to assert that the new basis is orthonormal, i.e., $\langle \mathbf{e}_i, \mathbf{e}_j \rangle = \delta^{ij}$, this has implications on if and how the inner product rule, $\langle \cdot, \cdot \rangle$, can be represented in the initial cartesian coordinate basis. It turns out we can easily find a bilinear operation in the initial cartesian coordinates which accomplishes the intended orthogonality rule. Let $\langle A, B \rangle = \sum_i \sum_j A^{ij} B^{ij}$. This rule ensures $\langle \mathbf{e}_i, \mathbf{e}_j \rangle = \delta^{ij}$ and, because of this fact, we

---

[1] From the Taylor expansion of displacement vector, $\boldsymbol{u} = \boldsymbol{x'} - \boldsymbol{x}$, around $\boldsymbol{x}_0$,

$$x^{\mu'} - x^\mu \approx {x_0}^{\mu'} - {x_0}^\mu + \frac{\partial u^\mu}{\partial x^\nu} \left(x^\nu - {x_0}^\nu\right) \Rightarrow x^{\mu'} - {x_0}^{\mu'} = \left(\delta^{\mu\nu} + \frac{\partial u^\mu}{\partial x^\nu}\right) \left(x^\nu - {x_0}^\nu\right) \Rightarrow \boldsymbol{v'} = \Lambda \boldsymbol{v}. \tag{D.2}$$

can write $\langle \mathbf{e}_i, A\rangle = A^i$. Hence, transforming back and forth is straightforward,

$$A^{xx} = \frac{\sqrt{2}}{2}\left(A^1 + A^2\right), \qquad A^{yy} = \frac{\sqrt{2}}{2}\left(A^1 - A^2\right), \qquad A^{xy} = A^{yx} = \frac{\sqrt{2}}{2}A^3, \tag{D.8}$$

$$A^1 = \frac{\sqrt{2}}{2}\left(A^{xx} + A^{yy}\right), \qquad A^2 = \frac{\sqrt{2}}{2}\left(A^{xx} - A^{yy}\right), \qquad A^3 = \frac{\sqrt{2}}{2}\left(A^{xy} + A^{yx}\right). \tag{D.9}$$

We also want to rewrite typical matrix operators for these types of objects, namely,

$$\det\left(A\right) = \frac{1}{2}\left(\left(A^1\right)^2 - \left(A^2\right)^2 - \left(A^3\right)^2\right), \qquad \mathrm{Tr}\left(A\right) = \sqrt{2}A^1, \tag{D.10}$$

$$A : B = A^{\mu\nu}B^{\mu\nu} = A^1B^1 + A^2B^2 + A^3B^3, \qquad \|A\|_{\mathrm{F}}^2 = \left(A^1\right)^2 + \left(A^2\right)^2 + \left(A^3\right)^2. \tag{D.11}$$

We are now in position of applying the one-form $\langle \mathbf{e}_i, \cdot\rangle$ to both sides of Eq. D.6, yielding

$$\Delta M^i = \sqrt{2}\varepsilon^1 M_0^i + \langle \mathbf{e}_i, \varepsilon^{\mu\alpha}M_0^{\alpha\nu} + \varepsilon^{\nu\beta}M_0^{\mu\beta}\rangle, \tag{D.12}$$

where $\Delta M = M - M_0$. For each basis vector we have,

$$\begin{aligned}\mathbf{e}_1 : \sqrt{2}\left(\varepsilon^{x\alpha}M_0^{\alpha x} + \varepsilon^{y\alpha}M_0^{\alpha y}\right) &= \frac{\sqrt{2}}{2}\Big(\left(\varepsilon^1 + \varepsilon^2\right)\left(M_0^1 + M_0^2\right) \\ &+ \left(\varepsilon^1 - \varepsilon^2\right)\left(M_0^1 - M_0^2\right) + 2\varepsilon^3 M_0^3\Big) = \sqrt{2}\left(\varepsilon^1 M_0^1 + \varepsilon^2 M_0^2 + \varepsilon^3 M_0^3\right),\end{aligned} \tag{D.13}$$

$$\begin{aligned}\mathbf{e}_2 : \sqrt{2}\left(\varepsilon^{x\alpha}M_0^{\alpha x} - \varepsilon^{y\alpha}M_0^{\alpha y}\right) = \sqrt{2}\left(\varepsilon^{xx}M_0^{xx} - \varepsilon^{yy}M_0^{yy}\right) &= \frac{\sqrt{2}}{2}\Big(\left(\varepsilon^1 + \varepsilon^2\right)\left(M_0^1 + M_0^2\right) \\ &+ \left(\varepsilon^1 - \varepsilon^2\right)\left(M_0^1 - M_0^2\right)\Big) = \sqrt{2}\left(\varepsilon^1 M_0^2 + \varepsilon^2 M_0^1\right),\end{aligned} \tag{D.14}$$

$$\begin{aligned}\mathbf{e}_3 : \sqrt{2}\left(\varepsilon^{x\alpha}M_0^{\alpha y} + \varepsilon^{y\alpha}M_0^{\alpha x}\right) &= \frac{\sqrt{2}}{2}\Big(\left(\varepsilon^1 + \varepsilon^2\right)M_0^3 + \varepsilon^3\left(M_0^1 + M_0^2\right) \\ &+ \varepsilon^3\left(M_0^1 - M_0^2\right) + \left(\varepsilon^1 - \varepsilon^2\right)M_0^3\Big) = \sqrt{2}\left(\varepsilon^3 M_0^1 + \varepsilon^1 M_0^3\right).\end{aligned} \tag{D.15}$$

In this new basis, the same set of equations can therefore be written as

$$\begin{alignedat}{3}\frac{\sqrt{2}}{2}\Delta M^1 &= 2M_0^1\varepsilon^1 \quad &&+M_0^2\varepsilon^2 &&+ M_0^3\varepsilon^3, \\ \frac{\sqrt{2}}{2}\Delta M^2 &= 2M_0^2\varepsilon^1 \quad &&+M_0^1\varepsilon^2, && \\ \frac{\sqrt{2}}{2}\Delta M^3 &= 2M_0^3\varepsilon^1 \quad && &&+ M_0^1\varepsilon^3.\end{alignedat} \tag{D.16}$$

The determinant of this linear system of equations is

$$\begin{vmatrix} 2M_0^1 & M_0^2 & M_0^3 \\ 2M_0^2 & M_0^1 & 0 \\ 2M_0^3 & 0 & M_0^1 \end{vmatrix} = 2M_0^1\left(\left(M_0^1\right)^2 - \left(M_0^2\right)^2 - \left(M_0^3\right)^2\right) = 2\sqrt{2}\mathrm{Tr}\left(M_0\right)\det M_0. \quad \text{(D.17)}$$

If M_0 was indeed computed from a polygon with Eq. D.3, then M_0 is symmetric and positive-definite[2], and the previous linear system of equations has the solution,

$$\varepsilon^1 = \frac{\sqrt{2}}{4}\frac{M_0^1\Delta M^1 - M_0^2\Delta M^2 - M_0^3\Delta M^3}{\left(M_0^1\right)^2 - \left(M_0^2\right)^2 - \left(M_0^3\right)^2}, \quad \text{(D.18)}$$

$$\varepsilon^2 = \frac{\sqrt{2}}{2}\frac{-M_0^1M_0^2\Delta M^1 + \left(\left(M_0^1\right)^2 - \left(M_0^3\right)^2\right)\Delta M^2 + M_0^3M_0^2\Delta M^3}{M_0^1\left[\left(M_0^1\right)^2 - \left(M_0^2\right)^2 - \left(M_0^3\right)^2\right]}, \quad \text{(D.19)}$$

$$\varepsilon^3 = \frac{\sqrt{2}}{2}\frac{-M_0^3M_0^1\Delta M^1 + M_0^3M_0^2\Delta M^2 + \left(\left(M_0^1\right)^2 - \left(M_0^2\right)^2\right)\Delta M^3}{M_0^1\left[\left(M_0^1\right)^2 - \left(M_0^2\right)^2 - \left(M_0^3\right)^2\right]}. \quad \text{(D.20)}$$

We can express the result in terms of the 2×2 cartesian matrices as

$$\begin{aligned}\varepsilon = {} & \frac{M - M_0}{\mathrm{Tr}\left(M_0\right)} - \frac{1}{2}\frac{M_0}{\mathrm{Tr}\left(M_0\right)}\frac{\mathrm{Tr}\left(M_0\right)\mathrm{Tr}\left(M - M_0\right) - M_0 : \left(M - M_0\right)}{\det\left(M_0\right)} \\ & - \frac{I}{2}\left(\frac{\mathrm{Tr}\left(M - M_0\right)}{\mathrm{Tr}\left(M_0\right)} - \frac{3}{4}\frac{\mathrm{Tr}\left(M_0\right)\mathrm{Tr}\left(M - M_0\right) - M_0 : \left(M - M_0\right)}{\det\left(M_0\right)}\right). \quad \text{(D.21)}\end{aligned}$$

For an isotropic rest shape we replace $M_0 = m_0 I$, $\mathrm{Tr}\left(M_0\right) = 2m_0$, $\det\left(M_0\right) = m_0^2$, and $M_0 : A = m_0\mathrm{Tr}\left(A\right)$, and get

$$\varepsilon = \frac{M - M_0}{\mathrm{Tr}\left(M_0\right)} - \frac{I}{4}\frac{\mathrm{Tr}\left(M - M_0\right)}{\mathrm{Tr}\left(M_0\right)}. \quad \text{(D.22)}$$

We can also rewrite the energy density, yielding

$$\begin{aligned}\psi &= \frac{c_1}{2\left(M_0^1\right)^2}\left(\left(\Delta M^1\right)^2 + \left(\Delta M^2\right)^2 + \left(\Delta M^3\right)^2\right) + \frac{c_2}{2\left(M_0^1\right)^2}\left(\Delta M^1\right)^2 \\ &= \frac{2\left(c_1 + c_2\right)}{2\left(M_0^1\right)^2}\left(\frac{\sqrt{2}}{2}\Delta M^1\right)^2 + \frac{2c_1}{2\left(M_0^1\right)^2}\left(\frac{\sqrt{2}}{2}\Delta M^2\right)^2 + \frac{2c_1}{2\left(M_0^1\right)^2}\left(\frac{\sqrt{2}}{2}\Delta M^3\right)^2. \quad \text{(D.23)}\end{aligned}$$

We simply have to differentiate to obtain stress, σ, by definition. By using Eq. D.16, the

---

[2] Let y^μ be a any two-dimensional unit vector and the region of integration, S, not be a single line or point, then

$$\boldsymbol{y}^T M \boldsymbol{y} = y^\mu \iint_S x^\mu x^\nu \mathrm{d}S y^\nu = \iint_S \left(x^\mu y^\mu\right)^2 \mathrm{d}S > 0.$$

components are simply[3],

$$\sigma^1 = \frac{4\sqrt{2}}{2\left(M_0^1\right)^2}\left[\left(c_1+c_2\right)M_0^1\Delta M^1 + c_1 M_0^2\Delta M^2 + c_1 M_0^3 \Delta M^3\right], \tag{D.24}$$

$$\sigma^2 = \frac{2\sqrt{2}}{2\left(M_0^1\right)^2}\left[\left(c_1+c_2\right)M_0^2\Delta M^1 + c_1 M_0^1\Delta M^2\right], \tag{D.25}$$

$$\sigma^3 = \frac{2\sqrt{2}}{2\left(M_0^1\right)^2}\left[\left(c_1+c_2\right)M_0^3\Delta M^1 + c_1 M_0^1\Delta M^3\right], \tag{D.26}$$

or, in matrix notation,

$$\begin{aligned}\sigma = 2c_1\frac{M-M_0}{\operatorname{Tr}\left(M_0\right)} + 2\left(c_1+c_2\right)\frac{\operatorname{Tr}\left(M-M_0\right)}{\operatorname{Tr}\left(M_0\right)}\frac{M_0}{\operatorname{Tr}\left(M_0\right)}& \\ + I\left[\left(c_2-2c_1\right)\frac{\operatorname{Tr}\left(M-M_0\right)}{\operatorname{Tr}\left(M_0\right)} + 4c_1\frac{M_0:\left(M-M_0\right)}{\operatorname{Tr}^2\left(M_0\right)}\right]&. \end{aligned} \tag{D.27}$$

For an isotropic rest shape matrix, we get

$$\sigma = 2c_1\frac{M-M_0}{\operatorname{Tr}\left(M_0\right)} + I\left(c_1+2c_2\right)\frac{\operatorname{Tr}\left(M-M_0\right)}{\operatorname{Tr}\left(M_0\right)}. \tag{D.28}$$

Lastly, the constitutive relation,

$$\sigma^i = C^{ij}\varepsilon^j, \tag{D.29}$$

is obtained by differentiation once again, $C^{ij} = \partial\sigma^i/\partial\varepsilon^j$. Note that Schwartz's theorem ensures C^{ij} is symmetric. Proceeding in the same way as for the stress components, the components of C^{ij} are, therefore,

$$C^{11} = 8\left[c_1+c_2+c_1\left(\frac{M_0^2}{M_0^1}\right)^2 + c_1\left(\frac{M_0^3}{M_0^1}\right)^2\right], \qquad C^{12} = 4\left(2c_1+c_2\right)\frac{M_0^2}{M_0^1}, \tag{D.30}$$

$$C^{22} = 2\left[c_1+\left(c_1+c_2\right)\left(\frac{M_0^2}{M_0^1}\right)^2\right], \qquad C^{13} = 4\left(2c_1+c_2\right)\frac{M_0^3}{M_0^1}, \tag{D.31}$$

$$C^{33} = 2\left[c_1+\left(c_1+c_2\right)\left(\frac{M_0^3}{M_0^1}\right)^2\right], \qquad C^{23} = 2\left(c_1+c_2\right)\frac{M_0^2}{M_0^1}\frac{M_0^3}{M_0^1}. \tag{D.32}$$

---

[3] Note that, using the chain rule,

$$\begin{aligned}\frac{\partial\psi}{\partial\varepsilon^1} &= \frac{\sqrt{2}}{2}\left(\frac{\partial\psi}{\partial\varepsilon^{xx}} + \frac{\partial\psi}{\partial\varepsilon^{yy}}\right) = \frac{\sqrt{2}}{2}\left(\sigma^{xx}+\sigma^{yy}\right) = \langle\mathbf{e}_1,\sigma\rangle = \sigma^1,\\ \frac{\partial\psi}{\partial\varepsilon^2} &= \frac{\sqrt{2}}{2}\left(\frac{\partial\psi}{\partial\varepsilon^{xx}} - \frac{\partial\psi}{\partial\varepsilon^{yy}}\right) = \frac{\sqrt{2}}{2}\left(\sigma^{xx}-\sigma^{yy}\right) = \langle\mathbf{e}_2,\sigma\rangle = \sigma^2,\\ \frac{\partial\psi}{\partial\varepsilon^3} &= \frac{\sqrt{2}}{2}\left(\frac{\partial\psi}{\partial\varepsilon^{xy}} + \frac{\partial\psi}{\partial\varepsilon^{yx}}\right) = \frac{\sqrt{2}}{2}\left(\sigma^{xy}+\sigma^{yx}\right) = \langle\mathbf{e}_3,\sigma\rangle = \sigma^3,\end{aligned}$$

For an isotropic rest shape, $M_0^2 = M_0^3 = 0$, the stiffness matrix is diagonal with components,

$$C^{11} = 8\left(c_1 + c_2\right), \qquad C^{22} = 2c_1, \qquad C^{33} = 2c_1. \tag{D.33}$$

The energy density for a linear elastic isotropic material is

$$\varphi = \mu \varepsilon^{\mu\nu} \varepsilon^{\mu\nu} + \frac{\lambda}{2}\left(\varepsilon^{\mu\mu}\right)^2, \tag{D.34}$$

where λ and μ are the first and second Lamé parameters of the material under strain ε. Using the representation developed here, we could equivalently write

$$\varphi = \left(\mu + \lambda\right)\left(\varepsilon^1\right)^2 + \mu\left(\varepsilon^2\right)^2 + \mu\left(\varepsilon^3\right)^2. \tag{D.35}$$

For a linear elastic isotropic material, therefore, the stiffness matrix is diagonal and can be written as

$$C'^{11} = 2\left(\mu + \lambda\right), \qquad C'^{22} = 2\mu, \qquad C'^{33} = 2\mu. \tag{D.36}$$

Since the stiffness matrix of the second moment of area model is not diagonal, we cannot generally find a mapping between the constants c_1, c_2, μ, and λ. Nevertheless, for an isotropic rest shape matrix we can find c_1 and c_2 as a function of μ and λ, and vice-versa. The result of the linear system of equations $C^{ij} = C'^{ij}$ is

$$c_1 = \mu, \qquad c_2 = \frac{\lambda - 3\mu}{4}, \qquad \lambda = 3c_1 + 4c_2, \tag{D.37}$$

or in terms of Young's modulus, E, and Poisson's ratio, ν,

$$c_1 = \frac{E}{2\left(1+\nu\right)}, \qquad c_2 = \frac{E\left(8\nu - 3\right)}{8\left(1+\nu\right)\left(1-2\nu\right)}, \tag{D.38}$$

$$E = c_1\left(3 - \frac{1}{4}\frac{c_1}{c_2 + c_1}\right), \qquad \nu = \frac{1}{2}\left(1 - \frac{1}{4}\frac{c_1}{c_2 + c_1}\right). \tag{D.39}$$

During this work we have exclusively used isotropic rest shape matrices. We note here that, in this specific case, the eigenvectors of $\left(M - M_0\right)/\mathrm{Tr}\left(M_0\right)$ are the same as the ones of strain and stress.

Tissue-wide integration of mechanical cues promotes effective auxin patterning

The European Physical Journal Plus
Supplementary Material

João R. D. Ramos[1]   Alexis Maizel[2]   Karen Alim[1,3,*]

[1]Max Planck Institute for Dynamics and Self-Organization, Göttingen, Germany
[2]Center for Organismal Studies, University of Heidelberg, Heidelberg, Germany
[3]Physik-Department, Technische Universität München, Garching, Germany
[*]e-mail: k.alim@tum.de (corresponding author)

Derivation of Auxin Transport Model

Geometrically, we consider the epithelial tissue to be composed of cells shaped as right prisms with the same height h. Effectively, under this assumption we can reduce the dimensionality of the system by considering just the shape of the base of the cells. We will also assume that the thickness of the walls is thin enough such that the volume of the cell is approximately hA_α, where A_α is the area of the base of the cell. Let ρ denote auxin concentration. Assuming auxin gets expressed at a rate γ per unit time and unit volume, and each auxin molecule decays at a rate δ per unit time, we can write the continuity equation inside any cell as

$$\dot{\rho} + \nabla \cdot \mathbf{J} = \gamma - \delta\rho. \tag{1}$$

where $\mathbf{J}$ is local current density of auxin.
Focusing on cell α, we can integrate inside the cell to obtain,

$$\dot{N}_\alpha + \oiint_{S_\alpha} \mathbf{J} \cdot \hat{\mathbf{n}} dS = hA_\alpha\gamma - \delta N_\alpha, \tag{2}$$

where we assume the volume V_α does not change over time, S_α is the surface enclosing volume V_α, and N_α represents the number of auxin molecules inside cell α. Another assumption we make is that the flux of $\mathbf{J}$ across the bases of the cell is zero, resulting in just flux across neighbours within the same layer.
To simplify notation we define $\mathcal{N}_\alpha$ as the set of all regions on the other side of each wall surrounding cell α. This set will contain the neighbouring cells. Note that with this definition there can be multiple occurrences of the same cell within the set, yet referred to as different regions. We can now uniquely refer to wall compartments around a cell with $\alpha\beta$ or $\beta\alpha$, $\beta \in \mathcal{N}_\alpha$.
If we let the wall between cells α and $\beta \in \mathcal{N}_\alpha$ be of length $l_{\alpha\beta}$ with normal vector $\hat{\mathbf{n}}_{\alpha\beta}$ pointing from α to β, then we can replace the surface integral by a sum of line integrals,

$$\dot{N}_\alpha + h \sum_{\beta \in \mathcal{N}_\alpha} \int_{l_{\alpha\beta}} \mathbf{J}(\mathbf{r}) \cdot \hat{\mathbf{n}}_{\alpha\beta} dl = hA_\alpha\gamma - \delta N_\alpha. \tag{3}$$

Assuming auxin diffuses quickly inside each cell, we can assume auxin concentration is the same everywhere inside the cell, $\rho_\alpha = N_\alpha/(hA_\alpha)$. This approximation is justified, since auxin is a very small molecule. Now, with a constant auxin concentration within a cell, we can write the passive transport with Fick's law, i.e., $\mathbf{J} = \mathbf{J}_{\text{pass}} + \mathbf{J}_{\text{act}}$, with $\mathbf{J}_{\text{pass}} = -D\nabla\rho$ and interpolating auxin concentration inside the cell wall. Therefore, the current density of auxin through wall $l_{\alpha\beta}$ from cell α to region β is

$$\mathbf{J}_{\text{pass}_{\alpha\to\beta}} \cdot \hat{\mathbf{n}}_{\alpha\beta} = -D\frac{\rho_\beta - \rho_\alpha}{T}, \tag{4}$$

where T is the thickness of the wall. We can also continue to simplify assuming that the active auxin flow is constant along the wall. Again, assuming that the area A_α does not change,

$$\dot{\rho}_\alpha = \gamma - \delta\rho_\alpha + \frac{D}{T}\sum_{\beta\in\mathcal{N}_\alpha}\frac{l_{\alpha\beta}}{A_\alpha}\left(\rho_\beta - \rho_\alpha\right) + \sum_{\beta\in\mathcal{N}_\alpha}\frac{l_{\alpha\beta}}{A_\alpha}\left[J_{\mathrm{act}_{\beta\to\alpha}} - J_{\mathrm{act}_{\alpha\to\beta}}\right], \tag{5}$$

where $J_{\mathrm{act}_{\alpha\to\beta}}$ is the amount of auxin transported per unit area, per unit time, from α to β.
Let $P_{\alpha\beta}$ be the density of auxin efflux carriers on the compartment of the wall facing cell α, pumping auxin into β. We model active auxin transport with

$$J_{\mathrm{act}_{\alpha\to\beta}} = \mathcal{A}P_{\alpha\beta}\frac{\rho_\alpha}{K_M + \rho_\alpha}, \tag{6}$$

with $\mathcal{A}$ being the maximum activity of the carrier and K_M the Michaelis-Menten constant of the reaction. This results in

$$\dot{\rho}_\alpha = \gamma - \delta\rho_\alpha + \frac{D}{T}\sum_{\beta\in\mathcal{N}_\alpha}\frac{l_{\alpha\beta}}{A_\alpha}\left(\rho_\beta - \rho_\alpha\right) + \mathcal{A}\sum_{\beta\in\mathcal{N}_\alpha}\frac{l_{\alpha\beta}}{A_\alpha}\left[P_{\beta\alpha}\frac{\rho_\beta}{K_M + \rho_\beta} - P_{\alpha\beta}\frac{\rho_\alpha}{K_M + \rho_\alpha}\right]. \tag{7}$$

We now need to model PIN molecule binding and unbinding. Let the number of internalized PIN molecules be M_α. Let the number of PIN molecules bound to wall $l_{\alpha\beta}$ of cell α pumping auxin into region β by $M_{\alpha\beta}$. Also, we define the binding and unbinding constants, k_{b} and k_{ub}. The rate equations for bound PIN molecules are

$$\dot{M}_{\alpha\beta} = k_{\mathrm{b}}\frac{l_{\alpha\beta}}{L_\alpha}M_\alpha - k_{\mathrm{ub}}M_{\alpha\beta}, \tag{8}$$

where $L_\alpha = \sum_{\beta\in\mathcal{N}_\alpha} l_{\alpha\beta}$ is the perimeter of the cell. If k_{b} takes into account how many PIN molecules are close enough to the walls of the cell, the factor $\frac{l_{\alpha\beta}}{L_\alpha}$ is necessary since it is the probability of being close to that particular wall. In terms of PIN density $P_{\alpha\beta}$ and concentration P_α instead of PIN number,

$$\dot{P}_{\alpha\beta} = k_{\mathrm{b}}\frac{A_\alpha}{L_\alpha}P_\alpha - k_{\mathrm{ub}}P_{\alpha\beta}, \tag{9}$$

We will consider the dynamics of PIN to be much faster than that of auxin, such that we can decouple the time scales of both processes. As such, we assume that between auxin time steps there is enough time for PIN to reach its steady state. The steady state of this equation is

$$P^*_{\alpha\beta} = \frac{k_{\mathrm{b}}}{k_{\mathrm{ub}}}\frac{A_\alpha}{L_\alpha}P^*_\alpha = f_{\alpha\beta}\frac{A_\alpha}{L_\alpha}P^*_\alpha, \tag{10}$$

where the binding and unbinding rates are a function of the features of the wall, $f_{\alpha\beta} = k_{\mathrm{b}}/k_{\mathrm{ub}}$.
Assuming all cells are competing for the same amount of PIN molecules, M_0, we have

$$A_\alpha P^*_\alpha + \sum_{\beta\in\mathcal{N}_\alpha} l_{\alpha\beta}P^*_{\alpha\beta} = M_0, \tag{11}$$

which, using $P^*_{\alpha\beta}$ from the previous expression, can be be solved for P^*_α, yielding

$$P^*_\alpha = \frac{M_0}{A_\alpha}\frac{1}{1 + \sum_{\beta\in\mathcal{N}_\alpha}\frac{l_{\alpha\beta}}{L_\alpha}f_{\alpha\beta}}, \tag{12}$$

and for $P^*_{\alpha\beta}$,

$$P^*_{\alpha\beta} = \frac{M_0}{L_\alpha}\frac{f_{\alpha\beta}}{1 + \sum_{\xi\in\mathcal{N}_\alpha}\frac{l_{\alpha\xi}}{L_\alpha}f_{\alpha\xi}} = \frac{M_0}{L_\alpha}p_{\alpha\beta}. \tag{13}$$

Note that if we replace $P^*_{\alpha\beta}$ for $P_{\alpha\beta}$ in auxin concentration rate equation with M_0 being a constant, when solving for steady state, we obtain that the steady state concentration of auxin is dependent on the geometry of the cell, namely its perimeter.
There are three choices we can make, in regards to how plant cells scale PIN. We can simply not scale resulting in a constant M_0, we can scale according to cell area, i.e., $M_0 = A_\alpha C_0$, or scale according to perimeter, $M_0 = L_\alpha D_0$. To minimise the impact of this effect on auxin patterning, we opt for a scaling according to perimeter, resulting in the density

$$P_{\alpha\beta} = D_0 p_{\alpha\beta}. \tag{14}$$

By replacing in the auxin concentration rate equation we finally get

$$\dot{\rho}_\alpha = \gamma - \delta\rho_\alpha + \frac{D}{T}\sum_{\beta\in\mathcal{N}_\alpha}\frac{l_{\alpha\beta}}{A_\alpha}\left(\rho_\beta - \rho_\alpha\right) + \mathcal{A}D_0\sum_{\beta\in\mathcal{N}_\alpha}\frac{l_{\alpha\beta}}{A_\alpha}\left[p_{\beta\alpha}\frac{\rho_\beta}{K_M+\rho_\beta} - p_{\alpha\beta}\frac{\rho_\alpha}{K_M+\rho_\alpha}\right], \tag{15}$$

where,

$$p_{\alpha\beta} = \frac{f_{\alpha\beta}}{1+\sum_{\xi\in\mathcal{N}_\alpha}\frac{l_{\alpha\xi}}{L_\alpha}f_{\alpha\xi}} \tag{16}$$

We adimensionalize the equation by choosing a characteristic length L and a characteristic time $1/f$. We can then replace, $\rho = \rho^*/L^3$, $dt = dt^*/f$, $l = Ll^*$, $K = K^*/L^3$ and $A = A^*L^2$,

$$\frac{d\rho^*_\alpha}{dt^*} = \frac{L^3\gamma}{f} - \frac{\delta}{f}\rho^*_\alpha + \frac{D}{LfT}\sum_{\beta\in\mathcal{N}_\alpha}\frac{l^*_{\alpha\beta}}{A^*_\alpha}\left(\rho^*_\beta - \rho^*_\alpha\right) + \frac{\mathcal{A}D_0L^2}{f}\sum_{\beta\in\mathcal{N}_\alpha}\frac{l^*_{\alpha\beta}}{A^*_\alpha}\left[p_{\beta\alpha}\frac{\rho^*_\beta}{K^*+\rho^*_\beta} - p_{\alpha\beta}\frac{\rho^*_\alpha}{K^*+\rho^*_\alpha}\right]. \tag{17}$$

Note that the auxin concentration in steady state, when all pin densities $p_{\alpha\beta}$ are the same, is $\rho^*_0 = L^3\gamma/\delta$. If we normalize the previous expression by choosing ρ^*_0 as our unit of auxin concentration and δ/f as our unit of time, we obtain

$$\frac{da_\alpha}{d\tau} = \frac{f}{L^3\gamma}\frac{d\rho^*_\alpha}{dt^*} = 1 - a_\alpha + \frac{D}{L\delta T}\sum_{\beta\in\mathcal{N}_\alpha}\frac{l^*_{\alpha\beta}}{A^*_\alpha}\left(a_\beta - a_\alpha\right) + \frac{\mathcal{A}D_0}{L\gamma}\sum_{\beta\in\mathcal{N}_\alpha}\frac{l^*_{\alpha\beta}}{A^*_\alpha}\left[p_{\beta\alpha}\frac{a_\beta}{K+a_\beta} - p_{\alpha\beta}\frac{a_\alpha}{K+a_\alpha}\right], \tag{18}$$

where $a_\alpha = \rho^*_\alpha/\rho^*_0$, $d\tau = dtf/\delta$ and $K = K^*/\rho^*_0$. The combination of parameters relevant for this process are $\mathcal{P} = \frac{\mathcal{A}D_0}{L\gamma}$ and $\mathcal{D} = \frac{D}{L\delta T}$. If the thickness of the wall is also adimensional, then $\mathcal{D} = \frac{D}{L^2\delta T^*}$. These two numbers are essentially a comparison between passive or active transport and auxin turnover rate. We can also have a stochastic production rate in order to break symmetry and to make the system closer to a biological one. Finally,

$$\frac{da_\alpha}{d\tau} = \gamma^* - \delta^* a_\alpha + \mathcal{D}\sum_{\beta\in\mathcal{N}_\alpha}\frac{l^*_{\alpha\beta}}{A^*_\alpha}\left(a_\beta - a_\alpha\right) + \mathcal{P}\sum_{\beta\in\mathcal{N}_\alpha}\frac{l^*_{\alpha\beta}}{A^*_\alpha}\left[p_{\beta\alpha}\frac{a_\beta}{K+a_\beta} - p_{\alpha\beta}\frac{a_\alpha}{K+a_\alpha}\right], \tag{19}$$

where $\gamma^* = 1$ and $\delta^* = 1$ are kept to reinforce that these are production and decay rates, and

$$p_{\alpha\beta} = \frac{f_{\alpha\beta}}{1+\sum_{\xi\in\mathcal{N}_\alpha}\frac{l_{\alpha\xi}}{L_\alpha}f_{\alpha\xi}}. \tag{20}$$

The connection of this model to tissue mechanics happens with modeling binding rates $f_{\alpha\beta}$ as a function of wall stress and modeling auxin-mediated cell wall loosening, by changing stiffness E_α.

Suppose stress $\sigma_{\alpha\beta}$ is the longitudinal component of stress acting on the wall between cell α and region $\beta \in \mathcal{N}_\alpha$, specifically in the wall compartment facing cell α. In accordance with [1], we model $f_{\alpha\beta}$ as a power-law,

$$f_{\alpha\beta} = f\left(\sigma_{\alpha\beta}\right) = \begin{cases}\eta\sigma^n_{\alpha\beta}, & \sigma_{\alpha\beta} > 0,\\ 0, & \sigma_{\alpha\beta} \le 0.\end{cases} \tag{21}$$

Finally, we look at cell wall loosening. We consider that all compartments surrounding a specific cell have the same stiffness. We model auxin-mediated cell wall loosening with a hill function similarly to [1],

$$E_\alpha = E\left(a_\alpha\right) = E_{\max} - \left(E_{\max} - E_{\min}\right)\frac{a^m_\alpha}{1+a^m_\alpha}, \tag{22}$$

where m is the Hill exponent, $a_\alpha = 1$ ($\rho_\alpha = \rho_0$) being the value of auxin where the stiffness is $\left(E_{\max} + E_{\min}\right)/2$, and $E_{\min}$ and $E_{\max}$ the minimum and maximum values stiffness in this system. It is also useful for linear stability analysis to rewrite this expression in terms of the parameters

$$E_0 = \left(E_{\max} + E_{\min}\right)/2, \qquad r = \frac{E_{\max} - E_{\min}}{E_{\max} + E_{\min}}. \tag{23}$$

Inverting this transformation we get,

$$E_{\max} = E_0\left(1 + r\right), \qquad E_{\min} = E_0\left(1 - r\right), \tag{24}$$

and the final expression for cell wall loosening becomes

$$E_\alpha = E\left(a_\alpha\right) = E_0\left(1 + r\frac{1 - a^m_\alpha}{1 + a^m_\alpha}\right). \tag{25}$$

Mechanical model details

We assign a mechanical energy to the tissue as a function of vertex positions. We can then minimise the mechanical energy with respect to vertex positions to find the current tissue configuration. To simplify notation, let $\mathcal{V}_\alpha$ be a set of vertices around the polygon representing cell α, ordered counter-clockwise. We will also have the set be cyclic, i.e., if the cell has V vertices, then $i \in \mathcal{V}_\alpha$, $i = 1, 2, \ldots, V$ implies $\mathbf{x}_{i+1} = \mathbf{x}_1$ when $i = V$ and $\mathbf{x}_{i-1} = \mathbf{x}_V$ when $i = 1$. This way we can uniquely define a wall compartment between two vertices.

The two main terms we are going to focus on is the work of the turgor pressure T_α, given by $-\int_{V_\alpha} T_\alpha dV_\alpha = -T_\alpha A_\alpha h$, and the elastic energy $\int_{V_\alpha} \psi_\alpha dV_\alpha$, where ψ_α is the elastic energy density $\frac{1}{2}\varepsilon_\alpha \colon \sigma_\alpha$, where the : represents the element-wise contraction of matrices. We will use form matrices M_α to write down a proxy to strain as

$$\varepsilon_\alpha = \frac{M_\alpha - M_\alpha^{(0)}}{\mathrm{Tr}\left(M_\alpha^{(0)}\right)}, \tag{26}$$

where $M_\alpha^{(0)}$ is a target shape matrix and where these shape matrices are given by,

$$M_{\alpha_{xx}} = \sum_{i \in \mathcal{V}_\alpha} \frac{n_i}{12}\left(x_i'^2 + x_i' x_{i+1}' + x_{i+1}'^2\right), \tag{27}$$

$$M_{\alpha_{yy}} = \sum_{i \in \mathcal{V}_\alpha} \frac{n_i}{12}\left(y_i'^2 + y_i' y_{i+1}' + y_{i+1}'^2\right), \tag{28}$$

$$\begin{aligned} M_{\alpha_{xy}} = M_{\alpha_{yx}} = \sum_{i \in \mathcal{V}_\alpha} \frac{n_i}{24} & \left(x_i' y_{i+1}' + 2x_i' y_i'\right. \\ & \left. + 2x_{i+1}' y_{i+1}' + x_{i+1}' y_i'\right), \end{aligned} \tag{29}$$

where the primed coordinates represent the translation transformation, $\mathbf{x}_i' = (x_i', y_i') = \mathbf{x}_i - \mathbf{X}_\alpha$, and $n_i = x_i' y_{i+1}' - x_{i+1}' y_i'$, $i \in \mathcal{V}_\alpha$. Also, we can easily compute the area with

$$A_\alpha = \frac{1}{2} \sum_{i \in \mathcal{V}_\alpha} n_i. \tag{30}$$

We make the approximation that the material is linear, isotropic, and uniform, which means that the constitutive equation is given by the ususal shape This means that stress under these assumptions has two free parameters, the Lamé constants μ and λ, and is given by

$$\sigma_\alpha = 2\mu\varepsilon_\alpha + \lambda I \mathrm{Tr}\left(\varepsilon_\alpha\right). \tag{31}$$

Another assumption that we make is that the Poisson ratio is small enough to disregard the second term of this expression. The factor 2μ is the auxin-dependent stiffness, yielding

$$\sigma_\alpha \approx E\left(a_\alpha\right) \varepsilon_\alpha. \tag{32}$$

Now we can write the energy density as $E\left(a_\alpha\right) \left|\left|\varepsilon_\alpha\right|\right|^2$, where $\left|\left|A\right|\right|^2 = A \colon A$. Integrating over the volume of the cell and summing the elastic term and turgor pressure for all cells, we arrive at the Hamiltonian

$$\mathcal{H} = \sum_\alpha \mathcal{H}_\alpha = \sum_\alpha \left[\frac{1}{2} A_\alpha E\left(a_\alpha\right) \frac{\left|\left|M_\alpha - M_\alpha^{(0)}\right|\right|^2}{\mathrm{Tr}^2\left(M_\alpha^{(0)}\right)} - A_\alpha T_\alpha\right], \tag{33}$$

where we factored out the cell height h since the minimum of this expression becomes independent from it. What remains is how to extract a longitudinal stress acting on each cell wall compartment.

Consider a composite wall of length l and cross section S made from two compartments A and B in parallel with different stiffness, E_A and E_B, under the same strain ε. The sum of the elastic energy in both compartments is $lSE_A\varepsilon^2/4 + lSE_B\varepsilon^2/4 = lS\bar{\sigma}\varepsilon/2$, i.e. $\varepsilon = 2\bar{\sigma}/\left(E_A + E_B\right)$. Therefore, $\sigma_A = E_A\varepsilon = 2E_A\bar{\sigma}/\left(E_A + E_B\right)$. A more rigorous derivation of the stress load division expression can be found in the last section of this supporting material. Note that we can approximate the turgor pressure by prescribing a value of stress, $\bar{\sigma}$, and bypass mechanical relaxation of the tissue. We will call this the uncoupled tissue approximation. Nevertheless, the pattern formation mechanism hinges on the assumption that the strain is the same on both compartments of the cell wall, meaning that we still have to estimate the strain a wall is under from average cell strain. In order to estimate that value, we interpolate strain between the two adjacent cells and project that value onto the wall to get the average longitudinal strain acting on that specific wall. Then, we can simply use the constitutive equation to get the longitudinal stress of each compartment based on their stiffness.

Table S1: Table of simulation parameters, their meaning and value or range. The parameters $M_\alpha^{(0)}$ were fitted such that the initial shape of the tissue (without auxin patterns) corresponds to a regular hexagonal lattice of side 1, M_α^{init}. From this initial stress configuration we can also extract $\bar{\sigma}$. Although we are interested in varying r, [2] suggests to be around $r = 2/3$ at the shoot apical meristem. Although not shown in the table, we chose to count auxin molecules such that $a_\alpha = 1$ corresponds to a concentration of 0.1μM. Due to numerical complexity difference, $t_{\max} = 2$ was used for the tissue-wide stress coupling model and $t_{\max} = 6$ for the disconnected tissue approximation. I is the 2×2 identity matrix.

symbol	meaning	value or range (a.u.)	Reference or means of determining
L	length unit	2.5μm	arbitrated
τ	time unit	1hr	arbitrated
γ^*	normalized auxin production rate	1	[3]
δ^*	normalized auxin decay rate	1	[3]
$\mathcal{D}$	diffusion magnitude	720	[4]
$\mathcal{P}$	active transport strength	3600	[4]
K	Michaelis-Menten constant	1	guess taken from [1]
η	stress-PIN coupling constant	$[1.0, 10.0]$	–
n	stress-PIN coupling power	3	guess taken from [1]
r	wall loosening effect	$[.30, .95]$	–
m	wall loosening power	2	guess taken from [1]
E_0	reference stiffness	300MPa	[5]
T_α	turgor pressure	1MPa $\forall\alpha$	[6]
$M_\alpha^{(0)}$	rest shape matrix	$\sim 0.53585I,\ \forall\alpha$	initial fit
$\bar{\sigma}$	normalized average stress	~ 0.49674MPa	computed from initial fit
Δt	simulation time step	10^{-4}hr	–
$t_{\max}$	total simulation time	2hr or 6hr	–

Algorithm and implementation details

The tissue geometry used was an hexagonal lattice in units such that the each side of each hexagon is of length $1L$. First we need the tissue in the vertex model and in the approximated model to have the same shape in the absence of auxin patterns, M_α^{init}, in order for the results between both approaches to be comparable. We minimise the difference between the end geometry and the current one with respect to $M_\alpha^{(0)}$, $\forall\alpha$, for the given T_α. After obtaining $M_\alpha^{(0)}$, we can then compute the stress acting currently on each wall. This stress value is what we will use as $\bar{\sigma}$.

We assume very different timescales for auxin transport and mechanical cue propagation through the tissue. This means that there is enough time for the tissue to relax to a local minimum in between auxin transport time steps, Δt. To simulate this model, we start by computing wall stress in the current configuration, calculate PIN density on all cell walls with (20), take a step Δt in the set of ODEs (19), with new auxin concentrations compute stiffness with (25), and, finally, minimise mechanical energy (33). This is done until the maximum simulation time $t_{\max}$ has been reached. The simulation parameters used can be found in Table S1.

Computationally the minimization procedure is the performance bottleneck. In order to overcome that, we used a gradient-based minimisation method (L-BFGS) and computed the gradient of (33), which is straightforward, albeit tedious.

Regarding boundary conditions, the outer vertices are free to expand due to turgor pressure and the boundary is considered to have null pressure. In regards to the auxin transport model, every flux across the boundary is set to zero (reflective boundary conditions). Also, to mitigate the influence of PIN competition in the boundary walls, we consider these compartments in contact with a compartment with the same mechanical properties.

Linear Stability Analysis

The auxin transport model in use is

$$\frac{da_\alpha}{d\tau} = 1 - a_\alpha + \mathcal{D} \sum_{\beta \in \mathcal{N}_\alpha} \frac{l^*_{\alpha\beta}}{A^*_\alpha} (a_\beta - a_\alpha) + \mathcal{P} \sum_{\beta \in \mathcal{N}_\alpha} \frac{l^*_{\alpha\beta}}{A^*_\alpha} \left[p_{\beta\alpha} \frac{a_\beta}{K + a_\beta} - p_{\alpha\beta} \frac{a_\alpha}{K + a_\alpha} \right], \tag{34}$$

where

$$p_{\alpha\beta} = \frac{f_{\alpha\beta}}{1 + \sum_{\xi \in \mathcal{N}_\alpha} \frac{l_{\alpha\xi}}{L_\alpha} f_{\alpha\xi}}, \tag{35}$$

$$f_{\alpha\beta} = f\left(\sigma_{\alpha\beta}\right) = \begin{cases} \eta \sigma_{\alpha\beta}^n, & \sigma_{\alpha\beta} > 0, \\ 0, & \sigma_{\alpha\beta} \leq 0, \end{cases} \tag{36}$$

and,

$$E_\alpha = E\left(a_\alpha\right) = E_0 \left(1 + r \frac{1 - a_\alpha^m}{1 + a_\alpha^m}\right) \tag{37}$$

Consider the case when all cells have the same auxin concentration $a_\alpha = 1$. All stiffnesses are the same and therefore we can regard the effect of turgor pressure as a constant stress of magnitude $\bar{\sigma}$ acting on all walls. As previously mentioned, two compartments of a strained wall will be under different stresses according to their stiffness difference. The stress acting on wall compartment between cells α and $\beta \in \mathcal{N}_\alpha$, facing cell α is

$$\sigma_{\alpha\beta} = \frac{2\bar{\sigma} E_\alpha}{E_\alpha + E_\beta}. \tag{38}$$

Therefore, all stiffnesses being the same, so are all stresses and, consequently, PIN densities. With these assumptions and conditions, $a_\alpha = 1$, $\forall \alpha$ is the trivial steady state of the system and no deformations other than pure inflation are present. This also means that for the specific case of a regular lattice, $l_{\alpha\beta}/L_\alpha$ is simply $1/R$, where R is the number of neighbours. Considering a regular lattice we can also factor out $W = L_\alpha^*/A_\alpha^* = (LL_\alpha)/A_\alpha$ as a lattice geometry dependent constant. For an hexagonal lattice of side L, $R = 6$ and $W = 4/\sqrt{3}$.

We can now expand auxin concentration around that state considering small perturbations to auxin ε_α, meaning we transform the system into $a_\alpha = 1 + \varepsilon_\alpha$ and, since ε_α is small, neglect higher order terms. The time evolution of this perturbation is

$$\frac{da_\alpha}{d\tau} = \frac{d\varepsilon_\alpha}{d\tau} = -\varepsilon_\alpha + \frac{\mathcal{D}W}{R} \sum_{\beta \in \mathcal{N}_\alpha} \left(\varepsilon_\beta - \varepsilon_\alpha\right) + \frac{\mathcal{P}W}{R} \sum_{\beta \in \mathcal{N}_\alpha} \left[p_{\beta\alpha} \frac{1 + \varepsilon_\beta}{K + 1 + \varepsilon_\beta} - p_{\alpha\beta} \frac{1 + \varepsilon_\alpha}{K + 1 + \varepsilon_\alpha}\right], \tag{39}$$

where we have yet to linearize the last term.

Expanding in Taylor series around $\varepsilon_\alpha = 0$ we can rewrite

$$\frac{1 + \varepsilon_\alpha}{K + 1 + \varepsilon_\alpha} = \frac{1}{K + 1} + \frac{K}{(K + 1)^2} \varepsilon_\alpha + O\left(\varepsilon^2\right). \tag{40}$$

The term $p_{\alpha\beta}$ is slightly less straightforward since it depends not only in the stress applied to the corresponding wall, but also on every other wall of cell α. Therefore, the Taylor expansion of $p_{\alpha\beta}$ becomes

$$p_{\alpha\beta} = \left[\left.\frac{f\left(\sigma_{\alpha\beta}\right)}{1 + \frac{1}{R} \sum_{\gamma \in \mathcal{N}_\alpha} f\left(\sigma_{\alpha\gamma}\right)}\right|_{\{\varepsilon\} = 0} + \left.\frac{\partial p_{\alpha\beta}}{\partial \varepsilon_\alpha}\right|_{\{\varepsilon = 0\}} \varepsilon_\alpha + \sum_{\gamma \in \mathcal{N}_\alpha} \left.\frac{\partial p_{\alpha\beta}}{\partial \varepsilon_\gamma}\right|_{\{\varepsilon = 0\}} \varepsilon_\gamma + O(\varepsilon^2). \tag{41}$$

The first term is simply

$$p_0 = \frac{f\left(\bar{\sigma}\right)}{1 + f\left(\bar{\sigma}\right)}, \tag{42}$$

given that at steady state all stresses are equal to $\bar{\sigma}$. For the second and third terms we need the quantity

$$\frac{\partial p_{\alpha\beta}}{\partial \varepsilon_\gamma} = \frac{\frac{\partial f_{\alpha\beta}}{\partial \varepsilon_\gamma}}{1 + \frac{1}{R} \sum_{\kappa \in \mathcal{N}_\alpha} f_{\alpha\kappa}} - \frac{1}{R} \sum_{\kappa \in \mathcal{N}_\alpha} \frac{f_{\alpha\beta} \frac{\partial f_{\alpha\kappa}}{\partial \varepsilon_\gamma}}{\left(1 + \frac{1}{R} \sum_{\lambda \in \mathcal{N}_\alpha} f_{\alpha\lambda}\right)^2}, \tag{43}$$

where, since stress will be always positive under these assumptions,

$$\frac{\partial f_{\alpha\beta}}{\partial \varepsilon_\gamma} = n\eta \sigma_{\alpha\beta}^{n-1} \frac{\partial \sigma_{\alpha\beta}}{\partial \varepsilon_\gamma}, \tag{44}$$

$$\frac{\partial \sigma_{\alpha\beta}}{\partial \varepsilon_\gamma} = \frac{2\bar{\sigma}}{\left(E_\alpha + E_\beta\right)^2} \left(E_\beta \frac{\partial E_\alpha}{\partial \varepsilon_\gamma} - E_\alpha \frac{\partial E_\beta}{\partial \varepsilon_\gamma}\right), \tag{45}$$

and

$$\frac{\partial E_\alpha}{\partial \varepsilon_\gamma} = E_0 r \delta_{\alpha\gamma} \frac{-2m\left(1+\varepsilon_\gamma\right)^{m-1}}{\left(1+\left(1+\varepsilon_\gamma\right)^m\right)^2}, \tag{46}$$

where $\delta_{\alpha\gamma}$ is the Kronecker delta ($\delta_{\alpha\beta} = 1$ when $\alpha = \beta$, 0 otherwise). Since these derivatives are evaluated in steady state, we have

$$\left.\frac{\partial E_\alpha}{\partial \varepsilon_\gamma}\right|_{\{\varepsilon=0\}} = -\frac{1}{2} E_0 m r \delta_{\alpha\gamma}, \tag{47}$$

,

$$\left.\frac{\partial \sigma_{\alpha\beta}}{\partial \varepsilon_\gamma}\right|_{\{\varepsilon=0\}} = \frac{\bar{\sigma} m r}{4}\left(\delta_{\beta\gamma} - \delta_{\alpha\gamma}\right), \tag{48}$$

and,

$$\left.\frac{\partial f_{\alpha\beta}}{\partial \varepsilon_\gamma}\right|_{\{\varepsilon=0\}} = f\left(\bar{\sigma}\right) \frac{nmr}{4}\left(\delta_{\beta\gamma} - \delta_{\alpha\gamma}\right) = \frac{1}{4} f\left(\bar{\sigma}\right) \mathcal{M}\left(\delta_{\beta\gamma} - \delta_{\alpha\gamma}\right), \tag{49}$$

where $\mathcal{M} = nmr$ contains just parameters related to the feedback between mechanics and PIN. Finally,

$$\left.\frac{\partial p_{\alpha\beta}}{\partial \varepsilon_\gamma}\right|_{\{\varepsilon=0\}} = \frac{1}{4} p_0 \mathcal{M}\left[\delta_{\beta\gamma} - \delta_{\alpha\gamma} - \frac{p_0}{R}\sum_{\kappa\in\mathcal{N}_\alpha}\left(\delta_{\kappa\gamma} - \delta_{\alpha\gamma}\right)\right] = \frac{1}{4} p_0 \mathcal{M}\left[\delta_{\beta\gamma} - \delta_{\alpha\gamma} + p_0\delta_{\alpha\gamma} - \frac{p_0}{R}\left(1 - \delta_{\alpha\gamma}\right)\right], \tag{50}$$

where we simplified $\sum_{k\in\mathcal{N}_\alpha} \delta_{\kappa\gamma} = 1 - \delta_{\alpha\gamma}$, since it is equal to 1 for $\gamma \in \mathcal{N}_\alpha$ or 0 for $\gamma \notin \mathcal{N}_\alpha$ and we are only interested in the two cases $\gamma = \alpha$ or $\gamma \in \mathcal{N}_\alpha$.
Now, substituting in (41), we get

$$p_{\alpha\beta} = p_0\left[1 + \frac{1}{4}\mathcal{M}\left(\left(\varepsilon_\beta - \varepsilon_\alpha\right) + p_0\varepsilon_\alpha - \frac{p_0}{R}\sum_{\gamma\in\mathcal{N}_\alpha}\varepsilon_\gamma\right)\right] + O(\varepsilon^2). \tag{51}$$

The active transport term is

$$\frac{\mathcal{P} W p_0}{R\left(K+1\right)}\left(\frac{K}{K+1} - \frac{\mathcal{M}}{2}\left(1 - \frac{p_0}{2}\right)\right)\sum_{\beta\in\mathcal{N}_\alpha}\left(\varepsilon_\beta - \varepsilon_\alpha\right) - \frac{\mathcal{P}\mathcal{M} W p_0^2}{4R^2\left(K+1\right)}\sum_{\beta\in\mathcal{N}_\alpha}\left[\sum_{\kappa\in\mathcal{N}_\beta}\varepsilon_\kappa - \sum_{\kappa\in\mathcal{N}_\alpha}\varepsilon_\kappa\right] + O\left(\varepsilon^2\right). \tag{52}$$

Finally, the linear approximation of the time evolution of the perturbation is

$$\frac{d\varepsilon_\alpha}{d\tau} = -\varepsilon_\alpha + \frac{W}{R}\left[\mathcal{D} + \frac{\mathcal{P} p_0}{K+1}\left(\frac{K}{K+1} - \frac{\mathcal{M}}{2}\left(1 - \frac{p_0}{2}\right)\right)\right]\sum_{\beta\in\mathcal{N}_\alpha}\left(\varepsilon_\beta - \varepsilon_\alpha\right) - \frac{\mathcal{P}\mathcal{M} W p_0^2}{4R^2\left(K+1\right)}\sum_{\beta\in\mathcal{N}_\alpha}\left[\sum_{\kappa\in\mathcal{N}_\beta}\varepsilon_\kappa - \sum_{\kappa\in\mathcal{N}_\alpha}\varepsilon_\kappa\right], \tag{53}$$

where

$$W = \frac{L^*}{A^*}, \qquad p_0 = \frac{f\left(\bar{\sigma}\right)}{1 + f\left(\bar{\sigma}\right)}, \qquad \mathcal{M} = nmr. \tag{54}$$

In this form the equation system resembles the class of ODEs studied in appendix A of [7], which we will closely follow. Now we expand ε_α in a Fourier series, exchanging the position of the center of cell α, $\mathbf{X}_\alpha$, with wave vectors $\mathbf{k}$,

$$\varepsilon_{\mathbf{k}} = \frac{1}{2\pi}\sum_\alpha \varepsilon_\alpha e^{-i\mathbf{k}\cdot\mathbf{X}_\alpha}. \tag{55}$$

Let the vectors $\mathbf{e}_p$ denote the vectors from the center of cell α to its $p = 1, 2, \ldots, R$ neighbour. We can define the lattice form factor as

$$S\left(\mathbf{k}\right) = \frac{1}{R}\sum_{p=1}^{R} e^{i\mathbf{k}\cdot\mathbf{e}_p} = \frac{1}{R}\sum_{p=1}^{R} e^{-i\mathbf{k}\cdot\mathbf{e}_p} = \frac{2}{R}\sum_{p=1}^{R/2}\cos\left(\mathbf{k}\cdot\mathbf{e}_p\right), \tag{56}$$

where the second and third equalities follows from considering a regular grid where for each direction p there is another directly opposed to it. This quantity is characteristic of the grid alone and we can rewrite it as

$$S\left(\mathbf{k}\right) = \frac{1}{R}\sum_{\beta\in\mathcal{N}_\alpha} e^{i\mathbf{k}\cdot\left(\mathbf{X}_\beta - \mathbf{X}_\alpha\right)} = \frac{1}{R}\sum_{\beta\in\mathcal{N}_\alpha} e^{-i\mathbf{k}\cdot\left(\mathbf{X}_\beta - \mathbf{X}_\alpha\right)}. \tag{57}$$

The temporal evolution of the quantity $\varepsilon_{\mathbf{k}}$ is

$$\frac{d\varepsilon_{\mathbf{k}}}{d\tau}=\frac{1}{2\pi}\sum_{\alpha}e^{-i\mathbf{k}\cdot\mathbf{X}_\alpha}\frac{d\varepsilon_\alpha}{d\tau}, \tag{58}$$

where we know $d\varepsilon_\alpha/d\tau$. We will treat the three terms in (53) separately. The first term is straightforward,

$$\frac{1}{2\pi}\sum_{\alpha}e^{-i\mathbf{k}\cdot\mathbf{X}_\alpha}\left(-\varepsilon_\alpha\right)=-\varepsilon_{\mathbf{k}}. \tag{59}$$

The second is[1]

$$\frac{1}{2\pi}\sum_{\alpha}e^{-i\mathbf{k}\cdot\mathbf{X}_\alpha}\mathcal{A}\sum_{\beta\in\mathcal{N}_\alpha}\left(\varepsilon_\beta-\varepsilon_\alpha\right)=\frac{\mathcal{A}}{2\pi}\left[\sum_{\alpha}\sum_{\beta\in\mathcal{N}_\alpha}e^{-i\mathbf{k}\cdot\mathbf{X}_\beta}e^{i\mathbf{k}\cdot\left(\mathbf{X}_\beta-\mathbf{X}_\alpha\right)}\varepsilon_\beta-R\varepsilon_{\mathbf{k}}\right]=\mathcal{A}R\left(S\left(\mathbf{k}\right)-1\right)\varepsilon_{\mathbf{k}}, \tag{60}$$

with $\mathcal{A}=\frac{W}{R}\left[\mathcal{D}+\frac{\mathcal{P}p_0}{K+1}\left(\frac{K}{K+1}-\frac{\mathcal{M}}{2}\left(1-\frac{p_0}{2}\right)\right)\right]$.
The third one is[2]

$$\begin{aligned}\frac{1}{2\pi}\sum_{\alpha}e^{-i\mathbf{k}\cdot\mathbf{X}_\alpha}\mathcal{B}\sum_{\beta\in\mathcal{N}_\alpha}\left[\sum_{\kappa\in\mathcal{N}_\beta}\varepsilon_\kappa-\sum_{\kappa\in\mathcal{N}_\alpha}\varepsilon_\kappa\right]&=\frac{\mathcal{B}}{2\pi}\left[\sum_{\alpha}\sum_{\beta\in\mathcal{N}_\alpha}\sum_{\kappa\in\mathcal{N}_\beta}e^{-i\mathbf{k}\cdot\mathbf{X}_\kappa}e^{i\mathbf{k}\cdot\left(\mathbf{X}_\kappa-\mathbf{X}_\beta\right)}e^{i\mathbf{k}\cdot\left(\mathbf{X}_\beta-\mathbf{X}_\alpha\right)}\varepsilon_\kappa-R^2S\left(\mathbf{k}\right)\right]\\&=\mathcal{B}R^2S\left(\mathbf{k}\right)\left(S\left(\mathbf{k}\right)-1\right)\varepsilon_{\mathbf{k}},\end{aligned} \tag{61}$$

where $\mathcal{B}=-\frac{\mathcal{P}\mathcal{M}Wp_0^2}{4R^2(K+1)}$. Therefore, adding these three terms together and rearranging we get

$$\frac{d\varepsilon_{\mathbf{k}}}{d\tau}=\left[-1+W\left(S\left(\mathbf{k}\right)-1\right)\left(\mathcal{D}+\frac{\mathcal{P}p_0}{K+1}\left[\frac{K}{K+1}-\frac{\mathcal{M}}{2}\left(1+\frac{p_0}{2}\left(S\left(\mathbf{k}\right)-1\right)\right)\right]\right)\right]\varepsilon_{\mathbf{k}}. \tag{62}$$

Therefore, the characteristic equation for a given $\mathbf{k}$ is simply an exponential growth or decay with coefficients

$$\lambda_{\mathbf{k}}=-1+W\left(S\left(\mathbf{k}\right)-1\right)\left(\mathcal{D}+\frac{\mathcal{P}p_0}{K+1}\left[\frac{K}{K+1}-\frac{\mathcal{M}}{2}\left(1+\frac{p_0}{2}\left(S\left(\mathbf{k}\right)-1\right)\right)\right]\right), \tag{63}$$

or equivalently, the characteristic equation is the eigenvalue problem $d/d\tau\left(\varepsilon_{\mathbf{k}}\right)=\lambda_{\mathbf{k}}\varepsilon_{\mathbf{k}}$ with eigenvalues $\lambda_{\mathbf{k}}$.
Since only S is a function of $\mathbf{k}$ and all other quantities are parameters, we can find what is the value of S that maximizes $\lambda_{\mathbf{k}}$, i.e. the value of S for the most unstable wave vector $\mathbf{k}^*$. This wave vector is the one which grows faster or decays slower meaning that at long times it will be the one that dominates the system. The value of $S^*=S\left(\mathbf{k}^*\right)$ obeys

$$\left.\frac{d\lambda_{\mathbf{k}}}{dS}\right|_{\mathbf{k}=\mathbf{k}^*}=W\left[\mathcal{D}+\frac{\mathcal{P}p_0}{K+1}\left(\frac{K}{K+1}-\frac{\mathcal{M}}{2}\left(1+p_0\left(S^*-1\right)\right)\right)\right]=0, \tag{64}$$

or, since in this case the eigenvalues are degenerate due to lattice symmetry, belonging to the set

$$\Omega=\left\{\mathbf{k}|S\left(\mathbf{k}\right)=1-\frac{\mathcal{M}-\frac{2K}{K+1}-\frac{2\mathcal{D}(K+1)}{\mathcal{P}p_0}}{\mathcal{M}p_0}\right\}. \tag{65}$$

A condition for patterns to exist is that $\left|S\left(\mathbf{k}\right)\right|\leq 1$ (by definition of S) , i.e.,

$$\mathcal{M}-\frac{2K}{K+1}-\frac{2\mathcal{D}\left(K+1\right)}{\mathcal{P}p_0}\geq 0, \tag{66}$$

---

[1] Where we can write

$$\sum_{\alpha}\sum_{\beta\in\mathcal{N}_\alpha}e^{-i\mathbf{k}\cdot\mathbf{X}_\beta}e^{i\mathbf{k}\cdot\left(\mathbf{X}_\beta-\mathbf{X}_\alpha\right)}\varepsilon_\beta=\sum_{\beta}\varepsilon_\beta e^{-i\mathbf{k}\cdot\mathbf{X}_\beta}\sum_{\alpha\in\mathcal{N}_\beta}e^{i\mathbf{k}\cdot\left(\mathbf{X}_\beta-\mathbf{X}_\alpha\right)}=RS\left(\mathbf{k}\right)\varepsilon_{\mathbf{k}}.$$

This amounts to reordering the terms being summed over on the condition the tissue is infinite.

[2] Where we rewrite,

$$\sum_{\alpha}\sum_{\beta\in\mathcal{N}_\alpha}\sum_{\kappa\in\mathcal{N}_\beta}e^{-i\mathbf{k}\cdot\mathbf{X}_\kappa}e^{i\mathbf{k}\cdot\left(\mathbf{X}_\kappa-\mathbf{X}_\beta\right)}e^{i\mathbf{k}\cdot\left(\mathbf{X}_\beta-\mathbf{X}_\alpha\right)}\varepsilon_\kappa=\sum_{\kappa}\varepsilon_\kappa e^{-i\mathbf{k}\cdot\mathbf{X}_\kappa}\sum_{\beta\in\mathcal{N}_\kappa}e^{i\mathbf{k}\cdot\left(\mathbf{X}_\kappa-\mathbf{X}_\beta\right)}\sum_{\alpha\in\mathcal{N}_\beta}e^{i\mathbf{k}\cdot\left(\mathbf{X}_\beta-\mathbf{X}_\alpha\right)}=R^2S^2\left(\mathbf{k}\right)\varepsilon_{\mathbf{k}},$$

which also amounts to reordering terms.

since $\mathcal{M}p_0 > 0$.
Another crucial condition is that the wave vector coefficient has to grow in order for the system to adopt the corresponding wave pattern, i.e., when the eigenvalue corresponding to the largest wave vector becomes positive, the fixed point we are expanding on becomes unstable and patterns form. Since we know what S should be for these wave vectors, the condition for pattern formation is

$$\lambda_{\mathbf{k}^*} = \lambda\left(S^*\right) = -1 + \frac{\mathcal{P}W}{4\left(K+1\right)\mathcal{M}}\left[\mathcal{M} - \frac{2K}{K+1} - \frac{2\mathcal{D}\left(K+1\right)}{\mathcal{P}p_0}\right]^2 > 0, \tag{67}$$

or rearranging,

$$\left[\mathcal{M} - \frac{2K}{K+1} - \frac{2\mathcal{D}\left(K+1\right)}{\mathcal{P}p_0}\right]^2 > \frac{4\left(K+1\right)\mathcal{M}}{\mathcal{P}W} > 0. \tag{68}$$

Thus, both conditions merge into just one,

$$\mathcal{M} - \sqrt{\frac{4\left(K+1\right)}{\mathcal{P}W}}\sqrt{\mathcal{M}} - \frac{2K}{K+1} - \frac{2\mathcal{D}\left(K+1\right)}{\mathcal{P}p_0} > 0, \tag{69}$$

where we always discard conditions where our parameters are negative. We can now solve for $\sqrt{\mathcal{M}}$ since it is just a second order polynomial. We take the only solution which yields $\sqrt{\mathcal{M}} > 0$ and square the result to obtain

$$\mathcal{M} > \frac{K+1}{\mathcal{P}W}\left[1 + \sqrt{1 + 2W\left(\frac{\mathcal{P}K}{\left(K+1\right)^2} + \frac{\mathcal{D}}{p_0}\right)}\right]^2. \tag{70}$$

Strain-based PIN regulation shows auxin spot focusing

With the stress-based PIN regulation assumption we were able to observe that patterns are more focused. In this section we show results that indicate that the same organising principle happens if we use a strain-based model instead. Consider the power law similar to Eq. 21 where, for positive strain,

$$f_{\alpha\beta} = f\left(\varepsilon_{\alpha\beta}\right) = \eta E_0^n \varepsilon_{\alpha\beta}^n. \tag{71}$$

Note that factoring out E_0 in this expression allows us to preserve the order of magnitude and units of η. Notice also that strain, in this case, is the same between compartments of the same wall. If we use this expression instead of the stress-based regulation of exocytosis/endocytosis ratio, we can model strain-based PIN regulation. Furthermore, the same approximation would now involve the computation of wall strain via $\bar{\varepsilon} = 2\bar{\sigma}/(E_\alpha + E_\beta)$ for each wall. Unfortunately, the range of values for which auxin patterns emerge differs from the stress-based one. We can compute this by following the same procedure of linear stability analysis for the stress-based model. The only difference arises in the expression (49), which changes to

$$\left.\frac{\partial f_{\alpha\beta}}{\partial \varepsilon_\gamma}\right|_{\{\varepsilon=0\}} = f\left(\frac{\bar{\sigma}}{E_0}\right)\mathcal{M}\left(\delta_{\beta\gamma} + \delta_{\alpha\gamma}\right). \tag{72}$$

This change ends up changing the pattern formation condition and most unstable wave vectors. The most unstable wave vectors belong to the set

$$\Omega = \left\{\mathbf{k}|S\left(\mathbf{k}\right) = 1 - \frac{\mathcal{M}p_0 - \frac{2K}{K+1} - \frac{2\mathcal{D}(K+1)}{\mathcal{P}p_0}}{\mathcal{M}p_0}\right\}, \tag{73}$$

and the condition for pattern formation is for the strain-based model,

$$\left(\mathcal{M}p_0 - \frac{2K}{K+1} - \frac{2D\left(K+1\right)}{\mathcal{P}p_0}\right)^2 > \frac{4\left(K+1\right)\mathcal{M}}{\mathcal{P}W} > 0, \tag{74}$$

which, solved for $\mathcal{M}$ yields

$$\mathcal{M} > \frac{K+1}{\mathcal{P}Wp_0^2}\left[1 + \sqrt{1 + 2W\left(\frac{\mathcal{P}Kp_0}{\left(K+1\right)^2} + \mathcal{D}\right)}\right]^2. \tag{75}$$

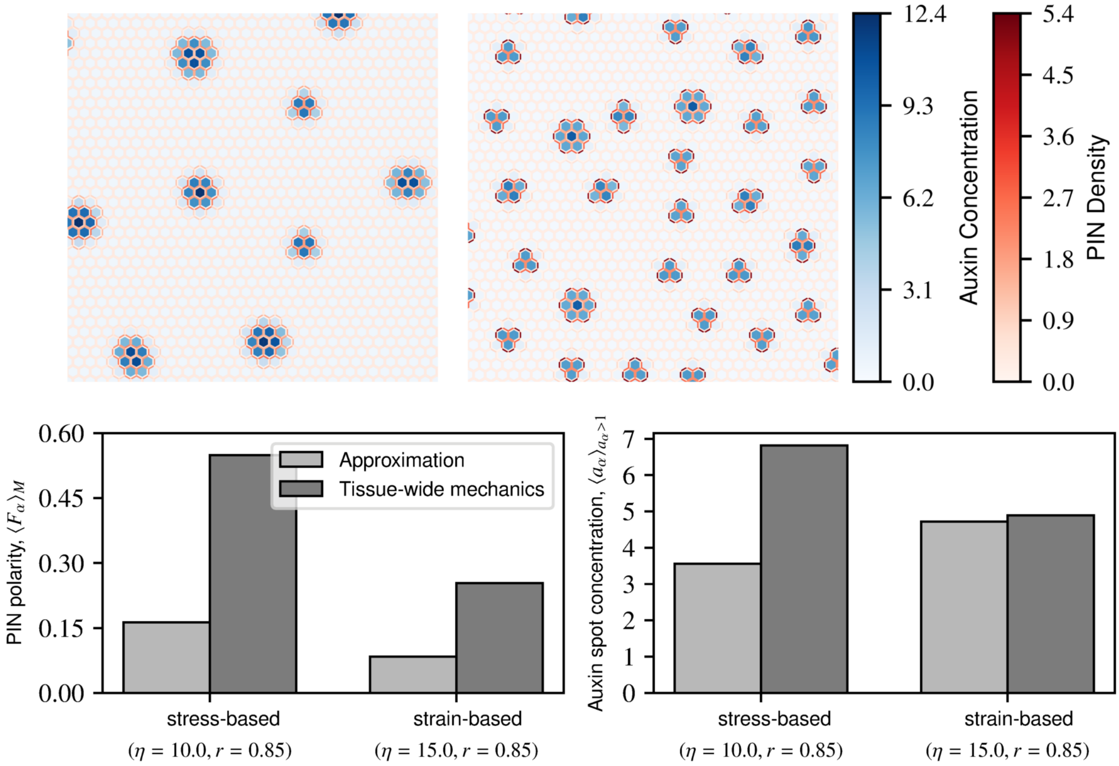

Figure S1: Simulations of the strain-based model (top) for the equivalent uncoupled tissue approximation (top left) and the tissue-wide mechanical model (top right). We quantified the same features as in the main text for the strain-based model as well as the stress-based model for comparison (bottom). Those are average PIN polarity (bottom left) and average auxin spot concentration (bottom right). Here we also observe auxin spot focusing and an enhancement of auxin flows when considering the tissue-wide model. The wavelength is also noticeably smaller even if spots are similar in size. Auxin concentrations, for the strain-based model, do not change much when considering tissue-wide mechanics.

Notably, we are able to explain why the wavelength of the stress-based PIN model is always lower than in the strain-based PIN model, a question raised in [8]. Comparing both expressions, since $0 \leq p_0 \leq 1$, the term $\mathcal{M}$ in the stress-based cased is replaced by $\mathcal{M}p_0 \leq \mathcal{M}$. Therefore, their relationship is the same for all parameter choices.

We performed simulations of the strain-based model and the corresponding approximation. We used $\eta = 15$ and $r = 0.85$. For this value of r, the threshold value of η for pattern formation for this model and parameters is around $\eta = 12.5$. We computed the PIN polarity and average auxin spot concentration as in the main text for the stress-based model. We show in Fig. S1 the results of the strain-based model simulations (Fig. S1 top) as well as PIN polarity and average auxin spot concentration for strain-based and stress-based models (Fig. S1 bottom) for the same r (we picked $\eta = 10$ for the stress-based case, the highest value of η in our data set). This is done to compare the qualitative behaviour change (from the approximated model to the tissue-wide model) between stress-based and strain-based models.

In accordance with the stress-based model, we observe for the strain-based model a higher PIN polarity when considering emerging strain patterns, as well as more focused spots and a lower pattern wavelength. In contrast, however, auxin spot sizes remain similar for the strain-based model and have similar levels of auxin on average. Yet, even though auxin levels are similar in the strain-based model the auxin spots themselves are again more distinguishable for the tissue-wide model like in the stress-based model.

It is also of note that even if the auxin levels are similar, the region near the threshold for this model remains unexplored and, as such, the sensitivity of auxin patterns to strain remains unknown for the strain-based model.

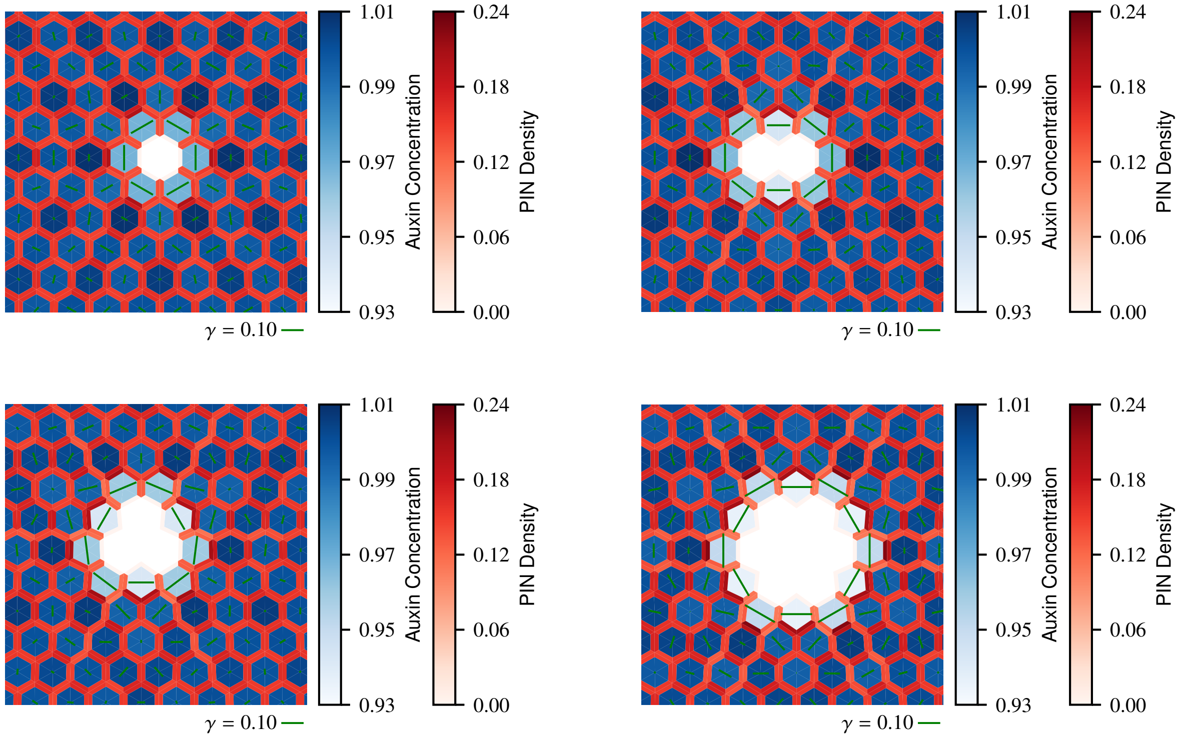

Figure S2: Ablation simulations for different wound sizes. Tissue-wide mechanical model predicts stress directions following the shape of the wound as shown by the ablation of two cells (top right). Green lines represent the magnitude and direction of principal stress, measured $\gamma = \frac{\lambda_+ - \lambda_-}{\lambda_+ + \lambda_-}$, where $\lambda_\pm$ are the largest and lowest eigenvalues of the stress tensor. The ablation perturbs auxin patterning by redirecting PIN. stress anisotropy increases slightly with wound size.

Stress follows ablation wound shape

We performed simulation for two, three and seven cells for the exact same parameters in the ablation simulation in the main text. We observe that the stress pattern follows the shape of the ablation wound closely (Fig. S2). It also shows a slight increase of stress anisotropy with wound size.

Noise in reference stiffness, E_0, is highly disruptive

The expression for total active auxin transport current is

$$\Delta J_{\mathrm{act}_{\alpha\to\beta}} = J_{\mathrm{act}_{\alpha\to\beta}} - J_{\mathrm{act}_{\beta\to\alpha}} = -\mathcal{P}_\alpha p_{\alpha\beta}\frac{a_\alpha}{K+a_\alpha} + \mathcal{P}_\beta p_{\beta\alpha}\frac{a_\beta}{K+a_\beta}, \tag{76}$$

where we have considered possible different active transport strengths, $\mathcal{P}_\alpha$ and $\mathcal{P}_\beta$. Note that K is less likely to be cell specific. The first thing we note is that a difference in turgor would change wall strain and stress. Since this would affect both walls, if no auxin difference exists, there would be zero$^{\text{th}}$ bias. Hence, we will focus on the prefactor $\mathcal{P}$ and reference stiffness E_0. Both of these introduce a zero$^{\text{th}}$ bias. We compare the sensitivity of $\Delta J_{\mathrm{act}_{\alpha\to\beta}}$ to a change of $\frac{\delta\mathcal{P}}{\mathcal{P}}$ and a change of $\frac{\delta E_0}{E_0}$ in one of the cells (i.e., $\mathcal{P}_\alpha = \mathcal{P}_\beta + \delta\mathcal{P} = \mathcal{P} + \delta\mathcal{P}$ and $E_{0_\alpha} = E_{0_\beta} + \delta E_0 = E_0 + \delta E_0$). If one carries this computation out, we get the expression, for auxin close to basal levels,

$$\frac{E_0 \left.\dfrac{\partial \Delta J_{\mathrm{act}_{\alpha\to\beta}}}{\partial \delta E_0}\right|_{a_\alpha = a_\beta = 1}}{\mathcal{P} \left.\dfrac{\partial \Delta J_{\mathrm{act}_{\alpha\to\beta}}}{\partial \delta \mathcal{P}}\right|_{a_\alpha = a_\beta = 1}} \approx \frac{n}{2}\left(1 - \frac{1}{6}\frac{\eta\bar{\sigma}^n}{1+\eta\bar{\sigma}^n}\right). \tag{77}$$

For the used parameters, this ratio is greater than 1 for all $\eta\bar{\sigma}^n$. This means that a relative change in stiffness implies a change in active current larger than a relative change in PIN content.

A derivation of wall stress load division including Poisson ratio

Consider the general constitutive equation for a linear elastic isotropic material and its inverse, in Einstein notation,

$$\sigma_{ij} = \frac{E}{1+\nu}\varepsilon_{ij} + \frac{\nu E}{(1+\nu)(1-2\nu)}\varepsilon_{kk}\delta_{ij}, \tag{78}$$

and

$$\varepsilon_{ij} = \frac{1}{E}\left((1+\nu)\sigma_{ij} - \nu\sigma_{kk}\delta_{ij}\right), \tag{79}$$

respectively. Here we are using $i, j = 1, 2, 3$ to be indices relating to three dimensions space. E is the Young's modulus and ν the Poisson ratio.

Consider now a wall of length l, height h and width w, composed of two compartments split equally along its length. Suppose these two compartments have different Young's modulus, E_α and E_β. If we assume that each compartment can be at rest simultaneously, then we have to assume that the strain is the same for either compartment, i.e., $\varepsilon_{ij_\alpha} = \varepsilon_{ij_\beta} = \varepsilon_{ij}$. The elastic energy of such a system is,

$$\Psi = \int_{\text{wall}} \frac{1}{2}\sigma_{ij}\varepsilon_{ij}dV = \frac{hwl}{4}\sigma_{ij_\alpha}\varepsilon_{ij} + \frac{hwl}{4}\sigma_{ij_\beta}\varepsilon_{ij}. \tag{80}$$

Substituting we can rewrite energy as

$$\Psi = \frac{hwl}{2}\left[\frac{\frac{E_\alpha+E_\beta}{2}}{1+\nu}\varepsilon_{ij}\varepsilon_{ij} + \frac{\nu\frac{E_\alpha+E_\beta}{2}}{(1+\nu)(1-2\nu)}\varepsilon_{kk}\varepsilon_{ll}\right], \tag{81}$$

which can be identified as the energy of an equivalent wall of with average stiffness. Since stress is by definition $\frac{\partial\psi}{\partial\varepsilon_{ij}}$ (where ψ is energy density), we get exactly the same form for the constitutive relation for the wall as a whole is

$$\sigma'_{ij} = \frac{\frac{E_\alpha+E_\beta}{2}}{1+\nu}\varepsilon_{ij} + \frac{\nu\frac{E_\alpha+E_\beta}{2}}{(1+\nu)(1-2\nu)}\varepsilon_{kk}\delta_{ij}. \tag{82}$$

Inverting it yields, predictably

$$\varepsilon_{ij} = \frac{2}{E_\alpha+E_\beta}\left((1+\nu)\sigma'_{ij} - \nu\sigma'_{kk}\delta_{ij}\right). \tag{83}$$

Note that $\varepsilon_{kk} = \frac{2(1-2\nu)}{E_\alpha+E_\beta}\sigma'_{kk}$. Consider wall face cell α. Its stress is, therefore,

$$\sigma_{ij_\alpha} = \frac{E_\alpha}{1+\nu}\varepsilon_{ij} + \frac{\nu E}{(1+\nu)(1-2\nu)}\varepsilon_{kk}\delta_{ij}, \tag{84}$$

which, substituting wall strain (both ε_{ij} and ε_{kk} expressions), results in

$$\sigma_{ij_\alpha} = \frac{E_\alpha}{1+\nu}\frac{2}{E_\alpha+E_\beta}\left[(1+\nu)\sigma'_{ij} - \nu\sigma'_{kk}\delta_{ij}\right] + \frac{\nu E_\alpha}{(1+\nu)(1-2\nu)}\frac{2(1-2\nu)}{E_\alpha+E_\beta}\sigma'_{kk}\delta_{ij}, \tag{85}$$

where the only remaining term is

$$\sigma_{ij_\alpha} = \frac{2E_\alpha\sigma'_{ij}}{E_\alpha+E_\beta}. \tag{86}$$

Therefore, for compartments of different stiffness, given an average wall stress we can compute how stress divides between compartments. This also validates the uncoupled tissue approximation even in the case of nonzero ν.

Note that for nonzero ν, even if strains are lower (as implied by the expression of ε_{kk}), a mismatch between neighbours still occurs. A local variation in stiffness, therefore would yield a strain field with the same organising principle and hence, stress patterns. Even if the Poisson ratio affects the relative magnitude of the auxin spot focusing and PIN polarity increase observed and discussed in the main text, it would always be present and aiding auxin pattern formation. We chose to set $\nu = 0$ to highlight these effects.

References

[1] M. G. Heisler, O. Hamant, P. Krupinski, M. Uyttewaal, C. Ohno, H. Jönsson, J. Traas, and E. M. Meyerowitz, “Alignment between PIN1 Polarity and Microtubule Orientation in the Shoot Apical Meristem Reveals a Tight Coupling between Morphogenesis and Auxin Transport,” *PLoS Biology*, vol. 8, p. e1000516, oct 2010.

[2] S. A. Braybrook and A. Peaucelle, “Mechano-Chemical Aspects of Organ Formation in Arabidopsis thaliana: The Relationship between Auxin and Pectin,” *PLoS ONE*, vol. 8, p. e57813, mar 2013.

[3] E. M. Kramer and E. M. Ackelsberg, “Auxin metabolism rates and implications for plant development,” *Frontiers in Plant Science*, vol. 6, pp. 1–8, mar 2015.

[4] H. L. Rutschow, T. I. Baskin, and E. M. Kramer, “The carrier AUXIN RESISTANT (AUX1) dominates auxin flux into Arabidopsis protoplasts,” *New Phytologist*, vol. 204, pp. 536–544, nov 2014.

[5] A. Weber, S. Braybrook, M. Huflejt, G. Mosca, A.-L. Routier-Kierzkowska, and R. S. Smith, “Measuring the mechanical properties of plant cells by combining micro-indentation with osmotic treatments,” *Journal of Experimental Botany*, vol. 66, pp. 3229–3241, jun 2015.

[6] L. Beauzamy, M. Louveaux, O. Hamant, and A. Boudaoud, “Mechanically, the shoot apical meristem of arabidopsis behaves like a shell inflated by a pressure of about 1 MPa,” *Frontiers in Plant Science*, vol. 6, no. NOVEMBER, pp. 1–10, 2015.

[7] P. Sahlin, B. Söderberg, and H. Jönsson, “Regulated transport as a mechanism for pattern generation: Capabilities for phyllotaxis and beyond,” *Journal of Theoretical Biology*, vol. 258, pp. 60–70, may 2009.

[8] J.-D. Julien, A. Pumir, and A. Boudaoud, “Strain- or stress-sensing in mechanochemical patterning by the phytohormone auxin,” *bioRxiv*, 2019.